Modern Aspects of Electrochemistry 53

Noam Eliaz *Editor*

Applications of Electrochemistry and Nanotechnology in Biology and Medicine II

Springer

MODERN ASPECTS OF ELECTROCHEMISTRY

No. 53

Series Editors:
Ralph E. White
Department of Chemical Engineering
University of South Carolina
Columbia, SC 29208

Constantinos G. Vayenas
Department of Chemical Engineering
University of Patras
Patras 265 00
Greece

Managing Editor:
Maria E. Gamboa-Aldeco
1107 Raymer Lane
Superior, CO 80027

For further volumes:
http://www.springer.com/series/6251

Noam Eliaz
Editor

Applications of Electrochemistry and Nanotechnology in Biology and Medicine II

Springer

Editor
Noam Eliaz
Faculty of Engineering
School of Mechanical Engineering
Tel-Aviv University
Ramat Aviv
Tel-Aviv 69978
Israel
neliaz@eng.tau.ac.il

ISSN 0076-9924
ISBN 978-1-4614-2136-8 e-ISBN 978-1-4614-2137-5
DOI 10.1007/978-1-4614-2137-5
Springer New York Dordrecht Heidelberg London

Library of Congress Control Number: 2011934050

Preface

The emergence of nanoscience and nanotechnology has led to new developments in and applications of electrochemistry. These two volumes of Modern Aspects of Electrochemistry, entitled: "Applications of Electrochemistry and Nanotechnology in Biology and Medicine," address both fundamental and practical aspects of several emerging key technologies. All Chapters were written by internationally renowned experts who are leaders in their area.

The Chapter by A. Heiskanen and J. Emnéus provides a lucid and authoritative overview of electrochemical detection techniques for real-time monitoring of the dynamics of different cellular processes. First, biological phenomena such as the cellular redox environment, release of neurotransmitters and other signaling substances based on exocytosis, and cellular adhesion, are discussed thoroughly. Next, the capabilities of electrochemical amperometric and impedance spectroscopic techniques in monitoring cellular dynamics are highlighted, in comparison to optical and other techniques. The applications of such techniques already include biosensors and microchip-based biological systems for cell biological research, medical research and drug development. Finally, the state-of-the-art and future developments, e.g. miniaturization of planar interdigitated electrodes in order to achieve a gap/width size regime on the nanometer scale and thus considerable signal amplification, are summarized.

Electron transfer by thermally activated hopping through localized centers is an essential element for a broad variety of vital biological and technological processes. The use of electrode/self-assembled monolayer (SAM) assemblies to explore fundamental aspects of long- and short-range electron exchange between electrodes and redox active molecules, such as proteins, is reviewed comprehensively in a Chapter by D.H. Waldeck and D.E. Khoshtariya. The authors, who are pioneers in this area, nicely demonstrate that such bioelectrochemical devices with nanoscopically tunable physical properties provide a uniquely powerful system for fundamental electron transfer studies and nanotechnological applica-

tions. Studies on protein systems also reveal how the binding motif of the protein to the electrode can be changed to manipulate its behavior, thus offering many promising opportunities for creating arrays of redox active biomolecules.

A microbial fuel cell (MFC) is a bio-electrochemical transducer that converts microbial biochemical energy directly to electrical energy. In their authoritative Chapter, J. Greenman, I.A. Ieropoulos and C. Melhuish overview lucidly the principles of biofilms, biofilm electrodes, conventional fuel cells, and MFCs. Potential applications of both biofilm electrodes and MFCs are suggested, including sensing, wastewater treatment, denitrification, power packs, and robots with full energy autonomy. The symbiotic association between microbial life-forms and mechatronic systems is discussed in detail by the authors, who are internationally renowned experts in this field.

The last three chapters in Volume I deal with surface modification of implants, namely surface biofunctionalization or coating. First, R. Guslitzer-Okner and D. Mandler provide concise survey of different electrochemical processes (electrodeposition, electrophoretic deposition, microarc deposition, electropolymerization, and electrografting) to form different coatings (conducting polymers, non-conducting polymers, sol-gel inorganic-organic polymer materials, oxides, ceramics, bioglass, hydroxyapatite and other calcium phosphates) on different substrates (titanium and its alloys, stainless steels, cobalt-chrome alloys, nitinol, and magnesium alloys). The authors who are highly experienced in this field demonstrate the applicability of these coatings for medical devices such as drug eluting stents and orthopedic implants.

Different electrochemical processes to render metal implants more biofunctional and various electrochemical techniques to characterize the corrosion resistance of implants or the adsorption of biomolecules on the surface are reviewed by T. Hanawa in his authoritative Chapter. Electrodeposition of calcium phosphates or polyethylene glycol (PEG), as well as anodizing and micro-arc oxidation processes to obtain TiO_2 nanotube-type oxide film on Ti substrate, or electrochemical treatment to obtain nickel-free oxide layer on nitinol alloys, are described. The effects of different surfaces on phenomena such as cell adhesion, bacterial attachment and calcification are presented.

The last Chapter in Volume I, by T. Kokubo and S. Yamaguchi, lucidly summarizes the pioneering work and inventions of these authors in the field of bone-bonding bioactive metals for orthopedic and dental implants. The metals include titanium, zirconium, niobium, tantalum and their alloys. The main surface modification technique presented in this chapter is chemical, followed by heat treatment, although other techniques such as ion implantation, micro-arc treatment, hydrothermal treatment and sputtering are also described. The bone-bonding ability of metals with modified surfaces is attributable to the formation of apatite on their surface in the body environment, which can be interpreted in terms of the electrostatic interaction of the metal surface with the calcium or phosphate ions in a body fluid. These findings open numerous opportunities for future work.

Volume II begins with a Chapter by P.S. Singh, E.D. Goluch, H.A. Heering and S.G. Lemay which provides a lucid overview of the fundamentals and applications of nanoelectrochemistry in biology and medicine. First, some key concepts related to the double layer, mass transport and electrode kinetics and their dependence on the dimension and geometry of the electrode are discussed. Next, various fabrication schemes utilized in making nano-sized electrodes are reviewed, along with the inherent challenges in characterizing them accurately. Then, the "mesoscopic" regime is discussed, with emphasis on what happens when the Debye length becomes comparable to the size of the electrode and the diffusion region. Quantum-dot electrodes and charging and finite-size effects seen in such systems are also described. Then, recent advances in the electrochemistry of freely-diffusing single molecules as well as electrochemical scanning probe techniques used in the investigations of immobilized biomolecules are presented by the authors, who have pioneered several of the developments in this area. Finally, a brief survey of the applications of nanoelectrodes in biosensors and biological systems is provided.

During the last decade, nanowire-based electronic devices emerged as a powerful and universal platform for ultra-sensitive, rapid, direct electrical detection and quantification of biological and chemical species in solution. In their authoritative Chapter, M. Kwiat and F. Patolsky describe examples where these novel electrical devices can be used for sensing of proteins, DNA, viruses

and cells, down to the ultimate level of a single molecule. Additionally, nanowire-based field-effect sensor devices are discussed as promising building blocks for nanoscale bioelectronic interfaces with living cells and tissues, since they have the potential to form strongly coupled interfaces with cell membranes. The examples described in this chapter demonstrate nicely the potential of these novel devices to significantly impact disease diagnosis, drug discovery and neurosciences, as well as to serve as powerful new tools for research in many areas of biology and medicine.

The Human Genome Project has altered the mindset and approach in biomedical research and medicine. Currently, a wide selection of DNA microarrays offers researchers a high throughput method for simultaneously evaluating large numbers of genes. Electrochemical detection-based DNA arrays are anticipated to provide many advantages over radioisotope- or fluorophore-based detection systems. Due to the high spatial resolution of the scanning electrochemical microscope (SECM), this technology has been suggested as a readout method for locally immobilized, micrometer-sized biological recognition elements, including a variety of DNA arrays with different formats and detection modes. In his concise review, K. Nakano explains the underlying electrochemistry facets of SECM and examines how it can facilitate DNA array analysis. Some recent achievements of Nakano and his colleagues in SECM imaging of DNA microdots that respond toward the target DNA through hybridization are presented.

Biological membranes are the most important electrified interfaces in living systems. They consist of a lipid bilayer incorporating integral proteins. In view of the complexity and diversity of the functions performed by the different integral proteins, it has been found convenient to incorporate single integral proteins or smaller lipophilic biomolecules into experimental models of biological membranes (i.e. biomimetic membranes), so as to isolate and investigate their functions. Biomimetic membranes are common in pharmaceuticals, as well as for the investigation of phase stability, protein-membrane interactions, and membrane-membrane processes. They are also relevant to the design of membrane-based biosensors and devices, and to analytical platforms for assaying membrane-based processes. The last two chapters in Volume II are dedicated to these systems. In their thorough Chapter, R. Guidelli and L. Becucci overview the principles and types of biomimetic

membranes, the advantages and disadvantages of these systems, their applications, their fabrication methodologies, and their investigation by electrochemical techniques – mainly electrochemical impedance spectroscopy (EIS). This authoritative Chapter was written by two authors who are among the leaders in the field of bioelectrochemistry worldwide.

Ion channels represent a class of membrane spanning protein pores that mediate the flux of ions in a variety of cell types. They reside virtually in all the cell membranes in mammals, insects and fungi, and are essential for life, serving as key components in inter- and intracellular communication. The last Chapter in Volume II, by E.K. Schmitt and C. Steinem, provides a lucid overview of the potential of pore-suspending membranes for electrical monitoring of ion channel and transporter activities. The authors, who are internationally acclaimed experts in this area, have developed two different methods to prepare pore-suspending membranes, which both exhibit a high long-term stability, while they are accessible from both aqueous sides. The first system, nowadays known as nano black lipid membrane (nano-BLM), allows for ion channel recordings on the single channel level. The second system – pore-suspending membranes obtained from fusing unilamellar vesicles on a functionalized porous alumina substrate – enables to generate membranes with high protein content. The electrochemical analysis of these systems is described thoroughly in this chapter, and is largely based on EIS.

I believe that the two volumes will be of interest to electrochemists, chemists, materials, biomedical and electrochemical engineers, surface scientists, biologists and medical doctors. I hope that they become reference source for scientists, engineers, graduate students, college and university professors, and research professionals working both in academia and industry.

I wish to thank Professor Eliezer Gileadi who was the driving force making me edit these two volumes. I dedicate this project to my wife Billie, our two daughters – Ofri and Shahaf, and our newborn – Shalev, for their infinite love and support.

N. Eliaz
Tel-Aviv University
Tel-Aviv, Israel

Professor Noam Eliaz

Noam Eliaz is an Associate Professor at Tel-Aviv University, Israel, where he serves as the Head of The Biomaterials and Corrosion Laboratory and as the first Head of the multi-faculty Materials and Nanotechnologies Program. He also serves as a Chief Editor of the journal *Corrosion Reviews* (jointly with Professor Ron Latanision). He received his B.Sc. and Ph.D. (direct track) in Materials Engineering, both *cum laude*, from Ben-Gurion University. After completing his doctorate, he became the first ever materials scientist to receive, simultaneously, a Fulbright postdoctoral award and a Rothschild postdoctoral fellowship. He then worked for two years in the H.H. Uhlig Corrosion Laboratory at M.I.T. To-date, he has contributed more than 220 journal and conference publications, including 28 invited talks, as well as 4 book chapters. He is currently editing a book on *Degradation of Implant Materials*, to be published by Springer during 2011. He has garnered numerous accolades, including the T.P. Hoar Award for the best paper published in *Corrosion Science* during 2001 (with co-authors), the 2010 Herbert H. Uhlig Award granted by NACE International in recognition of outstanding effectiveness in postsecondary corrosion education, and the 2012 NACE Fellow award. His main research interests include corrosion, electrodeposition, biomaterials and bio-ferrography.

Contents

Chapter 2

INTERFACING BIOMOLECULES, CELLS AND TISSUES WITH NANOWIRE-BASED ELECTRICAL DEVICES

Moria Kwiat and Fernando Patolsky

Chapter 3

SCANNING ELECTROCHEMICAL MICROSCOPY IMAGING OF DNA ARRAYS FOR HIGH THROUGHPUT ANALYSIS APPLICATIONS

Koji Nakano

Chapter 4

ELECTROCHEMISTRY OF BIOMIMETIC MEMBRANES

Rolando Guidelli and Lucia Becucci

List of Contributors, MAE 53

Dr. Lucia Becucci
Biolectrochemistry Laboratory, Deptartment of Chemistry, Florence University, Via della Lastruccia 3
50019 Sesto Fiorentino, Firenze, Italy
lucia.becucci@unifi.it

Dr. Edgar D. Goluch
Kavli Institute of Nanoscience, Delft University of Technology, Lorentzweg 1, 2628 CJ Delft, The Netherlands

Professor Rolando Guidelli
Biolectrochemistry Laboratory, Deptartment of Chemistry, Florence University, Via della Lastruccia 3
50019 Sesto Fiorentino, Firenze, Italy
guidelli@unifi.it
http://cf.chim.unifi.it

Professor Hendrik A. Heering
Leiden Institute of Chemistry, Leiden University, Einsteinweg 55, 2333 CC Leiden, The Netherlands

Moria Kwiat
School of Chemistry, Raymond and Beverly Sackler Faculty of Exact Sciences, Tel-Aviv University, Tel-Aviv 69978, Israel

Professor Serge G. Lemay
MESA$^+$ Institute and Faculty of Science and Technology, University of Twente, P.O. Box 217, 7500 AE Enschede, The Netherlands
s.g.lemay@utwente.nl
http://www.utwente.nl/tnw/ni/people/Serge_Lemay

Professor Koji Nakano
Department of Applied Chemistry, Faculty of Engineering, Kyushu University, 744 Motooka, Nishi-ku, Fukuoka 819-0395, Japan.
nakano@cstf.kyushu-u.ac.jp
http://hyoka.ofc.kyushu-u.ac.jp/search/details/K001258/english.html.

Professor Fernando Patolsky
School of Chemistry, Raymond and Beverly Sackler Faculty of Exact Sciences, Tel-Aviv University, Tel-Aviv 69978, Israel
fernando@post.tau.ac.il
http:// www5.tau.ac.il/~maxv/patolsky/

Dr. Eva K. Schmitt
Nuffield Department of Clinical Laboratory Science, John Radcliffe Hospital, University of Oxford, Oxford OX3 9DU, United Kingdom
eva.schmitt@chemie.uni-goettingen.de

Dr. Pradyumna S. Singh
Kavli Institute of Nanoscience, Delft University of Technology, Lorentzweg 1, 2628 CJ Delft, The Netherlands
P.S.Singh@utwente.nl

Professor Claudia Steinem
Institute of Organic and Biomolecular Chemistry, University of Göttingen, Tammannstr. 2, 37077 Göttingen, Germany
Claudia.Steinem@chemie.uni-goettingen.de
http://www.steinem.chemie.uni-goettingen.de

1

Nanoelectrochemistry: Fundamentals and Applications in Biology and Medicine

Pradyumna S. Singh,[1] Edgar D. Goluch,[1] Hendrik A. Heering,[2] and Serge G. Lemay[1,3]

[1]*Kavli Institute of Nanoscience, Delft University of Technology, Lorentzweg 1, 2628 CJ Delft, The Netherlands*
[2]*Leiden Institute of Chemistry, Leiden University, Einsteinweg 55, 2333 CC Leiden, The Netherlands*
[3]*MESA+ Institute and Faculty of Science and Technology, University of Twente, P.O. Box 217, 7500 AE Enschede, The Netherlands.*

I. INTRODUCTION

The compound word nanoelectrochemistry comprises the prefix *nano* and the noun *electrochemistry*. Both these components by themselves encompass a vast variety of meanings and envelop enormously diverse areas of scientific inquiry. For example, it can be argued that all of molecular electrochemistry occurs on a scale much smaller than nano—i.e., the molecular scale. The most basic aspects of a simple heterogeneous electron transfer reaction, from the description of the electrical double layer in the vicinity of the electrode to the theories for electron transfer and finally the reactants and products of such a reaction are all microscopic entities.

N. Eliaz (ed.), *Applications of Electrochemistry and Nanotechnology in Biology and Medicine II*, Modern Aspects of Electrochemistry 53,
DOI 10.1007/978-1-4614-2137-5_1,

Here, our primary focus will be on the fundamental and practical consequences of working with electrode systems with lateral dimensions that are below 100 nm. In some instances we will also consider nano-gap electrodes, where although the electrodes themselves are micrometer scale, they are separated from another electrode by distances < 100 nm. We will only deal with systems that involve some manner of *electron transfer* between molecules in solution and an electrode.

Therefore, although they may, in a sense, be considered *electrochemical*, we will refrain from considering advances in areas such as nanowires[1-3] and other low-dimensional nanomaterials[4-6] and nanopores[7]—areas which have witnessed great fundamental advances in the last decade and hold tremendous potential for analytical, biological, bio-medical and energy-related applications. We will also refrain from addressing the areas of solid-state electrochemistry as applicable in battery and fuel-cell research. The progress in using nanostructured materials as electrodes in these areas holds great promise, but again lies outside the scope of this chapter.[8-12] Finally, also omitted for purposes of brevity are electrodes based on arrays of nanoparticles or carbon nanotubes. In the last two decades carbon nanotubes as electrode materials of nanoscale dimensions and as components of sensing systems (for example, field-effect transistors (FETs) etc.) have received considerable attention, perhaps more than any other material. The accumulated body of literature is hence enormous and the interested reader is again referred to more specialized reviews.[13-16]

The underlying motivation for many researchers exploring nanoelectrochemistry is that shrinking the dimensions of electrodes is rife with many unexplored and potentially exciting fundamental phenomena that are, in principle, inaccessible to electrochemistry done on the macro-scale. Therefore, we attempt to provide a general appraisal of the promises inherent in nanoelectrochemistry, the progress made towards the realization of some of these goals, and finally the challenges that lie ahead.

The efforts to shrink dimensions of electrodes down to the nanoscale regime can be considered the logical denouement of a process than began nearly three decades ago with the introduction of microelectrodes and ultramicroelectrodes (UMEs). The expectation is that the key advantages of enhanced mass-transport and relatively easy access to the steady-state regime (on account of the

diffusion length being much larger than the dimension of the electrode) that came with the advent of UMEs will be further amplified as the electrode is made smaller still. While this is undoubtedly true, it is merely one among many other interesting possibilities that result from nanoscale electrodes.

Besides the critical dimension of the electrode itself, two other crucial scales are the double-layer thickness (or Debye length (*vide infra*)) and the number of molecules being probed at the electrode. An interesting question is what happens when the size of the electrode is of the same order or smaller than the Debye length. For a typical 0.1 M, 1:1 electrolyte at 25°C, the Debye length is about 1 nm. It is thus readily apparent that in order for the scale of the electrode to approach that of the double layer thickness, at least one dimension of the electrode will have to be on the order of 1 nm! This points to the fundamental difficulty in approaching truly nanoscale phenomena via the means of electrochemistry. Another interesting scale that opens up for investigation, particularly in the context of nano-gap electrodes, is the number of molecules being probed. As electrode dimensions shrink, it becomes possible to utilize them to electrochemically detect molecules in and across confined spaces such as membranes and cells. Thus, when dealing with a small, finite number of molecules, one enters a regime where the discreteness of individual molecules cannot always be ignored. The culmination of this scale is the single-molecule limit where individual molecules are probed, and interesting dynamical properties masked by ensemble averages can be revealed.

The present chapter is structurally organized on the basis of these disparate scales. Although in all instances our focus will be on nano-sized electrodes, we start off with the *classical* regime, wherein the Debye length is still shorter than the dimension of the electrode and ensemble averages of molecules are being probed. We briefly introduce some key concepts related to the double layer, mass transport and electrode kinetics and their dependence on the dimension and geometry of the electrode. We review various fabrication schemes utilized in making nano-sized electrodes, and discuss the inherent challenges in characterizing them accurately. We then move to discuss the *mesoscopic* regime—dimensions in which one or more of the assumptions of the *classical* regime break down. In particular, we discuss what happens when the De-

bye length becomes comparable to the size of the electrode and the diffusion region. We then discuss finite particle number fluctuations in the vicinity of the nanoelectrodes. We conclude the Section with a discussion on quantum-dot electrodes and charging and finite-size effects seen in these systems. We move in the next Section to the *single-molecule* limit and discuss the recent advances in the electrochemistry of freely-diffusing single molecules as well as electrochemical scanning probe techniques used in the investigations of immobilized biomolecules. We conclude the chapter with a brief survey of the applications of nanoelectrodes in biosensors and biological systems.

II. THE CLASSICAL REGIME

We begin our survey of nanoscale electrochemical measurements by focusing on cases in which no new effects appear upon downscaling, but rather where the formalisms that apply on the micrometer scale or higher are sufficient to explain observations. There are basically two different ways in which nanometer-scale dimensions can be introduced into electrochemical systems.

First, it is possible to scale down the size of the working electrode such that its lateral dimensions are nanometric. These experiments are essentially equivalent to those performed at ultramicroelectrodes, except that the smaller dimensions of the electrodes yield further enhancements in performance. These advantages include the ability to achieve a true steady-state in extremely short times, as well as the possibility of reaching higher current densities. The latter is particularly relevant for measuring fast heterogeneous kinetics.

Second, it is possible to create situations in which two or more electrodes or surfaces (each of which may or may not be nanometric in size) are separated by nanometer-scale distances. This has been most famously exploited in thin-layer cells and in the so-called positive feedback mode of scanning electrochemical microscopy (SECM), in which oxidation and reduction taking place at separate, closely spaced electrodes lead to enhanced mass transport.

1. Theory

Because heterogeneous kinetics feature prominently in the experiments reviewed below, we begin by briefly reviewing the relevant theory at the level of Butler-Volmer kinetics. While this topic will already be familiar to many readers, we aim through our exposition to bring particular attention to the role played by the electrode geometry in determining the predicted voltammogram shape.

We consider a simple outer-sphere heterogeneous electron-transfer reaction at an electrode surface, $O + e^- \leftrightarrows R$. O and R are present in the bulk solution at concentrations ${C_O}^b$ and ${C_R}^b$, respectively. We further assume the presence of a large excess of inert salt, such that mass transport in this simple system will be determined by the diffusion of the species O and R to or from the surface. Finally, we also assume for notational simplicity that the diffusion coefficients for O and R have an identical value, D. Quite generally for any electrode of finite size immersed in a volume of much larger size in all three dimensions (a condition which nearly always applies to nanoelectrodes immersed in a macroscopic volume), a true steady-state limiting current exists. The total rate of mass transport of O from the bulk solution to the electrode, J_O, can then be written as[17]

$$J_O = D(C_O^b - C_O^e)b \tag{1}$$

Here, ${C_O}^e$ is the concentration of O at the electrode surface (to be determined further into the calculation), while b is a parameter with units of length that characterizes the electrode geometry. The parameter b can be thought of consisting of two components: a numerical constant that depends only on the *shape* of the electrode, multiplied by a characteristic length that characterizes the *size* of the electrode. Determining the value of b is equivalent to solving the diffusion equation for this particular geometry. A well-known example is a shrouded semi-hemispherical electrode of radius R, for which $b = 2\pi R$. The corresponding expression for the rate of mass transport of reduced species R from the electrode surface to the bulk can be written as

$$J_R = D\left(C_R^e - C_R^b\right)b \tag{2}$$

Finally, the heterogeneous kinetics at the electrode surface are described by the Butler-Volmer (BV) expression

$$i = FA(k_f C_{\mathrm{O}}^e - k_b C_{\mathrm{R}}^e) \tag{3}$$

where i is the reduction current at the electrode (using the convention that *reduction* corresponds to a positive current), F is Faraday's constant, A is the area of the electrode, and the forward and backward rates are given by

$$\begin{aligned} k_f &= k^0 \exp\left(-\alpha f \eta\right) \\ k_b &= k^0 \exp\left((1-\alpha) f \eta\right) \end{aligned} \tag{4}$$

In the latter expressions k^0 is the standard heterogeneous rate constant, α is the transfer coefficient,[220] $\eta = (E - E^0)$ is the overpotential and $f = F/RT$ with R the gas constant and T the temperature.

Steady-state requires that the rate of mass transport of O, the rate of mass transport of R, and the net rate of electron transfer at the interface be equal: $i = FJ_{\mathrm{R}} = FJ_{\mathrm{O}}$. Applying this condition turns Eqs. (1), (2), and (3) into a set of three algebraic equations in three unknowns (the current i and the two surface concentrations C_{O}^e and C_{R}^e). These are easily solved, yielding for the current

$$i = \frac{C_{\mathrm{O}}^b e^{-\alpha f \eta} - C_{\mathrm{R}}^b e^{(1-\alpha) f \eta}}{e^{-\alpha f \eta} + e^{(1-\alpha) f \eta} + Db / Ak^0} \cdot FDb \tag{5}$$

For the special case of a pure oxidation reaction, $C_{\mathrm{O}}^b = 0$, this expression takes a simpler form,

$$i = -\frac{i_{\mathrm{lim}}}{1 + e^{-f\eta} + (Db / Ak^0) e^{-(1-\alpha) f \eta}} \tag{6}$$

Here we also introduced the so-called diffusion-limited current, i_{lim}, whose value is given by $i_{\mathrm{lim}} = FDC_{\mathrm{R}}^b b$.

Equation (6) indicates that the relative importance of heterogeneous kinetics compared to mass transport is entirely determined by the dimensionless ratio

$$\lambda = \frac{Ak^0}{Db} \tag{7}$$

a quantity known as the dimensionless rate constant. In the limit of very fast kinetics, $k^0 >> Db/A$ or, equivalently, $\lambda >> 1$, Eq. (6) reduces to the fully reversible result obtained from the Nernst equation. Redox species at the electrode surface are then in local equilibrium with the surface, and the heterogeneous kinetic parameters do not affect the shape of the voltammogram. Once λ becomes sufficiently small, however, kinetics begin to have an appreciable impact. As a rule of thumb, this occurs when λ decreases below a value of 10.

Very importantly, Eq. (6) indicates that the geometry influences the relative importance of kinetics through two closely related, yet separate, mechanisms. First, it determines the area A and, hence, the total electron transfer rate at a given surface concentration. Second, it influences the rate of mass transport of both R and O, as expressed by the parameter b. This makes it clear why electrodes with smaller dimensions are more sensitive to heterogeneous kinetics: for a given shape of electrode, scaling all the dimensions simultaneously by a factor γ causes A to change by a factor γ^2 and b by a factor γ, leading to a net change of λ by a factor γ. More simply put, shrinking all dimensions by a factor of 10 reduces the electrode area by a factor of 100 and is equivalent to speeding mass transport by a factor of 10.

The dual role played by geometry can, however, easily mislead our intuition, as we now illustrate through two numerical examples. First, consider the simple case of a shrouded semihemispherical electrode of radius R, as shown in Fig. 1a. In this case the area is simply given by $A = 2\pi R^2$, while $b = 2\pi R$, as discussed above. In this case Eq. (6) reduces to a more recognizable expression,

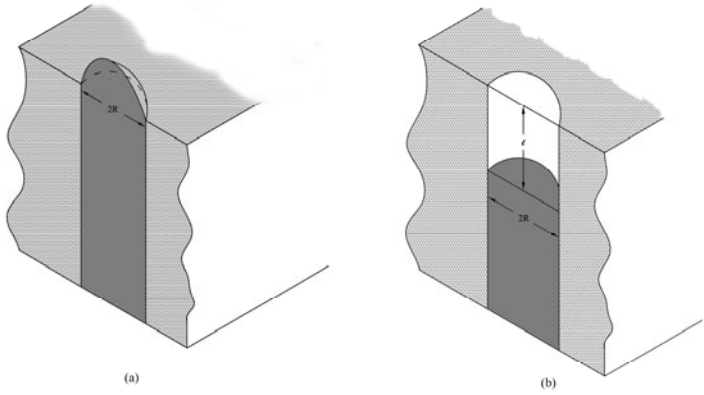

Figure 1. Sketch showing a cross-section of (a) a hemispherical electrode embedded in an insulator and (b) a disk electrode recessed a distance l into the surface of the insulator.

$$i = -\frac{i_{\lim}}{1 + e^{-f\eta} + (D/k^0 R)e^{-(1-\alpha)f\eta}} \tag{8}$$

Second, consider a disk electrode that is recessed a distance l into the surface, as sketched in Fig. 1b. Solving the diffusion equation for this system yields[18]

$$i_{\lim} = -\frac{4FDC_R^b R}{1 + 4l/\pi R} \approx -\frac{\pi FDC_R^b R^2}{l} \qquad l >> R \tag{9}$$

where the last simplification holds when $l >> R$. Substituting the corresponding values $A = \pi R^2$ and $b = \pi R^2/l$ into Eq. (6) yields for the current

$$i = -\frac{i_{\lim}}{1 + e^{-f\eta} + (D/lk^0)e^{-(1-\alpha)f\eta}} \qquad l >> R \tag{10}$$

While superficially very similar in form to Eq. (8), note that this result is actually independent of the electrode radius R (!).

This occurs because, in this case, both the area A, and the mass transport parameter b, are proportional to R^2. Nonetheless, as discussed above, isotropic downscaling of the device dimensions also leads to enhanced mass transport, since in this case the parameter l is also scaled down.

The above discussion was meant as a simple introduction to BV kinetics at electrodes with non-trivial geometries. Strictly speaking, this treatment only holds for cases where the symmetry of the electrode is such that the concentrations at the electrode surface, C_O^e and C_R^e, are uniform over the electrode surface. In cases where this is not strictly true, such as the system of Eq. (10), a slight numerical error is introduced (which becomes increasingly negligible as l/R increases in that particular example). For a far more general treatment that extends to non-uniform current densities, we refer the reader to the work of Oldham.[19]

2. Experimental Approaches to Nanoelectrochemistry

(*i*) *Fabrication of Nanoelectrodes*

As mentioned in the introduction, the efforts to miniaturize electrodes began in the early 1980s with the advent of microelectrodes and, later, ultra-microelectrodes (UMEs).[20,21]

Many of the advantages that accrued from shrinking electrode sizes from millimeter to micrometer dimensions are also expected to hold as the dimensions are further reduced into the nanometer regime. Nanoscale electrodes allow the extension of electrochemical measurements into new realms of space (cells, nanogaps, etc.) and time. The uncompensated resistance, R_u, scales with $1/r$, where r is the radius of the electrode, and the capacitance scales with the area (r^2). Thus, the RC time constant of the cell scales with r and, hence, reduces with smaller electrode sizes. With electrodes of $r \sim 100$ nm, one can in principle reduce the cell time constant to lower than 1 ns. Further, the complications arising from uncompensated solution resistance, iR_u, are significantly minimized. This feature makes it easier to do electrochemical experiments in media of low conductivity such as highly resistive organic solvents and solutions devoid of any supporting electrolyte. Lastly, the high

rates of mass transport enable fundamental aspects of electron transfer kinetics to be investigated.

By the late 1980s, electrodes with effective dimensions of 1–10 μm were being reliably and reproducibly made, and in some instances electrodes of 100 nm sizes were also reported.[22] Various approaches to make UMEs have been reviewed by Arrigan[23] and Zoski.[24]

Since then, several methods have been developed to further shrink the sizes of electrodes into the sub-micrometer regime. Most of the electrodes have geometries that can be generally classified as spherical, disk, band or cone. The earliest instance of a truly nanoscale electrode was a Au band electrode made by White and co-workers.[25] They deposited Pt and Au films, 2 to 50 nm thick, onto molecularly smooth cleaved mica. The top side of this metal layer was then coated with an epoxy insulating layer to create an epoxy-metal-mica sandwich structure. This structure was then ground flat perpendicular to the metal film with silicon carbide paper, to eventually expose a rectangular band-shaped electrode. The width of this band is simply determined by the thickness of the metal deposited. Because of the variable nature of the cutting procedure employed, the actual geometry of this band-shaped geometry was described as "a roughened surface that is broken at numerous positions along the length of the electrode". However, it was the first instance of an electrode geometry where at least one dimension of the electrode was shorter than the Debye length and approached the dimensions of the redox-active molecule being probed.

Advances in making disk and cone-shaped nanoelectrodes with lateral dimensions of a few nanometers were occasioned by the burgeoning interest in making very small tips for the purposes of imaging by scanning tunneling microscopy (STM). The key first step was to decrease the size of the active electrode area to that below the dimensions of the commercially available metal wire. The main procedure employed was electrochemical etching, as used commonly for STM tips.[26-29] A vast majority of disk or cone-shaped nanoelectrodes happen to be Pt electrodes, because other metals like Au, Ag or Cu either dissolve rapidly or form thin insulating oxide layers during the etching process, which introduces enormous complications especially when dealing with nanometer dimensions.[30] Typically, the metal wire is suspended in an

aqueous alkali solution and a voltage (AC or DC) is applied. The metal etches away at the air-water interface, leaving behind a sharpened tip. Electrodes sharpened in this way include Pt-Ir,[28, 31, 32] Pt,[33, 34] Ag[35] and even carbon.[36] The next step involves coating the sharpened electrode with an insulating material, except at the apex of the tip, thus leaving behind a very tiny exposed area. Various insulating materials have been used such as apiezon wax,[31, 32, 34,37] poly(α-methylstyrene),[28] polyimide,[38] Teflon[39] or, most commonly, electrodeposited electrophoretic paint.[35, 36, 40-45] In the latter case, after cathodic electrodeposition, the electrode is heat-cured to provide good insulation. During heat curing the paint shrinks, thus leaving the apex of the tip exposed. However, it is difficult to precisely control the curing step and one easily ends up with an electrode of ill-defined size or geometry.

Other approaches have included coating with glass.[28,33,46,47] A simple extension[48] of the above mentioned technique involves starting with a sharpened Pt wire and sealing it in a glass capillary. Heating to 1000°C ensures that the glass melts thereby sealing the Pt wire. Once the Pt is sealed, the capillary is polished until the very end of the Pt tip is exposed. Although it is very difficult to controllably make electrodes of a pre-determined dimension, this process was reported to be an inexpensive and quick way of producing electrodes with radii in the 100 nm–50 μm range. Electrodes with radii as small as 10 nm have been reported using this method. Following a procedure developed by Abruña,[46] a relatively more controlled and reproducible approach to making nanometer sized Pt electrodes involves the use of a laser puller using Pt wires sandwiched within borosilicate capillaries.[49-51] Briefly, a metal wire encased in a glass sheath is heated to a temperature which is close to the melting point of the metal but at the same time ensuring that the glass capillary is stable with respect to bending. By using a laser puller, both the glass capillary and the metal are rapidly heated. This ensures a tight sealing of the metal in the glass and when both are pulled simultaneously, a significant decrease in the diameter of the sealed Pt wire ensues and thus the formation of two Pt nanoelectrodes. As a consequence of the rapid scission of the capillary, the resulting surfaces are often not flat and suitable polishing procedures are required afterwards. More recently, after discovering with high-resolution transmission electron microscopy (HR-TEM) that the Pt wire is pulled into ultra-

small nanowires at the end of the sharp silica tip, Zhang's[52] group has extended the laser pulling method, by further encasing the pulled Pt wire tip into borosilicate glass tubing. This configuration was then further ground and polished using a home-made continuity tester to ensure that the polishing is aborted as soon as the very end of the Pt nanowire is exposed. Using this method, they report to have made Pt electrodes of radii 1–3 nm.[52, 53] The laser pulling approach has also been used for Pt wires sealed in Teflon[54] tubes. Images of several types of nanoelectrodes can be seen in Fig. 2.

Although the above mentioned techniques for producing nanoelectrodes are relatively simple and inexpensive, they have inherent uncertainties in the precise shape and size of the final electrode (*vide infra*) especially as dimensions shrink below 10 nm.

The main alternative is to use standard microfabrication /micromachining processes. Although these microfabrication processes require specialized equipment and are therefore more expensive, they also have considerable potential for commercialization if robust protocols for fabrication can be developed. The principal advantages of this approach are that the geometry of the electrodes is precisely and reproducibly controlled and that the size and shape can be determined independently of indirect (mainly electrochemical) methods. Some approaches to nanoscale electrodes have included focused ion-beam (FIB) sculpting to form ring-shaped nanoelectrodes around an AFM tip for use in SECM-type measurements.[60-64] FIB milling was also used to sculpt an electrophoretic paint-coated W tip to produce electrodes with dimensions of 100–1000 nm.[58] Other silicon-based microfabrication techniques[65,66] have also been used to make Pt nanoelectrodes. Carbon nanotube based nanoelectrodes have also been prepared.[56,67,68] Our group used lithographically fabricated nanopores in an insulated silicon membrane that are subsequently blocked on one side with metal to yield electrodes with lateral dimensions between 15–200 nm.[69] The fabrication protocol was later altered to obtain conically shaped Au electrodes with radii down to 2 nm.[57,70] Another bottom-up approach to making nanoelectrodes relies on depositing noble-metal nanoparticles on conducting substrates like carbon electrodes[59] and single-walled carbon nanotubes (SWNTs).

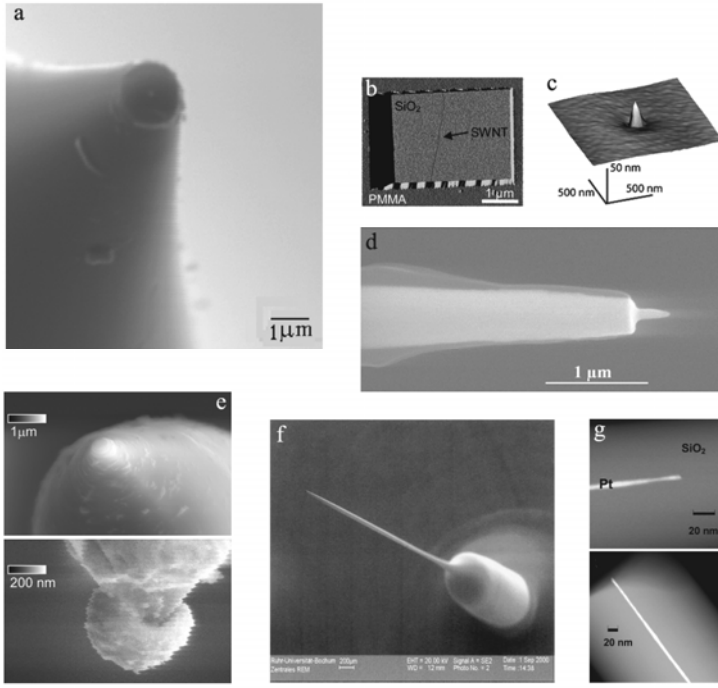

Figure 2. A collage of various nanoelectrodes. (a) Scanning electron microscope (SEM) image of a 70-nm radius pulled Pt nanoelectrode. Reproduced with permission from Ref. 55, Copyright (2006) American Chemical Society. (b) Atomic force microscope (AFM) amplitude image of an exposed single SWNT nanoelectrode crossing the bottom of a pit through PMMA and SiO_x layers. Reproduced with permission from Ref. 56, Copyright (2005) American Chemical Society. (c) AFM topography image of an Au nanoelectrode. Reproduced with permission from Ref. 57, Copyright (2006) American Chemical Society. (d) SEM image of electrophoretic paint insulated Tungsten (W) nanoelectrode. Reproduced with permission from Ref [58]; Copyright 2005 IOP Publishers. (e) SEM images of two carbon-UME supported Pt particles. Reproduced with permission from Ref. 59, Copyright (2003) American Chemical Society. (f) SEM image of a glass capillary pulled Pt nanoelectrode. Reproduced with permission from Ref. 50. Copyright (2002) Wiley-VCH Verlag GmbH & Co. KGaA. (g) TEM images of a 1.5 nm nanowire and 3 nm Pt nanoelectrode sealed in SiO_2. Reproduced with permission from Ref. 52, Copyright (2009) American Chemical Society.

[71,72] We used the exposed end of a SWNT as a template for *in situ* Pt electrodeposition. The SWNT itself served as a wire from the Pt interface to macroscopic leads. Using this approach we were able to obtain nanoparticle electrodes with radii as small as approximately 6 nm.[73]

(*ii*) *Redox Cycling (Thin Layer Cells, IDEs and SECM)*

Apart from shrinking the dimensions of individual electrodes, another pathway for approaching nanoscale dimensions in electrochemistry relies on having not one, but two electrodes separated from each other by small distances. If the electrodes are biased such that reduction takes place at one electrode and oxidation at the other, a steep concentration profile of reduced and oxidized species can be set up between the two electrodes. For planar electrodes separated by a distance z, the corresponding diffusion-limited current is given by

$$i_{\text{lim}} = \frac{nFADC}{z} \tag{11}$$

This result neglects fringing at the edges of the electrodes, a valid approximation so long as the spacing z is much smaller than the lateral dimensions of the electrodes. The current given by Eq. (11) corresponds to the same limiting current density, i_{lim}/A, as is achieved at a disk electrode with radius $R = 4z/\pi$, regardless of the actual area of the planar electrode. Small enough spacings z thus allow achieving current densities comparable to nanoelectrodes using electrodes that are actually much larger.

This idea was first realized in the early 1960s, through the development of thin-layer cells (TLCs).[74-77] An adjustable working distance was offered between the two plane-parallel electrodes, which were separated by tens of micrometers. The spacing was regulated by having the two ends of a micrometer screw gauge serve as the two electrodes. The screw was then used to both clamp the electrodes together and adjust the gap size. Using this approach, electrode spacing on the order of a few micrometers was achieved. As in SECM, the minimum electrode spacing achievable is ultimately limited by the ability to bring the two flat surfaces

into close proximity while maintaining a parallel orientation. Advances in microfabrication techniques have allowed the electrode spacing to be reduced to about 50 nm, and in the future will most likely be reduced even further.

As an alternative to TLCs, interdigitated electrodes (IDEs) can also be employed to study systems that involve redox cycling. As the name suggests, IDEs consist of two comb-shaped electrodes with the teeth of the two electrodes arranged in an interdigitated fashion, similar to a set of gears.

IDEs, also known as interdigitated arrays or band-array electrodes, have been fabricated and analyzed since the 1980s.[78-82] They became popular as the availability of microfabrication techniques increased. IDEs are much simpler to create using microfabrication techniques than TLCs. Since both electrodes in the IDE geometry are in the same plane, they can be created using a single lithographic step. The sensitivity of IDEs is generally determined by how small the spacing between electrodes can be made, which is determined by fabrication limitations.

IDEs are most often used as conductometric sensors[83-85] but they are also utilized in analytical[86-88] and bioanalytical[89-91] amperometric detection strategies. Recent fabrication improvements have rekindled interest in the technology. With electron-beam lithography becoming more widely available, there has been a move toward nanoscale electrode widths as well as spacing between electrodes. Several groups have demonstrated sub-micrometer wide electrodes and spacing[92-95], and novel geometries and designs have been analyzed using simulations.[96-99]

By reducing the space between electrodes, the chance that a molecule residing in the space between electrodes will undergo redox cycling increases. IDEs usually generate lower cycling currents than TLCs because they are not as efficient in trapping molecules between their electrodes. One way to increase the average time that a molecule spends between the electrodes of an IDE device is to purposely make the electrodes thicker.[92] This idea was taken one step further by Dam et al., who etched trenches in the substrate before patterning metal, so that the electrodes face each other.[100]

Although TLCs and IDEs have proven to be powerful tools in the study of electrochemical phenomena, their principal limitation is that the electrode spacing is fixed. By contrast, Scanning Elec-

trochemical Microscopy (SECM; the acronym also applies to the instrument) combines the best features of TLCs and IDEs as well as scanning probe techniques. Since its introduction in the late 80's, it has emerged as a powerful and versatile technique to probe a wide variety of chemical and biochemical phenomena.[101] Briefly, the technique employs the use of a UME or nanoelectrode, which is positioned close to a substrate. The faradaic current through the UME, as it is moved normal to or laterally across the substrate, yields information about the substrate and the intervening medium. The technique can also be used in the chronoamperometric mode, where the current is measured as a function of time at a fixed UME position. The substrate can be conducting, semiconducting or insulating. It can be solid or liquid. The instrument can be operated in several modes contingent on the nature of the substrate and the problem at hand. These modes of operation together with details of instrumentation have been summarized in a monograph.[102]

The use of electrodes of nanometer dimensions has further extended the capabilities of SECM. Besides offering higher spatial resolution in imaging experiments, they also enable higher mass-transport rates in the steady-state regime, thus allowing kinetic investigations of systems with very rapid electron-transfer rates. A recent review of SECM lays special emphasis on the use of nanometer-sized tips.[103] The biological applications of SECM have also been reviewed recently.[104-106]

3. Challenges of Characterization

While the fashioning of nanoscale electrodes is becoming more common and widespread, the precise characterization of the shape and size of these electrodes continues to remain a daunting challenge. As discussed previously, the issues of shape and size and their influence on the shape of the resulting voltammogram are intimately connected. If one knows the geometry of the electrode then one can, in principle, readily determine the size of the electrode from the steady-state currents. A key challenge, therefore, is the determination of the exact shape of the electrode. For micrometer sized electrodes, optical and electron microscopy can be used to assess the geometry. However, as dimensions shrink into the nanometer regime (and especially below 50 nm), it becomes increasingly difficult to image electrodes using electron microsco-

py. Besides inherent limitations of SEM in the sub-10 nm regime, the problem is compounded by the fact that the small electrode is buried in a thick layer of insulating material (for example, glass, wax, or electrophoretic paint), which complicates imaging due to sample instability and charging issues. A way to circumvent this issue is to deposit a thin metal layer on the insulating part of the electrode, but this is difficult to accomplish selectively, and further the contrast between the deposited layer and the metal electrode has to be high enough to yield useful images.

In conjunction with SEM as a general tool, most approaches to characterization of nanoelectrodes rely on indirect means that involve measuring electrochemical responses of the electrodes to quantify their geometry and size. Generally, it is common in cases where the dimensions of an electrode are not known *a priori* to determine them by measuring the diffusion-limited current, i_{lim}. For example, by assuming that the electrode is a shrouded hemisphere, one can determine an *effective radius* for an electrode using the relation $R_{eff} = i_{lim}/2\pi FDC_R^b$. In the notation introduced above, this is exactly equivalent to an experimental determination of the parameter b, since $b = i_{lim}/FDC_R^b = 2\pi R_{eff}$. Compared to a hemisphere, the limiting current at a disk-shaped electrode is $i_{lim} = 4FDC_R^bR$. It has been argued that if a shrouded hemispherical electrode is mistaken for a disc-shaped electrode, then the error in the determined R_{eff} is at most $2/\pi$, and therefore the error in an electrochemical experiment will rarely be greater than a factor of ~2.[30] While this may indeed not be a problem for spherical-segment electrodes (e.g., sphere, hemisphere, cone or disk) of the same radius, the complications for a recessed electrode can be more significant.

Problems can potentially arise if the value of R_{eff} is in turn used to estimate the true area of the electrode using $A = \pi R_{eff}^2$ for use in Eq. (6). Any discrepancy between the real and assumed geometry is further magnified by squaring and can lead to significant uncertainties in the measured heterogeneous rate constants. For instance, consider the case of a lagooned electrode with an orifice of radius r, and a disk-shaped electrode of radius R embedded in the lagoon as depicted in Fig. 3.

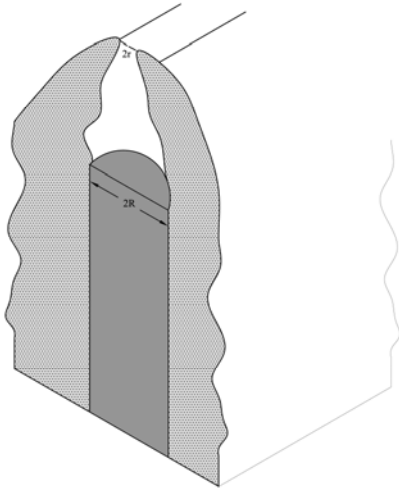

Figure 3. Sketch of a section of a disk electrode of radius R, embedded in a lagoon with an orifice of radius r.

The limiting current in the voltammogram will yield a value of $R_{\text{eff}} \approx r$, that corresponds to the radius of the orifice of the lagoon. The area of the electrode, however, is πR^2. Therefore, if the true area is instead expressed as πr^2, then the measured rate constant will be $k_m^0 = k^0 \left(\frac{R}{r} \right)^2$, where k_m^0 is the measured rate constant and k^0 is the true heterogeneous rate constant. It is readily apparent that in the limit $R >> r$, the measured rate constant will be highly overestimated. It has been argued that the unusually high rate constant (220 cm/s) for ferrocene oxidation in acetonitrile measured by Penner et al.[33] was likely an overestimation due to the formation of a lagoon around the conductive tip of the nanoelectrode.[19, 107, 108]

An ingenious approach to determining the electrode area was employed by White and co-workers,[44] wherein the active areas were determined by measuring the electrical charge (Q) associated with oxidation of adsorbed bis(2,2‘-bipyridine)chloro(4,4‘-trimethylenedipyridine)osmium(II) on Pt electrodes in fast-scan

voltammetric measurements (~1000 V/s). Knowing the surface coverage by way of measurements on bigger electrodes of known geometry, the area of the nanoelectrode can be calculated. If the limiting current for dissolved redox species agrees with that expected for the assumed geometry, then assumption of this geometry is deemed correct. Interestingly, they observed that only 50% of the electrodes prepared by the electrophoretic polymer-coating procedure were quasi-hemispherical, the remaining being recessed slightly below the polymer coating. This also points to another challenge of characterization of nanoelectrodes via indirect electrochemical means. Because of large variations in the size and shapes of electrodes fabricated using fairly uniform processes, the need arises to characterize each electrode independently, which complicates routine usage. In addition, indirect means of characterizing the electrodes often render the electrode unfit for further use.

Besides uncertainties in the geometry and size of the electrode itself, there may exist defects in the insulating layer, which may further complicate measurements. For instance, it has been observed that heat curing of electrophoretic paint around metal electrodes often leaves conductive pinholes in the insulating layer, rendering it ineffective for neurophysiological measurements.[58] Several coatings of paint are required to completely eliminate pinholes, which often makes it difficult to obtain an electrode with a conductive tip. Similar problems may exist for wax and glass-coated electrodes. In the earliest example of detection of single molecules with SECM using wax-coated nanoelectrodes, it was proposed that the observed slow fluctuations in the current trace was due to small channels formed in the insulating wax layer around the nanoelectrode tip that were connected to the small reservoirs or bulk solutions not in contact with the tip. When the redox-active molecules enter these channels, no current is seen until they traverse back out into the tip volume. This suggests that even slight uncertainty in the robustness of the insulator can have a significant effect, especially for sensitive measurements. Similarly, in the case of glass, Mirkin and coworkers[221] have recently observed that the effective surface area of a Pt nanoelectrode was much larger than the geometric surface area due to surface diffusion of adsorbed redox species at the Pt/glass interface. They also found that surface hydrogen formed on Pt/glass interface *spills over* into

the glass during cathodic scans in 0.5 M H_2SO_4 and can be subsequently re-oxidized during anodic scans. While the spill-over effect is fundamentally interesting, it also illustrates that glass might not be impervious to small molecules and ions. This could lead to significant complications, especially through the double layer effects of the adsorbed ions on electrode kinetics.

A more reliable method for characterizing the shape and size of electrodes involves the measurement of approach curves in an SECM-type measurement. An approach curve is obtained by plotting the tip current as a function of the tip-substrate distance as the tip is moved a distance several tip diameters away towards the substrate. Because the diffusional flux of molecules in the volume between the nanoelectrode and the substrate is very sensitive to the geometry of the electrode, one can obtain information about the geometry of the electrode. Normally, the theoretical approach curve is calculated numerically for both a conducting as well as an insulating substrate, and the experimental curve is compared to the theoretical curve to assess the accuracy of the expected geometry.[34, 102, 109]

4. Experimental Results

As stated earlier, the shrinking of electrode dimensions is expected to enable measurements in regimes which are not ordinarily accessible through larger electrodes. Since we are dealing with the so-called classical regime, we focus in this Section on results where much of the conceptual framework that underpins our understanding of macroscale electrodes continues to be relevant also at nanoelectrodes. As mentioned earlier, due to enhanced mass-transport and consequently much higher current densities, nanoelectrodes become sensitive to electrode kinetics. We recall from Eq. (7) that the dimensionless rate constant λ determines the relative importance of heterogeneous electrode kinetics compared to mass transport. As a rule of thumb, in the limit that $\lambda \leq 10$, the electron transfer step becomes the rate-limiting step in the overall voltammetric response. For the case of a spherical electrode of radius r, $\lambda = k^0 r / D$. Thus, for a typical value of diffusion constant $D = 10^{-5}$ cm^2/s and an electrode of radius $r = 10$ nm, one can in principle measure rate constants as high as $k^0 = 100$ cm/s. It is not surprising, therefore, that the most extensive application of nanoelectrodes has

been to measure fast electrode kinetics of various redox species in solution. Besides enabling the measurement of fast heterogeneous electron-transfer kinetics, nanoelectrodes also offer the opportunity to test the applicability of classical transport theories in explaining observed voltammetric behavior. In particular, in the regime where the diffusion length of the redox active molecules (which depends on the electrode geometry and size) becomes comparable to the Debye length, it is expected that the electric field in the vicinity of the electrode will affect mass transport. We will return to this issue in a later Section. For now we focus on the regime where mass transport is assumed to be entirely diffusive in nature.

The most common way of measuring heterogeneous rate constants from steady state voltammograms has been to fit Eq. (6) to the entire voltammogram and extract the relevant kinetic parameters (k^0 and α) if $E_{1/2}$ and the geometry and size of the electrode are independently known. This approach avoids the common pitfall of inadequate compensation of the *iR* drop that often affects data obtained with fast-scan voltammetry at conventional UMEs.[110, 111] The experimental voltammograms can be obtained through either the conventional two- or three-electrode set up with the nanoelectrode serving as the working electrode, or in an SECM experiment in the positive feedback mode with the nanoelectrode positioned close to a conducting substrate a distance *d* away. The latter approach allows independently tuning the mass-transport rate in two different ways: by changing the radius *r* of the nanoelectrode or by changing the tip-substrate distance. Using this approach with Pt nanoelectrodes (3.7–400 nm), Sun and Mirkin[55] were able to tune the mass-transport rate across two orders of magnitude and determine kinetic parameters for the oxidation of Ferrocene-methanol (Fc-CH_2OH) in aqueous solution, Ferrocene (Fc) in acetonitrile, and the reduction of Hexammineruthenium(III) chloride ($Ru(NH_3)_6^{3+}$) in aqueous solution and 7,7,8,8-tetracyanoquinodimethane (TCNQ) in acetonitrile. Interestingly, they found that there is little correlation between the electrochemical rate constants, k^0, and the homogeneous self-exchange rate constants, k_{ex}, for these redox couples, counter to the predictions of the Marcus theory for electron transfer.

Another approach to analysis of quasi-reversible steady-state voltammograms was developed by Mirkin and Bard.[112] This method relies on the measurement of experimental parameters, ($E_{1/4}$ –

$E_{1/2}$) and ($E_{1/2} - E_{3/4}$), where $E_{1/4}$ and $E_{3/4}$ are the potentials where the current is equal to ¼ and ¾ of the limiting current, respectively. These parameters are compared to the numerical look-up table in Ref. 112 to yield corresponding values of k^0 and α. Watkins et al. used this method to determine the rate constant for the oxidation of the ferrocenylmethyltrimethylammonium cation ($TMAFc^+$).[44] Watkins and White[113] also studied the oxidation of hexachloroiodate (III) anion ($IrCl_6^{3-}$) in either the presence or absence of supporting electrolyte. Interestingly, they found that the heterogeneous rate constant increases by an order of magnitude in the presence of supporting electrolyte compared to the conditions where no salt is present. In a separate study,[114] they investigated the kinetics of ion-pair formation between the $IrCl_6^{3-}$ and the cation of the supporting electrolyte (K^+, Ca^{2+} and tetraethylammonium (TEA^+)) and directly observed discrete oxidation waves for free and ion-paired $IrCl_6^{3-}$. More recently, Li et al.[52] have also used electrodes as small as 1 – 3 nm to measure the rate constants for Fc, $FcCH_2OH$ and $IrCl_6^{3-}$. The values they obtained are in general agreement with previous studies, although they obtained significantly higher values for the transfer coefficient α. While most studies have employed Pt nanoelectrodes, Velmurugan et al[115] have also studied fast heterogeneous kinetics on Au nanoelectrodes. Their motivation was to probe the extent of adiabaticity of electron transfer for various redox couples, by probing the effect of the electrode material (and, hence, the density of states, ρ_F, at the Fermi level) on the rate. Apart from $Ru(NH_3)_6^{3+}$ in KCl and KF, all other outer-sphere redox couples (Fc, $FcCH_2OH$ and tetrathiafulvalene) had nearly identical rates on both Au and Pt electrodes.

Zevenbergen et al.[116] used nanoscale TLCs with electrode spacing z = 50 nm to determine the rate constant for $Fc(CH_2OH)_2$ in KCl and $NaClO_4$. The current densities at electrodes in these TLCs were equivalent to those obtained at a 0.016 μm^2 hemispherical electrode.

III. THE MESOSCOPIC REGIME

We have heretofore considered cases in which the concepts and approximations that are used to describe electrochemistry at UMEs can be applied without modification to nanoscale electrodes. As

the dimensions of the electrodes are reduced, however, it is natural to expect that some simplifications that are perfectly reasonable on larger scales will start to break down, and that new concepts are needed to explain experiments. Below we will discuss several different ways in which this can occur. We employ the term *mesoscopic* to collectively describe these systems. The term refers to an intermediate size scale between *macroscopic*, where the classical results apply, and *microscopic*, where purely molecular-scale processes dominate.

1. Double-Layer Effects

Any charged surface in contact with an electrolyte induces a charged region in the electrolyte that is known as an electrical double layer. This induced charge has the same magnitude but the opposite sign to the charge of the surface, so that it effectively neutralizes the surface charge. The induced charge is composed of a local increase of the concentration of counterions near the surface, accompanied by a decrease of the concentration of coions. In many cases of interest, the electrical double-layer extends only of the order of a few nanometers away from the surface and into the solution. For macroscopic or micron-scale electrodes, this represents a perturbation that is localized essentially at the electrode surface. For sufficiently small electrodes, however, the lateral dimensions of the electrode can become comparable to the thickness of the double layer. When this happens, it becomes necessary to re-assess some of the simplifications on which our understanding of the classical regime is based.

The distribution of coions and counterions near a charged surface is most commonly described using a mean-field formalism embodied by the so-called Poisson-Boltzmann equation. This is a nonlinear differential equation that can be solved to deduce the electrostatic potential $\varphi(\boldsymbol{r})$ as a function of position $\boldsymbol{r}$ in the vicinity of the surface. Since a full discussion of the solutions would take us too far afield, we will simply summarize some of the key qualitative results of the Poisson-Boltzmann formalism. The reader is referred to the literature for a more thorough treatment.[117, 118]

The double layer can in many cases be described in terms of two different, spatially separated regions: a compact layer consisting of the few molecular layers next to the surface, and a diffuse

layer that extends into the bulk liquid away from the surface. This is illustrated in Fig. 4, which sketches the electrostatic potential (Fig. 4a) and the ion concentrations (Fig. 4b) as a function of distance from a charged surface. The Poisson-Boltzmann formalism provides a description of the diffuse part of the double layer that is relatively simple and consistent with most observations without the need for additional complications. Specifically, it predicts that the electrostatic potential, $\varphi(\boldsymbol{r})$, falls off exponentially with distance from the surface.[119] The decay length, known as the Debye length λ_d, therefore represents the characteristic *thickness* of the double layer. Its value is given by

$$\lambda_d = \left(\sum_i \frac{n_i^{\infty} Z_i^2 e^2}{\varepsilon \varepsilon_0 k_B T} \right)^{-1/2} \tag{12}$$

where e is the charge of the electron, ε is the relative permittivity of the solvent, ε_0 is the permittivity of free space, k_B is Boltzmann's constant, i represents the various ionic species present in the electrolyte, and n_i^0 and Z_i are the number density and valence of each species, respectively. To give some numerical examples, pure water at pH 7 has $\lambda_d \approx 1$ μm, while a 0.1 M aqueous solution of a monovalent salt has $\lambda_d \approx 1$ nm. The ionic charge in the diffuse layer consists of two components, as illustrated in Fig. 4b: excess counterions that are attracted to the surface, and a reduction of the coion concentration below its bulk value due to repulsion from the surface.

In contrast to the relative simplicity of the diffuse layer, the structure of the compact layer is extremely difficult to describe quantitatively. First, the nonlinearity of the Poisson-Boltzmann equation manifests itself strongly in this region except at weakly charged surfaces. The potential $\varphi(\boldsymbol{r})$ then exhibits a more complicated functional form than a simple exponential decay, while the ionic charge in this part of the double layer consists predominantly of counterions. Second, and more importantly, the inherent molecular scale of the compact layer means that a complete description calls for a treatment that includes details at the molecular level. Issues such as the finite size of the ions, crowding, the hydration state of the ions, the structure of the solvent near the surface, spa-

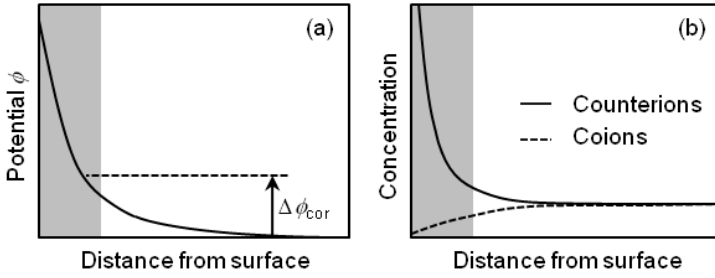

Figure 4. Sketch of the structure of the double layer showing the compact layer (gray) and the diffuse layer (white). (a) Electrostatic potential versus distance from the surface. In the diffuse layer, the potential decays exponentially with distance; the dependence can be more complicated in the compact layer. Because redox molecules must penetrate into the diffuse layer to undergo electron transfer, a fraction of the driving potential, labeled $\Delta\phi_{cor}$, does not contribute to assisting the electron transfer reaction. (b) Distribution of counterions and coions at the surface. In the diffuse layer, excess counterions and a dearth of coions contribute comparably to the net charge of the double layer. The compact layer consists predominantly of excess counterions.

tial correlations between ions, adsorption of ions to the surface and so forth can all play important roles. Different levels of sophistication are required to capture the salient features of different experiments, but in general our ability to describe the compact layer remains limited.

Because the value of λ_d is comparable to or greater than the thickness of the compact layer, however, the value of λ_d provides a good first estimate of the range of electrostatic interactions in solution. Does the existence of a double layer with characteristic size λ_d influence electrochemical experiments? It does, in at least two different ways. First, we implicitly assumed in Section II.1 that the full electrostatic potential imposed between an electrode and bulk solution is available for driving redox processes at the electrode surface. To undergo electron transfer, redox molecules must, however, approach within a distance from the electrode that roughly coincides with the extent of the compact layer. The fraction of the potential appearing across the diffuse part of the double layer (labeled $\Delta\phi_{cor}$ in Fig. 4a) is then *waste*d during the approach of the molecule to the surface, and only a fraction of the potential difference is available for driving the electrochemical reaction. To add

insult to injury, a second, separate effect also occurs for charged redox species: the electric field in the double layer acts on these molecules and modifies the surface concentrations from the purely diffusive case considered in Section II.1, which further influences the faradaic current. These two effects are collectively known as *Frumkin corrections*. Note that they are not specific to nanoelectrodes, and they also occur at the surface of macroscopic electrodes. Recent theoretical work, however, suggests that thin-layer cells may provide an ideal system for studying the Frumkin effect.[120]

In addition to the above, the existence of a double layer with characteristic dimension λ_d is expected to have further influence on voltammetry for the case of electrodes with characteristic dimensions comparable to or smaller than λ_d. In our theoretical treatment of the classical regime in Section II.1, we assumed that mass transport of the redox species was entirely specified by diffusion. Consider, however, a hemispherical electrode with radius R. The concentration profile for steady-state, purely diffusive transport from this electrode has the form $C(r) = (R/r)\ C_0$, where C_0 is a constant. While it is not possible to rigorously define an absolute length scale for this profile due to its power-law form, qualitatively, most of the concentration change occurs on a size scale of a few times R. More specifically, a value of $10R$ for the size of the diffusion region is conventional. For a sufficiently small electrode, however, the limit where λ_d becomes comparable to or greater than $10R$ can be reached. In this case, the assumption of purely diffusive transport clearly breaks down, since the electric field from the double layer at the electrode permeates the diffusion region.

This very regime was explored in a study by Chen and Kucernak.[43] While studying the voltammetric response for the reduction of $Ru(NH_3)_6^{3+}$ at carbon electrodes sized as low as 1 nm, they observed that the limiting current decreased considerably in the absence of supporting electrolyte compared to the case when 0.5M KCl was present. This effect, however, was observed only at electrodes having effective radii, r_{eff}, smaller than 20 nm. Similar observations were made regarding the suppression of rates of oxidation of $TMAFc^+$ and $IrCl_6^{3-}$ and reduction of $IrCl_6^{2-}$ in the absence of electrolyte at electrodes with radii less than 30 nm.[36, 41, 113] While a detailed understanding is yet lacking, these departures

from predicted classical theories of mass transport have been qualitatively attributed to dynamic changes within the diffuse double layer when the size of the diffusion region becomes comparable to λ_d . Similarly, Krapf et al.[70] studied oxidation of $TMAFc^+$ and found that transport to sub-10 nm electrodes increased sublinearly with concentration of the charged $TMAFc^+$. A similar dependence was not observed for the neutral $FcCH_2OH$. This observation is not captured by the Poisson-Nernst-Planck equations, and it was suggested that the discrepancies originate from the very high current densities at nanoelectrodes.

2. Small Volumes

A second way in which nanometer-scale systems can lead to qualitatively different behavior is in cases where very small volumes are being probed. Once again, this can influence electrochemical experiments in two different manners.

First, liquid-filled cavities with nanometer-scale dimensions have a higher surface-to-volume ratio than larger systems with the same geometry. Consequently, surface processes have a higher propensity to influence the properties of the bulk solution present in the cavity. In particular, changing the potential of an electrode can lead to different level of adsorption as well as the localization of charged species near the electrode surface through double-layer formation. At sufficiently high surface-to-volume ratios, this can lead to significant, potential-dependent changes in concentration in the solution if the nanoscopic volume is not connected to a bulk reservoir.

A dramatic manifestation of this effect was reported by Sun and Mirkin,[121] who studied redox cycling of $FcCH_2OH^{+/0}$ in nanoscopic cells at different concentrations of KNO_3 supporting electrolyte. Significant variations in the limiting current were already observed when the salt concentration was decreased to 100 times that of the redox species, and the wave disappeared entirely for a salt concentration 3 times that of the redox species. Even more pronounced changes in the limiting current were observed for the $Ru(NH_3)_6^{3+/2+}$ couple. These observations were attributed to depletion of ions in solution due to the charging of the double layers. Once the bulk solution in the cell is essentially depleted of ions, the electric field penetrates from the electrodes into the bulk of the

cell. At intermediate salt concentrations this electric field can assist mass transport, but at lower salt concentrations the potential drop near the electrode becomes so small that electron transfer can no longer take place.

Small volumes can also lead to new behavior by virtue of containing a relatively small number of redox molecules. Consider a small, solution-filled cavity connected to a reservoir. The cavity contains an average number of molecules, $\langle N \rangle$, which is given by $\langle N \rangle = CV N_A$. Here, C is the concentration of redox molecules, V is the volume of the cavity, and N_A is Avogadro's number, as per our previous notation. At any given instant in time, however, the number of redox molecules inside the cavity is not necessarily precisely equal to $\langle N \rangle$: as individual molecules diffuse in and out of the cavity and into the reservoir, the instantaneous number of molecules, $N(t)$, can deviate from $\langle N \rangle$. In typical experiments, these fluctuations are so small relative to $\langle N \rangle$ that they are utterly negligible. In the simplest case of non-interacting particles, for example, the fluctuations in $N(t)$ are given by the Poisson distribution, and the relative size of the fluctuations scales as $\langle N \rangle^{-1/2}$. It is thus seen explicitly that the fluctuations essentially vanish as $\langle N \rangle \rightarrow \infty$. In the opposite limit $\langle N \rangle \rightarrow 1$, however, the size of the fluctuations becomes comparable to the value of $\langle N \rangle$ itself. In this case the fluctuations can no longer be ignored. Note that these fluctuations are not some extrinsic noise imposed on the system. Rather, they are an intrinsic feature of systems in diffusive equilibrium with a reservoir, as embodied in the Gibbs sum of statistical mechanics.

Thin-layer cells present an excellent opportunity for observing these statistical fluctuations. Equation (11) can be rewritten in the form $i_{\text{lim}} = \langle N \rangle (eD/z^2)$. The quantity eD/z^2 thus represents the contribution of each individual molecule to the current, and its magnitude increases quadratically with decreasing electrode spacing. Shrinking z thus helps make the fluctuations visible in two ways: it decreases the volume and, correspondingly, the number of molecules $\langle N \rangle$, and it makes the contribution of each molecule to the current larger, rendering fluctuations easier to detect. In the case where the number of molecules varies very slowly compared to the time for individual molecules to cross the cavity (given by $z^2/2D$), the variations in $N(t)$ then lead to corresponding slow fluctuations in the instantaneous current, $i(t)$:

$$i(t) = N(t)\frac{De}{z^2} \tag{13}$$

In this limit, measuring fluctuations in the faradaic current provides a way to directly resolve the particle number fluctuations.

Using thin-layer cells with electrode spacing $z \sim 50$ nm, we recently observed these fluctuations. With sensitive electronics, such that extrinsic sources of noise are minimized, the equilibrium statistical fluctuations can easily become the dominant source of noise in these systems. In this case they can be observed with one's bare eyes on an oscilloscope screen; representative time traces are shown in Fig. 5a. The figure also illustrates an important signature of the fluctuations: because the reduction current at one electrode is essentially identical to the oxidation current at the other electrode, the fluctuations in the two currents are perfectly anti-correlated, contrary to what would be observed if the fluctuations were caused by extrinsic noise in the two (independent) measurement circuits.

Importantly for applications, statistical fluctuations thus place a fundamental limit on the noise properties of electrochemical sensors based on redox cycling. On the other hand, they also provide an opportunity for observing the time evolution of microscopic diffusive trajectories. Two types of information are available from the noise time traces. First, the *amplitude* of the fluctuations is dictated by Poisson statistics and is therefore universal (as long as the molecules are essentially non-interacting). The scaling of the amplitude with $\langle N \rangle^{1/2}$ is directly verifiable, as shown in Fig. 5b. Second, the *speed* at which the fluctuations take place depends on how fast mass transport takes place between the inside and outside of the cavity. For example, doubling the diffusion constant of the redox molecules preserves the typical shape of the fluctuations in $i(t)$, but compresses the time axis by a factor of 2. Additional quantitative information can be gleaned from a detailed analysis of the spectral density of the noise.[122] Because of the analogy with Fluorescence Correlation Spectroscopy (FCS), we refer to this approach as Electrochemical Correlation Spectroscopy (ECS).

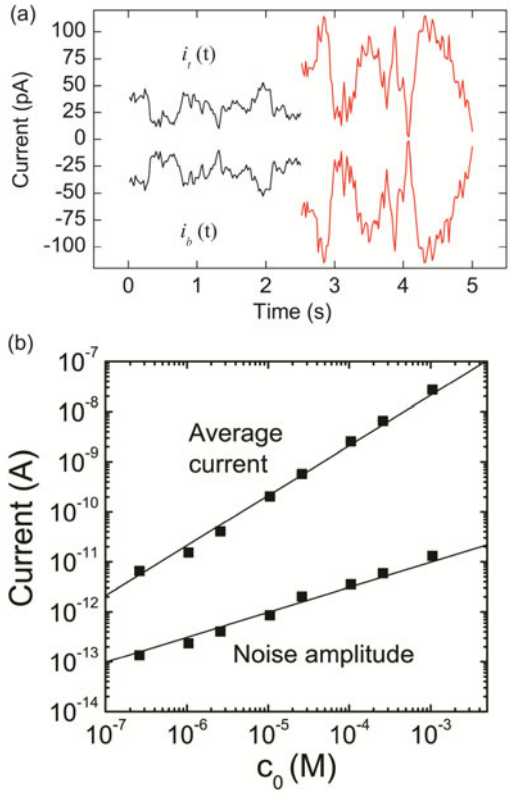

Figure 5. (a) Current measured through the top and bottom electrodes of a thin-layer cell during redox cycling. The fluctuations are not due to instrumental noise, as can be seen from the fact that the two independently measured signals are perfectly anticorrelated. This signal instead arises from equilibrium statistical fluctuations in the (small) number of molecules present in the device at any given instant. Adapted with permission from Ref. 122, Copyright (2009) American Chemical Society . (b) The average current scales linearly with concentration or, equivalently, with average number of molecules in the device, $\langle N \rangle$. Instead, the noise amplitude scales with $\langle N \rangle^{1/2}$, as predicted by Poisson statistics. Note that the signal-to-noise ratio therefore decreases with decreasing $\langle N \rangle$, placing a fundamental limit on the performance of this type of sensor. Adapted with permission from Ref. 123, Copyright (2006) American Chemical Society.

3. Quantization Effects

The double-layer and small-volume effects considered above were mostly a consequence of employing electrode systems with nanoscale critical dimensions. A separate class of mesoscopic effect concerns redox species that are themselves mesoscopic entities. The most common example is small clusters of metallic or semiconducting materials commonly referred to as quantum dots. While the composition of these particles is similar to that of the corresponding bulk materials, their small size can lead to qualitatively new behavior.

The free energy cost for adding an electron to a bulk conductor is given by the chemical potential for electrons in the conductor, μ. Adding electrons to a piece of conducting material leads to an increase in μ because the electrons in the conductor tend to occupy the quantum states with the lowest energy; adding additional electrons requires accessing electronic states with ever higher energy. Extracting electrons similarly leads to a decrease in μ. In a macroscopic conductor, the difference in energy between quantum states is, however, extremely small. As a result, the shifts in μ caused by charge transfer normally remain small and do not need to be taken into account in describing experiments. As the dimensions of the conducting particle are reduced, however, this simplification ceases to be valid. There are two main mechanisms through which this occurs.

First, confinement of the electrons to smaller particles leads to an increase in the energy level spacing. This is directly analogous to the classic *particle-in-a-box* problem from quantum mechanics, and leads to the energy level spacing scaling as V^{-1}, where V is the volume of the particle. For small enough particles, the energy-level spacing becomes comparable to k_BT. When this occurs, the quantization of electronic levels becomes manifest in the form of discrete states available for reduction or oxidation rather than a continuum of states as in a conventional conductor. Electron transfer for each of these discrete states then occurs at a different formal potential in voltammetric experiments.

Second, reducing the dimensions of conducting particles leads to discretization of the voltammetric response through the Coulomb blockade effect, also commonly referred to as quantized double-layer (QDL) charging in the electrochemical context. This

is a classical effect in the sense that quantum mechanics does not play an explicit role; the effect arises solely from the fact that electrons are discrete particles with a fixed charge e. Consider a quantum dot in solution to which a single electron is added; in response, the double layer around the particle adjusts itself to screen this change in the charge. The electrostatic potential of the dot thus changes by an amount $\Delta E_{dot} = -e/C_{tot}$, where C_{tot} is the total capacitance between the quantum dot and its environment. The successive addition of multiple electrons thus results in a corresponding step-wise increase in the electrostatic potential of the dot with respect to the solution. Furthermore, the change in electrostatic energy stored in C_{tot} due to electron transfer must ultimately be supplied by the electrode. This leads to a corresponding shift in the formal potential toward higher overpotential for the addition of each successive electron. To a first approximation, the magnitude of this shift is simply given by $\Delta E \approx \Delta E_{dot} = -e/C_{tot}$. Smaller systems have a smaller C_{tot}; once a system becomes sufficiently small that $|\Delta E| \approx k_B T/e$, the different waves for each charge state can be resolved in voltammograms.

Electron confinement and Coulomb blockade effects are not mutually exclusive, and in practice they often coexist in electrochemical experiments. As a rough approximation, C_{tot} scales approximately with the surface area of the dot or, equivalently, as $V^{2/3}$. Therefore, confinement, which as we have seen scales as V^{-1}, tends to dominate for the smallest particles. For intermediate size nanoparticles, on the other hand, Coulomb blockade can become the dominant effect. This is further facilitated by the layer of ligands that is often necessary to stabilize conducting nanoparticles, and which essentially acts as a non-conducting dielectric shell. The increased distance between the conductor and the double layer in solution leads to a smaller value of C_{tot} and a corresponding increase in the relevance of Coulomb blockade.

First reported in Au nanoparticle voltammetry in 1997,[124] advances in the preparation of monodisperse nanoparticles have enabled increasingly sophisticated and quantitative studies of Coulomb blockade in electrochemical systems. Its dramatic impact on the properties of metal nanoparticles is illustrated in Fig. 6, where each of the 15 equally-spaced peaks corresponds to the transfer of one additional electron per particle. The data also illustrate the cross-over from pure Coulomb blockade behavior to more com-

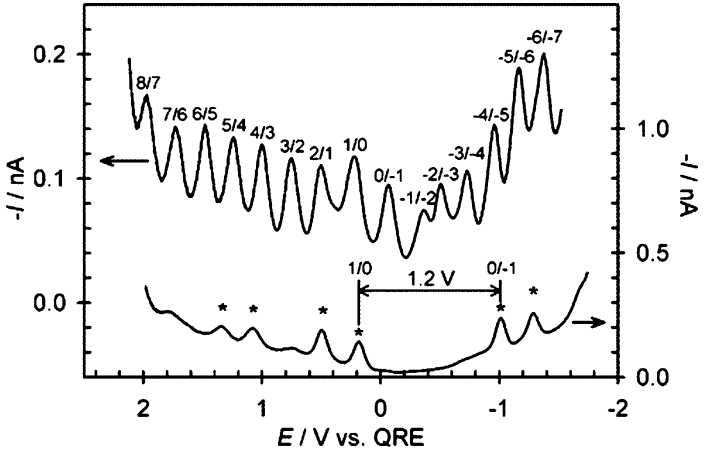

Figure 6. Coulomb blockade and electronic state quantization in metal nanoparticles. Differential pulse voltammetry on suspensions of DPV responses for hexanethiol-capped Au nanoparticles with core diameters of 1.6 and 1.1 nm (top and bottom curve, respectively). The 1.6 nm diameter particles exhibit 15 equally spaced Coulomb blockade peaks, each corresponding to the transfer of one additional electron per particle. The 1.1 nm diameter particles exhibit a gap and unequal peak spacing due to additional contributions from the discretization of the electronic spectrum. Reprinted with permission from Ref. 126, Copyright (2003) American Chemical Society.

plex, molecular-like behavior upon further reduction of the nanoparticle dimensions. For a more extensive survey of metal nanoparticles electrochemistry and associated discreteness effects, we refer the reader to the recent review by Murray.[125]

Step-like voltammograms were also reported for experiments in which two nanoelectrodes were immersed in a bulk solution containing a 1:1 mixture of the reduced:oxidized forms of a ferrocene derivative.[127] This behavior was attributed to Coulomb blockade, supported by the observation that the double-layer capacitances of the nanoelectrodes, estimated to be <1 aF by virtue of their small area, is consistent with the observed ΔE. This argument, however, neglects the contribution to C_{tot} of the capacitance between the dot and its environment. While this is often a good ap-

proximation when the dot is very small, this is not the case here since the dot instead consists of a macroscopic volume of fluid. A simple estimate for the self-capacitance of a 10 mL beaker of fluid in a shielded enclosure yields a value in the range 1–10 pF, which makes it by far the dominant contribution to C_{tot}. The predicted peak spacing for Coulomb blockade is therefore several orders of magnitude smaller than what was observed in the experiment. In our opinion, this analysis indicates that the experimental observations of Ref. 127 cannot therefore be explained by the double-junction Coulomb blockade model, and that the actual mechanism remains undetermined. A hint of an alternative interpretation is perhaps provided by the observation that the observed ΔE also approximately corresponds to the potential needed to add a single ion to the double layer at one of the electrodes.

IV. SINGLE-MOLECULE LIMIT

The ability to study single molecules is desirable for several reasons. Studies of individual (macro)molecules at the nanoscale enable the unraveling of static and dynamic heterogeneities that are characteristic at this scale. Static heterogeneity refers to the situation that static properties of different molecules constituting an ensemble might be very different. Dynamic heterogeneity is used to describe the time-dependent fluctuation of a property of an individual molecule. Both these heterogeneities result in a broad distribution of molecular properties of ensembles.[128] Ensemble-averaged measurements, as a consequence, probe only the averages (or first moments) of these distributions. By contrast, single-molecule measurements enable the construction of the entire probability distribution function of a particular parameter and all higher moments, thereby revealing the full range of properties and their relative significance.[129] From a metrology point of view, single molecule measurements represent the ultimate sensitivity in any kind of measurement, thus obviating the need for any artificial means for enhancement of the signal. Single molecule studies have contributed much to physics and chemistry, and are currently being intensely employed to the study of biological problems.[130]

The advent of single molecule techniques owes to several spectacular advances in the 1980s and -90s. In the 1980s, Binnig

and Rohrer introduced Scanning Tunneling Miscroscopy (STM)[131] and Atomic Force Microscopy (AFM)[132] – techniques which used sharp nanoscale tip probes to investigate surfaces on the atomic scale. Below we consider advances made in the studies of individual molecules using electrochemical methods either alone or in conjunction with other techniques. We have divided the treatment into two categories, one dealing with immobilized molecules and the other with freely diffusing molecules.

1. Immobilized Molecules

Immobilization of molecules and nanoparticles on electrode surfaces has several important advantages. When redox-active molecules are in permanent direct contact with the electrode, all molecules are rapidly synchronized to the applied potential, and are relatively easy to find and track. When electrochemistry is combined with spectroscopy (e.g., fluorescence, surface-enhanced Raman) or scanning probe microscopy, and the spacing is compatible with the lateral resolution (which requires dilute submonolayer surface coverage), this allows for detailed thermodynamic and kinetic analysis of individual molecules. Statistical analysis of many individual molecules and of time-dependent fluctuations is pivotal for the interpretation of single-molecule data. Surface confinement greatly facilitates long-time data accumulation on individual features, and repeated addressing of many individual molecules (scanning with a confocal spot or a thin optical fiber, or by scanning probe microscopy) as well as many molecules in parallel (wide-field or total internal reflection imaging).

Single-molecule spectro-electrochemistry requires a spectroscopic method that amplifies a single electron-transfer event into a multi-photon signal. Notably, laser-induced fluorescence and surface-enhanced (resonant) Raman spectroscopy, and electrogenerated chemiluminescence (ECL) can be applied to probe the redox state of individual molecules

A pioneering example of combining spectroscopic and electrochemical detection was the work of Bard, Barbara and coworkers.[133] In this study of a luminescent polymer widely used in solar cells and organic light emitting diodes (OLEDs), poly(9,9-dioctylfluorene-*co*-benzothiadiazole) (F8BT), the fluorophore was immobilized on a transparent (ITO) electrode, embedded in a pol-

ystyrene matrix. The potential of the working electrode was linearly swept anodically while simultaneously measuring the fluorescence intensities as a function of time. Most intensity curves exhibited a large intensity drop associated with the fluorescence quenching due to the electrochemical oxidation of F8BT. In effect, this was a cyclic voltammetry experiment wherein instead of the current, the fluorescence intensity of the redox-active molecule was being measured. Using this technique the authors were able to determine the broad distribution in the half-wave potentials, $E_{1/2}$, for the individual molecules. They extended these measurements in a later study[134] to probe the hole-injection charging dynamics in the individual F8BT nanoparticles. A variation on the same theme was the study of ECL at the single-particle level.[135] Together with the supporting electrolyte, some co-reactant tri-n-propylamine (TPrAH) was also added. As the potential was scanned anodically, both the F8BT and TPrAH were oxidized and the reaction between the $F8BT^{+}$ and $TPrA^{\bullet}$ so produced generated an excited state in the nanoparticle, resulting in chemiluminescence. A key advantage of ECL over photoluminescence experiments is the significantly lower background signal leading to higher sensitivities and spatial resolution.

Lei, Hu and Ackerman[136] used scanning confocal fluorescence microscopy to detect individual cresyl violet molecules (strongly fluorescent only in the oxidized state) as these pass the confocal volume when diffusing to and from a transparent ITO electrode during cyclic voltammetry. In a second paper[137], this method was applied to immobilized cresyl violet on a clay nanoparticle-modified ITO electrode. In this way, individual molecules could be followed over long time periods, yielding single-molecule spectroelectrochemical voltammograms. However, the response was convoluted with blinking, and no statistical analysis was presented. Xu and co-workers[138] report on single-molecule fluorescence, following the electrocatalytic generation of a fluorogenic product by single-walled carbon nanotube (SWNT) deposited on ITO. The electroreduction of nonfluorescent resazurin to fluorescent resorufin during cyclic voltammetry was detected by total internal reflection microscopy. Statistical and single-molecule kinetic analysis revealed the catalytic mechanism and the heterogeneous reactivity of discrete nanoscopic sites on the SWNT.

The groups of Aartsma and Davis[139] demonstrated that instead of the intrinsic fluorescence of a reactant, a fluorescent reporter label can be attached to a non-fluorescent redox molecule. They attached Cy5 to the blue copper protein azurin, which has a strong absorption band around 600 nm when oxidized, but is colorless when reduced. The Cu(II) state absorption overlaps with the dye emission spectrum, resulting in quenching of the fluorescence due to FRET. The labeled protein was immobilized on an alkanethiol SAM on transparent gold, and TIRF microscopy was used to follow the redox-state dependent switching of the fluorescent intensity during cyclic voltammetry. Although not yet accomplished at single-molecule level, this promises to be a powerful and versatile method that does not require an intrinsically fluorogenic reactant.

Surface enhancement results in a spectacular amplification of Raman scattering, provided that the molecules are in direct contact with the electrode, the excitation wavelength matches the plasmon frequency of the metal, and the surface is nanoscopically structured.[140] This has opened the way to single-molecule Surface-enhanced Raman scattering (SERS) studies.[141] Electrochemical SERS developments are now also approaching the single-molecule level. Islam et al.[142,143]combined SERS spectroscopy with nanostructured interdigitated array electrodes. The potential-dependent orientation of the molecules resulted in notably potential-dependent SERS response. By varying the electrode spacing, the redox cycling by ferricyanide or crystal violet molecules, the collection efficiency, and surface amplification could be optimized. A real step towards single-molecule SERS spectro-electrochemistry was reported by DosSantos and co-workers.[144] Time-dependent fluctuations were observed from a roughened silver electrode in dilute solutions of rhodamine and congo red, attributed to the very small number of SERS-active molecules probing nanoscopic *hot spots*. The tailed statistics as a function of applied potential were linked to single-molecule dynamics. An interesting development is to use an AFM or STM tip as an external Raman-enhancing unit for single-molecule studies.[145,146] This technically challenging method has recently been applied *in-situ*.[147]

When a single molecule is trapped between two electrodes, a continuous current can be passed through. This amplification allows for the purely electronic detection of individual molecules. Such two-electrode junctions can either be pre-designed and nano-

fabricated, or created by controlled deformation of a thin metal sheet to create a break-junction. The addition of a third electrode, not in direct contact with the trapped molecule, acts as a tunable *gate*, because the voltage difference tunes the molecular electronic levels as well as the occupation of these with electrons, which in turn modulates the conductivity of the molecule at a given bias voltage between the two contacting electrodes. Such field-effect transistor devices are typically regarded as molecular electronics that are strictly speaking not electrochemical (defining electrochemistry as the translation between electronic and ionic current) and thus beyond our scope. However, when the junction device is immersed in an electrolyte, a reference electrode can be used as *liquid gate*, creating a molecular electrochemical transistor. Such a configuration can be applied to probe the redox-properties of a single molecule.[148-156]

Trapping a single molecule between two electrodes can be conveniently and repeatedly achieved by scanning probe microscopy (STM and AFM) on a flat macroscopic electrode with a dilute sub-monolayer of adsorbed target redox molecules. For electrochemical *in-situ* STM and AFM, the conducting probe tip, together with the substrate, reference and auxiliary electrodes are immersed in electrolyte and connected to a bipotentiostat. To suppress diffusive background current, all but the very end of the tip needs to be insulated, thereby creating a nanoscopic electrode with all the fabrication and characterization consequences discussed above. Electrochemical STM and electrochemical AFM can thus be regarded as enhanced nanoscopic equivalents of SECM, by which adsorbed molecules can be individually addressed, the direct tunneling junction or diffusive mediator-bridged gap can be modulated, and the surface topography can be simultaneously probed.

Following early breakthroughs of *in-situ* STM in water[157] in 1986, EC-STM under potentiostatic control[158] in 1988, and tunneling spectroscopy[159,160] in vacuum in 1993, Tao was the first to demonstrate resonant enhancement of the *in-situ* tunneling current under potentiostatic control with added reference and auxiliary electrodes.[161] By co-adsorbing Fe(III)-protoporphyrin IX and protoporphyrin IX without iron on graphite, he was able to directly verify resonant tunneling due to the redox-active Fe(III). Starting from high potential, he observed an increasing apparent height of

the Fe-containing molecules when the Fermi levels of the source and drain electrodes (the substrate and tip, held at constant bias of 0.1 V) aligned with the lowest unoccupied molecular orbital in Fe(III). This resonant effect disappeared again when the potentials of the electrodes were set more negative than the redox potential of the Fe-containing molecules (Fig. 7).

In the years to follow, several groups have similarly applied electrochemical STM, observing comparable resonant effects with other types of redox molecules and, since the earliest days of the field, with redox-active protein molecules. The examples are too numerous to be summarized here and have already been extensively reviewed elsewhere.[153,156] Along with experimental work, the theoretical underpinning was developed (summarized in the reviews cited in the introduction of junction devices), e.g., models

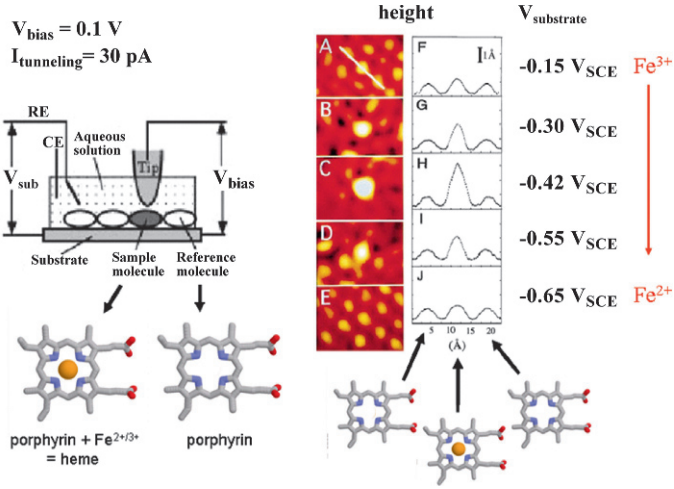

Figure 7. The first experimental demonstration of electrochemical resonant tunneling enhancement. Left: Schematic *in-situ* STM cell design (RE = Reference Electrode, CE = Counter Electrode), with both FE(III)-protoporphyrin IX and metal-free protoporphyrin IX on the substrate electrode. Right: Resonant tunneling due to the redox-active Fe(III) (reduction potential –0.48 V vs. SCE. Adapted with permission from Ref. 161, Copyright (1996) American Physical Society.

based on the Marcus theory and partial relaxation, with major contributions by Ulstrup and Kuznetzov.[153]

Baier and Stimming[162] demonstrated that *in-situ* STM can be performed not only in constant potential mode (ECSTM) and but also in constant current mode (scanning electrochemical potential microscopy, SECPM). The authors used the latter to probe the electrochemical double layer potential as it changes around adsorbed individual ferritin and peroxidase molecules on HOPG. The SECPM potential distribution images compare favorably to ECSTM conductivity images.

STM probes can provide very good lateral resolution (<1 nm) but at the close proximity required for this resolution, the z-dimension is controlled only by the exponentially distance dependent tunneling current. In a liquid environment with inherently variable background leakage, and as soon as the tip contacts the molecule, the z-dimension becomes poorly controllable, which may lead to excessive forces that distort the probed molecule. Therefore, *in-situ* AFM is preferable for probing large molecules and in particular to contact soft and fragile bio-molecules.[163] However, traditional gold or platinum-coated conducting AFM tips are rather large (~50 nm), posing limits on the lateral resolution and sensitivity due to the background current. For that reason, particular efforts have been undertaken to reduce both the tip apex size and the exposed tip area. Patil et al. recently reported on the fabrication of electrochemical AFM nanoprobes made by SEM-controlled mounting of a single multiwalled carbon nanotube fiber on a traditional conducting AFM probe. The complete cantilever was insulated with parylene polymer, after which the nanotube tip end was re-exposed by laser ablation.[164] An interesting alternative approach has been followed by Kueng and co-workers[165]: a combined SECM/AFM tip was fabricated by focused ion beam milling to expose a sharp non-conducting tip from a parylene-insulated and gold-coated conducting AFM tip. In this way, a nanoscopic gold ring electrode was created at a defined distance above and around the AFM tip apex. This bifunctional tip was used to detect hydrogen peroxide generated by micron-sized patches of immobilized glucose oxidase molecules while simultaneously imaging with tapping mode AFM.

Yet another strategy was followed by Anne et al.[166] They argue that the efforts to reduce the size of the SECM electrode create

a paradox: when decreasing the tip size to nanoscopic dimensions (e.g., by using a conductive AFM tip) the finite interfacial reduction/oxidation rate of the shuttling mediator will not be able to outcompete the lateral diffusion rate out of the gap, thus leading to loss of resolution and sensitivity. Their solution is to tether the mediator (ferrocene) via a short PEG polymer chain to a conducting AFM tip, such that the mediator will provide diffusive feedback but cannot escape. Tip-attached redox mediator (TARM) AFM-SECM simultaneously provides high resolution topography and current images in tapping mode. Because the lateral resolution is governed by the length of the tether and not by the tip size and lateral diffusion as in classical SECM, the local electrochemical activity of the surface can be probed at a resolution comparable with the AFM topographical image.

The methods discussed above strive to detect single redox molecules by way of enhancing the number of passed electrons across a junction (i.e., without relaxation to electrochemical equilibrium), by coupling single-electron transfer reactions to multiple photons via subsequent excitation/emission, or rapidly shuttling electrons via a diffusing molecule. An alternative method is to utilize the intrinsic chemical amplification provided by catalysis. The large (10–100 pA) electrocatalytic water splitting or formation current generated by a Pt or Pd particle is relatively easy to detect above the background. When such particles are permanently adsorbed to an electrode surface with a much lower catalytic activity, the catalytic nanoparticle generates a localized diffusive reaction layer in which the electrolyte composition (pH, concentrations of hydrogen and oxygen) is distinctly altered. This can be detected with SECM, or at higher resolution—with electrochemical STM. An added advantage of STM is that a small part of the scanning tip can be deposited on the surface to create a single catalytically active nanoscopic feature, the shape and size of which can be instantaneously characterized. Potentiometric and amperometric electrochemical STM methods to detect the reaction layer around such deposited catalytic nanoparticles have been pioneered by Stimming and co-workers.[167, 168]

Even more challenging is the application of enzyme molecules as nanoscopic catalytic particles. Although the dimensions are similar to metallic nanoparticles, enzyme molecules harbor only one or few catalytic sites, while metallic nanoparticles support a

large number of catalytic crystal facets and atomic steps, and display the cumulative activity of this large heterogeneous ensemble of catalytic sites. With typical enzymatic turnover rates between 10 and 10000 per second, the current generated per molecule will be in the range of attoamperes to femtoamperes. For that reason, most single-enzyme electrochemistry efforts concentrate either on the detection of a fluorescent product, or sensing an accumulated electroactive product with nano-SECM or scanning probe methods, as described above, or with interdigitated electrodes. Nonetheless, our group recently achieved direct protein film voltammetry of <50 hydrogenase molecules immobilized on a 100x100 nm^2 gold electrode, generating 20 fA of electrocatalytic current when reducing protons to hydrogen (Fig. 8).[169]

2. Electrochemistry of Freely-Diffusing Molecules

Time-resolved electrochemical detection of a single or few freely-diffusing molecules is a very challenging enterprise for the simple reason that ordinarily, a redox-active molecule contributes only one or a few electrons to the measured current with each encounter at the electrode. While these days it is routinely possible to measure currents in the low picoamperes (pA) with commercial potentiostats, and even femtoamperes (fA) with electrometers, currents on the order of a few attoamperes (aA) present a great challenge (an attoampere corresponds to merely 6 electrons per second!).

Redox cycling provides a means by which a single molecule can shuttle multiple electrons between the two electrodes, thus giving rise to a continuous, measurable current. As discussed in Section III.2 (Eq. 13) the quantity eD/z^2 represents the contribution of a single molecule to the current, and its magnitude increases quadratically with decreasing electrode spacing. It is therefore conceivable that for small enough spacing, z, even a single molecule may yield a measurable current.

An implementation of this idea by Fan and Bard[37] stands as the first example where electrochemical detection of a single molecule was reported. In this instance they used an Apiezon wax-coated Pt-Ir nanoelectrode tip with the wax shrouding the electrode, and used it to trap a small solution in close proximity (~ 10 nm) to a conducting substrate (ITO). In the positive feedback mode, they were able to amplify the current $\sim 10^6$ fold and observed stochastic

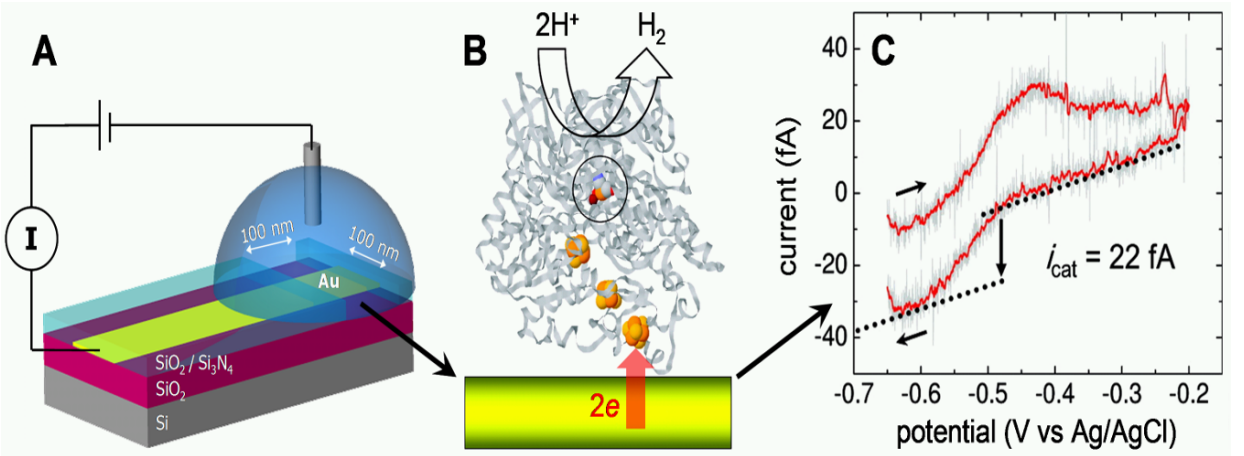

Figure 8. A. Fabricated $(100\ nm)^2$ gold nanoelectrode; B. Cartoon of hydrogenase immobilized on the nanoelectrode; C. Background-subtracted voltammogram, revealing the proton-reduction current generated by ~20 hydrogenase molecules (scan rate 1.5 mV/s, pH 5.7; 1 fA = 6250 electrons/s). Adapted with permission from Ref. 169, Copyright (2008) American Chemical Society.

signals of amplitude 0.5–1 pA[32] that corresponded to the redox cycling of one or few $FcTMA^+$ molecules. Slow fluctuations in current and the shape of responses were also seen. In the absence of any clear picture of the exact cell geometry, it was proposed that the wax shroud had cracked in places leading to microscopic crevices in which the molecules could get trapped and hence not contribute to the current until they egressed back into the cell. Another possible cause was identified as being the slow drift in the tip-substrate spacing due to temperature fluctuations.

An approach similar to the above was used by Sun and Mirkin[121] where they prepared a glass encased disc-type platinum electrode (5 to 150 nm radius) which was etched to create a recessed zeptoliter-sized cavity. This cavity was filled with an aqueous solution containing redox species and the etched electrode was dipped in a pool of mercury (Hg) to create a TLC geometry. With redox cycling, steady-state voltammograms of the trapped molecules were obtained which were assigned to a few and even single molecules. By repeating the experiments, different steady-state current values were obtained, which was ascribed to different number of molecules being trapped. It remains unclear to what extent the geometry of the device varied between experiments. Since the volume of the TLC was closed off, there was no way of observing statistical fluctuations in the TLC cavity.

In both the approaches mentioned above, the measured signal is a consequence of multiple electron-transfer events as the molecule redox cycles between the two electrodes. The measured current thus results from a large number of electron transfer events, and the advantage of probing an individual molecule as opposed to an ensemble measurement is thus lost. This situation can be partly ameliorated by employing a detection configuration that is a hybrid of electrochemical and optical methods, as discussed in Section IV.1, although this invariably requires the immobilization of target molecules.

Another ingenious strategy to detect single nanoparticles relies on amplification through electrocatalytic reactions that occur only on the metal nanoparticle in question but not on the underlying electrode.[170] Ordinarily, the nanoparticle charging events would transfer only one or a few electrons, yielding a current that would be essentially indistinguishable from the background noise. However, if there is a species present in solution whose reduction

or oxidation the metal nanoparticle can catalyze, then upon contact of the nanoparticle and the electrode, a much larger current will flow (assuming the flux of the species to the nanoparticle is much higher than the flux of the particle itself to the electrode surface). This principle was demonstrated by immersing a carbon fiber electrode in an acidic aqueous solution of Pt nanoparticles, and the reduction of protons and hydrogen peroxide was used as the electrocatalytic reaction to detect single nanoparticle collisions at the electrode.[170]

V. APPLICATIONS IN BIOLOGY AND MEDICINE

Nanoelectrodes are finding increasing use in both fundamental as well as applied studies of biological systems. In addition to the performance enhancements discussed above, a benefit of miniaturization with respect to sensors is that it becomes possible to fit more electrodes onto a given device footprint. Depending on the applications, this can be harnessed either to provide spatial resolution or for the realization of massively parallel measurements. Apart from directly shrinking the dimensions of the working electrode, another approach to nanoelectrochemical systems relies on functionalizing macro-scale electrodes with nanostructured materials like metal nanoparticles,[125] carbon nanotubes,[171] quantum dots etc. to interface with biological macromolecules.[172] Besides increased surface areas, these nanostructured bio-interfaces can also provide access to unique electrical and optical properties of nanoscale phenomena through confinement effects etc.[125,173] The use of nanostructured materials represent interesting and important advancements. Since their application to biology and medicine are discussed in much more detail in the other chapters of this double volume, however, we concentrate here on only a few examples that are linked to the concepts discussed in the earlier Sections of this Chapter.

The limited selectivity of electrochemical detection is one of the key bottlenecks to the development and widespread adoption of (nano)electrochemical technologies in biology and medicine. Without a means of boosting selectivity, electrochemical detection remains mostly limited to *in-vitro* measurements with purified systems or situations where it can be coupled either with separa-

tions techniques, such as chromatography or electrophoresis[174, 175], or in combination with other, mainly optical detection schemes, such as fluorescence[139] or SERS.[143] Two possible strategies that may alleviate these problems include the functionalization of nanoelectrodes with enzymes and the deployment of selective membranes. The inherent selectivity and high catalytic activity of enzymatic reactions can be effectively utilized provided the long-standing problems of robust functionalization and effective wiring of the enzymes are overcome. The coupling between redox enzymes and nanoscopic electrode structures has been the subject of several reviews.[172, 176-179]

These above limitations notwithstanding, electrochemical sensor applications have still found their way into the marketplace. The most common and commercially significant application of electrochemical sensors is in the detection of glucose.[180] Hundreds of millions of people suffer from diabetes and require daily monitoring of blood glucose levels. Further improvements are still needed, most notably in the development of continuous and *in-vivo* sensing strategies. The use of nanostructured materials, especially as electrical interconnects with the enzymes, together with nanoelectrodes holds considerable potential for improvement of sensor response of these devices.[181] An interesting device made by Tao's group, comprised of a nanojunction formed by bridging of two nanoelectrodes separated by 20-60 nm, with polyaniline/glucose oxidase. The signal transduction mechanism relied on the change in the conductance of the nanojunction as a consequence of glucose-oxidation induced changes in the polymer redox state. Due to the small size of the nanojunction sensor, the enzyme was regenerated naturally without the need of redox mediators and gave a very fast response (<200 ms). [182]

Another direction in continuous monitoring is in the development of implantable devices. These types of devices will have to be very small, robust, resistant to fouling, and bio-compatible.[183] Carbon nanotube based devices are actively investigated for these applications, as they may exhibit many of these desired qualities.[184] In one of the first examples of carbon nanotube sensors, Lin et al. created a Clark type glucose sensor by covalently immobilizing glucose oxidase on carbon nanotube nanoelectrode ensembles.[185]

The detection of nucleic acids (DNA, RNA) by hybridization to a known complementary sequence (usually in the form of immobilized arrays) is pivotal for clinical diagnostic applications, such as pathogen and cancer detection, and genomic screening and profiling. Nucleic acid fragments are biomarkers for diseases, but since often only a few copies of a particular DNA or RNA fragment are present, the ability to scale hybridization arrays down to a detection level of a few duplex molecules is highly desirable. Many efforts have been reported to achieve this sensitivity via nano-electrochemistry, applied in large-scale arrays of nanostructured microelectrodes.[186, 187] Zhang and co-workers reported the detection of 3000 DNA molecules, using a secondary probe strand labeled with peroxidase, followed by electrochemical detection of the catalytically produced hydrogen peroxide with an Os-containing redox hydrogel on a microelectrode.[188] Munge et al. described the electrochemical detection of as few as 80 DNA copies (3 per μL), which is the highest electrochemical sensitivity to date.[189] This was achieved via layer-by-layer electrostatic self-assembly of alkaline phosphatase enzyme molecules and polyion layers on a carbon nanotube template. The enzyme catalyzed the conversion of alpha-naphtyl phosphate to redox-active product alpha-naphtaphenol. By using a hybridization-controlled sandwich assay in combination with magnetic nanoparticles to collect the analyte, a large number of enzyme molecules per analyte strand were obtained.

1. Sensor Fabrication

One of the limitations of nanoelectrodes is the difficulty of fabrication. Within the framework of sensor technology, the added requirements of robustness and reproducibility are imposed. As a result, some very interesting ways to make them have emerged.

(*i*) *Nano Interdigitated Electrode Arrays (nIDEA)*

Interdigitated electrodes have many applications within electrical sensing. Typical applications are capacitive sensing, surface acoustic wave resonators, and with some modification, accelerometers. Jaffrezic-Renault and Dzyadevych provide an excellent review of conductometric sensors for environmental monitoring.[85]

Interdigitated electrodes are of particular interest in the detection of electroactive species, as they allow for redox cycling. The effect of various interdigitated geometries on the redox cycling amplification factor have been investigated and recently reported.[190, 191] Finot et al. employ interdigitated electrodes to detect DNA hybridization.[192] The DNA was coupled with an electroactive species to facilitate detection. They show that using interdigitated nanoelectrodes in combination with square-wave voltammetry improves the signal-to-noise and concentration sensitivity versus standard macro- or microelectrodes.

Geometry can also be used to manipulate chemical properties at the nanoscale. Under physiological conditions, adrenaline undergoes cyclization when oxidized, therefore making it difficult detect at very low concentration. By employing a nIDEA, at low concentrations it is possible to reduce the oxidized adrenaline back to its stable form before it reacts with another molecule and thus measure a redox current.[193] In recent work by Goluch et al. the stability of a molecule was exploited to achieve the opposite effect. It is difficult to detect electroactive species in bodily fluids because high concentrations of ascorbic acid are present that mask the target signal. By confining the sample inside of a nanofluidic channel placed over a nIDEA, as shown in Fig. 9, the signal from ascorbic acid was suppressed by oxidative decomposition of the molecule, allowing paracetamol (a.k.a. acetaminophen), present in much lower concentrations, to be detected.[190]

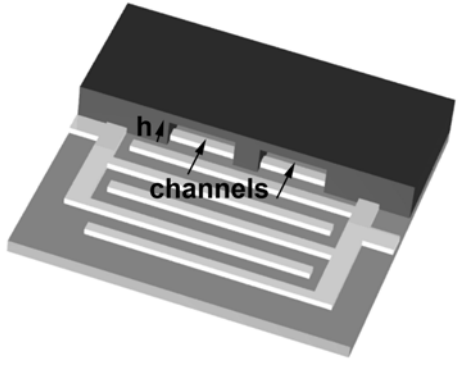

Figure 9. nIDEA with nanofluidic channels placed over it to confine molecules near the electrodes.

(*ii*) *Nanopillars and Nanoelectrode Ensembles*

The terms nanopillars and nanoelectrode ensembles (NEE) are often used interchangeably. In general, these nanostructures are created by depositing metal within a porous material that is removed afterwards, leaving behind freestanding structures. They are another way to introduce nanostructure on electrodes. A few examples are presented here, in which these pillar/mesh structures have been employed for detecting biologically relevant molecules.

Nickel nanopillars have been specifically cited as exhibiting innate selectivity. For example, Lu et al. employed nickel nanopillars as a nonenzymatic glucose sensor.[194] They postulated that glucose oxidation is catalyzed by nickel species on the electrode surface. Hubalek et al. employed a similar approach to detect and distinguish between native and denatured urease, which is a nickel-binding protein.[195]

In 2003, Gooding and co-workers[196], and Rusling and co-workers[197] independently presented the first two examples of electrodes modified with a *forest* of end-on oriented carbon nanotubes. Gooding et al. achieved this by covalent linkage of the carboxylic acid functionalities of the nanotube ends with a cysteamine SAM on gold, while the Rusling group assembled a nanotube forest non-covalently on a mixed Nafion/$Fe(OH)_3$ layer on graphite. Both groups applied these new nanowire array electrodes to covalently attach redox enzymes (microperoxidase by Gooding et al.; myoglobin and horseradish peroxidase by the Rusling group) via amide bonds to the water-exposed carboxylic acid functionalities of the nanotube ends, and observed the electrochemical response of these *wired* enzyme molecules. This was shortly followed by a report from the Willner group[198] on the wiring of glucose oxidase by a carbon nanotube forest electrode similar to that of the Gooding group, via a direct amide bond to the amine-functionalized FAD cofactor.

Ugo et al. demonstrated that a gold nanoelectrode ensemble (NEE) is much more sensitive to *cytochrome c* than standard electrodes. This added sensitivity has an added benefit because *cytochrome c* undergoes concentration dependent adsorption, therefore a significantly lower amount of the protein is needed for electrochemistry experiments involving the protein when these structures are employed.[199] A similar system was used to detect phenothia-

zine, an organic compound whose structure occurs in various antipsychotic and antihistaminic drugs that also exhibits concentration dependent adsorption.[200]

So far, empirical evidence has been demonstrated for these new and improved sensor properties employing nanoscale structures. Much work remains to be done to gain a better understanding of how nanostructure affects chemical properties. A very nice overview of nanowire ensemble devices is provided by Walcarius.[201] At the moment, pillars and electrodes in these arrays cannot be individually addressed, but in the future, these structures may have individual sensors poised at different potentials, coated with different modifications or even located within different regions of a sample matrix.

(*iii*) *Other Techniques*

Tyagi et al. employed a nice nanofabrication trick to create gold nanowires with a thickness of 30 nm, that they then used to detect dopamine.[202] They exploit undercut, a typical problem of microfabrication processing, to create nanostructures. By intentionally overetching nickel that is covered by photoresist, they create a recessed structure. Gold is then electrodeposited in the positions where the nickel is exposed, but since it is covered by resist, the gold structure is of the same thickness as the nickel film. The resist and nickel are removed, leaving behind gold nanowires.

While optical lithography hails as a champion of mass production, the equipment and processes necessary to achieve sub-micron resolution are still very expensive, and in the case of electron beam lithography, quite slow. Another way to achieve nanometer scale separation between electrodes is to partially remove an insulating material that is sandwiched between two electrodes.[203] This creates a series of nanopores, inside which proteins can be selectively patterned. Some amplification is achieved due to redox cycling in the confined space that is created.

Wolfrum et al. fabricated thin-layer cells with electrodes separated by a few tens of nanometers by employing a thin film as a sacrificial material and demonstrated their sensor capabilities by detecting catechol in the presence of excess ascorbic acid.[204]

Another alternative fabrication scheme utilizes nanoimprint lithography. The process employs a stamp that transfers a design

onto the surface of interest. Using this approach, Beck et al. created gold interdigitated electrodes, with electrodes as narrow as 200 nm being made on a 2-in wafer scale in one step.[205] This approach offers an appealing alternative to lithographic processing.

2. Probing Cells

The use of electrodes for detection of neurotransmitters *in-vivo* has a long history beginning with the pioneering work of Adams, where the direct electrochemistry of catecholamines in the central nervous system was first demonstrated.[206, 207] With the advent of UMEs in the early 1980s, the spatio-temporal resolution of these methods was greatly extended in both *in-vivo* as well as cultured cells, and Wightman's group demonstrated that individual exocytotic events could be directly monitored on the millisecond timescale by use of amperometric measurements.[208] Since then, cellular exocytosis has been investigated on a variety of cell types, including adrenal chromaffin cells, rat pheochromocytoma (PC12) cells and human or mouse pancreatic β-cells. The candidate cell systems are limited to those that release an oxidizable substance, which are often catecholamines, serotonin or tyrosine/tryptophan-type compounds. The most common measurement techniques employed are amperometry and fast-scan cyclic voltammetry (FSCV). FSCV is more suitable for *in-vivo* studies, since the cyclic voltammograms of species serve as *signatures* useful for identification. Amperometry is more suitable for direct measurement of exocytosis in culture cells.

Since the literature in this area is enormous we will only deal briefly with the possibilities of using nanoelectrodes in such amperometric measurements. For more background information, the reader is directed to several recent reviews. [209-212] Nanoelectrodes are expected to yield several benefits over UMEs for the studies of exocytosis. As mentioned earlier, by virtue of a faster RC time-constant, the temporal resolution of amperometric measurements can be lowered to the sub-millisecond domain. Most studies of exocytosis are conducted on nonsynaptic cell models that have large vesicles (0.25–1 μm diameter). With nanoelectrodes one can hope to measure release from synaptic vesicles (20–50 nm diameter). Because of reduced effects of uncompensated resistance (*iR* drop), they can also help mitigate peak distortions in FSCV. Spa-

tially, they will allow measurements of release at single-vesicle resolution. Wu et al. have already observed dopamine release from single living vesicles using carbon-fiber nanoelectrodes.[213] With sufficient miniaturization they may also enable measurements in the synaptic clefts, thereby directly probing neuronal communication. Smaller electrodes also have potential for lesser tissue damage in *in-vivo* studies. Much of the work to date has been performed with carbon fiber microelectrodes. This is because carbon fiber microelectrodes are biocompatible and more resistant to fouling than noble metal electrodes. Since most efforts in making nanoelectrodes have hitherto focused on noble-metal electrodes, a key challenge will be to make similar carbon-based nanoelectrodes. Chen et al. have fabricated carbon-fiber electrodes (100–300 nm diameter) covered with sheets of SWNTs that increase the surface area, while remaining nanometric in overall dimensions. These modified electrodes lowered the detection limit of select neurotransmitters 10-fold compared to the unmodified electrodes.[214] An alternative approach would be to utilize surface-modification of noble-metal electrodes to increase sensitivity and selectivity. However, these modifications can compromise the response time of the electrodes, thus lowering the time resolution.[215] They might also complicate the inherent uncertainties in the exact geometry of the electrode, especially in context of quantitative studies involving spatial resolution.

With the ability to make structures that are much smaller than an average mammalian cell (ca. 10–20 μm), the field is approaching a point at which it is possible to insert nanosized electrochemical probes inside cells. Recently, Sun et al. demonstrated electrochemical measurements obtained inside of a cell.[216] A 42 nm Pt, pulled glass electrode, was used to successfully penetrate a human epithelial cell and measure intracellular redox species. A schematic diagram of the measurement concept is shown in Fig. 10. The decrease in size of electrochemical tranducers corresponds with developments in the semiconductor industry, thus smaller electrode structures that permit measurements of still unknown exocytosis properties can be anticipated. Future application of nanostructures and electroanalytical measurements on living systems will necessitate investigating and answering questions associated with how *nondestructive* they really are and how the penetration of nano-

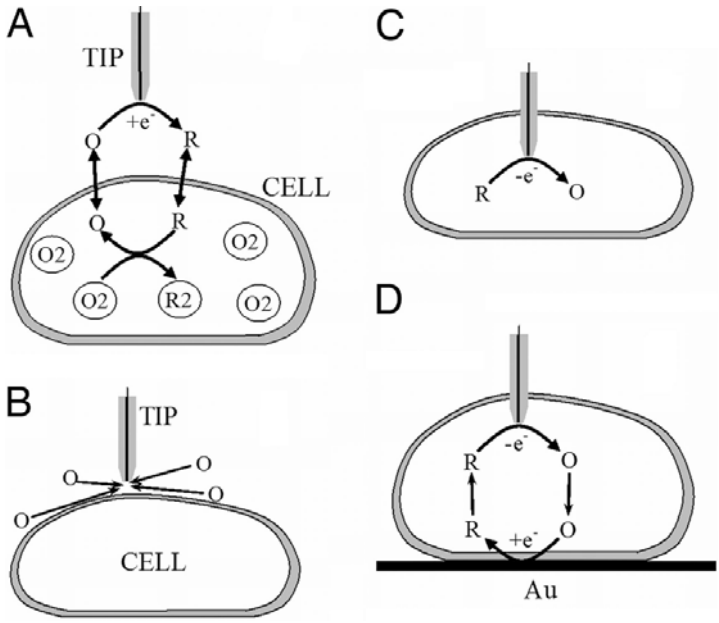

Figure 10. Schematic diagram of an SECM experiment with a single cell. (A) The tip is positioned in the solution close to the cell surface. Positive feedback is due to bimolecular electron transfer between the hydrophic redox mediator (O/R) and cell-bound redox moieties (O2/R2). (B) The lipid cell membrane is impermeable for a hydrophilic redox mediator. Negative feedback is due to the hindered diffusion of redox species to the tip electrode. (C) Nanoelectrode voltammetry inside the cell. (D) Positive feedback is produced by mediator regeneration by way of electron transfer at the underlying Au surface. Reproduced with permission from Ref. 216, Copyright (2008) National Academy of Sciences, U.S.A.

structures into cells with a subsequent electrical measurement affect the cellular functions.

Heller et al. took a different, non-invasive approach to probe cellular electrochemical activity. By coating a suspended single-walled carbon nanotube electrochemical (electrolyte-gated) FET device with antibodies, they were able to persuade macrophage cells to ingest (engulf) the nanotube. After positioning an individual cell over the device, both FET and electrochemical signals associated with cellular activity were separately detected. When the carbon nanotube was coated with Pt nanoparticles, sharp bursts of current due to electrocatalytic reduction of reactive oxygen and

nitrogen species were detected, which they attributed to discrete vesicular release events of these reactive species by the cell.[217]

3. Lab-On-A-Chip

One area where there is a clear need for miniaturization of electrodes is in lab-on-a-chip detection. The advantage of chip-based sensors is that some of selectivity and sensitivity issues may be avoided by combining electrochemical detection with purification, separation, and preconcentration techniques. There is also the possibility for integration of electronic components that will lead to more advanced handheld sensing devices, as shown in Fig. 11. Zhu and Ahn demonstrated a coulometry based system to detect p-aminophenol interacting with the working electrode. Importantly, the required electronics can be integrated onto a single chip by utilizing CMOS technology.[218]

The combination of fluidic systems with electrochemical detection offers automation and quantitative control over experimental conditions. This is especially important for cellular studies. As a result, many applications involving single-cell analysis on a chip have already been demonstrated.[219] In these types of experiments, the extracellular environment can be controlled very accurately. As the field matures, it is expected that system biology experiments will be conducted where discrete signals are obtained simultaneously from dozens or even hundreds of cells on a single device.

ACKNOWLEDGEMENTS

The continued support of the Lemay lab by NWO, NanoNed and FOM is gratefully acknowledged.

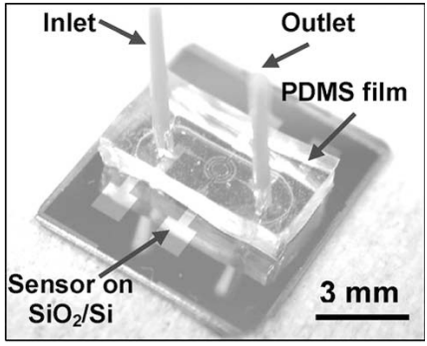

(a)

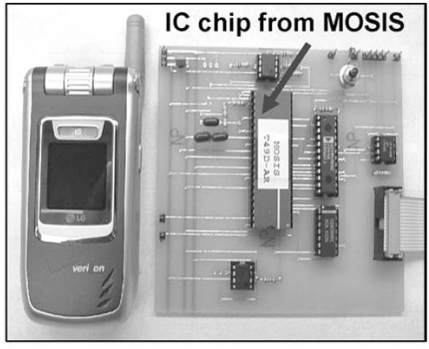

(b)

Figure 11. Handheld electrochemical analysis system: (a) electrochemical sensor embedded in a PDMS microfluidics channel, and (b) CMOS chip for sensor signal processing. Reproduced with permission from Ref. 218, Copyright (2006) IEEE.

REFERENCES

[1]A. I. Hochbaum and P. Yang, *Chem. Rev.* **110** (2009) 527.
[2]F. Patolsky, B. P. Timko, G. Zheng, and C. M. Lieber, *MRS Bull.* **32** (2007) 142.
[3]F. Patolsky, G. Zheng, and C. M. Lieber, *Anal. Chem.* **78** (2006) 4260.
[4]A. Chen and P. Holt-Hindle, *Chem. Rev.* ACS ASAP (2010) **DOI:** 10.1021/cr9003902
[5]N. L. Rosi and C. A. Mirkin, *Chem. Rev.* **105** (2005) 1547.
[6]B. K. Teo and X. H. Sun, *Chem. Rev.* **107** (2007) 1454.
[7]C. Dekker, *Nat. Nanotechnol.* **2** (2007) 209.
[8]A. S. Arico, P. Bruce, B. Scrosati, J.-M. Tarascon, and W. van Schalkwijk, *Nat. Mater.* **4** (2005) 366.
[9]P. G. Bruce, B. Scrosati, and J.-M. Tarascon, *Angew. Chem. Int. Ed.* **47** (2008) 2930.
[10]J. Chen and F. Cheng, *Acc. Chem. Res.* **42** (2009) 713.
[11]Y.-G. Guo, J.-S. Hu, and L.-J. Wan, *Adv. Mater.* **20** (2008) 2878.
[12]J. W. Long, B. Dunn, D. R. Rolison, and H. S. White, *Chem. Rev.* **104** (2004) 4463.
[13]G. Gruner, *Anal. Bioanal.Chem.* **384** (2006) 322.
[14]R. J. Chen, S. Bangsaruntip, K. A. Drouvalakis, N. Wong Shi Kam, M. Shim, Y. Li, W. Kim, P. J. Utz, and H. Dai, *Proc. Nat. Acad. Sci. U.S.A.* **100** (2003) 4984.
[15]R. J. Chen, H. C. Choi, S. Bangsaruntip, E. Yenilmez, X. Tang, Q. Wang, Y.-L. Chang, and H. Dai, *J. Am. Chem. Soc.* **126** (2004) 1563.
[16]Z. Liu, S. Tabakman, K. Welsher, and H. Dai, *Nano Res.* **2** (2009) 85.
[17]X. Liu, J. Lu, and C. Cha, *J. Electroanal. Chem.* **294** (1990) 289.
[18]A. M. Bond, D. Luscombe, K. B. Oldham, and C. G. Zoski, *J. Electroanal. Chem.* **249** (1988) 1.
[19]K. B. Oldham, *J. Electroanal. Chem.* **323** (1992) 53.
[20]M. A. Dayton, J. C. Brown, K. J. Stutts, and R. M. Wightman, *Anal. Chem.* **52** (1980) 946.
[21]R. M. Wightman, *Anal. Chem.* **53** (1981) 1125A.
[22]M. Fleischmann, S. Pons, D. R. Rolison, and P. P. Schmidt, *Ultramicroelectrodes*, Datatech Systems Inc., Morganton, NC, 1987.
[23]D. W. M. Arrigan, *Analyst* **129** (2004) 1157.
[24]Cynthia G. Zoski, *Electroanalysis* **14** (2002) 1041.
[25]R. B. Morris, D. J. Franta, and H. S. White, *J. Phys. Chem* **91** (1987) 3559.
[26]M. Fotino, *Rev. Sci. Instrum.* **64** (1993) 159.
[27]B. Zhang and E. Wang, *Electrochim. Acta* **39** (1994) 103.
[28]R. M. Penner, M. J. Heben, and N. S. Lewis, *Anal. Chem.* **61** (1989) 1630.
[29]A. J. Melmed, *Fifth international conference on scanning tunneling microscopy/spectroscopy* **9** (1991) 601.
[30]J. J. Watkins, B. Zhang, and H. S. White, *J. Chem. Educ.* **82** (2005) 712.
[31]L. A. Nagahara, T. Thundat, and S. M. Lindsay, *Rev. Sci. Instrum.* **60** (1989) 3128.
[32]F.-R. F. Fan, J. Kwak, and A. J. Bard, *J. Am. Chem. Soc.* **118** (1996) 9669.
[33]R. M. Penner, M. J. Heben, T. L. Longin, and N. S. Lewis, *Science* **250** (1990) 1118.
[34]M. V. Mirkin, F. R. F. Fan, and A. J. Bard, *J. Electroanal. Chem.* **328** (1992) 47.
[35]N. J. Gray and P. R. Unwin, *Analyst* **125** (2000) 889.
[36]S. L. Chen and A. Kucernak, *Electrochem. Comm.* **4** (2002) 80.

[37]F.-R. F. Fan and A. J. Bard, *Science* **267** (1995) 871.
[38]P. Sun, Z. Zhang, J. Guo, and Y. Shao, *Anal. Chem.* **73** (2001) 5346.
[39]B. Liu, J. P. Rolland, J. M. DeSimone, and A. J. Bard, *Anal. Chem.* **77** (2005) 3013.
[40]C. J. Slevin, N. J. Gray, J. V. Macpherson, M. A. Webb, and P. R. Unwin, *Electrochem. Comm.* **1** (1999) 282.
[41]J. L. Conyers and H. S. White, *Anal. Chem.* **72** (2000) 4441.
[42]J. V. Macpherson and P. R. Unwin, *Anal. Chem.* **72** (2000) 276.
[43]S. L. Chen and A. Kucernak, *J. Phys. Chem. B* **106** (2002) 9396.
[44]J. J. Watkins, J. Y. Chen, H. S. White, H. D. Abruna, E. Maisonhaute, and C. Amatore, *Anal. Chem.* **75** (2003) 3962.
[45]J. Abbou, C. Demaille, M. Druet, and J. Moiroux, *Anal. Chem.* **74** (2002) 6355.
[46]B. D. Pendley and H. D. Abruna, *Anal. Chem.* **62** (1990) 782.
[47]B. Zhang, J. Galusha, P. G. Shiozawa, G. L. Wang, A. J. Bergren, R. M. Jones, R. J. White, E. N. Ervin, C. C. Cauley, and H. S. White, *Anal. Chem.* **79** (2007) 4778.
[48]B. Zhang, Y. Zhang, and H. S. White, *Anal. Chem.* **76** (2004) 6229.
[49]Y. H. Shao, M. V. Mirkin, G. Fish, S. Kokotov, D. Palanker, and A. Lewis, *Anal. Chem.* **69** (1997) 1627.
[50]B. B. Katemann and W. Schuhmann, *Electroanalysis* **14** (2002) 22.
[51]G. Fish, O. Bouevitch, S. Kokotov, K. Lieberman, D. Palanker, I. Turovets, and A. Lewis, *Rev. Sci. Instrum.* **66** (1995) 3300.
[52]Y. X. Li, D. Bergman, and B. Zhang, *Anal. Chem.* **81** (2009) 5496.
[53]Y. Li, J. T. Cox, and B. Zhang, *J. Am. Chem. Soc.* **132** (2010) 3047.
[54]X. Zhang and B. Ogorevc, *Anal. Chem.* **70** (1998) 1646.
[55]P. Sun and M. V. Mirkin, *Anal. Chem.* **78** (2006) 6526.
[56]I. Heller, J. Kong, H. A. Heering, K. A. Williams, S. G. Lemay, and C. Dekker, *Nano Lett.* **5** (2005) 137.
[57]D. Krapf, M. Y. Wu, R. M. M. Smeets, H. W. Zandbergen, C. Dekker, and S. G. Lemay, *Nano Lett.* **6** (2006) 105.
[58]Y. Qiao, J. Chen, X. Guo, D. Cantrell, R. Ruoff, and J. Troy, *Nanotechnology* **16** (2005) 1598.
[59]S. L. Chen and A. Kucernak, *J. Phys. Chem. B* **107** (2003) 8392.
[60]C. Kranz, G. Friedbacher, B. Mizaikoff, A. Lugstein, J. Smoliner, and E. Bertagnolli, *Anal. Chem.* **73** (2001) 2491.
[61]A. Lugstein, E. Bertagnolli, C. Kranz, and B. Mizaikoff, *Surf. Interface Anal.* **33** (2002) 146.
[62]S.-J. Bai, T. Fabian, F. B. Prinz, and R. J. Fasching, *Sens. Actuators, B* **130** (2008) 249.
[63]R. J. Fasching, S. J. Bai, T. Fabian, and F. B. Prinz, *Microelectron. Eng.* **83** (2006) 1638.
[64]R. J. Fasching, Y. Tao, and F. B. Prinz, *Sens. Actuators, B* **108** (2005) 964.
[65]K. L. Saenger, G. Costrini, D. E. Kotecki, K. T. Kwietniak, and P. C. Andricacos, *J. Electrochem. Soc.* **148** (2001) C758.
[66]P. Thiébaud, C. Beuret, N. F. de Rooij, and M. Koudelka-Hep, *Sens. Actuators, B* **70** (2000) 51.
[67]J. K. Campbell, L. Sun, and R. M. Crooks, *J. Am. Chem. Soc.* **121** (1999) 3779.
[68]T. Ito, L. Sun, and R. M. Crooks, *Electrochem. Solid-State Lett.* **6** (2003) C4.
[69]S. G. Lemay, D. M. van den Broek, A. J. Storm, D. Krapf, R. M. M. Smeets, H. A. Heering, and C. Dekker, *Anal. Chem.* **77** (2005) 1911.

[70]D. Krapf, B. M. Quinn, M. Y. Wu, H. W. Zandbergen, C. Dekker, and S. G. Lemay, *Nano Lett.* **6** (2006) 2531.
[71]T. M. Day, P. R. Unwin, N. R. Wilson, and J. V. Macpherson, *J. Am. Chem. Soc.* **127** (2005) 10639.
[72]B. M. Quinn, C. Dekker, and S. G. Lemay, *J. Am. Chem. Soc.* **127** (2005) 6146.
[73]B. M. Quinn and S. G. Lemay, *Adv. Mater.* **18** (2006) 855.
[74]L. B. Anderson and C. N. Reilley, *J. Electroanal. Chem.* **10** (1965) 295.
[75]D. M. Oglesby, S. H. Omang, and C. N. Reilley, *Anal. Chem.* **37** (1965) 1312.
[76]A. Yildiz, P. T. Kissinger, and C. N. Reilley, *Anal. Chem.* **40** (1968) 1018.
[77]L. B. Anderson and C. N. Reilley, *J. Electroanal. Chem.* **10** (1965) 538.
[78]D. G. Sanderson and L. B. Anderson, *Anal. Chem.* **57** (1985) 2388.
[79]C. E. Chidsey, B. J. Feldman, C. Lundgren, and R. W. Murray, *Anal. Chem.* **58** (1986) 601.
[80]O. Niwa, M. Morita, and H. Tabei, *Anal. Chem.* **62** (1990) 447.
[81]M. I. Montenegro, M. A. Queiros, J. L. Daschbach, and eds., *Microelectrodes: Theory and Applications*, Kluwer Academic Publishers, Dordrecht, the Netherlands, 1991.
[82]I. Rubinstein, *Physical Electrochemistry: Principles, Methods, and Applications*, Marcel Dekker, Inc., New York, 1995.
[83]N. F. Sheppard, R. C. Tucker, and C. Wu, *Anal. Chem.* **65** (1993) 1199.
[84]B. Timmer, W. Sparreboom, W. Olthuis, P. Bergveld, and A. van den Berg, *Lab Chip* **2** (2002) 121.
[85]N. Jaffrezic-Renault and S. V. Dzyadevych, *Sensors* **8** (2008) 2569.
[86]Z. Liu, O. Niwa, R. Kurita, and T. Horiuchi, *Anal. Chem.* **72** (2000) 1315.
[87]R. S. Martin, A. J. Gawron, S. M. Lunte, and C. S. Henry, *Anal. Chem.* **72** (2000) 3196.
[88]K. B. Male and J. H. T. Luong, *J. Chromatogr. A* **1003** (2003) 167.
[89]O. Niwa, M. Morita, and H. Tabei, *Electroanalysis* **3** (1991) 163.
[90]W. R. Vandaveer IV, D. J. Woodward, and I. Fritsch, *Electrochim. Acta* **48** (2003) 3341.
[91]E. Nebling, T. Grunwald, J. Albers, P. Schafer, and R. Hintsche, *Anal. Chem.* **76** (2004) 689.
[92]K. Ueno, M. Hayashida, J.-Y. Ye, and H. Misawa, *Electrochem. Commun.* **7** (2005) 161.
[93]A. Bange, J. Tu, X. S. Zhu, C. Ahn, H. B. Halsall, and W. R. Heineman, *Electroanalysis* **19** (2007) 2202.
[94]M. A. G. Zevenbergen, D. Krapf, M. R. Zuiddam, and S. G. Lemay, *Nano Lett.* **7** (2007) 384.
[95]K. Hayashi, J. Takahashi, T. Horiuchi, Y. Iwasaki, and T. Haga, *J. Electrochem. Soc.* **155** (2008) J240.
[96]J. H. Min and A. J. Baeumner, *Electroanalysis* **16** (2004) 724.
[97]J. Strutwolf and D. E. Williams, *Electroanalysis* **17** (2005) 169.
[98]X. L. Yang and G. G. Zhang, *Sens. Actuators, B* **126** (2007) 624.
[99]M. Odijk, W. Olthuis, V. A. T. Dam, and A. van den Berg, *Electroanalysis* **20** (2008) 463.
[100]V. A. T. Dam, W. Olthuis, and A. van den Berg, *Analyst* **132** (2007) 365.
[101]A. J. Bard, F. R. F. Fan, J. Kwak, and O. Lev, *Anal. Chem.* **61** (1989) 132.
[102]A. J. Bard, Mirkin, M. V., ed., *Scanning Electrochemical Microscopy*, Marcel Dekker, New York, 2001.

[103]S. Amemiya, A. J. Bard, F.-R. F. Fan, M. V. Mirkin, and P. R. Unwin, *Annu. Rev. Anal. Chem.* **1** (2008) 95.
[104]M. A. Edwards, S. Martin, A. L. Whitworth, J. V. Macpherson, and P. R. Unwin, *Physiol. Meas.* **27** (2006) R63.
[105]W. S. Roberts, D. J. Lonsdale, J. Griffiths, and S. P. J. Higson, *Biosens. Bioelectron.* **23** (2007) 301.
[106]S. Amemiya, J. D. Guo, H. Xiong, and D. A. Gross, *Anal. Bioanal.Chem.* **386** (2006) 458.
[107]A. S. Baranski, *J. Electroanal. Chem.* **307** (1991) 287.
[108]K. B. Oldham, *Anal. Chem.* **64** (1992) 646.
[109]Y. Shao, M. V. Mirkin, G. Fish, S. Kokotov, D. Palanker, and A. Lewis, *Anal. Chem.* **69** (1997) 1627.
[110]W. R. Fawcett and M. Opallo, *Angew. Chem. Int. Ed.* **33** (1994) 2131.
[111]D. H. Evans, *Chem. Rev.* **108** (2008) 2113.
[112]M. V. Mirkin and A. J. Bard, *Anal. Chem.* **64** (1992) 2293.
[113]J. J. Watkins and H. S. White, *Langmuir* **20** (2004) 5474.
[114]J. J. Watkins and H. S. White, *J. Electroanal. Chem.* **582** (2005) 57.
[115]J. Velmurugan, P. Sun, and M. V. Mirkin, *J. Phys. Chem. C* **113** (2009) 459.
[116]M. A. G. Zevenbergen, B. L. Wolfrum, E. D. Goluch, P. S. Singh, and S. G. Lemay, *J. Am. Chem. Soc.* **131** (2009) 11471.
[117]A. J. Bard and L. R. Faulkner, *Electrochemical Methods: Fundamentals and Applications*, John Wiley & Sons Inc., New York, 2001.
[118]D. Andelman, *Soft Condensed Matter Physics in Molecular and Cell Biology*, Taylor & Francis, Boca Raton, FL, 2006.
[119]For a planar surface the potential far from the surface simply has the form $\varphi(x) = \varphi^0 \exp(-x/\lambda_d)$ with φ^0 a constant and x the distance from the surface. For other geometries the full dependence is more complex, but the exponential cutoff with characteristic length λ_d is retained.
[120]P. M. Biesheuvel, M. van Soestbergen, and M. Z. Bazant, *Electrochim. Acta* **54** (2009) 4857.
[121]P. Sun and M. V. Mirkin, *J. Am. Chem. Soc.* **130** (2008) 8241.
[122]M. A. G. Zevenbergen, P. S. Singh, E. D. Goluch, B. L. Wolfrum, and S. G. Lemay, *Anal. Chem.* **81** (2009) 8203.
[123]M. A. G. Zevenbergen, D. Krapf, M. R. Zuiddam, and S. G. Lemay, *Nano Lett.* **7** (2006) 384.
[124]R. S. Ingram, M. J. Hostetler, R. W. Murray, T. G. Schaaff, J. T. Khoury, R. L. Whetten, T. P. Bigioni, D. K. Guthrie, and P. N. First, *J. Am. Chem. Soc.* **119** (1997) 9279.
[125]R. W. Murray, *Chem. Rev.* **108** (2008) 2688.
[126]B. M. Quinn, P. Liljeroth, V. Ruiz, T. Laaksonen, and K. s. Kontturi, *J. Am. Chem. Soc.* **125** (2003) 6644.
[127]F.-R. F. Fan and A. J. Bard, *Science* **277** (1997) 1791.
[128]X. S. Xie and H. P. Lu, *J. Biol. Chem.* **274** (1999) 15967.
[129]W. E. Moerner, *J. Phys. Chem. B* **106** (2002) 910.
[130]N. G. Walter, C.-Y. Huang, A. J. Manzo, and M. A. Sobhy, *Nat. Methods* **5** (2008) 475.
[131]G. Binnig, H. Rohrer, C. Gerber, and E. Weibel, *Phys. Rev. Lett.* **49** (1982) 57.
[132]G. Binnig, C. F. Quate, and C. Gerber, *Phys. Rev. Lett.* **56** (1986) 930.
[133]R. E. Palacios, F.-R. F. Fan, A. J. Bard, and P. F. Barbara, *J. Am. Chem. Soc.* **128** (2006) 9028.

[134]R. E. Palacios, F.-R. F. Fan, J. K. Grey, J. Suk, A. J. Bard, and P. F. Barbara, *Nat. Mater.* **6** (2007) 680.
[135]Y.-L. Chang, R. E. Palacios, F.-R. F. Fan, A. J. Bard, and P. F. Barbara, *J. Am. Chem. Soc.* **130** (2008) 8906.
[136]C. Lei, D. Hu, and E. J. Ackerman, *Chem. Comm.* (2008) 5490.
[137]C. Lei, D. Hu, and E. Ackerman, *Nano Lett.* **9** (2009) 655.
[138]W. Xu, H. Shen, Y. J. Kim, X. Zhou, G. Liu, J. Park, and P. Chen, *Nano Lett.* **9** (2009) 3968.
[139]J. J. Davis, H. Burgess, G. Zauner, S. Kuznetsova, J. Salverda, T. Aartsma, and G. W. Canters, *J. Phys. Chem. B* **110** (2006) 20649.
[140]R. J. C. Brown and M. J. T. Milton, *J. Raman Spectrosc.* **39** (2008) 1313.
[141]P. G. Etchegoin and E. C. L. Ru, *Phys. Chem. Chem. Phys.* **10** (2008) 6079.
[142]M. M. Islam, K. Ueno, S. Juodkazis, Y. Yokota, and H. Misawa, *Anal. Sci.* **26** (2010) 13.
[143]M. M. Islam, K. Ueno, and H. Misawa, *Anal. Sci.* **26** (2010) 19.
[144]D. P. dos Santos, G. F. S. Andrade, M. L. A. Temperini, and A. G. Brolo, *J. Phys. Chem. C.* **113** (2009) 17737.
[145]B. Pettinger, G. Picardi, R. Schuster, and G. Ertl, *Single Mol.* **3** (2002) 285.
[146]W. Kiefer, *J. Raman Spectrosc.* **40** (2009) 1335.
[147]T. Schmid, B.-S. Yeo, G. Leong, J. Stadler, and R. Zenobi, *J. Raman Spectrosc.* **40** (2009) 1392.
[148]J. J. Davis, D. A. Morgan, C. L. Wrathmell, D. N. Axford, J. Zhao, and N. Wang, *J. Mater. Chem.* **15** (2005) 2160.
[149]Y. Selzer and D. L. Allara, *Annu. Rev. Phys. Chem.* **57** (2006) 593.
[150]N. J. Tao, *Nat. Nanotechnol.* **1** (2006) 173.
[151]S. N. Kim, J. F. Rusling, and F. Papadimitrakopoulos, *Adv. Mater.* **19** (2007) 3214.
[152]I. V. Pobelov, Z. Li, and T. Wandlowski, *J. Am. Chem. Soc.* **130** (2008) 16045.
[153]J. Zhang, A. M. Kuznetsov, I. G. Medvedev, Q. Chi, T. Albrecht, P. S. Jensen, and J. Ulstrup, *Chem. Rev.* **108** (2008) 2737.
[154]F. Chen and N. J. Tao, *Acc. Chem. Res.* **42** (2009) 429.
[155]R. J. Nichols, W. Haiss, S. J. Higgins, E. Leary, S. Martin, and D. Bethell, *Phys. Chem. Chem. Phys.* **12** (2010) 2801.
[156]A. Alessandrini, S. Corni, and P. Facci, *Phys. Chem. Chem. Phys.* **8** (2006) 4383.
[157]R. Sonnenfeld and P. K. Hansma, *Science* **232** (1986) 211.
[158]K. Itaya and E. Tomita, *Surf. Sci.* **201** (1988) L507.
[159]M. F. Crommie, C. P. Lutz, and D. M. Eigler, *Phys. Rev. B: Condens. Matter* **48** (1993) 2851.
[160]W. Schmickler, *Surf. Sci.* **295** (1993) 43.
[161]N. J. Tao, *Phys. Rev. Lett.* **76** (1996) 4066.
[162]C. Baier and U. Stimming, *Angew. Chem. Int. Ed.* **48** (2009) 5542.
[163]J. Zhao, J. J. Davis, M. S. P. Sansom, and A. Hung, *J. Am. Chem. Soc.* **126** (2004) 5601.
[164]A. V. Patil, A. F. Beker, F. G. M. Wiertz, H. A. Heering, G. Coslovich, R. Vlijm, and T. H. Oosterkamp, *Nanoscale*
[165]A. Kueng, C. Kranz, A. Lugstein, E. Bertagnolli, and B. Mizaikoff, *Angew. Chem. Int. Ed.* **42** (2003) 3238.
[166]A. Anne, E. Cambril, A. Chovin, C. Demaille, and C. Goyer, *ACS Nano* **3** (2009) 2927.
[167]J. Meier, K. A. Friedrich, and U. Stimming, *Faraday Discuss.* **121** (2002) 365.

[168]J. Meier, J. Schiøtz, P. Liu, J. K. Nørskov, and U. Stimming, *Chem. Phys. Lett.* **390** (2004) 440.
[169]F. J. M. Hoeben, F. S. Meijer, C. Dekker, S. P. J. Albracht, H. A. Heering, and S. G. Lemay, *ACS Nano* **2** (2008) 2497.
[170]X. Xiao and A. J. Bard, *J. Am. Chem. Soc.* **129** (2007) 9610.
[171]N. Chopra, V. G. Gavalas, B. J. Hinds, and L. G. Bachas, *Anal. Lett.* **40** (2007) 2067.
[172]D. Chen, G. Wang, and J. Li, *J. Phys. Chem. C* **111** (2006) 2351.
[173]A. C. Pereira, A. Kisner, N. Duran, and L. T. Kubota, *J. Nanosci. Nanotechnol.* **10** (2010) 651.
[174]D. M. Radzik and S. M. Lunte, *Crit. Rev. Anal. Chem.* **20** (1989) 317.
[175]N. A. Lacher, K. E. Garrison, R. S. Martin, and S. M. Lunte, *Electrophoresis* **22** (2001) 2526.
[176]Y. Lin, S. Taylor, H. Li, K. A. S. Fernando, L. Qu, W. Wang, L. Gu, B. Zhou, and Y.-P. Sun, *J. Mater. Chem.* **14** (2004) 527.
[177]J. J. Gooding, *Electrochim. Acta* **50** (2005) 3049.
[178]B. Willner, E. Katz, and I. Willner, *Curr. Opin. Biotechnol.* **17** (2006) 589.
[179]I. Willner, R. Baron, and B. Willner, *Biosens. Bioelectron.* **22** (2007) 1841.
[180]A. Heller and B. Feldman, *Chem. Rev.* **108** (2008) 2482.
[181]J. Wang, *Chem. Rev.* **108** (2007) 814.
[182]E. S. Forzani, H. Zhang, L. A. Nagahara, I. Amlani, R. Tsui, and N. Tao, *Nano Lett.* **4** (2004) 1785.
[183]S. Vaddiraju, I. Tomazos, D. J. Burgess, F. C. Jain, and F. Papadimitrakopoulos, *Biosens. Bioelectron.* **25** (2010) 1553.
[184]M. Trojanowicz, *Trac-Trends Anal. Chem.* **25** (2006) 480.
[185]Y. H. Lin, F. Lu, Y. Tu, and Z. F. Ren, *Nano Lett.* **4** (2004) 191.
[186]H. Lord and S. O. Kelley, *J. Mater. Chem.* **19** (2009) 9284.
[187]O. A. Sadik, A. O. Aluoch, and A. L. Zhou, *Biosens. Bioelectron.* **24** (2009) 2749.
[188]Y. C. Zhang, H. H. Kim, and A. Heller, *Anal. Chem.* **75** (2003) 3267.
[189]B. Munge, G. D. Liu, G. Collins, and J. Wang, *Anal. Chem.* **77** (2005) 4662.
[190]E. Goluch, B. Wolfrum, P. Singh, M. Zevenbergen, and S. Lemay, *Anal. Bioanal. Chem.* **394** (2009) 447.
[191]K. Ueno, M. Hayashida, J.-Y. Ye, and H. Misawa, *Electrochem Commun* **7** (2005) 161.
[192]E. Finot, E. Bourillot, R. Meunier-Prest, Y. Lacroute, G. Legay, M. Cherkaoui-Malki, N. Latruffe, O. Siri, P. Braunstein, and A. Dereux, *Ultramicroscopy* **97** (2003) 441.
[193]K. Hayashi, J.-i. Takahashi, T. Horiuchi, Y. Iwasaki, and T. Haga, *J. Electrochem. Soc.* **155** (2008) J240.
[194]L.-M. Lu, L. Zhang, F.-L. Qu, H.-X. Lu, X.-B. Zhang, Z.-S. Wu, S.-Y. Huan, Q.-A. Wang, G.-L. Shen, and R.-Q. Yu, *Biosens. Bioelectron.* **25** (2009) 218.
[195]J. Hubalek, J. Hradecky, V. Adam, O. Krystofova, D. Huska, M. Masarik, L. Trnkova, A. Horna, K. Klosova, M. Adamek et al., *Sensors* **7** (2007) 1238.
[196]J. J. Gooding, R. Wibowo, J. Q. Liu, W. R. Yang, D. Losic, S. Orbons, F. J. Mearns, J. G. Shapter, and D. B. Hibbert, *J. Am. Chem. Soc.* **125** (2003) 9006.
[197]X. Yu, D. Chattopadhyay, I. Galeska, F. Papadimitrakopoulos, and J. F. Rusling, *Electrochem. Commun.* **5** (2003) 408.
[198]F. Patolsky, Y. Weizmann, and I. Willner, *Angew. Chem. Int. Ed.* **43** (2004) 2113.
[199]P. Ugo, N. Pepe, L. Maria Moretto, and M. Battagliarin, *J. Electroanal. Chem.* **560** (2003) 51.

[200]B. Brunetti, P. Ugo, L. M. Moretto, and C. R. Martin, *J. Electroanal. Chem.* **491** (2000) 166.
[201]A. Walcarius, *Anal. Bioanal. Chem.* **396** (2010) 261.
[202]P. Tyagi, D. Postetter, D. L. Saragnese, C. L. Randall, M. A. Mirski, and D. H. Gracias, *Anal. Chem.* **81** (2009) 9979.
[203]S. Neugebauer, L. Stoica, D. Guschin, and W. Schuhmann, *Microchim. Acta* **163** (2008) 33.
[204]B. Wolfrum, M. Zevenbergen, and S. Lemay, *Anal. Chem.* **80** (2008) 972.
[205]M. Beck, F. Persson, P. Carlberg, M. Graczyk, I. Maximov, T. G. I. Ling, and L. Montelius, *Microelectron. Eng.* **73-74** (2004) 837.
[206]R. N. Adams, *Anal. Chem.* **48** (1976) 1126A.
[207]P. T. Kissinger, J. B. Hart, and R. N. Adams, *Brain Res.* **55** (1973) 209.
[208]R. M. Wightman, J. A. Jankowski, R. T. Kennedy, K. T. Kawagoe, T. J. Schroeder, D. J. Leszczyszyn, J. A. Near, E. J. Diliberto, and O. H. Viveros, *Proc. Nat. Acad. Sci. U.S.A.* **88** (1991) 10754.
[209]K. L. Adams, M. Puchades, and A. G. Ewing, *Annu. Rev. Anal. Chem.* **1** (2008) 329.
[210]C. Amatore, S. Arbault, M. Guille, and F. Lemaître, *Chem. Rev.* **108** (2008) 2585.
[211]D. L. Robinson, A. Hermans, A. T. Seipel, and R. M. Wightman, *Chem. Rev.* **108** (2008) 2554.
[212]W. Wang, S.-H. Zhang, L.-M. Li, Z.-L. Wang, J.-K. Cheng, and W.-H. Huang, *Anal. Bioanal. Chem.* **394** (2009) 17.
[213]W.-Z. Wu, W.-H. Huang, W. Wang, Z.-L. Wang, J.-K. Cheng, T. Xu, R.-Y. Zhang, Y. Chen, and J. Liu, *J. Am. Chem. Soc.* **127** (2005) 8914.
[214]R.-S. Chen, W.-H. Huang, H. Tong, Z.-L. Wang, and J.-K. Cheng, *Anal. Chem.* **75** (2003) 6341.
[215]E. W. Kristensen, W. G. Kuhr, and R. M. Wightman, *Anal. Chem.* **59** (1987) 1752.
[216]P. Sun, F. O. Laforge, T. P. Abeyweera, S. A. Rotenberg, J. Carpino, and M. V. Mirkin, *Proc. Natl. Acad. Sci. U. S. A.* **105** (2008) 443.
[217]I. Heller, W. T. T. Smaal, S. G. Lemay, and C. Dekker, *Small* **5** (2009) 2528.
[218]X. Zhu and C. H. Ahn, *IEEE Sens. J.* **6** (2006) 1280.
[219]C. Spegel, A. Heiskanen, Lars Henrik D. Skjolding, and J. Emnéus, *Electroanalysis* **20** (2008) 680.
[220]We use α to denote the transfer coefficient in the present case in accordance with much of the literature on heterogeneous kinetics of simple one-electron outer-sphere reactions. We acknowledge that the literature is varied on this particular notation, with several authors preferring to use the symmetry factor, β, to denote what we have, while retaining α to be used in the description of multi-electron transfer processes.
[221]D. Zhan, J. Velmurugan, M. V. Mirkin, *J. Am. Chem. Soc.* **13** (2009) 14756.

Pradyumna S. Singh

Pradyumna S. Singh obtained his Ph.D. in 2005 under the direction of Prof. Dennis H. Evans at the University of Arizona, USA. His graduate work dealt with studies of electrochemical proton-coupled electron transfer (PCET) reactions. After a brief foray into the field of artificial photosynthesis as a postdoctoral researcher in Leif Hammarström's lab at Uppsala University, Sweden, he joined Prof. Serge Lemay's lab at the Kavli Institute for Nanoscience at Delft University of Technology in the Netherlands. His current research interests include mesoscopic and single-molecule electrochemistry and development of nanofabricated devices to address fundamental and applied electrochemical problems.

Edgar D. Goluch

Edgar is a N.S.F. International Research Program Postdoctoral Fellow at the Kavli Institute for Nanoscience at Delft University of Technology in the Netherlands, working with Professor Serge Lemay in the Molecular Biophysics Group. He received his B.S. in Chemical Engineering, M.S. in Mechanical Engineering, and Ph.D. in Bioengineering from the University of Illinois at Urbana-Champaign. Edgar's graduate work involved detection of protein cancer markers using Lab-on-a-Chip devices. His current research interests focus on investigating biological phenomena associated with disease states using nanofabricated devices.

Hendrik A. Heering

Hendrik (Dirk) Heering obtained his PhD in 1995 for studies in bio-electrochemistry under the supervision of professors W. R. Hagen and C. Veeger at Wageningen University, The Netherlands. He carried out postdoctoral research projects with professor F. A. Armstrong at Oxford University, England, with Dr. G. Smulevich at University of Florence, Italy, and with professors S. de Vries and C. Dekker at Delft University of Technology, The Netherlands. He currently is assistant professor at the Leiden Institute of Chemistry, The Netherlands. His research interests are in redox biochemistry and respiratory enzymology, combining electrochemical, physical, spectroscopic, nanotechnological, and computational methods.

Serge G. Lemay

Serge G. Lemay was born in Rimouski, Canada, in 1970. He received the B.A.Sc. degree in electrical engineering with minor in physics from the University of Waterloo, Canada, in 1993, and the Ph.D. degree in experimental physics from Cornell University, USA, in 1999. He currently holds a dual professor appointment at the MESA$^+$ Institute for Nanotechnology, University of Twente and at the Kavli Institute of Nanoscience, Delft University of Technology, in the Netherlands. His current research interests include electrostatics in liquids, the fundamentals of electroosmosis, and the development of new nanofluidic devices based on electrochemical detection and actuation.

2

Interfacing Biomolecules, Cells and Tissues with Nanowire-based Electrical Devices

Moria Kwiat and Fernando Patolsky

School of Chemistry, Raymond and Beverly Sackler Faculty of Exact Sciences, Tel-Aviv University, Tel-Aviv 69978, Israel

I. INTRODUCTION

Detection and qualification of biological and chemical species are critical to many areas of health care and the life sciences, from diagnostic disease to the discovery and screening of new drug molecules. Central to detection is the transduction of a signal associated with the selective recognition of a species of interest. Several approaches have been reported for the detection of biological molecules, including ELISA,[1] surface plasmon resonance,[2] nanoparticles,[3] chemically sensitive field-effect transistors[4] and microcantilevers.[5] Although all have shown feasibility and promising progress applicability, none has yet demonstrated the combination of features required for rapid, highly sensitive multiplexed detection of biomolecules.

Nano-science and technology, whose unifying theme is the control of matter in this size range, allows revolutionary changes of the fundamental properties of matter and phenomena that are often drastically different compared to those they exhibit on the

N. Eliaz (ed.), *Applications of Electrochemistry and Nanotechnology in Biology and Medicine II*, Modern Aspects of Electrochemistry 53,
DOI 10.1007/978-1-4614-2137-5_2,

bulk phase. Since dimensionality plays a critical role in determining the qualities of matters, the realization of the great potential of nanoscale science and technology has opened the door to other disciplines such as life sciences and medicine, where the interface between them offers exciting new applications along with basic science research. The application of nanotechnology in life sciences, nanobiotechnology, is already having an impact on sensing, diagnostics and drug delivery. Several nanostructures have been reported for this task, including nanoparticles,[3] carbon nanotubes[6] and nanowires.[7] Inorganic nanowires, nanocrystals and carbon nanotubes exhibit unique electrical, optical and magnetic properties that can be exploited for sensing and imaging.[7] Advances in nanoscale materials have enabled to construct electronic circuits in which the component parts are comparable in size to the biological and chemical entities being sensed, therefore represent excellent primary transducers for producing signals that ultimately interface to macroscopic instruments. The ability to transduce chemical/biological binding events into electronic/digital signals suggests the potential for highly sophisticated interface between nanoelectronic and biological information processing systems.

Specifically, semiconducting nanowires are emerging as remarkably powerful building blocks in nanoscience, with the potential to have a significant impact on numerous areas of science and technology. Critical to the advances now being made worldwide with nanowires has been the well-developed understanding of nanowires growth mechanism, which has enabled the reproducible synthesis of nanowires of homogenous composition and diameter with controllable electronic and optical properties. Nowadays, semiconductor nanowires can be rationally and predictably controlled with all key parameters, including diameter, length, chemical composition and doping/electronic properties[8,9] with the ability to integrate arrays of discrete elements. Significantly, these characteristics make semiconductor nanowires one of the best defined and most versatile nanomaterial systems available today, thus enabling scientists to move beyond device proof-of-concept studies to the exploration of new areas of science and technology.

During the last decade nanowire-based electronic devices emerged as a powerful and universal platform, demonstrating key advantages such as rapid, direct, highly sensitive multiplexed de-

tection, for a wide-range of biological and chemical species from single molecules up to ultimate level of living cells.

In this manuscript we present representative examples in which these novel electrical devices have been used for living cells and tissues. Recording electrical signals from cells and tissues is a substantial tool for interrogating areas ranging from the fundamental biophysical studies of function in, for example, the heart and brain, through medical monitoring and intervention. NW-FET devices have the potential to form strongly coupled interfaces with cell membranes due to their inherent intrinsic characteristics, thus they can be used as highly sensitive local probes for extracellular and intracellular recordings, as recently demonstrated. As basic research, the direction is most stimulating and fruitful; however, it is important to realize that these powerful tools, if integrated with fundamental biology, can provide essential breakthroughs. Pulling down the barriers between very different sciences and technologies leads to surprising and new insights. The field is certainly most inter-disciplinary.

II. NANOWIRE FIELD-EFFECT DEVICES AS SENSORS

Detectors based on semiconductor nanowires are configured as field-effect-transistors (FETs), which exhibit a conductance change in response to variations in the electric field or potential at the surface of the channel region.[7,10a] In a standard FET, a semiconductor is connected to metal source and drain electrodes, through which a current is injected and collected, respectively. The conductance of the semiconductor is switched on and off or modulated by a third gate electrode capacitively coupled through a thin dielectric layer,[10b] Fig. 1A. In the case of a p-Si or other p-type semiconductor, applying a positive gate voltage depletes carriers and reduces the conductance, whereas applying a negative gate voltage leads to an accumulation of carriers and increases the conductance. Conductance modulations are dependent on the thickness of the oxide dielectric layer of the gate.[11] The dependence of the conductance on gate voltage makes FETs natural candidates for electrically based sensing, because the electric field resulting from the binding of a charged species to the gate dielectric is ana-

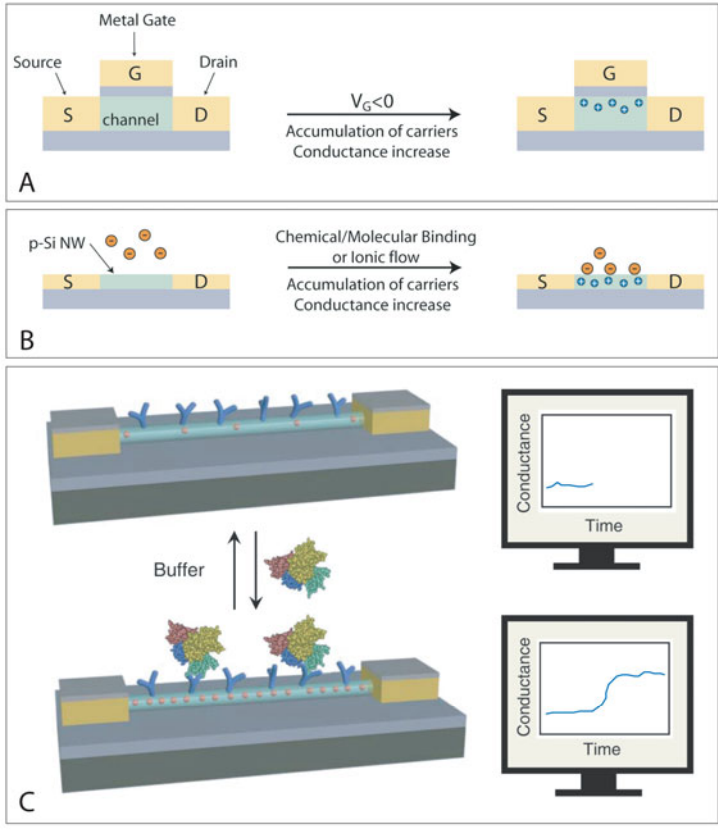

Figure 1. (A) Schematic of a p-type planar FET device, where S, D and G correspond to source, drain and gate electrodes, respectively. (B) Schematic of electrically based sensing using a p-type NWFET, where binding of a charged biological or chemical species to the chemically modified gate dielectric is analogous to applying a voltage using a gate electrode. (C) (left) Schematic illustration of a nanowire field-effect transistor configured as a sensor with antibody receptors (blue). (right) Binding of a protein with a net negative charge to a p-type nanowire yields an increase in conductance.

logues to the effect of applying a voltage with a gate electrode. The idea for sensing with FETs was introduced several decades ago,[12] but with planar FET sensors of previous planar devices which precluded their application due to their limited sensitivity.

Semiconductor nanowires and carbon nanotubes can also be configured as FETs. These devices overcome limitations of planar CHEMFETS by the use of their 1D nanoscale morphology, because the extremely high surface-to-volume ratios associated with these nanostructures make their electrical properties extremely sensitive to species adsorbed on their surfaces.[13]

The diameter of single wall carbon nanotubes, naturally occurring as hollow cylinders, is in the 1-nm range, the diameter of a DNA duplex. Because of the tubular structure of the nanotube, all the current flows at the surface of the channel, in direct contact with the environment.[14] In the case of nanowire device, an analyte binding to the surface of the nanowire leads to a change through the entire cross section of the device versus only a thin region near the surface of a planar device, resulting in a much greater change in device conductance for the NW versus a planar FET,[15] increasing the sensitivity to a point that single molecule detection is possible.[13]

Specifically, Si-nanowires configured as FETs exhibit performance characteristics comparable to or better than the best reported in the microelectronics industry for planar silicon devices [16]. Silicon-based nanotechnology is particularly promising since it is compatible with the conventional silicon microtechnology; silicon has been without doubt the basic building material for the semiconductor industry and the workhorse for micro-and nanotechnologies. SiNWs can be prepared as single crystal structures with diameters as small as 2–3 nm,[17] with complementary n- and p-type doping. Their electronic characteristics are well controlled during growth in contrast to carbon nanotubes and are also achieved with high reproducibility.[16b] The fabrication of SiNW-FET devices is relatively straightforward compared to conventional planar silicon FET devices, and combines bottom-up assembly of the nanowires on the device chip together with a single step of photolithography to make the metal contacts. Furthermore, SiNWs can be assembled on nearly any type of surface, including those that are typically not compatible with standard CMOS processing, such as flexible plastic substrates.[18] Lastly, their native oxide surfaces allow to chemi-

cally modify them and to bind them specific receptors groups to their surfaces.

The reproducible and tunable conducting properties of semiconducting nanowires, combined with the ability to bind desired analytes on their surface yields electrical readout that offers revolutionary conception, which has many advantages over conventional organic molecular dyes for labeling and optical–based detection of biological and chemical entities.[19a]

III. NANOWIRE FIELD EFFECT DEVICES FOR THE DETECTION OF MOLECULAR SPECIES

The unique features of semiconductor nanowires have enabled to produce highly sensitive devices that have been demonstrated for variety of biological and chemical applications. In all reports, key features such as direct, label free, real time, ultrahigh sensitivity, exquisite selectivity and the potential for integration of addressable arrays were shown, which set these devices apart from other sensor technologies available today. In the following Section we discuss representative examples which clearly demonstrate the potential of these devices to significantly impact many areas of biology and medicine.

NW-based FET can be configured as sensing device for biological and chemical molecules by linking receptor groups that recognize specific molecules to the surface of the NWs, Fig. 1B **and C**. SiNWs have native oxide coating that is naturally formed with their exposure to air. Extensive data exist for the chemical modification of silicon oxide or glass surfaces from planar chemical and biological sensors.[19b] Practically, the receptor solutions are delivered by a mated microfluidic channel to the chemically modified nanowires and the linkage is straightforward. When the sensor device with surface receptor is exposed to a solution containing a macromolecule like a protein or a chemical agent who has a net charge in the aqueous solution, specific binding will lead to a change in the surface charge that surrounds the nanowire and a change in the conductance respectively.

As a proof of concept, a flexible integrated NW sensor platform was developed, that incorporates SiNWs with well defined p- or n-type doping; source and drain electrodes that are insulated

from the aqueous environment so that only processes occurring at the SiNW surface contribute to the electrical signals; and a mated microfluidic channel (formed between a poly-dimethylsiloxane (PDMS) mold and the sensor chip) for delivery of solution suspensions onto specific locations on the SiNW-FET surface, Fig. 2A.

The detection capability of nanowire devices was first demonstrated in 2001 for pH monitoring, as well as selective detection of strepavidin and calcium ions.[10a] Notably, biotin-modified NWs were able to detect strepavidin down to the picomolar concentration range. The potential of Si-NW FET devices as a tool for drug discovery was illustrated in 2005 for the identification of molecular inhibitors of tyrosine kinases whose constitutive activity is responsible for chronic myelogenous leukemia.[20]

For diagnostic purposes of DNA, NW-based devices were demonstrated for detection of the activity and inhibition of telomerase, a ribonucleoprotein that is active in ≥80% of known human cancers, from unamplified extracts from as few as ten tumor cells, in solutions with relatively high (mM) ionic strength.[15b] In addition, the detection of genetic single mutation associated with cystic fibrosis was carried out at concentrations down to the 10-fM level,[21] which is 2–5 orders of magnitude better than that demonstrated for real-time measurements including SPR,[22] nanoparticles enhanced SPR[22] and quartz crystal microbalance[23] for DNA detection.

In 2004, the limit of biological detection, single particle sensitivity, was achieved by detecting, in real time, the reversible and selective binding of virus particles to antibody modified NWFETs. Delivery of a highly diluted virus solution on the order of ~80 aM or 50 viruses/ml yielded clear conductance changes that were supported by simultaneous optical imaging of fluorescently labeled influenza viruses indicating on the binding and unbinding of a single virus,[15a] Fig. 2B.

Ultimately, the multiplexed real time detection with ultrahigh sensitivity and exquisite selectivity was demonstrated in 2005 for the detection of cancer biomarkers, at concentrations down to ~2 fM,[15b] Fig. 3A. These results represent a sensitivity limit 10^4–10^9 times below that afforded by ion sensitive planar FETs.[24] Also, the detection can be carried out on as little as drop of blood instead of the milliliters needed for current analyses. The multiplexed detection of protein biomarkers is especially important in the diagnosis

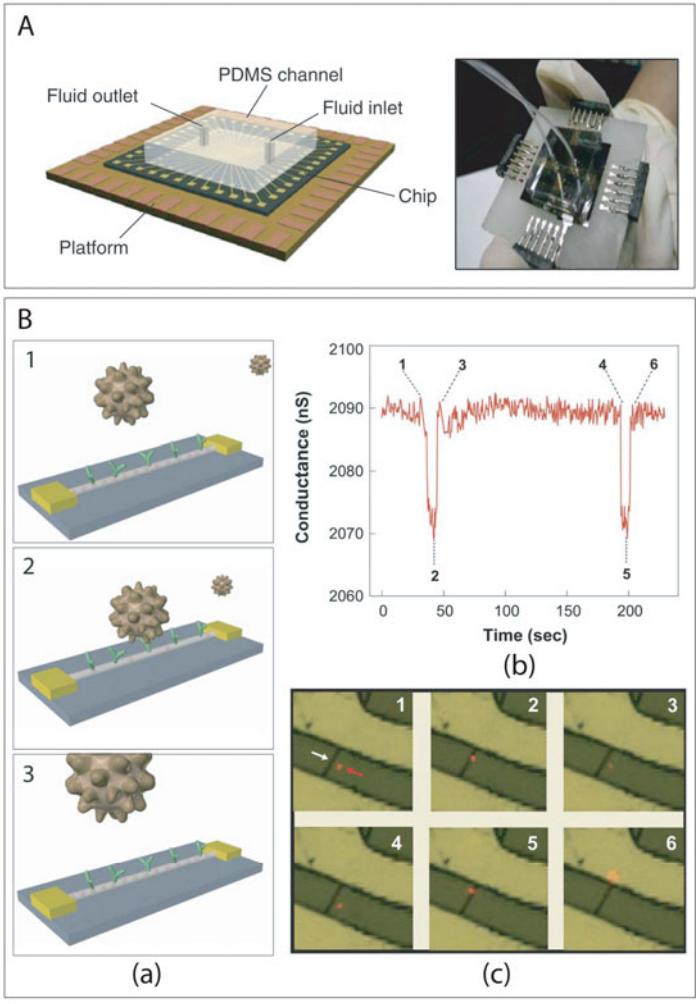

Figure 2. A) (left) Schematic and (right) photograph of a prototype nanowire sensor biochip with integrated microfluidic sample delivery. B) (a) Schematic illustration of a single virus binding and unbinding to the surface of a NWFET modified with antibody receptors. (b) Conductance vs. time data recorded from a single device modified with anti-influenza type A antibody. (c) Optical data recorded simultaneously with conductance data in (b). Combined bright-field and fluorescence images correspond to time points 1-6 indicated in the conductance data; virus appears as a red dot in the images.

of complex diseases like cancer because disease heterogeneity makes single marker tests inadequate. Moreover, detection of markers associated with different stages of disease pathogenesis could facilitate early detection.

The examples described in this Section illustrate the unique capabilities of nanowire-based field-effect sensor device arrays for medicine and life sciences, broadly defined. Throughout these experiments, devices have shown very good device-to-device absolute detection reproducibility and simultaneous false positive signals were discriminated; complementary electrical signals from p- and n-type devices provide a simple yet robust means for detecting false positive signals from either electrical noise or nonspecific binding of protein. It is important to note that these exquisite sensitivities were also verified by Reed's group in 2007 that used top-down fabricated NWs to demonstrate specific label free detection of proteins below 100 fM concentration, as well as real-time monitoring of the cellular immune response.

However, some limitations also exist. An intrinsic limitation of FET devices is that the detection sensitivity depends on solution ionic strength [25a]. In the case of nanowire FET-sensing, low salt (<1 mM) buffers are required to prevent screening of the charge-based electronic signal. Because blood serum samples have high ionic strength, diagnostic will require means to overcome the deceptive shielding. A simple desalting step before analysis was demonstrated to allow for highly sensitive assays.[15b] Recently, to overcome these limitations, Reed's group[25b] has developed an in-line microfabricated device that operates upstream of the nanosensors to purify biomarkers of interest prior to the detection step. The microfluidic purification chip captures the protein biomarkers directly from physiological solutions and, after a washing step is performed, the antigens are released into a clean low ionic strength buffer suitable for high-sensitivity sensing, as schematically described in Fig. 3B. First, a blood sample flows through the chip and the chip-bound antibodies bind to the soluble biomarkers, essentially purifying these molecules from whole blood. After this capture step, wash and sensing buffers are perfused through the device. Flow is then halted, and the sensing buffer-filled chip is irradiated with ultraviolet (UV) light, resulting in cleavage of the photolabile group and release of the bound biomarker–antibody complexes. Finally, the released purified antigen molecules, bound

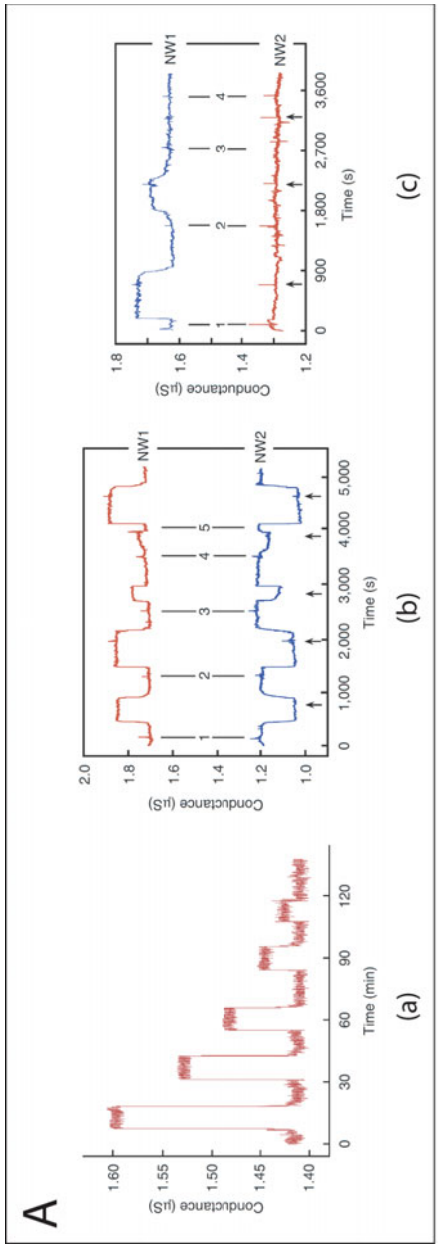

Figure 3. (A) Real-time nanowire sensing results. (a) Conductance versus time data recorded following alternate delivery of PSA and pure buffer solutions; the PSA concentrations were 5 ng/ml, 0.9 ng/ml, 9 pg/ml, 0.9 pg/ml, and 90 fg/ml, respectively. The buffer solutions used in all measurements were 1 mM phosphate (potassium salt) containing 2 mM KCl, pH 7.4. (b) Complementary sensing of PSA using p-type (NW1) and n-type (NW2) devices. Points 1-5 correspond to the addition of PSA solutions of (1,2) 0.9 ng/ml, (3) 9 pg/ml, (4) 0.9 pg/ml, and (5) 5 ng/ml. (c) Conductance-versus time data recorded simultaneously from 2 p-type silicon nanowire devices in an array, where NW1 was functionalized with PSA Ab1, and NW2 was modified with ethanolamine. Points 1-4 correspond to times when solutions of (1) 9 pg/ml PSA, (2) 1 pg/ml PSA, (3) 10 μg/ml BSA, (4) a mixture of 1 ng/ml PSA and 10 μg/ml PSA Ab1 were delivered.

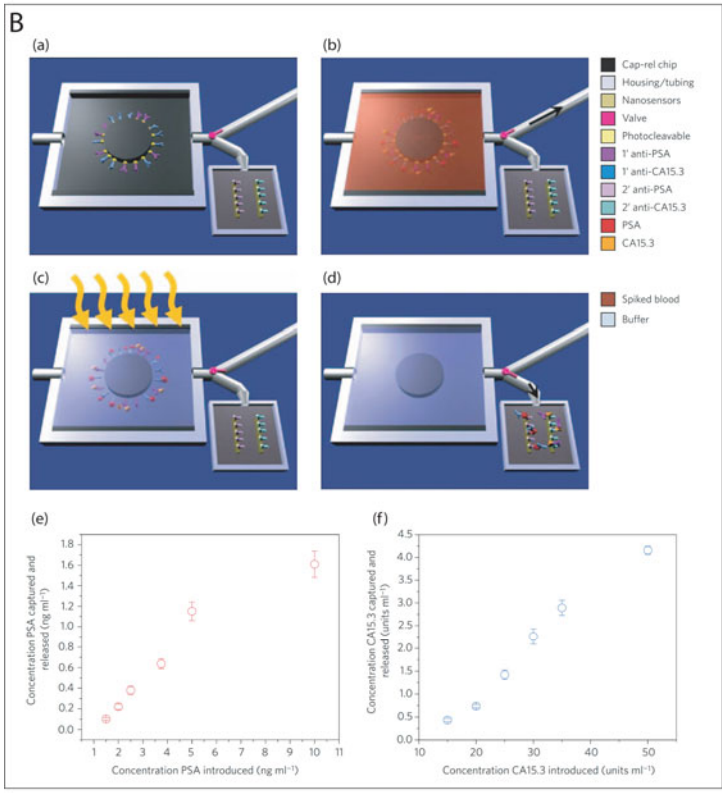

Figure 3. Continuation. (B) Schematic of MPC operation. (a) Primary antibodies to multiple biomarkers, here PSA and carbohydrate antigen 15.3, are bound with a photocleavable crosslinker to the MPC. The chip is placed in a plastic housing and a valve (pink) directs fluid flow exiting the chip to either a waste receptacle or the nanosensor chip. (b) Whole blood is injected into the chip with the valve set to the waste compartment (black arrow shows the direction of fluid flow) and, if present in the sample, biomarkers bind their cognate antibodies. (c) Washing steps follow blood flow, and the chip volume (5 ml) is filled with sensing buffer before UV irradiation (orange arrows). During UV exposure, the photolabile crosslinker cleaves, releasing the antibody–antigen complexes into solution. (d) The valve is set to the nanosensor reservoir (black arrow shows the direction of fluid flow) and the 5 ml volume is transferred, enabling label free sensing to be performed to determine the presence of specific biomarkers. (e, f) Scatter plots showing the concentration of PSA (e) and CA15.3 (f) released from the MPC versus the concentration of PSA and CA15.3 introduced in whole blood, respectively. Each data point represents the average of three separate MPC runs, and error bars represent one standard deviation.

to their specific antibody, are flowed into the sensing compartment where the sensing events occur on the nanoribbon-based devices. However, this sensing platform requires the use of a pair of antibodies against each biomarker of interest, one during the purification capturing step and one during the sensing step. Additionally, the use of silicon *nanoribbons* limited the detection sensitivity of the platform to ~1 ng/mL.

IV. NANOWIRE FET ARRAYS FOR THE ELECTRICAL MONITORING OF SINGLE NEURON AND NEURAL CIRCUITS

Previous studies provided strong support that NW and CNT devices have substantially higher sensitivity than planar FETs and thus can offer advantages for cellular recording beyond other technologies available today. Methods for measuring the electrical activity produced by electroactive cells include techniques such as glass micropipette electrodes,[26] voltage sensitive dyes,[26c] multi electrode arrays (MEAs)[27] and planar FETs,[28] which have and continue to play an important role in understanding the electrical behavior of individual cells and cellular networks.[29b] Micropipette electrodes can stimulate and record extracellular potentials *in vitro* and *in vivo* but more importantly, it can measure intracellular potentials with relatively good spatial resolution,[29b,30] capability that the other technologies still cannot reach. Yet, this method is invasive and especially difficult to multiplex where multiple recordings from different neurons are intended. Extracellular recordings are noninvasive and allow recording from multiple sites, from both individual cells and neural networks,[29,31] but suffer from very low signal-to-noise (S/N) ratio because of the use of relatively large electrodes and their imprecise positioning relative to the cell.[31]

Nanotechnogy–based devices are particularly attractive for interfacing with neurons since they are compatible with the size of neuron projections, and are able to detect and stimulate cellular activity at the level of individual axons or dendrites. A unique intrinsic feature of these devices compared with conventional planar devices is that the nanodevices protrude from the plane of the substrate, and hence can increase NW/cell interfacial coupling, forming naturally tighter junctions with the local cell membrane.

Indeed, studies have shown that nanostructured interfaces can enhance neuronal adhesion and activity.[14,32] It has been demonstrated that CNT networks or etched silica promote cellular adhesion, spreading and guidance, even in the absence of conventional adhesion factors such as polylysine.[32b,33] Neuronal stimulation through carbon nanotubes was demonstrated for the first time in 2005, by capacitive coupling to micron-scale pads consisting of tightly-packed carbon nanotube pillars.[34] Then, in 2006, nanotubes were assembled into mats using a layer-by-layer technique, and stimulation was achieved by passing lateral current pulses through the conductive mat.[35] In a follow-up work in 2007, the same technique was used to assemble close-packed films of photoactive HgTe nanoparticles; illumination of the film resulted in photochemistry and charge-transfer that subsequently stimulated an interfaced neuron.[36] Two other separate studies demonstrated that neurons cultured on CNT mats exhibit enhanced spiking activity (vs. those cultured on planar control surfaces), and suggest that the conductive, nanostructured surface enhances membrane excitability.[37]

The first electronic interface between NWs and neurons was reported by Lieber's group in 2006 in which hybrid structures consisting of nanowires FET arrays and patterned neurons were assembled and electrically characterized.[38] An important aspect of this work is the surface patterning and the incorporation of cells with respect to the NW-FET-devices with the ability to explore the cellular activity with the nanowires positioned directly at the vicinity of the cell surface. For a FET array to be used to record neuronal signals, the gate dimensions should ideally be on the nanometer scale, and the neurons have to *sit* on the non-metallized gate of the FET, affecting the source-drain current by capacitive coupling when the neuron undergoes a membrane voltage change. Several recent studies provided strong support that neurons growing according to pattern exhibit healthy electrophysiological properties and synaptic connections.[39] Nevertheless, this task is intriguing due to the difficulty of culturing cells in well defined orientations over nanoscale devices while maintaining good device characteristics.

In this work, p- and n-type Si-NWs were incorporated into FET device array structures in well defined positions in which they were spatially located along the axon and dendrites or at the junc-

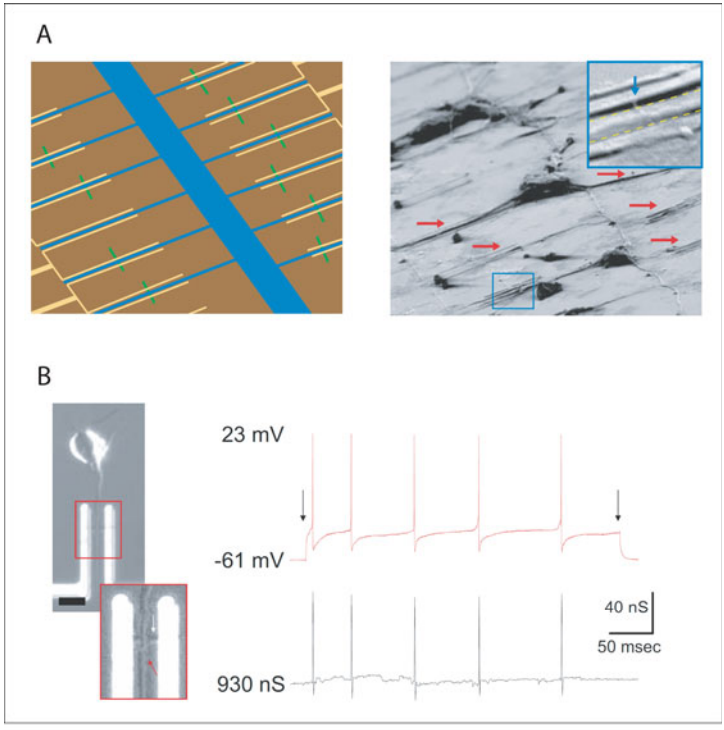

Figure 4. (A) NW/neuron interfaces. Schematic of interconnected neuron motif and SEM image of fixed neurons exhibiting a neural network where multiple neurites are interfaced with NW devices (red arrows). Inset: Zoom depicting an axon (denoted by yellow dotted lines) guided between source and drain electrodes across a NWFET (highlighted by blue arrow). (B) (left) Optical image of a cortical neuron aligned across a NWFET; (inset) High resolution image of region where axon (red arrow) crosses a NW (yellow arrow). (right) red trace- Intracellular potential of an aligned cortex neuron (after 6 days in culture) during stimulation with a 500 msec long current injection step of 0.1 nA; black trace- time-correlated signal from axon measured using a p-type NWFET.

tion with the cell body, creating *small* hybrid junctions with a typical junction area of 0.01–0.02 μm^2 which is at least two orders of magnitude smaller than microfabricated electrodes and planar FETs. Neuron cell growth was guided with respect to the device element by using chemically adhesive and repealing factors of poly-D-lysine and fluorosilane, respectively, Fig. 4A. Action po-

tential signals were elicited and recorded either by a conventional glass microelectrode impaled in the soma or by NW electrodes interfaced with an axon or dendrite.

Various set-ups of device structures were designed, for instance, a repeating 1-neuron/1-nanowire motif with the soma and the axon directed across the respective nanowire element. The results show the direct temporal correlation between the intracellular spikes initiated and recorded in the soma and the corresponding conductance peaks measured by the nanowire at the axon nanowire junction, Fig. 4B. For a p-type NW, an action potential will result in enhanced conductance followed by reduced conductance (the relative potential at the outer membrane becomes more negative and then more positive). Also, stimulation with the NW at the NW/axon junction resulted in somatic action potential spikes, which were detected with the intracellular electrode.

In this work it was shown that nanowire devices can be used to stimulate, inhibit, or reversibly block signal propagation along specific pathways while simultaneously following the signal flow throughout the network, capabilities that current techniques are not able to.

Following this work, other groups reported on the effective electrical interfacing between nanowire-based devices and bioelectrical cells.[40]

In a later work, reported in 2010, Si NWFET arrays were used for mapping neural circuits in the brain,[40a] Fig. 5A. Neural circuits are organized into hierarchical networks operating on spatial and temporal scales that span multiple orders of magnitude.[40d] It is highly desirable to map the activities in large populations of neurons with high position accuracy and precise timing. Revealing the functional connectivity in natural neuronal networks is central to understanding circuits in the brain. It was shown that silicon nanowire field-effect transistor (Si NWFET) arrays fabricated on transparent substrates can be reliably interfaced to acute brain slices. Devices were readily designed to record across a wide-range of length scales. Simultaneous NWFET and patch clamp studies enabled unambiguous identification of action potential signals, with signal amplitudes of 0.3 to 3 mV, Fig. 5B.

These results demonstrate that the NWFET arrays detect local activity of the pyramidal cell layer and lateral olfactory tract on at least the 10-μm scale, and thus can be used to understand the func-

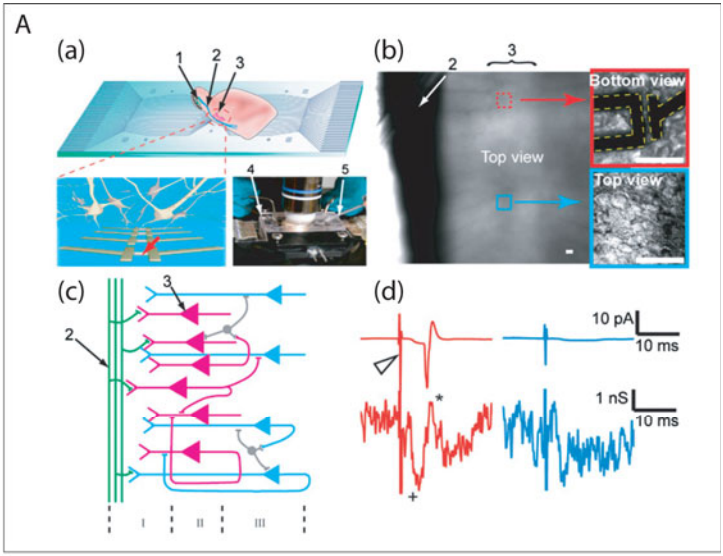

Figure 5. (A) NW-arrays for mapping neural circuits in the brain. (a) Measurement schematics. (Top) Overview of a NWFET array fabricated on a transparent substrate with slice oriented with pyramidal cell layer over the devices. (Bottom Left) Zoom-in of device region illustrating interconnected neurons and NWFETs. (Bottom Right) Photograph of the assembled sample chamber. 1, 2, and 3 indicate the mitral cells in the olfactory bulb, the lateral olfactory tract, and the pyramidal cells, resp. 4 and 5 mark the stimulation electrode and the patch clamp pipette, resp. (b) Top view of the NWFET array/brain slice region in fully assembled chamber with medium. Red Box shows a higher resolution image of a single device in contact with the neurons at the bottom of the slice. Blue Box shows the outermost neurons of the slice through an immersed lens from the top. (c) Laminar organization and input circuitry of the piriform cortex (Layer I–III). (d) Conductance recording from a NWFET (Lower Traces) in the same region as neuron used to record cell-attached patch clamp results (Upper Traces). Stimulation in the LOT was performed with strong (200 μA, Red Traces) and weak (50 μA, Blue Traces) 200 μs current pulses. The open triangle marks the stimulation pulse. (B) Localized detection with NWFET arrays. (a) (left) Optical image of brain slice over Si NWFET arrays defined by electron beam lithography. The dashed frames mark the positions of devices 1-4 and 5-6. (right) Schematics of the devices. (b) Signals obtained from devices 1-6 with 200 μs stimulation of 2.5 (left) and 1 mA (right); n=21. The dashed oval marks the region where signals of opposite polarity were recorded from devices 30 μm apart.

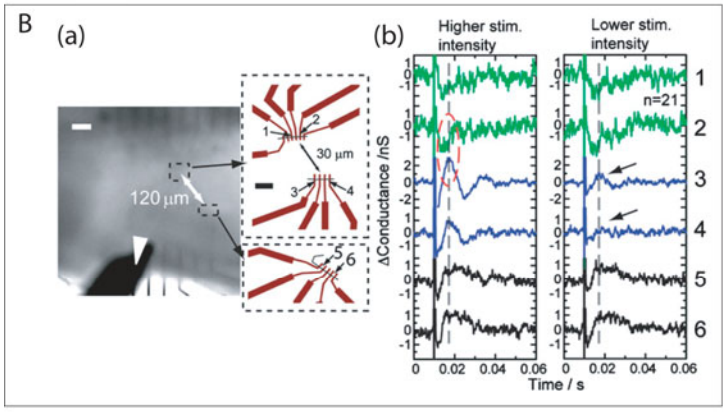

Figure 5. Continuation.

tional connectivity of this region. Furthermore, the plasticity of olfactory system suggests that the network is highly dynamic. Thus, highly localized direct recording of ensembles of neurons in the context of spatially resolved stimulation could serve as a powerful tool to visualize the dynamic, functional connection map and provide information necessary to understand the circuits and plasticity in this and other neural systems.

We believe that in the future this novel approaches would enable to study experimentally the complete dynamics not just of individual cells, but of a complete neuronal network or neural circuits in the brain. These integrated *living* electronic circuits will clearly provide meaningful information about the real mechanisms involved in electrical signal transduction in neuronal arrays, simulating the activity in the brain.

V. NANOWIRE BASED ELECTRICAL DEVICES AS TISSUE MONITORING ELEMENTS

The ability of NW-FETs devices to measure cellular and subcellular activity gave the motivation to step forward to the next level of complexity with biological interfaces and to use these nanoelectronic devices for the recording from a whole organ, from

a beating heart.[41] Recording electrical signals *in vitro* and *in vivo* from whole hearts is applied in areas ranging from basic studies of cardiac function to patient healthcare.[42] Different techniques are used across the surface of the heart to examine cardiac dysfunction such as arrhythmia,[42,26c] including macroscale metallic electrodes, [42] optical microscopy of dyed tissue,[26c] or multielectrode arrays (MEAs), but all suffer from relatively low resolution signals that in part is related to their being planar rigid structures that cannot conform to organs, such as the heart, which are intrinsically three-dimensional (3D) soft objects.

NW and nanotube device arrays, besides being exquisite sensors, can be fabricated on flexible and transparent polymer substrates, [18a, 18b] allowing the chip to bent and conform to 3D curved surfaces.

In this work, electrical recordings from whole embryonic chicken hearts were recorded using p-type NWFET arrays in both planar and bent conformations, Fig. 6A. Initially, planar NWFET chip configuration was used to record a freshly isolated heart. After a brief period of equilibration with medium, hearts beat spontaneously at a typical frequency of 1–3 Hz. Signals were recorded simultaneously from the NWFET and from a conventional glass pipette inserted into the heart, showing close temporal correlation between peaks, with ca. 100 ms consistent time difference between pipette and NW peaks since the pipette was inserted into a spatially remote region with respect to the NWFET devices, Fig. 6Ba. Examination of individual NW signals revealed a peak shape with a fast initial phase (full width at half maximum, FWHM = 6.8 ± 0.7 ms) followed by a slower phase (FWHM = 31 ± 9 ms), corresponding to transient ion channel current and mechanical motion, respectively. NW-FET signals were reproducible, with the chips being stable for multiple experiments, exhibiting excellent S/N. However, the voltage calibrated for these peaks depend on the device transconductance, that is, the water gate potential being applied which determines the sensitivity of the device, $G/_{V_g}$. While the conductance of the fast transient decreased from ca. 55 to 11 nS with the water gate varied from –0.4 to 0.4 V (Fig. 6Bc) in correlation with the decrease in device sensitivity, the voltage-calibrated signal determined using the device transconductance was essentially constant at 5.1 ± 0.4 mV for this same variation of water gate voltage. These results confirm the stability of the inter-

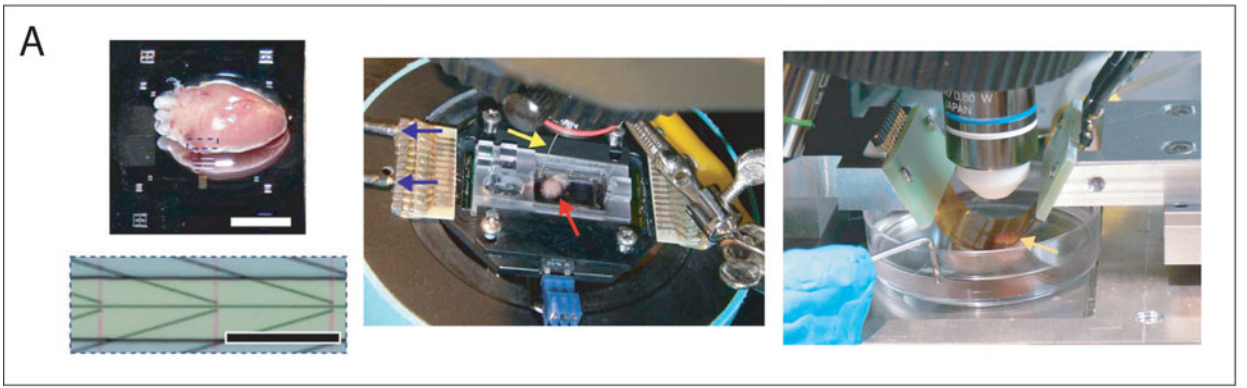

Figure 6. (A) NW/heart interfaces. (top left) Magnified image of heart on surface of planar chip; (bottom left) Zoom of dotted region in upper image showing three pairs of NW devices; (middle) Photograph of experimental setup showing heart on NWFET chip in temperature regulated cell. Arrows show position of heart (red), Ag/AgCl reference electrode (yellow) and source/drain interconnect wires (blue); (right) Photograph of heart (yellow arrow) located underneath bent substrate with NWFETs on the lower concave face of the substrate.

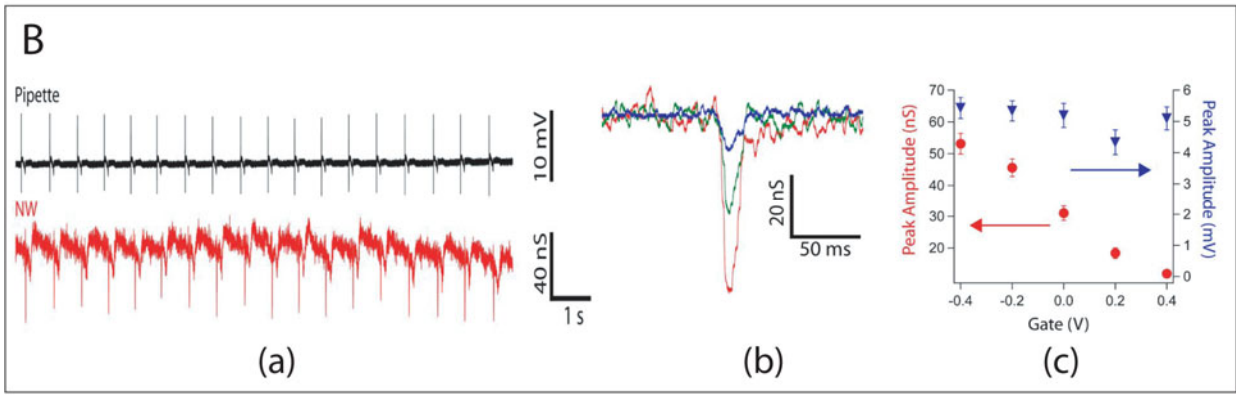

Figure 6. Continuation. (B) (a) Simultaneous recordings from a glass pipette (black trace) and a NW device (red trace). (b) Expansion of single fast transients measured from a heart for V_g = -0.3 (red), 0 (green) and 0.3 V (blue). (c) Plots of peak conductance amplitude (red) and calibrated peak voltage amplitude (blue) vs. V_g for same experiment shown in (b).

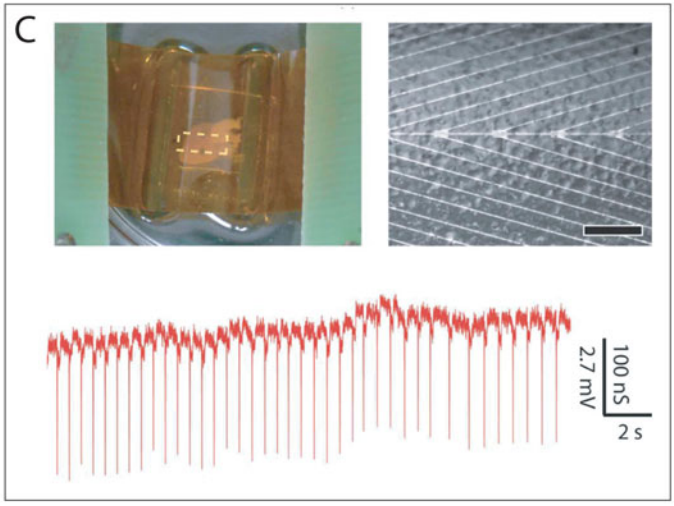

Figure 6. Continuation. (C) (left) Top-down photograph of a heart located underneath bent substrate with NWFETs on the lower concave face of the substrate, which enables overall registration between heart and lithographically-defined markers on the substrate. (right) Optical image taken with the same system showing features on the heart surface versus position of individual NW devices, which are located along the central horizontal axis. (bottom) Recorded conductance data from a NWFET in this configuration.

face between the NWFETs and the beating heart, and highlight the necessity of recording explicit device sensitivity to interpret corresponding voltages.[41]

As mentioned, the fabrication of NWs and CNT FETs on flexible plastic substrates allows the entire chip to wrap the tissue and increase the contact area with the recording elements (Fig. 6A, right panel). Furthermore, it can be used for *in vivo* studies as demonstrated in the case of polymer-based MEAs.[43] NWFETs were assembled on 50-μm thick flexible and transparent Kapton substrates. To confirm the robustness of the measurements, the heart was rotated 180° and a consistent inversion of signal was observed. Secondly, the deformed conformation was investigated by a bent device chip with concave surface facing a beating heart immersed in medium, Fig. 6C. The Kapton is a flexible and trans-

parent substrate allowing simultaneous optical imaging and electronic recording in configurations that are not readily accessible with traditional planar device chips, yet advantageous for producing diverse, functional tissue-device interfaces. It allows for both visual inspection, which enables rough orientation of the device array to the heart, and higher-resolution imaging through the transparent substrate while recording from NWFET devices. Notably, recording from a representative NWFET device in this inverted configuration demonstrated excellent S/N fast component peaks correlated with the spontaneously-beating heart. Still, the average magnitude of the conductance peaks and calibrated voltage are similar to that recorded in more traditional planar configuration. In addition, similar recording were achieved on beating hearts in which bent chips were oriented with convex NWFET surface wrapped partially around the heart.

These results demonstrate that these flexible and transparent NW chips can be used to record electronic signals from organs in configurations not achievable by conventional electronics. We believe that NWFET arrays fabricated on flexible plastic and/or biopolymer substrates can become unique tools for electrical recording from other tissue/organ samples or as powerful implants.

VI. NANOWIRES-BASED TRANSISTOR FLEXIBLE ARRAYS FOR THE ELECTRICAL RECORDING OF CARDIOMYOCYTES

One of the difficulties of culturing live cells over electrical devices is maintaining good device characteristics. Devices can suffer from destructive effects such as corrosion, solution drift, electrical shorts, etc. To address these key issues, a flexible approach was developed to interface NW FET arrays with cultures of cardiomyocyte monolayers cultured on optically-transparent PDMS sheets that were brought into contact with the devices.[44] It allowed to grow the cells separately, identify desired specific cell regions and place them over the NWFET devices, and more importantly, to investigate the relationship between the interface and signal magnitude which is critical to understand in relation to cells and nanoscale structures. Rat cardiomyocytes were shown to grow on

top-down NW FETs by another group with high S/N and millivolts amplitudes, [45a] but not on bottom-up NW or CNT FETs.

Embryonic chicken cardiomyocytes were cultured on 100–500 μm thick rectangular pieces of PDMS to form cell monolayers, and then the PDMS/cardiomyocyte substrate was transferred into a well, which contains extracellular medium, over a NWFET chip fabricated on a standard substrate (Fig. 7a-d). PDMS/cardiomyocyte cell substrates were positioned using a x-y-z manipulator under an optical microscope to bring spontaneously beating cells into direct contact with the NWFETs (Fig. 7e). This approach enabled to manipulate the PDMS/ cells substrate independently of the NWFET chip and to contact specific monolayer regions with specific devices, and subsequently change the region that is being monitored with the NWFETs. Notably, the ability to identify and register specific cellular regions over NWFET elements has not been demonstrated previously for either planar or nanoscale FET where cells have been cultured directly over device chips.

Measurement of the conductance versus time from a Si NWFET in contact with a spontaneously beating cardiomyocyte cell monolayer (Fig. 7f) yields regularly spaced peaks with a frequency of ca. 1.5 Hz and S/N $\geq$ 4. Signal amplitudes that were tuned by varying device sensitivity through changes in water gate-voltage potential, V_g, showed an average calibrated voltage of 2.8 ± 0.5 mV. The calibration was further illustrated by data recorded with V_g values from –0.5 to 0.1 V (Fig. 7g), where the conductance signal amplitudes decrease from 31 to 7 nS, respectively, but the calibrated voltage, 2.9 ± 0.3 mV, remained unchanged, indicating a robust NWFET/cell interface.

Signal amplitude was further increased by using a micropipette to displace the PDMS/cells substrate at a fixed distance towards the device, Figs. 7h and 7i. A direct comparison of single peaks recorded for different ΔZ values shows a consistent monotonic increase in peak amplitudes without any observable change in peak shape or peak width over >2x change in amplitude, and that the peak width is consistent with time-scales for ion fluxes associated with ion-channel opening/closing [28a]. A plot of the experimental results (Fig. 7j) summarizes the systematic 2.3-fold increase in conductance and calibrated voltage peak amplitude, and moreover, demonstrates that these amplitude changes are reversible for increasing and decreasing PDMS/cells displacement.

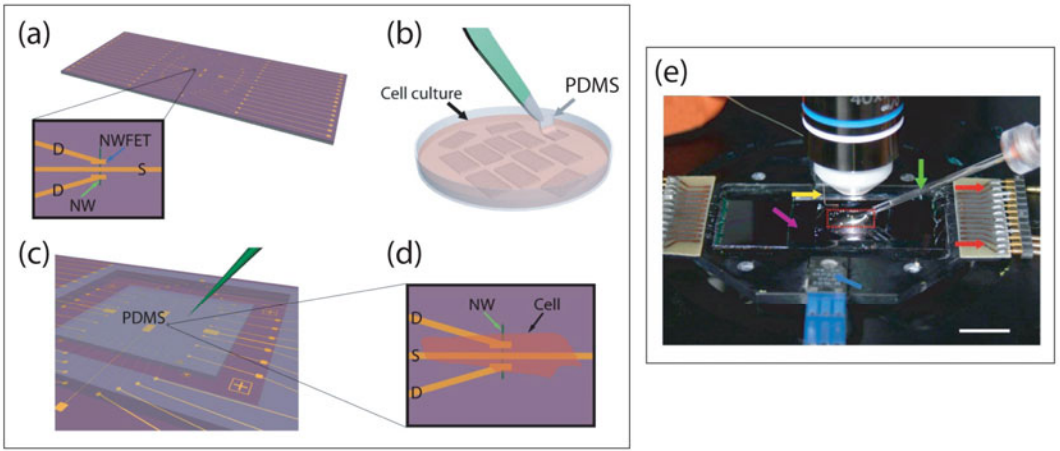

Figure 7. (A) Schematic of the experimental approach. (a) NWFET chip, where NW devices are located at the central region of the chip. The visible linear features (gold) correspond to NW contacts and interconnect metal. Zoom-in showing a source (S) and 2 drain (D) electrodes connected to a vertically oriented NW (blue arrow) define 2 NWFETs. (b) Cardiomyocytes cultured on thin flexible pieces of PDMS, where one piece is being removed with tweezers (green). (c) PDMS substrate with cultured cells oriented over the device region of the NWFET chip. The green needle-like structure indicates the probe used to both manipulate the PDMS/cell substrate to specific NW device locations. (d) Schematic of a cardiomyocyte (black arrow) oriented over a NW (green arrow) device. (e) Photograph of the experimental setup showing the PDMS piece (red dashed box) on top of a NWFET chip within a solution well that is temperature-regulated with an integrated heater (blue arrow). Additional yellow, purple, green, and red arrows highlight positions of the Ag/AgCl reference electrode, solution medium well, glass manipulator/force pipette connected to *x-y-z* manipulator, and plug-in connectors between NWFET interconnect wires and measurement electronics, respectively.

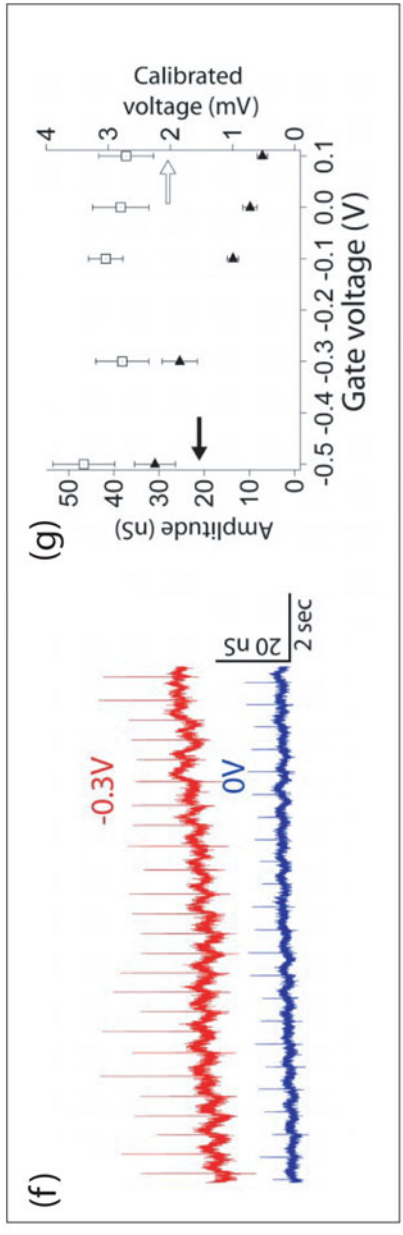

Figure 7. Continuation. (f) Conductance vs. time traces recorded at V_g= -0.3 V (red) and 0 V (blue) for the same NWFET–cardiomyocyte interface; the device sensitivities at -0.3 and 0 V were 9.2 and 3.5 nS/mV, respectively. (g) Plots of peak conductance amplitude (filled triangles) and calibrated peak voltage amplitude (open squares) vs. V_g; data were obtained from the same experiments shown in f. Error bars correspond to ±1 SD.

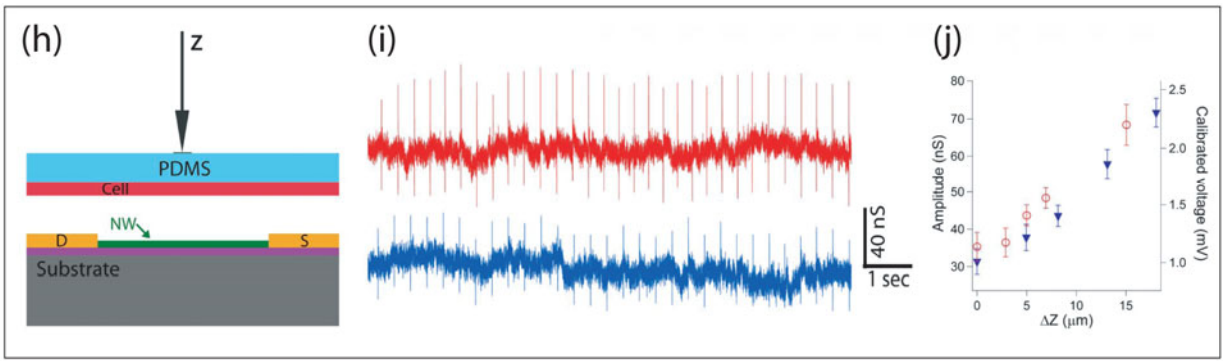

Figure 7. Continuation. Effect of applied force on recorded signals. (h) Schematic illustrating displacement (Z) of the PDMS/cell substrate with respect to a NWFET device. (i) Two representative traces recorded with the same device for ΔZ values of 8.2 μm (blue) and 18.0 μm (red). (j) Summary of the recorded conductance signals and calibrated voltages vs. ΔZ, where the open red circles (filled blue triangles) were recorded for increasing (decreasing) ΔZ.

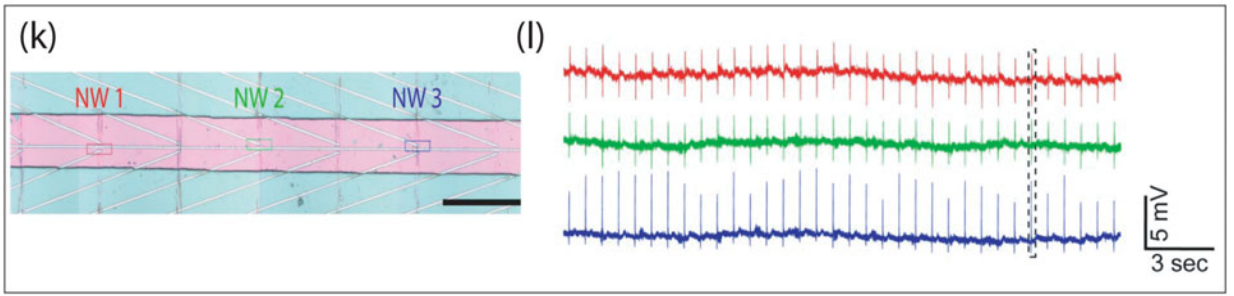

Figure 7. Continuation. Multiplexed NWFET recording. (k) Optical micrograph showing 3 NWFET devices (NW1, NW2, NW3) in a linear array, where pink indicates the area with exposed NW devices. (l) Representative conductance vs. time signals recorded simultaneously from NW1, NW2, and NW3.

Pushing the limits of PDMS/cell displacement experiments close to but below the point of cell disruption yielded peaks with average conductance amplitude of 299 ± 7 nS and corresponding calibrated signal amplitudes as large as 10.5 ± 0.2 mV. In comparison to previous studies, cardiomyocytes cultured on conventional planar FET devices have yielded peaks with S/N of 2–6 and amplitudes from 0.2–2.5 mV, which highlight this approach and the high performance of the Si-NWFET devices used.

Lastly, multiplexed measurements of NWFET devices were carried out and configured in a linear array with an average spacing of 300 μm so that signal propagation within the cardiomyocyte monolayers could be characterized. Simultaneous recordings from three NW devices in contact with spontaneously beating monolayer (Fig. 7k-l) yielded very stable and high S/N (~10) peaks. Using the individually characterized sensitivities for each NW, calibrated voltages with relative large magnitude of 4.6 ± 0.4, 4.0 ± 0.3 and 5.9 ± 0.9 mV were obtained, indicating that a good junction is formed between each of the NWFETs and PDMS/cell substrate in the experiment. These results and device separations yield approximate propagation speeds of 0.07–0.21 m/s that are consistent with measurements on monolayers of neonatal rat cardiomyocytes.[45b]

VII. NANOSCALE 3D-FLEXIBLE FET BIOPROBES

The studies reviewed here demonstrate that NW electrical devices, fabricated on rigid or flexible planar substrates, can be used for ultrasensitive detection of biological markers and high-resolution extracellular recording from cells and tissues with relevance to healthcare and medicine. However, localized and tunable 3D intracellular recording using nanoscale field-effect transistor devices, in a similar manner to glass micropipette, has never been demonstrated before.[46] The design of minimally-invasive nanoFET probe for intracellular recording applications is a significant fabrication challenge because the S (source) and D (Drain) typically dominate the overall device size and define a planar and rigid structure regardless of whether the nanoFET is on or suspended above a substrate.[47] Nevertheless, this kind of nanoFET could function as mechanically non-invasive probe capable of entering cells through endocytic pathways in a similar manner to nanoparticles.[48] Moreo-

ver, when interfacing with cells, the FETs process input/output information without the need for direct exchange with cellular ions, thus interfacial impedance and biochemical invasiveness to cells can be minimized. Lastly, it could be integrated for multiplexed intracellular measurements.

Recently, it was demonstrated that variation of reactant partial pressures during the VLS silicon nanowire (SiNW) growth could introduce reproducible 120° kinks,[49] and that the junction regions could be doped to create p-n diodes and FETs. This methodology was used to create a two-terminal FET probe in a cis crystal conformation that could be inserted into single cells by selective in-situ doping during synthesis to localize the nanoscale FET element (Figure 8a, magenta segments), and simultaneously *wire-up* the FET channel with nanowire S/D components (Fig. 8a, blue segments). The authors used heavy n^{++}-type doping for the nanowire S/D arms, and reduced the concentration to light n-type doping to introduce a short ~200 nm region serving as the FET detector of the overall probe.

In the next step, an unconventional nanoelectronic device fabrication approach was developed to allow these probes to be free standing. Remote electrical interconnects were made to the S/D nanowire arms on ultrathin SU-8 polymer ribbons above a sacrificial layer (Fig. 8c, upper panel). The interfacial stress between materials [50] was used to bend the probe upward after a final lift-off process (Fig. 8c, lower panel). The acute-angle kinked nanowire geometry and the extended S/D arms spatially separate the functional nanoscale FET from the bulky interconnects for a minimum interference by a distance up to ~ 30 μm, comparable to the size of single cells. The sensitivity of the 3D nanoscale FET probes was characterized and found to yield similar sensitivities to kinked nanowire devices fabricated on planar substrates.

In order to use the 3D nanoFET probes in cells (Fig. 8e, f), the negatively charged SiO_2 surface of the SiNWs was modified with unilamellar vesicles of phospholipid bilayers, which can fuse with cell membranes.[51] Examination of the dye-labeled modified probes revealed a continuous shell on the acute-angle nanoprobes, and < 1% changes in both the nanoFET conductance and sensitivity.

Initially, phospholipid-modified nanoFET probe was used to monitor the calibrated potential change of an isolated HL-1 cell (Fig. 8g), clamped by a micropipette to intracellular potential of

–50 mV, showing a sharp ~52 mV drop within 250 ms after cell/tip contact. During recording, the potential maintained at a relatively constant value of ca. –46 mV, and returned to baseline when the cell was detached. Interestingly, nanoFET probes of sim-

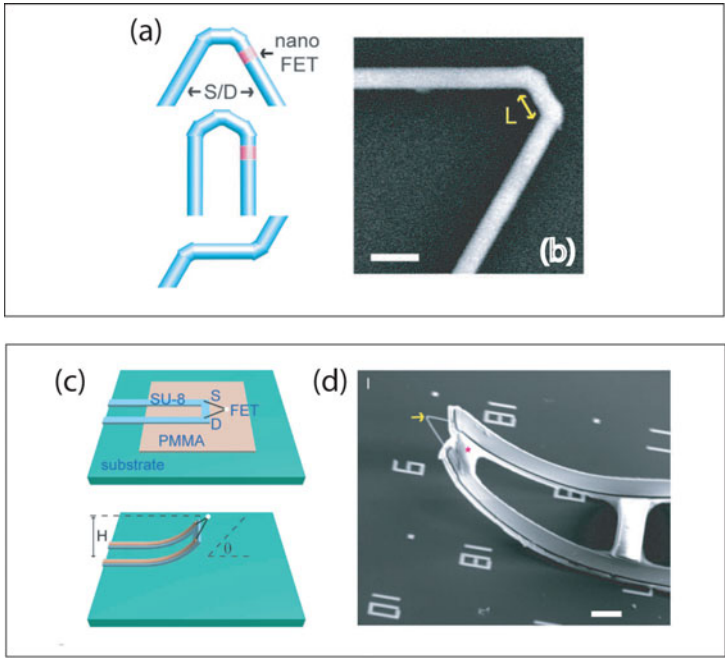

Figure 8. 3D kinked nanowire probes. (a) Schematics of 60° (top) and 0° (middle) multiply kinked nanowires and cis (top) and trans (bottom) configurations in nanowire structures. The blue and pink regions designate the source/drain (S/D) and nanoscale FET channel, respectively. (b) SEM image of a doubly kinked nanowire with a cis configuration. (c) Schematics of device fabrication. Patterned poly (methylmethacrylate) and SU-8 microribbons serve as a sacrificial layer and flexible device support, respectively. The dimensions of the lightly doped n-type silicon segment (white dots) are ~80 by 80 by 200 nm^3. H and q are the tip height and orientation, respectively, and S and D designate the built-in source and drain connections to the nanoscale FET. (d) SEM image of an as-made device. The yellow arrow and pink star mark the nanoscale FET and SU-8, respectively.

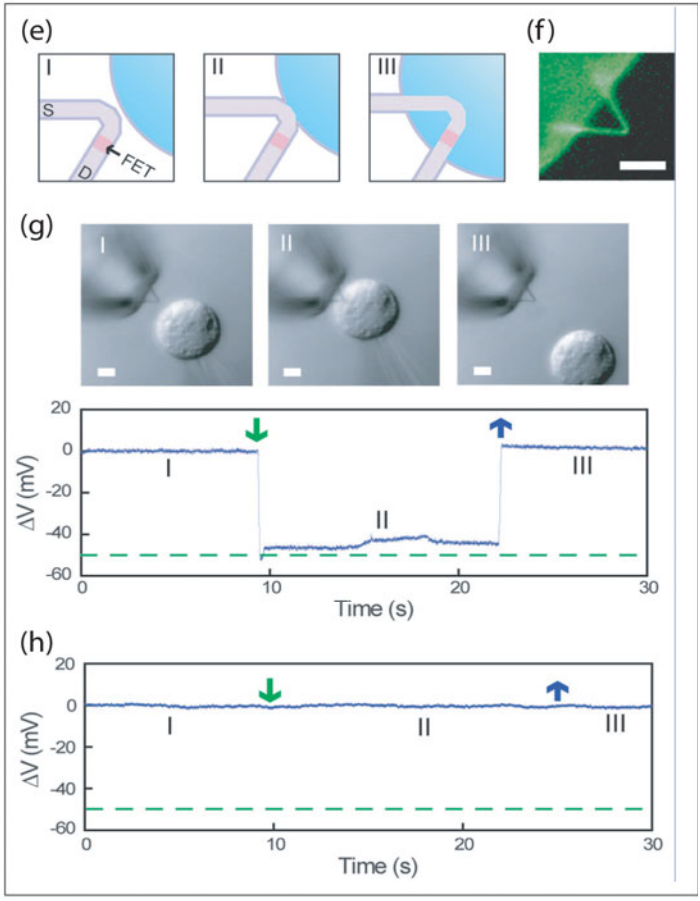

Figure 8. Continuation. (e) Schematics of nanowire probe entrance into a cell. Dark purple, light purple, pink, and blue colors denote the phospholipid bilayers, heavily doped nanowire segments, active sensor segment, and cytosol, respectively. (f) False-color fluorescence image of a lipidcoated nanowire probe. (g) Differential interference contrast microscopy images (upper panels) and electrical recording (lower panel) of an HL-1 cell and 60° kinked nanowire probe as the cell approaches (I), contacts and internalizes (II), and is retracted from (III) the nanoprobe. A pulled-glass micropipette (inner tip diameter ~ 5 mm) was used to manipulate and voltage clamp the HL-1 cell. The dashed green line corresponds to the micropipette potential. Scale bars, 5 mm. (h) Electrical recording with a 60° kinked nanowire probe without phospholipids surface modification. Green and blue arrows in (g) and (h) mark the beginnings of cell penetration and withdrawal, respectively.

when the cell was detached. Interestingly, nanoFET probes of similar sensitivity that were not coated with a phospholipid bilayer exhibited only baseline fluctuations (< ±1 mV) (Fig. 8h), suggesting that the biochemical modification is crucial for assisting access to the intracellular region, possibly through membrane fusion.

Next, the formation of intracellular interface between the 3D nanoFET probes and spontaneously beating cardiomyocytes was investigated. Embryonic chicken cardiomyocytes were cultured on PDMS substrates [44] and then positioned to place individual cells over the phospholipid bilayer-modified vertical ($\theta = 90^{o}$) nanoprobes[44,52] (Fig. 9A). Representative conductance versus time data recorded from a 3D nanoFET probed in gentle contact with a beating cell showed regularly spaced spikes with a frequency of ca. 2.3 Hz consistent with beating cardiomyocyte (Fig. 9B, I). The peaks have a potential change of ~3–5 mV, S/N ≥2, and a submillisecond width (Fig. 9C, I). The peak amplitude, shape and width have characteristics of extracellular recordings made with nanowire devices on substrates,[44] supported by optical images recorded at the same time. After a relatively brief (~40 s) period of extracellular signals, several pronounced changes in recorded signals were observed (Figs. 9B and C, II and III) without application of external force to the PDMS/cell support. Specifically, the initial extracellular signals gradually disappeared (Figs. 9B and B, II, magenta stars). There was a concomitant decrease in baseline potential and new peaks emerged that had an opposite sign, similar

Figure 9. Electrical recording from beating cardiomyocytes. (A) Schematics of cellular recording from the cardiomyocyte monolayer on PDMS (left) and highlight of extracellular (middle) and intracellular (right) nanowire/cell interfaces. The cell membrane and nanowire lipid coatings are marked with purple lines. (B) Electrical recording from beating cardiomyocytes: (i) extracellular recording, (ii) transition from extracellular to intracellular recordings during cellular entrance, and (iii) steady-state intracellular recording. Green and pink stars denote the peak positions of intracellular and extracellular signal components, respectively. The red-dashed boxes indicate regions selected for (C). (C) Zoom-in signals from the corresponding red-dashed square regions in (B). Blue and orange stars designate features that are possibly associated with inward sodium and outward potassium currents, respectively. The red-dashed line is the baseline corresponding to intracellular resting state.

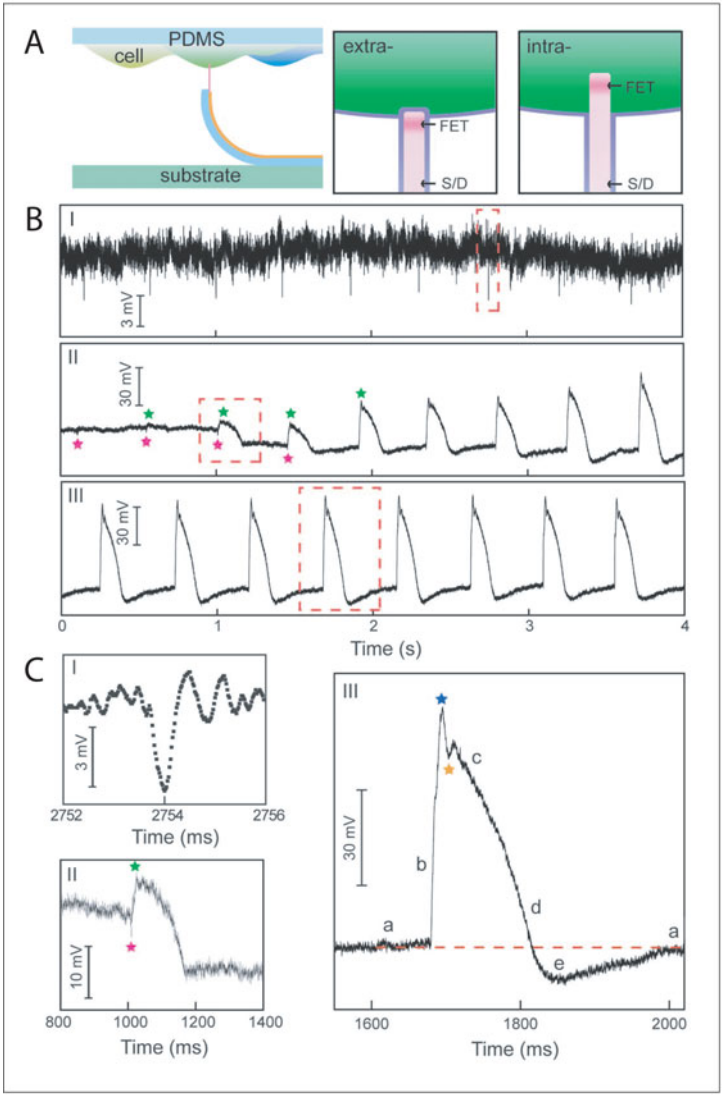
A
PDMS
cell
substrate
extra-
FET
S/D
intra-
FET
S/D
B
I
3 mV
II
30 mV
III
30 mV
0
1
2
3
4
Time (s)
C
I
3 mV
2752
2754
2756
Time (ms)
II
10 mV
800
1000
1200
1400
Time (ms)
III
30 mV
a
b
c
d
e
a
1600
1800
2000
Time (ms)

frequency, much greater amplitude, and longer duration (Fig. 9C, II, green stars). These new peaks, which are coincident with cell beating, rapidly reached a steady state (Fig. 9C, III) with an average calibrated peak amplitude of ~80 mV and duration of ~200 ms. The amplitude, sign, and duration are near those reported for whole-cell patch clamp recordings from cardiomyocytes,[42,53] and thus it was concluded that these data represent a transition to steady-state intracellular recording with the 3D nanowire probe. When the PDMS/cell substrate was mechanically-retracted from the 3D kinked nanowire devices, the intracellular peaks disappeared, but reappeared when the cell substrate was brought back into gentle contact with the device.

Additional work remains in order to develop this new synthetic nanoprobe as routine tool like the patch-clamp micropipette,[54] although we believe that there are already clear advantages: Electrical recording with kinked nanowire probes is relatively simple without the need for resistance or capacitance compensation,[55] the nanoprobes are chemically less invasive than pipettes as there is no solution exchange, the small size and biomimetic coating minimizes mechanical invasiveness, and the nanoFETs have high spatial and temporal resolution for recording.

VIII. CONCLUSIONS

We have shown that NW-based field-effect sensor devices represent a powerful detection platform for a broad range of biological and chemical species in solution. The examples described in this chapter show clearly the potential of NW-based field-effect sensor devices to significantly impact disease diagnosis, drug discovery, neurosciences, as well as serve as powerful new tools for research in many areas of biology and medicine. We believe that these advances could be developed at the commercial level in simple NW sensor devices and probes that would represent a clear application of nanotechnology, and, more importantly, a substantial benefit to humankind.

REFERENCES

[1]A. M. Ward, J. W. Catto, F. C. Hamdy, *Ann Clin Biochem*, **38** (2001) 633.
[2]C. Campagnolo, K. J. Meyers, T. Ryan, R. C. Atkinson, Y. T. Chen, M. J. Scanlan, G. Ritter, L. J. Old, C. A. Batt, *J Biochem Biophys Methods* **61 (**2004) 283.
[3]C. A. Mirkin, R. L. Letsinger, R. C. Mucic, J. J. Storhoff, *Nature* **382** (1996) 607.
[4] a) K. Domansky, J. Janata, M. Josowicz, D. Petelenz, *Analyst* **118** (1993) 335; b) J. Janata, *Analyst* **119** (1994) 2275.
[5]G. H. Wu, R. H. Datar, K. M. Hansen, T. Thundat, R. J. Cote, A. Majumdar, *Nat Biotechnol*, ***19*** **(**2001) 856.
[6]a) R. J. Chen, S. Bangsaruntip, K. A. Drouvalakis, N. W. S. Kam, M. Shim, Y. M. Li, W. Kim, P. J. Utz, H. J. Dai, *P Natl Acad Sci USA* **100** (2003) 4984; b) R. J. Chen, H. C. Choi, S. Bangsaruntip, E. Yenilmez, X. W. Tang, Q. Wang, Y. L. Chang, H. J. Dai, *J Am Chem Soc*, **126** (2004) 1563.
[7]C. M. Lieber, *Mrs Bull*, **28** (2003) 486.
[8]M. S. Gudiksen, J. F. Wang, C. M. Lieiber, *J Phys Chem B* **105** (2001) 4062.
[9]Y. Cui, X. F. Duan, J. T. Hu, C. M. Lieber, *J Phys Chem B* **104** (2000) 5213.
[10]a) Y. Cui, Q. Q. Wei, H. K. Park, C. M. Lieber, *Science* **293** (2001) 1289; b) SM Sze: *Physics of semiconductor devices*, Wiley, New York, USA, 431(1981).
[11]X. F. Duan, Y. Huang, Y. Cui, J. F. Wang, C. M. Lieber, *Nature* **409** (2001) 66.
[12]P. Bergveld, *Ieee T Bio-Med Eng* 1972, *Bm19*, 342.
[13]Y. N. Xia, P. D. Yang, Y. G. Sun, Y. Y. Wu, B. Mayers, B. Gates, Y. D. Yin, F. Kim, Y. Q. Yan, *Adv Mater* **15** (2003) 353.
[14]G. Gruner, *Anal Bioanal Chem*, **384** (2006) 322.
[15]a) F. Patolsky, G. F. Zheng, O. Hayden, M. Lakadamyali, X. W. Zhuang, C. M. Lieber, *P Natl Acad Sci USA* **101** (2004) 14017; b) G. F. Zheng, F. Patolsky, Y. Cui, W. U. Wang, C. M. Lieber, *Nat Biotechnol*, **23** (2005) 1294.
[16]a) Y. Cui, Z. H. Zhong, D. L. Wang, W. U. Wang, C. M. Lieber, *Nano Lett* **3** (2003) 149; b) S. Jin, D. M. Whang, M. C. McAlpine, R. S. Friedman, Y. Wu, C. M. Lieber, *Nano Lett* **4** (2004) 915.
[17]a) Y. Wu, Y. Cui, L. Huynh, C. J. Barrelet, D. C. Bell, C. M. Lieber, *Nano Lett.* **4** (2004) 433; b) D. D. D. Ma, C. S. Lee, F. C. K. Au, S. Y. Tong, S. T. Lee, *Science* **299** (2003) 1874.
[18]a) A. Javey, S. Nam, R. S. Friedman, H. Yan, C. M. Lieber, *Nano Lett*, **7** (2007) 773; b) M. C. McAlpine, R. S. Friedman, S. Jin, K. H. Lin, W. U. Wang, C. M. Lieber, *Nano Lett* **2003**, *3*, 1531; c) B. P. Timko, T. Cohen-Karni, G. H. Yu, Q. Qing, B. Z. Tian, C. M. Lieber, *Nano Lett.* **9** (2009) 914.
[19]a) P. Alivisatos, *Nat Biotechnol.* **22** (2004) 47; b) Bartlett, P.N. In *Handbook of Chemical and Biological Sensors;*Taylor, R.F., Schultz, J. S., Eds.; IOP Publishing: Philadelphia, PA, 1996, p. 139.
[20]W. U. Wang, C. Chen, K. H. Lin, Y. Fang, C. M. Lieber, *P Natl Acad Sci USA* **102** (2005) 3208.
[21]a) J. Hahm, C. M. Lieber, *Nano Lett***. 4** (2004) 51; b) Z. Li, B. Rajendran, T.I. Kamins, X. Li, Y. Chen, R.S. Williams, *App.Phys A* **80** (2005) 1257; c) Y.L. Bunimovich, Y.S. Shin, W.S. Yeo, M. Amori, G. Kwong, J.R. Heath, *J Am. Chem Soc.* **128** (2006) 16323; d) Z.Q. Gao, A. Agarwal, A.D. Trigg, N. Singh, C. Fang, C.H. Tung, Y. Fan, K.D. Buddharaju, J.M. Kong, *Anal. Chem.* **79** (2007) 3291; e) A. Cattani-Scholz, D. Pedone, M. Dubey, S. Neppl, B. Nickel, P. Feulner, J. Schwartz , G. Abstreiter, M. Tornow, *ACS Nano* **2** (2008) 1653.

[22]L. He, M. D. Musick, S. R. Nicewarner, F. G. Salinas, S. J. Benkovic, M. J. Natan, C. D. Keating, *J Am Chem Soc* **122** (2000) 9071.
[23]X. L. Mao, L. J. Yang, X. L. Su, Y. B. Li, *Biosens Bioelectron* **21** (2006) 1178.
[24]a) M. J. Schoning, A. Poghossian, *Analyst*, **127** (2002) 1137; b) A. P. Soldatkin, J. Montoriol, W. Sant, C. Martelet, N. Jaffrezic-Renault, *Biosens Bioelectron* **2003**, *19*, 131; c) W. Sant, M. L. Pourciel-Gouzy, J. Launay, T. Do Conto, R. Colin, A. Martinez, P. Temple-Boyer, *Sensor Actuat B-Chem* **103** (2004) 260.
[25]a) F. Patolsky, G. F. Zheng, C. M. Lieber, *Anal Chem* **78** (2006) 4260; b) E. Stern, A. Vacic, N. K. Rajan, J. M. Criscione, J. Park, B. R. Ilic, D. J. Mooney, M. A. Reed, T. M. Fahmy, *Nat. Nanotech*. **5** (2010) 138.
[26]a) A. G. Kleber, Y. Rudy, *Physiol Rev*. **84** (2004) 431; b) B. Hille *Ion Channels of Excitable Membranes*, Sinauer, Sunderland, MA, 2001; c) Dhein S, Mohr FW, Delmar M., *Practical Methods in Cardiovascular Research*, Springer, Berlin, 2005.
[27]a) M. Halbach, U. Egert, J. Hescheler, K. Banach, *Cell Physiol Biochem* **13** (2003) 271; b) F. Heer, S. Hafizovic, T. Ugniwenko, U. Frey, W. Franks, E. Perriard, J. C. Perriard, A. Blau, C. Ziegler, A. Hierlemann, *Biosens Bioelectron* **22** (2007) 2546; c) T. Meyer, K. H. Boven, E. Gunther, M. Fejtl, *Drug Saf.* **27** (2004) 763.
[28]a) S. Ingebrandt, C. K. Yeung, M. Krause, A. Offenhausser, *Biosens Bioelectron* **16** (2001) 565; b) S. Ingebrandt, C. K. Yeung, W. Staab, T. Zetterer, A. Offenhausser, *Biosens Bioelectron* **18** (2003) 429.
[29]a) P. Fromherz, *Chemphyschem*, **3** (2002) 276; b) U. Windhorst and H. Johansson, *Modern Techniques in neuroscience research: Electrical activity of Individual Neurons* In situ: *Extra and Intracellular,* Springer, New York, 1999.
[30]H. Oviedo, A. D. Reyes, *J Neurosci* **25** (2005) 4985.
[31]a) A. Lambacher, M. Jenkner, M. Merz, B. Eversmann, R. A. Kaul, F. Hofmann, R. Thewes, P. Fromherz, *Appl Phys a-Mater* **79** (2004) 1607; b) A. Offenhausser, C. Sprossler, M. Matsuzawa, W. Knoll, *Biosens Bioelectron* **12** (1997) 819; c) M. Voelker, P. Fromherz, *Small* **1** (2005) 206.; d) N. Li, A. Tourovskaia, A. Folch, *Crit Rev Biomed Eng* **31** (2003) 423.
[32]a) G. Cellot, E. Cilia, S. Cipollone, V. Rancic, A. Sucapane, S. Giordani, L. Gambazzi, H. Markram, M. Grandolfo, D. Scaini, F. Gelain, L. Casalis, M. Prato, M. Giugliano, L. Ballerini, *Nat Nanotechnol*, **4** (2009) 126; b) N. Sniadecki, R. A. Desai, S. A. Ruiz, C. S. Chen, *Ann Biomed Eng* **34** (2006) 59; c) M. M. Stevens, J. H. George, *Science* **310** (2005) 1135; d) J. Park, S. Bauer, K. von der Mark, P. Schmuki, *Nano Lett.* **7** (2007) 1686.
[33]T. Gabay, E. Jakobs, E. Ben-Jacob, Y. Hanein, *Physica A* **350** (2005) 611.
[34]K. Wang, H. A. Fishman, H. J. Dai, J. S. Harris, *Nano Lett* **6** (2006) 2043.
[35]M. K. Gheith, T. C. Pappas, A. V. Liopo, V. A. Sinani, B. S. Shim, M. Motamedi, J. R. Wicksted, N. A. Kotov, *Adv Mater* **18** (2006) 2975.
[36]T. C. Pappas, W. M. S. Wickramanyake, E. Jan, M. Motamedi, M. Brodwick, N. A. Kotov, *Nano Lett*, **7** (2007) 513.
[37]a) V. Lovat, D. Pantarotto, L. Lagostena, B. Cacciari, M. Grandolfo, M. Righi, G. Spalluto, M. Prato, L. Ballerini, *Nano Lett* **5** (2005) 1107; b) G. Cellot, E. Cilia, S. Cipollone, V. Rancic, A. Sucapane, S. Giordani, L. Gambazzi, H. Markram, M. Grandolfo, D. Scaini, F. Gelain, L. Casalis, M. Prato, M. Giugliano, L. Ballerini, *Nat Nanotechnol* **4** (2009) 126.
[38]F. Patolsky, B. P. Timko, G. Yu, Y. Fang, A. B. Greytak, G. Zheng, C. M. Lieber, *Science **313*** (2006) 1100.

[39]a) C. Wyart, C. Ybert, L. Bourdieu, C. Herr, C. Prinz, D. Chatenay, *J Neurosci Methods* ***117*** (2002) 123; b) J. Zhang, S. Venkataramani, H. Xu, Y. K. Song, H. K. Song, G. T. Palmore, J. Fallon, A. V. Nurmikko, *Biomaterials* **27** (2006) 5734; c) W. C. Chang, D. W. Sretavan, *Langmuir* **24** (2008) 13048.
[40]a) Q. Qing, S. K. Pal, B. Tian, X. Duan, B. P. Timko, T. Cohen-Karni, V. N. Murthy, C. M. Lieber, *Proc Natl Acad Sci U S A* **107** (2010) 1882; b) J. F. Eschermann, R. Stockmann, M. Hueske, X. T. Vu, S. Ingebrandt, A. Offenhäusser, *App. Phys. Lett.*, **95** (2009) 083703; c) T.-S. Pui, A. Agarwal, F. Ye, N. Balasubramanian, P. Chen, *Small*, **5** (2009) 208; d) G. M. Shepherd, *The synaptic Organization of the brain,* Oxford Univ Press, New York, 5th Ed., 2004.
[41]B. P. Timko, T. Cohen-Karni, G. Yu, Q. Qing, B. Tian, C. M. Lieber, *Nano Lett.* **9** (2009) 914.
[42]a) M. Reppel, F. Pillekamp, Z. J. Lu, M. Halbach, K. Brockmeier, B. K. Fleischmann, J. Hescheler, *J Electrocardiol Suppl* **37** (2004) 104; b) Z. J. Lu, A. Pereverzev, H. L. Liu, M. Weiergraber, M. Henry, A. Krieger, N. Smyth, J. Hescheler, T. Schneider, *Cell Physiol Biochem* **14** (2004) 11; c) B. Hille, *Ion channels of excitable membranes,* Sinauer, Sunderland, 2001; d) D.P. Zipes, J. Jalife *Cardiac electrophysiology : From cell to bedside,* Saunders, Philadelphia, 2004.
[43]a) C. Adams, K. Mathieson, D. Gunning, W. Cunningham, M. Rahman, J. D. Morrison, M. L. Prydderch, *Nucl Instrum Meth A* **546** (2005) 154; b) K. C. Cheung, P. Renaud, H. Tanila, K. Djupsund, *Biosens Bioelectron* **22** (2007) 1783.
[44]T. Cohen-Karni, B. P. Timko, L. E. Weiss, C. M. Lieber, *Proc Natl Acad Sci U S A*, **106** (2009) 7309.
[45]a) T. S. Pui, A. Agarwal, F. Ye, N. Balasubramanian, P. Chen, *Small* **5** (2009) 208; b) V. G. Fast, A. G. Kleber, *Circ Res* **75** (1994) 591.
[46]B. Z. Tian, T. Cohen-Karni, Q. A. Qing, X. J. Duan, P. Xie, C. M. Lieber, *Science* **329** (2010) 830.
[47]a) I. Heller, W. T. T. Smaal, S. G. Lemay, C. Dekker, *Small* **5** (2009) 2528; b)W. Lu, C. M. Lieber, *Nat Mater* **6** (2007) 841.
[48]M. Ferrari, *Nat Rev Cancer* **5** (2005) 161.
[49]B. Z. Tian, P. Xie, T. J. Kempa, D. C. Bell, C. M. Lieber, *Nat Nanotechnol* **4** (2009) 824.
[50]T. G. Leong, C. L. Randall, B. R. Benson, N. Bassik, G. M. Stern, D. H. Gracias, *P Natl Acad Sci USA* **106** (2009) 703.
[51]L. V. Chernomordik, M. M. Kozlov, *Nat Struct Mol Biol* **15** (2008) 675.
[52]Q. Qing, S. K. Pal, B. Z. Tian, X. J. Duan, B. P. Timko, T. Cohen-Karni, V. N. Murthy, C. M. Lieber, *P Natl Acad Sci USA* **107** (2010) 1882.
[53]D. M. Bers, *Nature* **415** (2002) 198.
[54]a) B. Sakmann, E. Neher, *Annu Rev Physiol* **46** (1984) 455; b) A. Molleman, *Patch Clamping: An introductory guide to patch clamp electrophysiology* ,Wiley, Chichester, England, 2003.
[55]R. D. Purves, *Microelectrode methods for intracellular recording and ionophoresis,* Academic Press, London, 1981.

Fernando Patolsky

Fernando Patolsky is an Associate Professor in the department of Chemistry at Tel Aviv University. His research has focused on the development of molecular and biomolecular electronic and optical systems, aiming to establish fundamental principles for the construction of optical and electronic sensors and biosensors. These scientific activities represented an interdisciplinary effort to bridge chemistry, biology and materials science. These days, Prof. Patolsky is involved in pioneering research in the field of nanomedicine, where he made seminal advances at the interface between nanoelectronics and biological systems.

3

Scanning Electrochemical Microscopy Imaging of DNA Arrays for High Throughput Analysis Applications

Koji Nakano

Department of Applied Chemistry, Faculty of Engineering, Kyushu University, 744 Motooka, Nishi-ku, Fukuoka 819-0395, Japan.

I. INTRODUCTION

With the completion of the human genome sequencing efforts, functional genomics, which aims to understand the relationship between an organism's genome and its phenotype, has become a primary research field.[1] Various kinds of biochips, a bio-micro-array device, are extensively used for substantial analysis purposes by promoting the effective use of the vast wealth of data produced by genomic projects.[2] The strength of biochips lies in the spatial grid of miniaturized specific binding sites, at which unique binding events can be analyzed simultaneously. Moreover, by introduction into a microfluidic device, the next generation of biochips has been found to possess both biochemical reaction capabilities, including amplification, and chemical analysis. Such a device will be used on a single platform with multiple reactions being carried out on individual sites.

N. Eliaz (ed.), *Applications of Electrochemistry and Nanotechnology in Biology and Medicine II*, Modern Aspects of Electrochemistry 53,
DOI 10.1007/978-1-4614-2137-5_3,

The earliest DNA arrays were developed as filter arrays that are capable of the Southern blot technique and the many derivatives thereof. Subsequent improvements in laboratories led to the creation of high-density macroarrays, in which two different microarray-based technologies arose; one was the DNA microarrays from the Stanford University group of Davis and Brown,[3] and the other was the GeneChip® from Affymetrix (Santa Clara, CA, USA).[4] Currently, a wide selection of DNA microarrays offers researchers a high throughput method for simultaneously evaluating large numbers of genes. Some of these arrays have been accumulating real results in gene expression analysis, and these are useful for disease diagnosis, drug discovery studies and toxicological research. Additionally, with a DNA array, it is possible to discover any single nucleotide polymorphisms (SNPs); the inter-individual differences in the genome. Moreover, a DNA array has been employed to determine the expression level of RNA and the abundance of genes that cause this expression of RNA. On one single DNA array, scientist can simultaneously perform tens of thousands of bioaffinity reactions, including hybridizations.

To an electrochemist, the microelectronic array, the most recent entry in this class of device, has been an appealing feature for the last decade. The widget was originally developed to place biomolecules arbitrarily at the test sites through the application of an electric field.[5] The electronic biochip is typically composed of arrayed pairs of working electrodes and counter electrodes. Thus, with any electronically addressable electrode design, electrochemical detection also becomes feasible. In particular, the intimate combination of this tool with the electrochemical DNA biosensor has led to a dramatic increase in research using this technology; the electrochemical detection-based DNA arrays are anticipated to provide many advantages over radioisotope- or fluorophore-based detection systems.

Various kinds of scanning probe microscopy (SPM) approaches have served as engines for a variety of nanotechnology achievements. The scanning electrochemical microscope (SECM) that falls under this category has also produced successful results in a wide range of electrochemical studies, from the fundamental analysis of the electrode reaction to electrochemical fabrication of

functional surfaces.[6] Due to the high spatial resolution of SECM, this technology has been demonstrated as a readout method for locally immobilized, micrometer-sized biological recognition elements, including a variety of DNA arrays with different formats and detection modes.

This review examines how a SECM can facilitate DNA array analysis and provides the underlying electrochemistry facets of SECM. We also introduce some of our latest achievements in SECM imaging of DNA microdots that respond toward the target DNA through hybridization. Several comprehensive reviews, including of electrochemical DNA sensors, have been published recently.[7-11] Given the pace of advancement in this field, the development of any high-throughput device, even point-of-care DNA diagnostics that takes the full, latent strength of electrochemical measurements, appears to be a realistic goal.

II. DNA ARRAYS FOR GENOMIC ANALYSIS

Completed in 2003, the Human Genome Project has identified all the 20,000–25,000 genes present in human DNA. The task has also determined the sequence of the 3 billion chemical base pairs that make up human DNA. With this knowledge, how transcription occurs and is regulated has become a challenge for biologists. Genetic alterations in tumor cells which are recognized often lead to the emergence of growth stimulatory autocrine and paracrine signals. Single-nucleotide polymorphisms (SNPs) are a common form of genome variations where alternation of a single nucleotide occurs within the base sequence. Current methods for DNA testing are restricted because they need extensive sample treatment undertaken by skilled researchers. DNA arrays should aid scientists to screen for SNPs throughout genomes, as these arrays will permit the parallel processing of human DNA for a number of genetic disorders.

1. Types and Manufacture Methods of DNA Arrays

The earliest DNA arrays may be classed as filter arrays that were able to accommodate the Southern blot technique and the many derivatives thereof. Subsequent improvements led to the creation of high-density filter arrays, termed macroarrays. Subsequently, two different microarray-based technologies arose: the DNA microarray, better known as the spotted microarray, developed at Stanford University,[3] and the oligonucleotide arrays synthesized *in situ*, such as Affymetrix GeneChips®.[4]

In preparing a DNA array, gene-specific probes are created and immobilized on a solid support. When the DNA sequence information is available, oligonucleotides that hybridize with each gene can be synthesized. This approach precludes the need to manage large clone libraries as it is guided by sequence information. Moreover, this strategy is particularly well suited to the expression profile analysis of organisms with completely sequenced genomes, as the focused custom array can analyze all predicted genes in a single experiment.

In the case of the DNA microarray, the method starts by synthesizing cDNA from a cell's messenger RNA using reverse transcriptase polymerase chain reaction. Robotically operated, small pipettes or a piezoelectric device similar to an inkjet printer produces the microarrays by accurately placing large numbers of spots of the cDNA onto a substrate, usually glass (Fig. 1). This type of DNA array can either be homemade on a microscope glass slide, or custom made with 1,000 to 10,000 different spots per slide. Spot sizes of 20 to 50 μm are commonly used and each spot can be analyzed with a fluorometry scanner with a conventional design. This type of DNA array is particularly suitable for *in-house* fabrication of each experiment with its relative ease of custom array preparation by choosing the probes, the printing and the array settings.

The light-directed, combinatorial solid-phase chemistry method can directly synthesize complete sets of oligonucleotide probes on a substrate, as developed by Affymetrix Corp (Fig. 2). In this method, a fused silica substrate is coated with a hydroxyl terminated, silane coupling agent to render the surface active. The treatment is followed by the reaction with the DMT-hexa-ethyl-

Figure 1. (Top) An example of microarrayer and (middle two panels) its printhead assembled with spotting pins. In the microarray picture, 20 samples were printed in quintuplicate at 200-µm spacing on a glass substrate.(bottom) Samples were mixtures of green- and yellow-dye in arbitrary compositions. Photographs provided with permission from Arrayit Corporation.

(A)

Figure 2. (A) The GeneChip® from Affymetrix (http://www.affymetrix.com / about_affymetrix / media / image-library.affx). Courtesy of Affymetrix. (B) Procedures of photolithography process for on-chip oligonucleotide synthesis. The lithographic exposure (a) converts the protective group on the terminal nucleotide into a hydroxyl group (b) for further coupling reaction with a nucleoside phosphoramidite with a light-sensitive protecting group becomes feasible (c). Another type of photomask can direct the reaction to occur at appropriate regions for the next extension reaction (d), (e). Finally, an oligonucleotide array whose surface is modified arbitrary with different oligonucleotide probes sequences in full length, usually 25 nucleotides is available (f).

oxy-O-cyanoethyl phosphoramidite linker that is protected with (α-methyl-2-nitropiperonyl oxycarbonyl) (MeNPOC) at the 5'-OH function. Deprotection is achieved upon irradiation with UV light, in which the subsequent phosphoramidite coupling reaction becomes feasible. Therefore, the deprotection–extension reaction cycle can be repeated as necessary to obtain the DNA array with the intended oligonucleotide probes prepared at a specific length. Moreover, by using a lithography mask with a segmented, blocked/unblocked regions for UV light, and by suitable use of the A-, T-, G-, C-base reactant, a DNA array that is composed of every oligonucleotide probe attached can be prepared with unique base

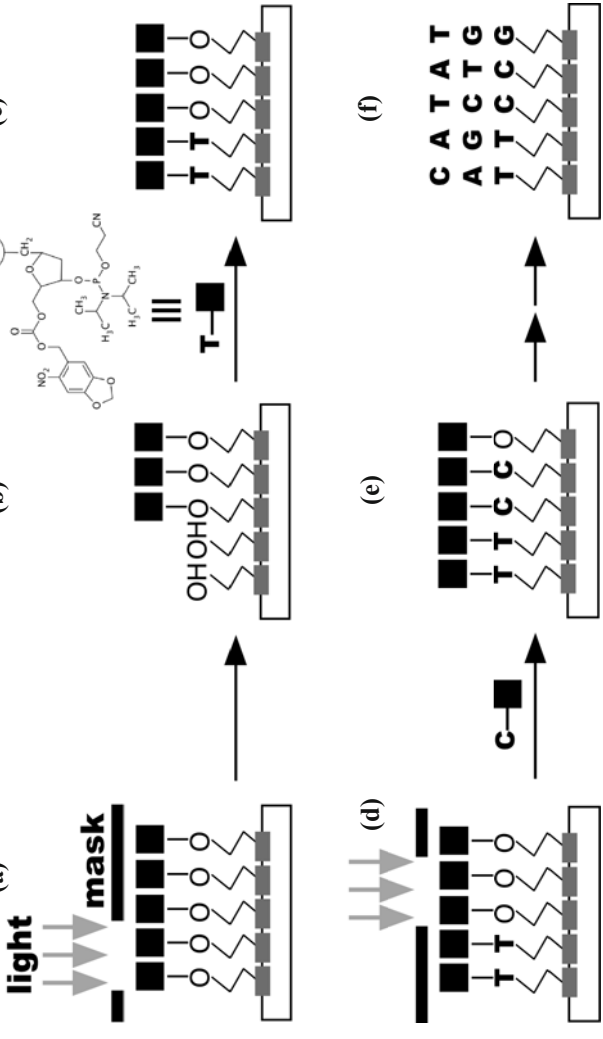

Figure 2. Continuation.

sequences. The oligonucleotide probe has a chain length, typically a 25-mer, or possibly longer (60-mer). Although longer oligonucleotide probes are more expensive, they can provide several advantages over shorter sequences. For fluorometry readout, the smaller size of the target site (20 × 20 μm or less) requires a high-resolution fluorescence scanner with laser excitation.

Besides these two types of DNA arrays, macroarrays and microelectronic arrays with a variety of formats have also been investigated. They are summarized in Table 1 and some of these are commercially available. Here, only the spot density distinguishes the macro- and micro-array: the spot size is 300 μm or larger for the macroarrays. Choice of any one of these DNA arrays would be dependent on the research applications and budget. The microelectronic arrays can be considered as a new entry in this field and will be discussed in the following section.

2. Gene Expression Profiling

Hybridization of DNA, the process whereby complementary nucleic acid sequences pair by forming hydrogen bonds between complementary bases (e.g., A-T and G-C), is the core principle behind microarrays. The noncovalent binding between the two strands becomes stronger with increasing sequence length; as such, only strongly paired strands remain hybridized even after some nonspecific bonding sequences are removed by exhaustive washing. Most labeling for DNA microarray analysis involves the use of fluorescence, which possesses the particular benefit of allowing the simultaneous reading of several experimental parameters in samples, otherwise known as multiplexing.

Figure 3 shows a typical dual-color microarray experiment with a cDNA-pair prepared from two specimen materials to be compared, such as a particular type of cancer cells vs. normal cells. Commonly used fluorescent dyes include Cy3, which shows fluorescence at 570 nm (green-colored emission) and Cy5 with fluorescence at 670 nm (red-colored emission). To convert the mRNA samples to the labeled cDNA, reverse transcription is carried out in the presence of the fluorescent-labeled nucleotide precursors. These cDNA products are then combined to hybridize on a corre-

Table 1. A Summary for the Types and the Features of DNA Microarrays in Different Formats.

	Probe DNA preparation method	Array size and probe DNA density	Labeling and detection method	Functionality and significant application	Suppliers
Microarrays	Robotic printing or piezoelectric inkjet printing of synthesized DNA probes or PCR products.	2.5-cm by 7.5-cm glass slide with approximately 10,000 genes.	Fluorescent labeling prior to hybridization; fluorophore is added after hybridization.	Complimentary DNA (cDNA) library.	Agilent Technologies, GE Healthcare Life Science, and others.
Oligonucleotide arrays	*In-situ* synthesis by light-directed, combinatorial solid-phase chemistry.	1-cm by 1-cm fused silica with approximately 40,000 genes	Fluorescent labeling prior to hybridization.	The densest array.	Affymetrix, NimbleGen (Roche), Febit, CombiMatrix.
Macroarrays	Probes are spotted onto nylon membrane, plastic or nitrocellulose solid matrix.	8-cm by 12-cm with approximately 200 to 5,000 genes.	Radioactive labeling; use of phosphorimager detector.	The most sensitive detection.	Clontech Laboratories, Research Genetics.
Microelectronics array	Electrical field or current delivers DNA probes to chip surface.	Dependent on the number of ultramicroelectrode array that can be formed on substrate surface.	Fluorescent labeling prior to hybridization.	Active hybridization; electrical or electrochemical lead-out of hybridization..	ELI Tech Molecular Diagnostic.

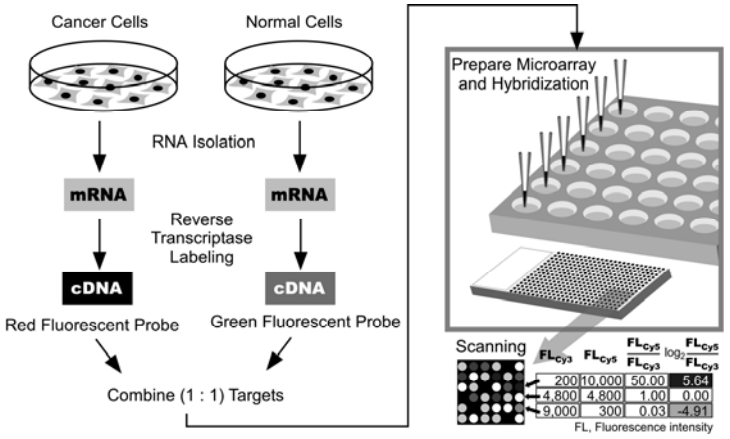

Figure 3. Diagram of typical dual-color microarray experiment. The cDNA prepared from two samples to be compared (e.g. cancer cells versus normal cells) and that are labeled with two different fluorescent dyes, namely Cy3 (λ_{em} 570 nm) and Cy5 (λ_{em} 670 nm). The two Cy-labeled cDNA samples are mixed and hybridized to a single microarray that is then scanned in a microarray scanner. Relative intensities of each fluorophore may then be used in ratio-based analysis to identify up-regulated and down-regulated genes.

sponding DNA array. After hybridization, a scanning fluorescence microscope illuminates each DNA feature or spot and measures the fluorescence from each dye separately. The yellow-colored spot means that the particular gene can be equally expressed in both disease and normal cells, as indicated by the additive color mixing caused by the labeled cDNA binding. Other coloring observations represent the presence of either downregulation or upregulation in the corresponding cells. Ratio-based analysis of the relative intensities of each fluorophore quantifies this.

3. Sequencing by Hybridization

Current advanced modern instrumental analytical techniques can sequence genome DNAs most efficiently. However, sequencing of megabase to gigabase quantities of DNA still requires significant

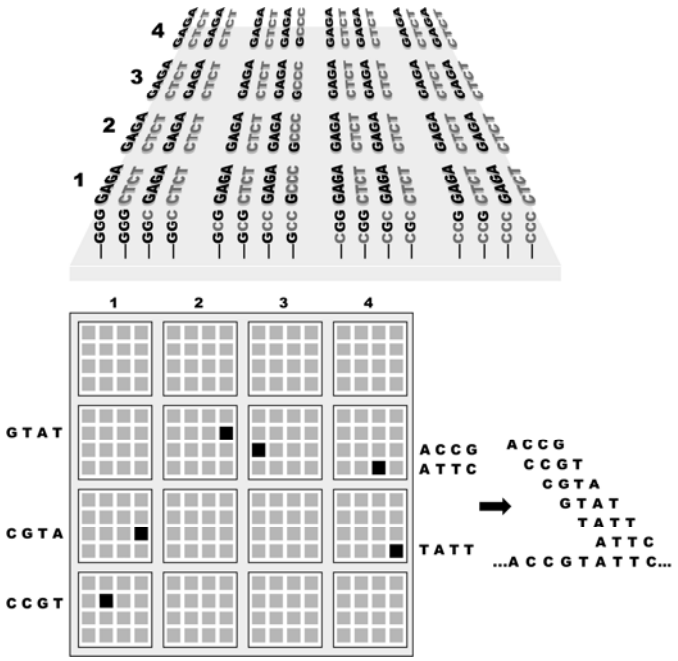

Figure 4. Top: An array consisting of tetranucleotides with $4^4 = 256$ spots. Although each spots is depicted only one strand per spot, it contains many copies of the same oligonucleotide. Bottom: Summary of the SHB experiment. With treating by a partially digested DNA strand, hybridization occurred in six different spots, colored in black. After identifying the sequence of these spots and sorting them, the sequence of the sample DNA strand can be reconstructed.

improvement in the methods used. Normally employed methods of sequencing (direct methods such as gel electrophoresis and pyrosequencing) determine each consecutive base position in the DNA chain individually. In contrast, an indirect method assembles the DNA sequence based on experimental determination of the oligonucleotide content of the DNA chain. Sequencing by hybridization (SBH) is a promising indirect method in which sets of oligonucleotides are hybridized under conditions that allow detection of complementary sequences in the target nucleic acid.[12]

Figure 4 shows the procedure of base sequence determination exemplifying a tetramer DNA sample. An array consisting of 256

tetranucleotide probe sequences can be built based on the 4^4 combinations of nucleotide bases. Each spot contains multiple copies of the particular tetramer sequence. When the array is treated with labeled, partially digested sample DNA, hybridization may occur at several probe sequence sites. In this case, we assume that hybridization occurred in six different sites. After identifying the base sequences of these spots, the sequences of the sample DNA can be reconstructed by sorting the detected sequences.

Constructing arrays with longer oligonucleotides enables the analysis of longer strands of sample DNA. With massively constructed DNA arrays, it is expected that simple, straightforward, and yet reliable methods of SBH should eventually be feasible. The SBH method was introduced at a very early stage of genome research. Quite recently, an innovative method of SBH has been reported which can further improve the traditional SBH based on the shotgun principle.[13]

4. Microelectronics Array for an Electrochemistry Approach

As outlined in the foregoing section, DNA arrays help biochemists to achieve their goals by providing the opportunities of examining every gene simultaneously. Because of its benefits such as low expense, high throughput and miniaturization, this technology is firmly established as one of the most powerful tools ever developed and is valuable in various research areas including clinical research, diagnostics, toxicology studies, drug development and personalized medicine. At the same time, there are problems for DNA microarrays due to the architecture and intended operation, e.g., probe saturation in the capturing spots, washing artifacts and spot-to-spot variations. Such experimental uncertainties limit the scope of applications to only a semi-quantitative platform. In addition, the current DNA arrays have not been designed for real-time analysis but for before-after operations. In this regard, Hassibi et al. have developed a real-time DNA array system by tuning fluorophore labels involving fluorescence energy transfer upon hybridization.[14] They reported that the sensing performance was improved by measuring the fluorescence in the presence of excess amounts of target DNA in the solution phase. Moreover, the hybridization

kinetics was quantitatively evaluated based on a time-course analysis of the fluorescence intensity.

Compared with radioisotope assays or fluorometry, electrochemical methods certainly include rapid detection, a sensitive transducer, minimal power consumption and even low production costs. By offering those advantages, electrochemical DNA biosensors, which have been used in a range of unique research activities, should have the potential to overcome the limits of the current DNA array platforms. Microelectronics arrays are composed of patterned, typically platinum ultramicroelectrodes, fabricated on thermally oxidized silicon substrates by using a standard photolithography process. Initially, they were intended to electrostatically allow traffic of any charged species to and from electronic test sites by a superimposed potential from an outer power source.[15] An agarose permeation layer containing streptavidin coats the chips, to prevent denaturation of the biological materials by the harsh electrochemical environment near the electrode, and allows the binding of biotinylated DNA samples. Each electrode may be individually polarized positively or negatively to concentrate or exclude the test species arbitrarily. This type of *active* hybridization is up to 1000 times faster than a traditional, passive mode.

Collaboration with the lab-on-a-chip technology[16] has recently redefined the position of the microelectronics arrays as versatile automated gene analysis devices. Liu et al. reported an electronics array with 12,000 features, which can handle automate fluidic handling steps required to carry out a gene expression study by integrating them into a single microfluidic apparatus (Fig. 5).[17,18] Aside from DNA arrays, DNA biosensors that rely on electrochemical principles have continued to earn cross-disciplinary innovations. For example, they now include conjugation with a wide variety of enzyme labels[19] and artificial nanoarchitectures involving gold nanoparticles[20] and carbon nanotubes.[21] Useful interfacial parameters have been actively prompted for measurements; they cover intrinsic charge,[22] space charge,[23-25] impedance[26] and capacitance.[27] These achievements can definitely boost research on electronics arrays, which are currently in the early phase of development.

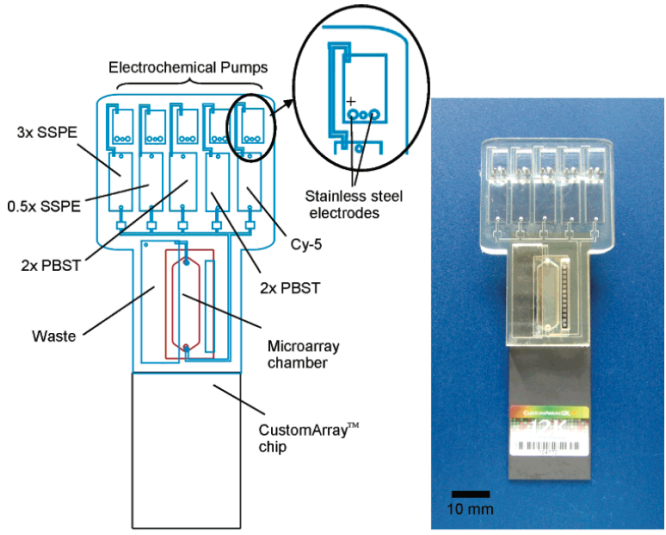

Figure 5. (a) Schematic and a picture of a microfluidic biochip equipped with microelectronics array. (b) Schematic and a close-view picture for a microelectronics array with installed integrated circuits. The circuit controls each microelectrode (over 12,000 features) for being addressable individually from an outer electrical source. Reprinted with permission from Ref. 17, Copyright (2006) American Chemical Society.

III. SECM AS A DNA SENSOR AND DNA ARRAY READOUT

The astonishing success of scanning tunneling microscopy has cultivated many variants. SECM is such a technique and can provide chemical information of the surface.[6, 28] Moreover, SECM requires the samples to undergo nearly no complex pretreatment, only having to be transferred into a solution containing redox-active, small molecules or ions (mediator). This makes SECM uniquely suitable not only for basic physical chemistry purposes but also to address biological applications including biosensors and biodevices. SECM can provide detailed information on their

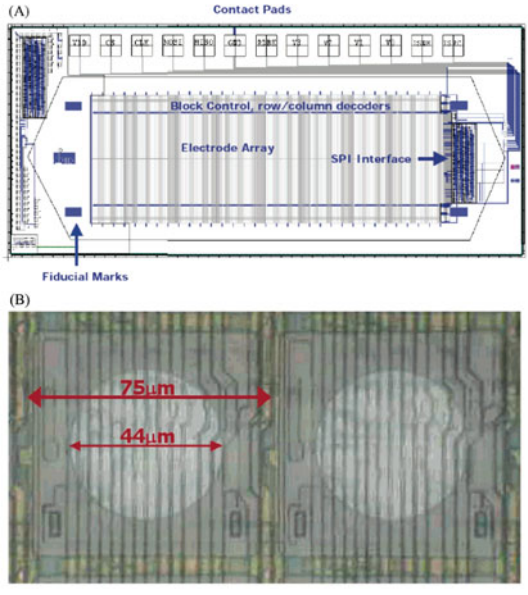

(b)

Figure 5. Continuation.

interfacial phenomena since neither insulating substrates nor electrochemically-inactive substances limit SECM applications. As introduced in the preceding section, current research on DNA arrays suggests that the electronics arrays are best suited for electrochemical DNA analysis purposes. However, for their potential high-throughput capabilities, electronics arrays require a multiplexer circuit element or hardware equipment to readout the massive signal in a single procedure. SECM imaging, with its high spatial resolution, clearly has the potential to be an alternative method, even if it is subjected to a spot-type DNA array with a conventional design. During the last few decades, theoretical descriptions of SECM have been built and include

(a) how the Faradaic current flow varies into/out of the tip according to the tip-to-substrate distance, and

(b) how the mass transport or heterogeneous electron transfer kinetics occur.

In this Chapter, after a brief introduction to the theory of SECM, recent progress in SECM studies toward DNA arrays including simple DNA-attached electrodes will be summarized. Some of our achievements will be included. For additional reviews on SECM for bioimaging, the reader is guided to recent reviews.[29, 30]

1. Introduction and Principle of SECM

(*i*) *Operation of SECM for Surface Imaging*

SECM is a type of scanning probe technique in which the current detected is caused by an electrochemical reaction at the tip (Fig. 6). The apparatus includes a positioning stage combined with a bipotentiostat, which enables the tip to scan in the *x*–*y* plane (raster) across a surface in micrometer steps with the electrode potential of the tip remaining constant. For electrodes, typically a Pt or C disk with radii of 5 to 25 μm is sealed in glass and then polished to form an ultramicroelectrode (UME). The tip, together with auxiliary and reference electrodes, is immersed in a solution containing an electrolyte and a mediator. The sample to be investigated is often connected to the bipotentiostat as a second working electrode. When polarized at the appropriate potential for the oxidoreduction reaction of the mediator, e.g., $O + ne^- \leftrightarrow R$ at concentration of C_O* and with diffusion coefficient of D_O for substance O, a diffusion-limited current will be detected at the tip as given by:

$$i_{T,\infty} = 4nFD_O C_O^* a \tag{1}$$

where n is the number of electrons transferred, F is the Faraday's constant and a represents the radius of the disk electrode. When the positioning stage brings the tip very near the substrate surface, typically within the radius of the tip, two effects can perturb the diffusion-limited current, depending on the substrate. If the substrate is insulating, spatially hindered mass-transport of O to the tip tends to decrease the reduction current of the mediator. In case of

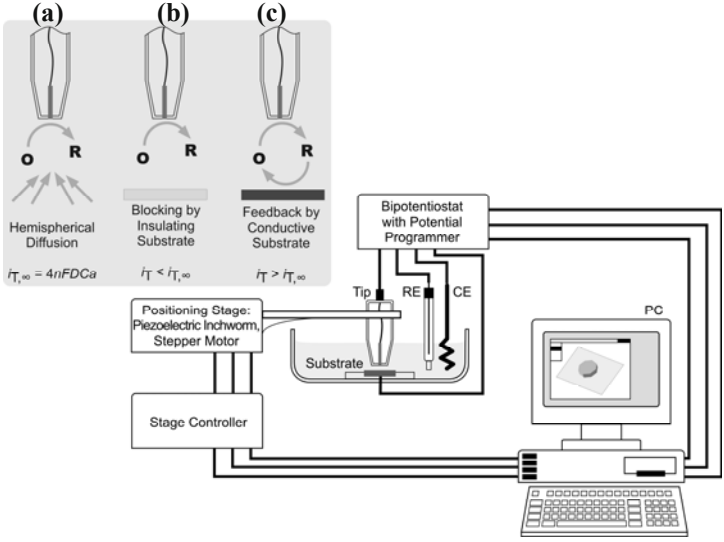

Figure 6. Schematic diagram of SECM apparatus. The inset compares the principle of SECM, showing hemispherical diffusion of the mediator ion to disk-shaped tip located far from the substrate (a), blocking of the mass-transport process by approaching of the tip to an insulating substrate (b), and positive feedback when the exhausted mediator ions are regenerated by redox reaction occurring at a conductive substrate surface (c).

a conductive substrate, on the other hand, if a particular electrochemical condition is attained, the substrate can regenerate O, which is further re-reduced at the tip, giving rise to the reduction current of the mediator. This type of operating control, in which the tip generates and simultaneously detects the mediator in relation to its oxidation state, is termed feedback mode imaging. In the two extreme conditions, the term of *negative feedback* has been adopted for the former case, whereas in the latter case an enhancement of the Faradaic current is termed *positive feedback*.

If the tip is rastered above the substrate, the surface topography that relates to changes in the tip–substrate distance d, can be imaged by recording the changing current vs. tip position in the x–y plane. With a substrate that consists both of conductive and

insulating regions, the current response at a given d differs over dissimilar regions: over a conductor we see $i_T > i_{T\infty}$, while $i_T < i_{T\infty}$ is given over the insulating portions and, thus, we can differentiate them. Figure 7 shows an example of SECM imaging of a 8 × 8 array electrode prepared on a glass substrate; each electrode was prepared from a 50-μm-diameter evaporated gold film with 500 μm of spacing.[31] In the raster image of the tip current, the Au microdot is recognized by a rise in the current from the background exhibited by glass, which distinctly indicates the occurrence of positive feedback. The particular mode of feedback can be explained by the formation of a concentration cell, which promotes the lateral charge transport and the interfacial reaction at the surface; R will be oxidized to O at the sample vicinity of the tip and, for compensation, O will be converted to R at a point distant from the tip.[32] Each 50-μm microdot is resolved as ca. 80 μm in the current mapping image, showing that the method possesses sufficient lateral resolution for use in typical DNA array experiments. Finer UME is acknowledged to give higher resolution and further improvements hold promise in providing a clearer result.

In addition to the SECM experiments, using the feedback mode it is possible to work in the generation-collection mode. Here, if the substrate or the substrate-attached functional material can produce any electrochemically labile material, the tip held close to the substrate could readily detect such species by converting them into other oxidation states. The current flowing along with the reaction is used for imaging. This type of measurement is useful when used for studying biological entities including DNA tests using enzyme labels. Examples of SECM imaging will be presented in the next section.

(*ii*) *Approach Curve at Various Substrate Surfaces*

As described, the current at the tip depends specifically on d, the distance from the substrate. A plot of the tip current, i_T, as a function of tip-substrate, d, is called an approach curve, which provides information about the nature of the substrate. From the results achieved up to now, we can obtain sets of numerical constants to drive theory data. Figure 8 shows the approach curves for

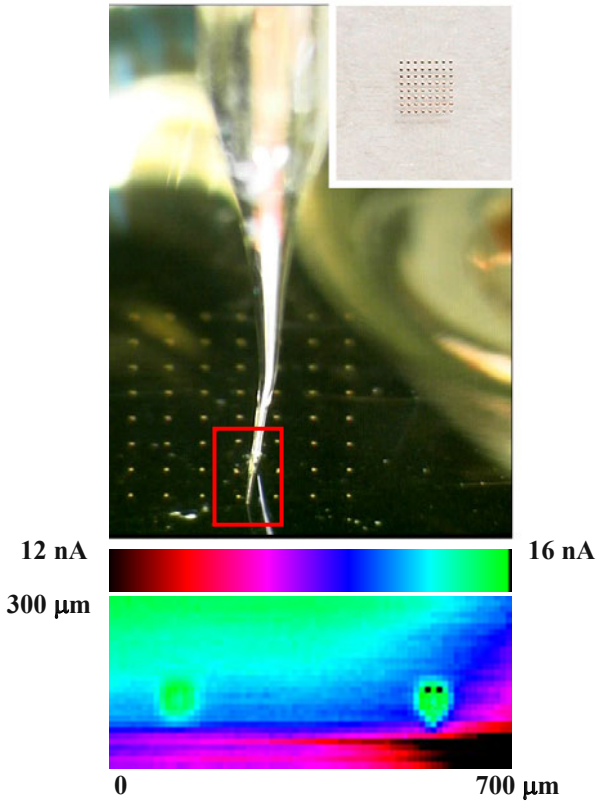

Figure 7. An example of SECM imaging of microelectrode array. Top: Setup of the electrochemical cell: An UME (Pt, r = 10 µm) approaches an 8 × 8 array electrode consisting of each 50-µm diameter Au-UME that was embedded in a glass substrate with 500-µm spacing. Inset shows a top-view of the array electrode. Bottom: A representative current mapping image on an arbitrarily chosen two electrodes. The entire electrode setup was soaked in an electrolyte solution containing 10 mM $K_4[Fe(CN)_6]$ (0.1 M KCl) as mediator. The electrode potential of the tip was kept at +0.6 V (Ag/AgCl) for mediator oxidization while those for the target electrodes were left at their open-circuit potentials. Changes of the oxidation current evolved with raster scan of the tip were measured and encoded into each pixel.

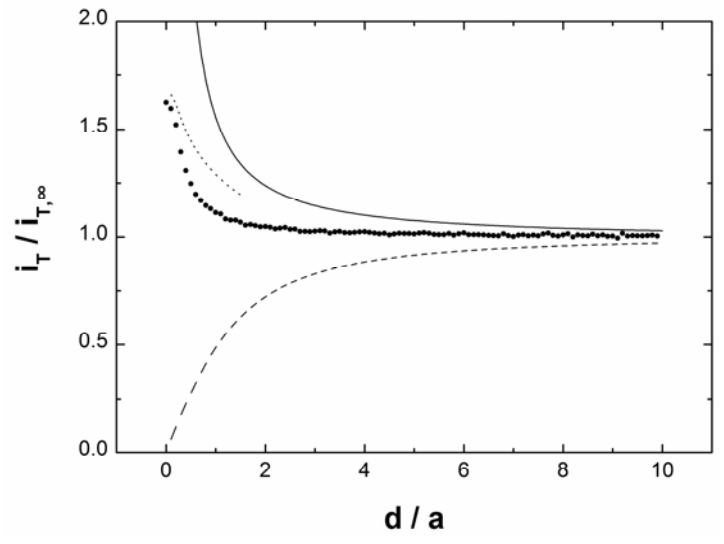

Figure. 8 Calculated current–distance curves toward conducting (solid line) and insulating (broken line) substrates. Plots represent an approach curve obtained for a DNA-grafted, redox-polymer coated electrode (for the detailed description, refer to Section III.3). Equations (4) and (5) that fit into a finite reaction, which follows primary kinetics, yield the theoretical curves shown in dotted line, which can explain, in part, the experimental curve.

a disk-shaped tip in a thin insulating planar sheath, either at an ideally insulating substrate or at a conducting substrate. These curves are presented in the dimensionless form of $i_T/i_{T,\infty}$ vs. d/a. Later $i_T(L)$ denotes $i_T/i_{T,\infty}$ with $L = d/a$. Furthermore, these curves are independent of disk diameter, diffusion coefficient and solute concentration. Here, *RG* value given by the ratio between the radius of the insulating sheath and the radius *r* of the tip electrode can be used for the definition of the geometry of UMEs. When we take examples of UMEs with $RG = 10.2$, numerical results[33] have proposed the following approximate forms for an insulating substrate:

$$I_T^{ins}(L) = \frac{i_r}{i_{T,\infty}} = \frac{1}{0.40472 + \frac{1.60185}{L} + 0.58819\,exp\left(-\frac{2.37294}{L}\right)} \quad (2)$$

and for a conductive substrate:

$$I_T^{cond}(L) = \frac{i_r}{i_{T,\infty}} = 0.72627 + \frac{0.76651}{L} + 0.26015\,exp\left(-\frac{1.41332}{L}\right) \quad (3)$$

These limiting cases indicate that the mediator regeneration either does not occur or proceeds at a diffusion-controlled rate. However, in the actual course of the reaction, an electron-transfer reaction occurs at a finite rate, to give a specific approach curve that lies in between the insulating and the conductive cases. Figure 8 shows an example of an approach curve obtained for a DNA-grafted, redox-polymer coated electrode (for the detailed description, refer to section III.3). For a finite reaction that follows primary kinetics, an analytical approximation, given by Eqs. (4) and (5), is sometimes used for normalized distances $0.1 \leq L \leq 1.5$.[30,34]

$$I_T(L) = \frac{i_L}{i_{T,\infty}} = I_T^{ins}(L) + I_S^{kin}(L)\left(1 - \frac{I_T^{ins}(L)}{I_T^{cond}(L)}\right) \quad (4)$$

$$I_S^{kin}(L, k_{eff}) = \frac{0.78377}{L\left(1 + \frac{1}{\kappa L}\right)} + \frac{0.68 + 0.3315\,exp\left(-\frac{1.0672}{L}\right)}{1 + \frac{\left(\frac{11}{\kappa L}\right) + 7.3}{110 - 40L}} \quad (5)$$

Here, I_T^{ins} and I_T^{cond} are given in Eqs. (2) and (3), respectively. The parameter $\kappa = k_{eff}\, r_T/D$, is the dimensionless rate constant derived from the first-order rate constant k_{eff}, the UME radius r_T and the diffusion constant D of the mediator. For the particular DNA-electrode system, this type of estimation provided more favorable results leading to a rough estimation of $\kappa = 1.8$ as shown in Fig. 8.

2. Examples of Negative Feedback Mode Imaging

As previously pointed out,[6] the first SECM imaging of DNA involved a scanning tunneling microscopy (STM) experiment that took advantage of the lateral conductivity in surface-adsorbed water layers.[35] Later, STM experiments towards DNA self-assembly were extended to an electrochemical-mode of imaging.[36] Conversely, in an early stage of DNA array development, SECM was used to examine such a device, including the detection of hybridization. Takenaka et al. reported SECM imaging of spotted-type DNA microarrays by a combined use of an electrochemically-active, DNA binding molecule (intercalator) and a mediator ion.[37] Wang and Zhou reported SECM imaging of poly[G] and calf-thymus DNA by using a ruthenium bipyridine complex, $Ru(bpy)_3^{3+/2+}$, as both a mediator for SECM imaging and simultaneously, an oxidizing agent of the guanine bases found in the DNA.[38] However, these achievements suffered from either lower detection sensitivity compared with fluorometry, or one-way use of the sample due to the irreversible nature of the guanine oxidation. As described below, progress has been made in this area.

Schuhmann's group developed an electrostatic approach to visualizing the surface bound DNA dots including their hybridization response (Fig. 9).[39,40] This group used $Fe(CN)_6^{3-}$ as a mediator, which can report changes in the surface-charge status. The sample DNA was a 20-mer synthetic oligonucleotide and the DNA molecules were attached as 150-μm-diameter dots through standard 5'-modified chemisorption on gold-covered glass slides. Over the blank areas pretreated with propanethiol, the particular SECM confirmation gave responses in the positive feedback mode. In contrast, the tip current decreased considerably over the DNA

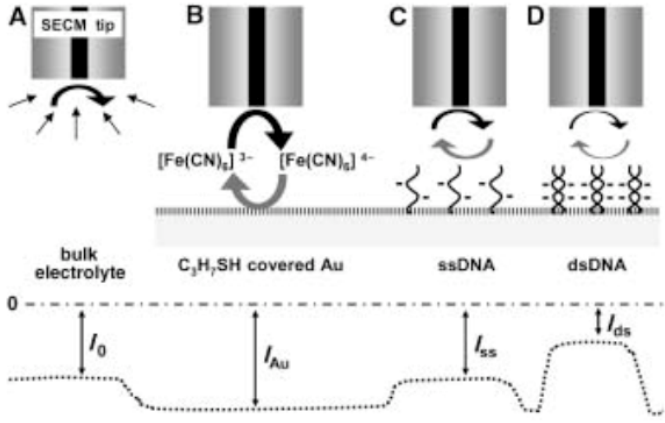

(a)

Figure 9. (a) Schematic representation of repelling-mode SECM. A) A diffusion-limited current flows due to the reduction of $[Fe(CN)_6]^{3-}$ at a tip potential of 0 mV (vs. Ag/AgCl in 3M KCl). B) Recycling of tip-generated $[Fe(CN)_6]^{4-}$ at the propane thiol-modified Au surface causes positive feedback. C) Above a DNA spot, tip-generated $[Fe(CN)_6]^{4-}$ hindered to diffuse into of the Au surface due to the electrostatic repulsion. D) Upon hybridization, mass transport is further suppressed due to the increasing degree of electrostatic repulsion that further increases. (b) Three-dimensional SECM image of an individual spot of a single stranded 20-base oligonucleotide as obtained by the repelling-mode SECM in 5 mM $[Fe(CN)_6]^{3-}$ in 0.1 M phosphate buffer (pH 5.7) containing 3 M NaCl. For the tip electrode a 10-µm-diameter Pt UME was used and its electrode potential was fixed at 0 mV for $[Fe(CN)_6]^{3-}$ reduction. (c) Detection of hybridization through electrostatic repulsion and visualization of DNA duplex formation by means of repelling-mode SECM. A selected spot of a 20-base oligonucleotide was exposed to the hybridization buffer (1 M NaCl–0.1 M phosphate buffer, pH 6.3) containing 2 µM of the complementary oligonucleotide target. A neighboring spot was subjected to target-free hybridization buffer (control). SECM line scans were measured by operating the tip of a 10-µm-diameter Pt microelectrode (0 mV vs. Ag/AgCl in 3M KCl) in solutions of 5 mM $[Fe(CN)_6]^{3-}$ in 3 M NaCl–0.1M phosphate buffer (pH 5.7). All pictures were reprinted from Ref. 39, Copyright (2004) Wiley-VCH Verlag GmbH& Co. KGaA. Reproduced with permission..

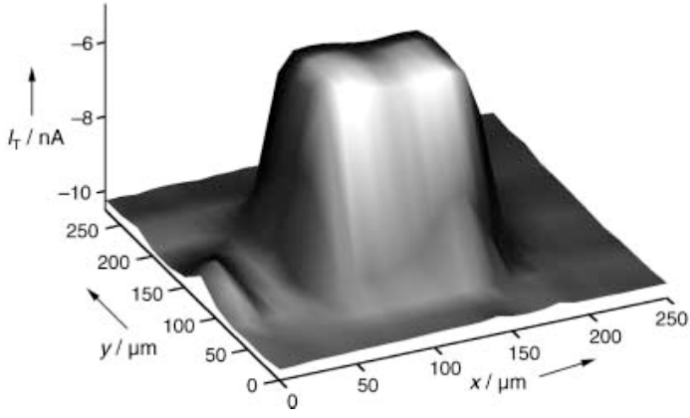

(b)

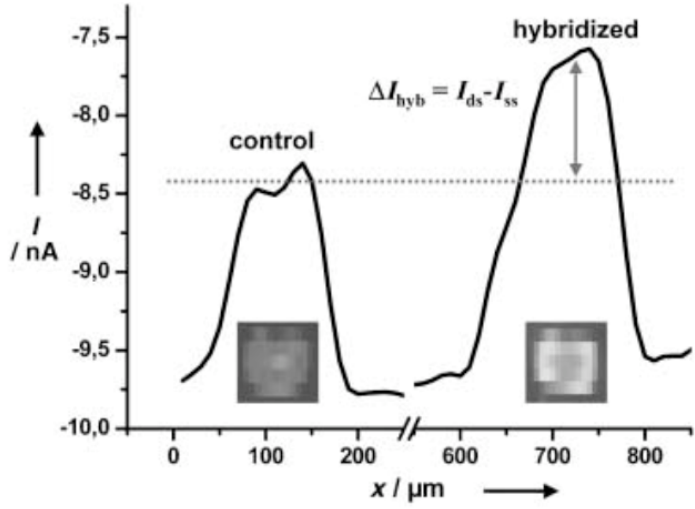

(c)

Figure 9. Continuation.

sites. As a control experiment, a positively charged mediator, $[Ru(NH_3)_6]^{3+}$ gave no such behavior. They explained that the response was caused by the electrostatic repulsion between the mediator ion and the negatively charged DNA molecules (repelling mode). This mode of SECM successfully developed 3D images for the DNA dots including their hybridization.

This type of SECM imaging has been extended for single-nucleotide mismatch detection by Diakowski and Kraatz.[41] They prepared spotted-type DNA arrays with 50-μm-diameter dots with 200 μm spacing through the standard 5'-modified chemisorption on gold-covered silicon wafers. The oligonucleotide sequences (25-mer), including the probe DNA are shown below, and the DNA array prepared was examined by SECM imaging using $[Fe(CN)_6]^{3-}$ as a mediator. As shown in Fig. 10, each DNA spot that was clearly visualized in the current mapping, gave a small but reproducible difference of the tip current, varying with their mismatched structure. This sort of SECM responses was in agreement with previous work.[42] Interestingly, the results of this study showed that the mismatch response could be detected with certain enhancements by examination in the presence of Zn^{2+}. Based on these findings, this research team concluded that the differences in the tip current were due to the variability of the $Fe(CN)_6^{3-/4-}$ redox probe in penetrating the film, as previously reported.[43] Mathematical simulations based on the finite element method determined and further discussed the apparent electron transfer coefficients.

1: HO–$(CH_2)_6$–S–S–$(CH_2)_6$–
5'-GGT-CAA-CAA-ATC-ATA-AAG-ATA-TTG-G-3'

2: 3'-CCA-GTT-GTT-TAG-TAT-TTC-TAT-AAC-C-5'
(full match)

3: 3'-CCA-GT<u>C</u>-GTT-TAG-TAT-TTC-TAT-AAC-C-5'

4: 3'-CCA-GTT-GTT-TAG-<u>C</u>AT-TTC-TAT-AAC-C-5'

5: 3'-CCA-GTT-GTT-TAG-TAT-TTC-<u>C</u>AT-AAC-C-5'

(The underlined base corresponds to the location of the mismatch.)

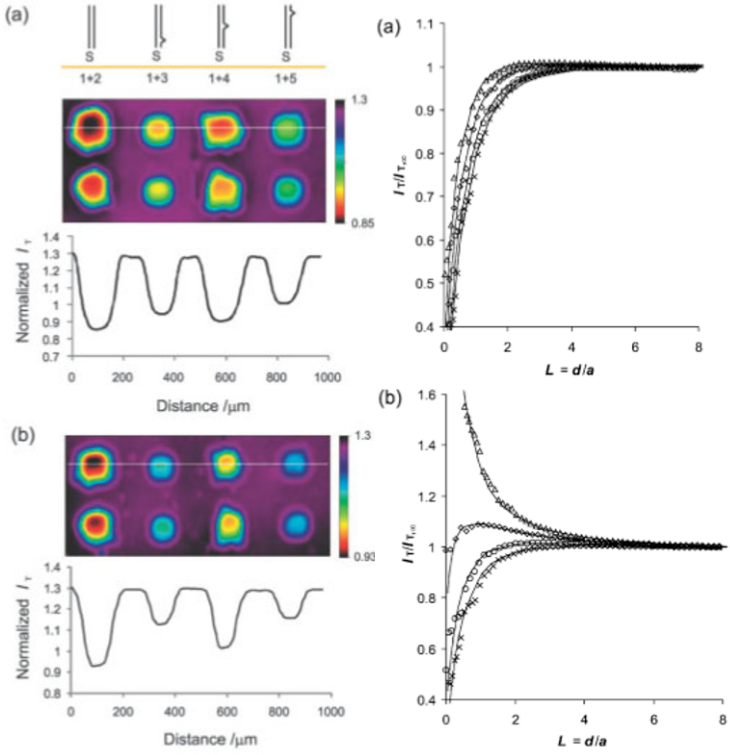

Figure 10. Left: Typical SECM image and current profile recorded over a ds-DNA microarray on a Au substrate in the absence of Zn^{2+} (a) Each spot follows the order, **1** + **2**, **1** + **3**, **1** + **4**, and **1** + **5** from left to right. Typical SECM image and current profile recorded above DNA microarray in the presence of Zn^{2+} (b) Data were obtained for the same sample after incubation in $Zn(ClO_4)_2$ solution. Experiment carried out in 1 mM $K_4Fe(CN)_6$ (50 mM $NaClO_4$–20 mM Tris–ClO_4, pH 8.6) using 25-μm Pt tip. During measurements, the electrode potential of the tip was kept at +0.5 V (Ag/AgCl) for ferrocyanide oxidation. Right: Typical normalized approach curves observed above individual ds-DNA spots for strands **1** + **2** (×), **1** + **3** (◊), **1** + **4** (o) and **1** + **5** (Δ) measured in the absence (a) and presence (b) of Zn^{2+}. Solid lines represent simulated approach curves. All pictures taken from Ref. 41–Copyright (2009) Reproduced by permission of the Royal Society of Chemistry.

As an alternative for DNA microarrays with electrochemical configurations, physisorption of salmon sperm DNA on screen-printed carbon electrodes having dotted polyethylenimine cast membranes on the surfaces was investigated using SECM.[44]

3. Examples of Positive Feedback Mode Imaging

SECM imaging of DNA arrays in the positive feedback mode was also established in an early stage of the research. For the particular mode of imaging to be feasible, each DNA spots must possess a certain degree of electrical conductivity to form a concentration cell. Wang et al. developed a specific property in which electroinactive DNA spots were activated by the application of silver staining: with biotinylated DNA as the target DNA each spot was first treated with a streptavidin-gold conjugate and subsequently subjected to silver staining.[45] The resulting silver nanoparticle-covered DNA spots were highly practical for use in positive mode SECM-type operation. A higher level of sensitivity was achieved for detecting a 17-mer DNA target at only 30 amol per spot, which was comparable to what is usually achievable by fluorometry detection.

The earlier example of SECM experiments using a DNA intercalative agent as a redox-active binder has been revived in recent years. Wain and Zhou reported a detailed study of SECM imaging of DNA arrays using methylene blue (MB) as a redox–active intercalator (Fig. 11).[42] For imaging experiments, they prepared spotted-type DNA arrays with 100-μm-diameter dots and 100 μm spacing on a polycrystalline gold disk. The base sequences of the oligonucleotides (15-mer) are shown below,

1: 5' HS–$(CH_2)_6$–AGT-ACA-GTC-ATC-GCG-3',

2: 5'-CGC-GAT-GAC-TGT-ACT-3',

3: 5'-CGC-GAT-<u>A</u>AC-TGT-ACT-3',

4: 5'-CGC-GAT-<u>A</u>AC-T<u>A</u>T-ACT-3',

5: 5'-CGC-G<u>G</u>T-<u>A</u>AC-T<u>A</u>T-ACT-3',

(The underlined base corresponds to the location of the mismatch).

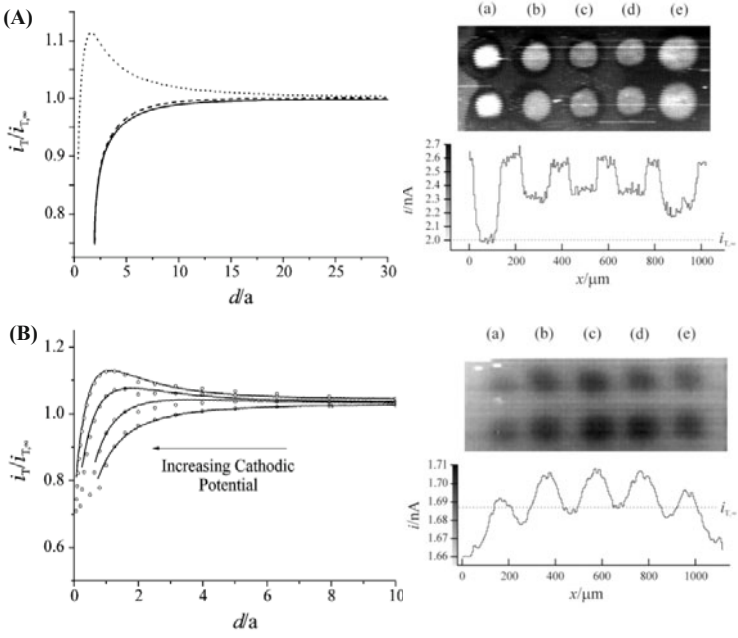

Figure 11. Left: SECM approach curves obtained at a ds-DNA-modified gold substrate in pH 7.2 PBS containing 2 mM $K_4Fe(CN)_6$. The SECM tip was a 25-μm-diameter Pt disk held at a potential of 0.5 V. (A) Unbiased substrate in the absence of MB (—), substrate biased at –0.4 V in the absence of MB (---), and substrate biased at –0.4 V in the presence of 2 μM MB (···). (B) Effect of substrate potential (E_s) in the presence of 2 μM MB (E_s = –0.1, –0.2, –0.3, and –0.4 V). Circles show theoretical curves for finite electron-transfer kinetics. Right: (A) SECM image of a DNA microarray immobilized on a gold disk substrate biased at –0.4V in pH 7.2 PBS solution containing 2 mM $K_4Fe(CN)_6$ and 2 μM MB. Both rows of spots correspond to (a) ss-DNA, (b) ds-DNA (complementary), (c) ds-DNA (one base mismatch), (d) ds-DNA (two base mismatches), and (e) ds-DNA (three base mismatches). The spots are surrounded by 6-mercaptohexanol. The section profile reveals negative-feedback-mode imaging. (B) SECM image of a DNA microarray immobilized on a gold disk substrate biased at –0.4 V in pH 7.2 PBS solution containing 2 mM $K_4Fe(CN)_6$ and 2 μM MB. Both rows of spots correspond to (a) ss-DNA, (b) ds-DNA (complementary), (c) ds-DNA (one base mismatch), (d) ds-DNA (two base mismatches), and (e) ds-DNA (three base mismatches). The exposed gold surface was blocked with triethylene glycol mono-11-mercaptoundecyl ether. The section profile describes that the tip current enhances at the DNA spot showing positive-feedback response. Reprinted with permission from Ref. 42. Copyright (2008) American Chemical Society.

As standard use, immobilization of the probe DNA was made through normal 5'-thiol modification chemistry. A $Fe(CN)_6^{3-/4-}$ redox pair was chosen for the mediator and SECM experiments were made in the presence of MB. Initially, the approach curve was measured with the electrode potential of the DNA array controlled. They found that, with the electrode potential cathodically polarized, the feedback behavior of the $Fe(CN)_6^{3-/4-}$ turned positive even though it was initially in the negative feedback mode. This was due to the cathodic atmosphere providing the reduced form of MB (leucomethylene blue, LB), which could reduce the mediator ion for the positive feedback functions at the tip, Eqs. (6)–(8).

$$\text{SECM tip (0.5 V):} \qquad Fe(CN)_6^{4-} - e^- \rightarrow Fe(CN)_6^{3-} \tag{6}$$

$$\text{DNA surface (–0.4V):} \qquad MB^+ + 2e^- + H^+ \rightarrow LB \tag{7}$$

$$\text{Overall:} \qquad 2\,Fe(CN)_6^{3-} + LB \rightarrow 2\,Fe(CN)_6^{4-} + MB^+ + H^+ \tag{8}$$

SECM experiments were achieved with varying visualization conditions from the negative to the positive feedback mode. The DNA microarray was imaged at a detection level of 14 fmol per spot for the particular dsDNA consisting of 15 base pairs. More importantly, the feasibility of detecting base pair mismatches was demonstrated. Later, Barton's group independently reported a similar type of SECM experiment using Nile Blue as the mediator.[46]

Previously, we reported the surface-grafting immobilization of capture-probe (CP) DNA sequences on carbon electrodes coated with poly(1,4-benzoquinone), PQ, that were oxidatively polymerized using peroxidase.[47] The DNA-polymer conjugate film was found to be electrochemically responsive, allowing the label-free detection of hybridization. Furthermore, the potentially electroconductive nature of the covalently linked, redox-active conjugate molecule was expected to be suitable for the robust, positive-feedback detection in SECM. From these viewpoints, we adopted the surface modification, as a DNA array model, towards a carbon fiber (CF) electrode that was 33 μm in diameter and examined the material by SECM characterization.[48] The CP DNA

(12-mer) was a 5'-NH_2 modified synthetic oligonucleotide with the sequence, 5'-GCC-ACC-AGC-TCC-3'. The DNA probe was covalently grafted into the PQ matrices developed on CF surfaces. The target DNA was the K-ras12 gene, 5'-GGA-GCT GGT GGC-3', one of the human oncogenes found at high rates in colon cancer, pancreatic cancer and lung cancer. We employed the positive feedback mode of operation using $Fe(CN)_6^{3-/4-}$ as the mediator, Eq. (9)–(11). The results are summarized in Fig 12.

SECM tip (+0.6 V): $Fe(CN)_6^{4-} - e^- \rightarrow Fe(CN)_6^{3-}$ (9)

CF substrate (–0.4V): $Q + 2\,H^+ + 2\,e^- \rightarrow H_2Q$ (10)

Overall: $2\,Fe(CN)_6^{3-} + H_2Q \rightarrow 2\,Fe(CN)_6^{4-} + Q + 2H^+ + 2\,e^-$ (11)

From the SECM approach curves, we found that the polymer matrices, even after conjugation with CP DNA, possess a certain degree of charge-transfer capability and thus allow for positive feedback mode imaging. We have successfully obtained well-resolved micrometer-sized dot images (diameter 60–100 μm) of the microelectrodes: they generate a considerable magnitude of current rise over 10 nA while they gave a current decrease, typically 1 nA, in response to the hybridization event at the CP DNA. The sensor response was found to fall slightly more than the background current (0.6–0.8 nA). However, the particular SECM measurement system gave a good signal-to-noise ratio, thereby reliably allowing the detection of DNA hybridization.

4. Examples of Enzymic-Reaction-Coupled Imaging

The use of SECM shows promise in characterizing a variety of biomacromolecules and biomacromolecular reactions at surfaces including enzymic reaction kinetics. The achievements in this area have been applied in DNA biosensors and DNA arrays. Initially, the substrate generation, tip collection mode (SG/TC) imaging was used for such kinds of measurements, and Gyuurcsányi et al. reported a preliminary study on detecting DNA hybridization using

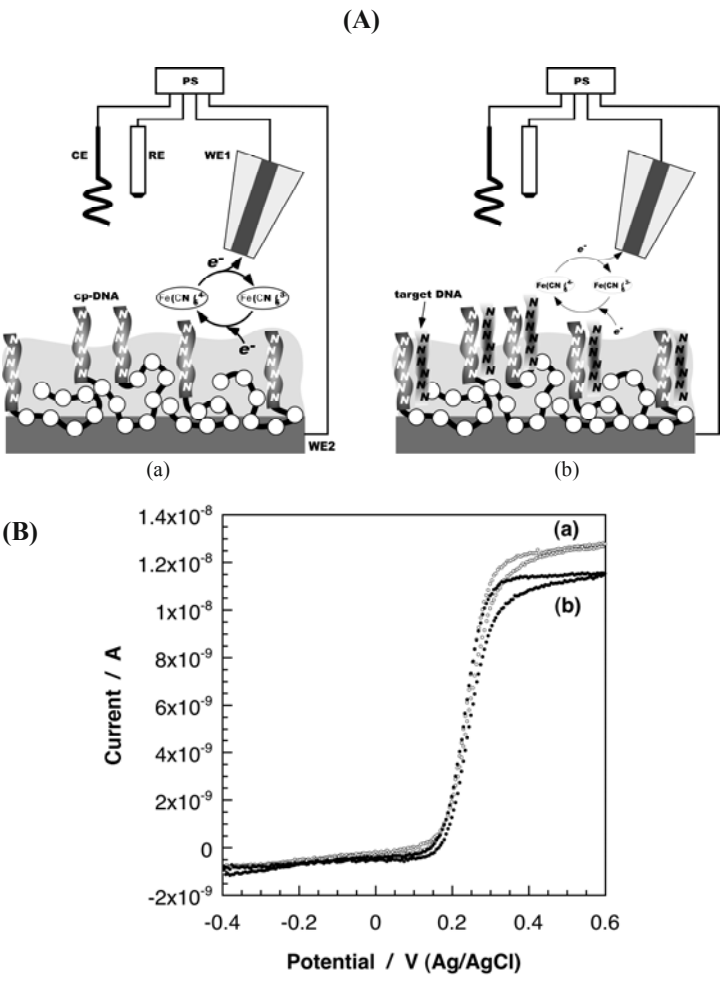

Figure 12. (A) Schematic illustration for the SECM imaging at the CP-DNA/PQ microdots (**a**) and the surface state after hybridization (**b**). (B) Detection of hybridization of CP-DNA confined in the substrate electrode with the tip CV measurements. CVs were obtained with a potential scan rate of 50 mV s^{-1} and the substrate was fixed at –0.2 V. During the measurements, the electrodes were hold adjacent at 20 μm-distance. The substrate surface was varied form the CP-DNA-attached (**a**) to the hybridized state (**b**). The mediator solution was 10 mM $Fe(CN)_6^{4-}$ containing 0.1 M KCl.

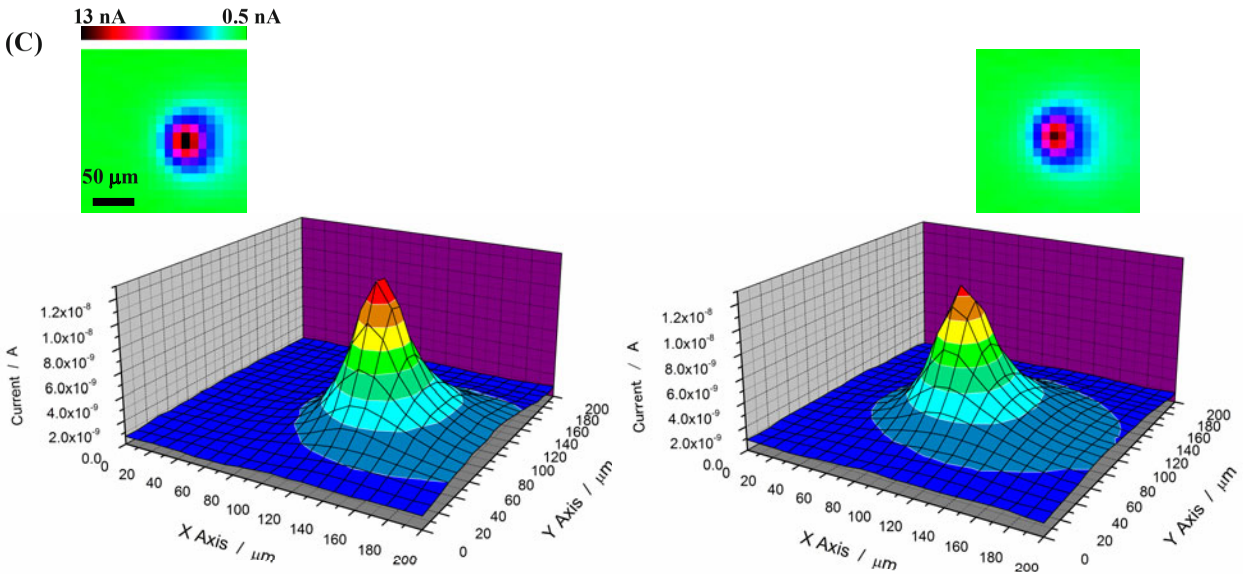

Figure 12. Continuation. (C) Representative SECM images (raw data) and their 3D expressions for the CP DNA/PQ/CF electrodes (**a**), and after hybridization (**b**). All data were obtained at 19-µm s^{-1} scan rate and +0.6 V for the Pt tip electrode, whereas the electrode potential of the substrate was fixed at 0 V.

glucose oxidase to SG.[49] In SG/TC mode imaging, the use of mediator ions is not required and measurements are not limited to conductive surfaces, in contrast to the particular cases of positive feedback. With these potential advantages, SG/TC imaging has become particularly important in studying biological entities. Examination of the SG/TC mode through DNA array developments indicates that the method suffers from lower resolution and often requires a very active enzyme to be used and/or high enzyme loading. Recently, Fortin's and Palchetti's groups independently reported an enzyme-linked method for feedback moderation for imaging.

Fortin and his colleagues described a patterning / immobilization method for a pyrrole-oligonucleotide (ODN) conjugate (Fig. 13).[50] They used the direct mode SECM, in which the electrical field is established between the tip and the substrate (gold) to deposit the poly(pyrrole/pyrrole-ODN) copolymer in the vicinity of the tip through electro-oxidative polymerization. For the detection of the hybridization reaction, they combined a subsequent reaction with streptavidin and biotinylated horseradish peroxidase after hybridization with the target ODN covalently modified with biotin. With the resulting DNA-peroxidase conjugate at the substrate surface, catalytic oxidation of 4-chloro-1-naphthol in the presence of H_2O_2 led to the formation of 4-chloro-3,4-dihydronaphthalen-1(2*H*)- one as the product. Accumulation of the precipitate at the substrate surface caused a local alteration of the conductivity, which was detected with sufficiently high sensitivity using the negative feedback operation. With SPR measurements, they determined the film thickness of the precipitate to be 22 nm. The results of this study should be interesting for the possible application of nanometer-sized film detection using formation SECM.

Palchetti's group has extended this sort of enzyme-linked precipitation method to a sandwich assay.[51] First, they prepared spotted-type DNA microarray using a capture probe DNA (12-mer) through the standard 5'-SH modification method on evaporated gold films. The DNA arrays were next treated with the target, 35-mer DNA in the presence of the biotinylated signaling probe. Finally, the DNA array was reacted with streptavidin–alkaline phosphate to form the surface conjugates. The DNA array was

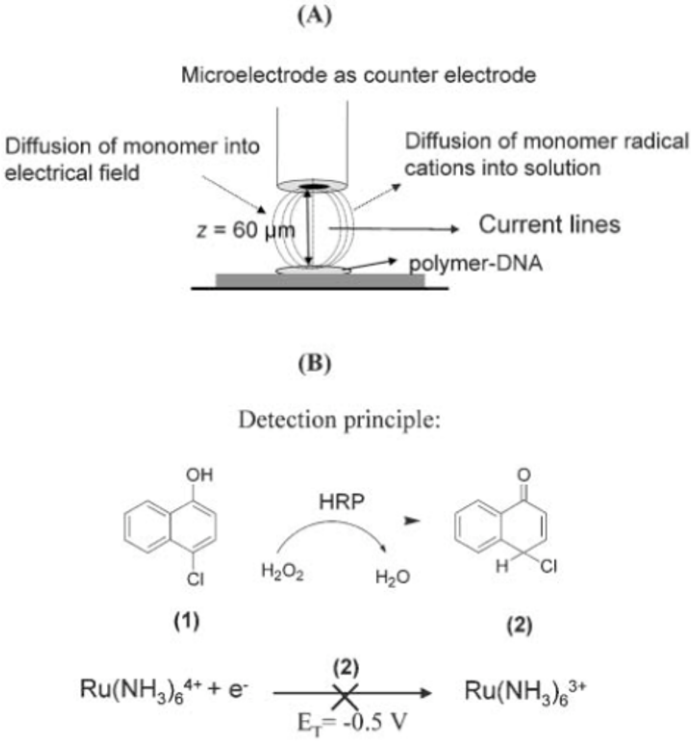

Figure 13. (A) Schematic representation of the direct mode of SECM for the localized electro-oxidative polymerization of pyrrole-oligonucleotide (ODN) probes. For the copolymerization of pyrrole/pyrrole-ODN, solutions of 200 mM pyrrole/10 µM pyrrole-ODN in LiClO4 (0.1M in water) were used. The potential applied was +0.7 V vs. Ag/AgCl and the polymerization time was 20 ms. The distance between the substrate (gold) and the microelectrode used here as the counter electrode was 60 µm. (B) Schematic of the assembly process. The horseradish peroxidase (HRP)-biocatalyzed oxidation of (**1**) in the presence of H_2O_2, and produces precipitates of the insoluble product (**2**). (C) *Molecular Assembly* process. The detection of the hybridization reaction of the ODN probes with their biotinylated complementary strands using SECM was possible after subsequent reactions with streptavidin and biotinylated HRP. The insoluble product (**2**) precipitated on the Au film caused a local alteration of conductivity, which can be sensitively detected by the SECM tip and allowed imaging of DNA arrays in a fast and straightforward way. Reprinted from Ref. 50. Copyright (2006). Reproduced by permission of the Royal Society of Chemistry.

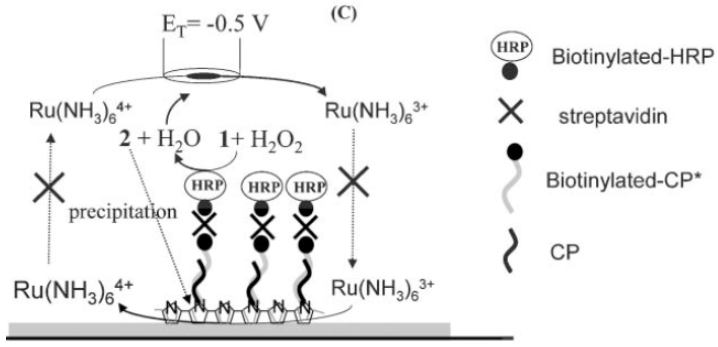

Figure 13. Continuation.

incubated in a 5-bromo-4-chloro-3-indoyl phosphate/nitro blue tetrazolium mixture to precipitate the insoluble reaction product. Simple negative feedback mode SECM gave surface images as shown Fig. 14. As a possible application to real samples, they demonstrated the SECM detection of a long PCR amplicon (255 bp) at a very low concentration (60 nM).

IV. CONCLUSIONS AND FUTURE OUTLOOK

The Human Genome Project has altered the mindset and approach in biomedical research and medicine. The sequencing of genomes has become a central research tool. With faster, yet cheaper DNA sequencing technologies anticipated, the burgeoning field of personal genome analysis will soon be routine practice.[52] Currently, dye-terminating methods with capillary electrophoresis separation is the primary DNA sequencing tool used; however, significant efforts are being explored to develop sequencing technologies with improvements in miniaturization, parallelism and simplification, e.g., the parallel bead array (pyrosequencing),[53] nanopore devices and biochips. DNA-array-based methods include shotgun sequencing by hybridization.[13] An individual addressable microelec-

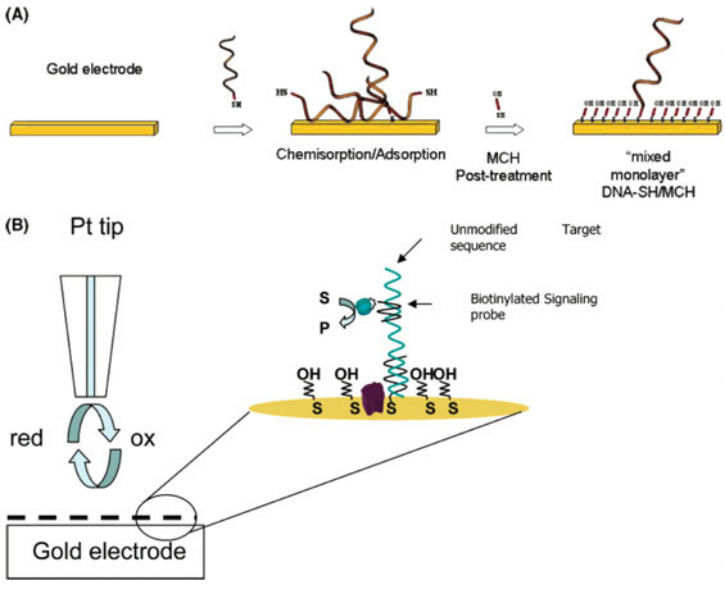

(a)

Figure 14. (a) Scheme of the enzyme-linked precipitation method to a sandwich assay. A capture probe DNA (12-mer) formed spotted-type DNA microarray based on the standard 5'-SH modification chemistry on evaporated gold films. The DNA arrays were next treated with the target, 35-mer DNA in the presence of the biotinylated signaling probe and subsequently reacted with streptavidin–alkaline phosphate. Precipitation of the insoluble reaction product deteriorates the conductivity of the substrate. Simple negative feedback mode SECM report that to give surface images. (b) SECM images of DNA spots. (A) Area scan of array of spots of 2.5 × 2.0 mm, with the capture probes arrayed in spots in three rows at a distance of 1 mm, center to center. (B) A cross-section line scan reporting the current values vs. relative horizontal distance of a part of the area described by the white line depicted in (A). The concentration of target was 40 nM. Imaging measurements were carried out using 2 mM ferrocenemonocarboxylic acid in 0.1 M phosphate buffer, pH 7.4, 0.1 M NaCl as mediator, E_{tip} +0.6 V, $E_{substrate}$ -0.1 V (Ag/AgCl). The tip was a disk Pt microelectrode with a diameter of 10 µm and scanned at a constant speed of 10 µm s^{-1}. Reprinted with permission from Ref. 51. Copyright (2007) American Chemical Society.

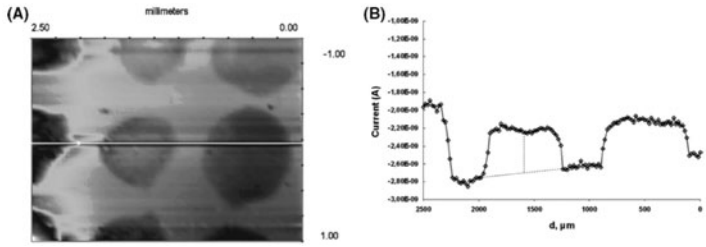

(b)

Figure 14. Continuation.

trode array represents an interesting option, but multiplexing of high-density arrays remains a major instrumental challenge. SECM represents a potential option; however, to meet the criteria of the next generation of instruments, SECM-based approaches will require improvements in

(a) the lateral resolution for massive analysis using high-density arrays;
(b) flexible detection that is inexpensive; and
(c) shortened operation times and high throughput.

As a stand-alone technique, SECM is a powerful tool for particular applications, but when combined with other imaging tools, its power of resolution, in terms of the quality of information provided, is greatly enhanced. *Hyphenation* or *hybridization* with scanning force microscopy[30] and surface plasmon resonance imaging[54] should represent an interesting approach. Current sequencing technologies are too expensive and labor intensive. Prospects seem to indicate that SECM-based detection methods lessen the cost, to a considerable extent, as they allow diverse modes of measurements with label-free detection in some cases. As seen in the examples of impedance-based DNA biosensors, combined detection with impedance measurements would offer a versatile way to readout hybridization events. Recent activities in microelectromechanical systems (MEMS) have been generating various types of micro-fluidic devices and *lab-on-chip* sensing technologies.

Microfabrication of each recognition electrode equipped with a near-field, cantilever-type tip electrode may streamline and accelerate current SECM operations.

Although electrochemical methods are often instrumentally simple and cost-effective, they remain under-developed and their applications are not as widespread as standard fluorescence based techniques. With current advances, electroanalytical methods may soon rival other detection methods.

ACKNOWLEDGEMENT

The author acknowledges the financial support by a Grant-in-Aid for Scientific Research from the Ministry of Education, Culture, Sports, Science and Technology (MEXT), Japan.

REFERENCES

[1] T. A. Brown, *Genomes 3*, Garland Science Publishers, New York, 2006.
[2] G. Hardman (ed), *Microarray Innovations*, CRC Press, Florida, 2009.
[3] M. Schena, D. Shalon, R. W. Davis, and P. O. Brown, *Science* **270** (1995) 467.
[4] S. P. A. Fodor, J. L. Read, M. C. Pirrung, L. Stryer, A. T. Lu, and D. Solas, *Science* **251** (1991) 767.
[5] R. Sosnowski, M. J. Heller, E. T. Anita, H. Foster, and R. Radtkey, *Psychiat. Genet*. **12** (2002) 181.
[6] A. J. Bard and M. V. Mirkin (Eds.), *Scanning electrochemical microscopy*, Marcel Dekker, NY, 2001.
[7] C. M. Li. H. Dong, Q. Zhou, and K. H. Dou, Biochip–fundamentals and application, in *Electrochemical Sensors, Biosensors and Their Biomedical Applications* (X. Zhang, H. Ju, and J. Wang eds.), Academic Press, Oxford, UK, 2008.
[8] T. G. Drummond, M. G. Hill, and J. K. Barton, *Nat. Biotechnol*. **21** (2003) 1192.
[9] A. Sassolas, B. D. Leca-Bouvier, and L. J. Blum, *Chem. Rev*. **108** (2008) 109.
[10] S. Cosnier and P. Mailley, *Analyst* **133** (2008) 984.
[11] S. Cagnin, M. Caraballo, C. Guiducci, P. Martini, M. Ross, M SantaAna, D. Danley, T. West, and G. Lanfranchi, *Sensors* **9** (2009) 3122.
[12] R. Drmanac, S. Drmanac, G. Chui, R. Diaz, A. Hou, H. Jin, P. Jin, S. Kwon, S. Lacy, B. Moeur, J. Shafto, D. Swanson, T. Ukrainczyk, C. Xu, and D. Little, *Adv. Biochem. Eng. Biot.* **77** (2002) 75.
[13] A. Pihlak, G. Baurén, E. Hersoug, P. Lönnerberg, A. Metsis, and S. Linnarsson, *Nat. Biotechnol*. **26** (2008) 676.

[14]A. Hassibi, H. Vikalo, J. L. Riechmann, and B. Hassibi, *Nucleic Acids Res*. **37** (2009) e132.
[15]R. G. Sosnowski, E. Tu, W. F. Butler, J. P. O'Connell, and M. J. Heller, *Proc. Natl. Acad. Sci. USA* **94** (1997) 1119.
[16]D. Figeys and D. Pinto, *Anal. Chem*. **72** (2000) 330A.
[17]R. H. Liu, T. Nguyen, K. Schwarzkopf, H. S. Fuji, A. Petrova, T Siuda, K. Peyvan, M. Bizak, D. Danley, and A. McShea, *Anal. Chem*. **78** (2006) 1980.
[18]A. L. Ghindilis, M. W. Smith, K. R. Schwarzkopf, K. M. Roth, K. Peyvan, S. B. Munro, M. J. Lodes, A. G. Stöver, K. Bernards, K. Dill, and A. McShea, *Biosens. Bioelectron*. **22** (2007) 1853.
[19]E. Katz and I. Willner, *Electroanalysis*. **15** (2003) 913.
[20]S.-J. Park, T. A. Taton, and C. A. Mirkin, *Science* **295** (2002) 1503.
[21]G. A. Rivas, M. D. Rubians, M. C. Rodríguez, N. F. Ferreyra, G. L. Luque, M. L. Pedano, S. A. Miscoria, and C. Parrado, *Talanta* **74** (2007) 291.
[22]J. Fritz, E. B. Cooper, S. Gaudet, P. K. Sorger, and S. R. Manalis, *Proc. Natl. Acad. Sci. USA* **99** (2002) 14142.
[23]D.-S. Kim, Y.-T. Jeong, H.-J. Park, J.-K. Shin, P. Choi,. J.-H. Lee, and G. Lim, *Biosens. Bioelectron*. **20** (2004) 69.
[24]C. Stangi, C. Guiducci, L. Benini, B. Ricco, S. Carrara, C. Paulus, M. Shienle, and R. Thewes, *IEEE Sens J*. **7** (2007) 577.
[25]L. Bandiera, G. Cellere, S. Cagnin, A. De Toni, E. Zanoni, G. Lanfranchi, and L. Lorenzelli, *Biosens. Bioelectron*. **22** (2007) 2108.
[26]F. Lisdat and D. Scäfer, *Anal. Bioanal. Chem*. **391** (2008) 1555.
[27]L. Benini, C. Guiducci, and C. Paulus, *IEEE Design and Test of Computers* **24** (2007) 38.
[28]A. J. Bard and L. R. Faulkner, *Electrochemical Methods 2nd Ed*., Wiley, New York, 2001.
[29]W.S. Roberts, D. L. Lonsdale, J. Griffiths, and S. Higson, *Biosens. Bioelectron*. **23** (2007) 301.
[30]G. Wittstock, M. Burchardt, S. E. Pust, Y. Shen, and C. Zhao, *Angew. Chem. Int. Ed.* **46** (2007) 1584.
[31]Unpublished result from the author's group.
[32]D. O. Wipf and A. J. Bard, *J. Electrochem. Soc*. **138** (1991) 469.
[33]J. L. Amphlett and G. Denuault, *J. Phys. Chem. B* **102** (1998) 9946.
[34]C. Wei, A. J. Bard, and M. V. Mirkin, *J. Phys. Chem*. **99** (1995) 16033.
[35]R. Guckenberger, M. Heim, G. Cevc, H. F. Knapp, W. Wiegräbe, and A. Hillebrand, *Science* **266** (1994) 1538.
[36]Z.-L. Zhang, D.-W. Pang, R.-Y. Zhang, J.-W. Yan, B.-W- Mao, and Y.-P. Qi, *Bioconjugte Chem*. **13** (2002) 104.
[37]K. Yamashita, M. Takagi, K. Uchida, H. Kondo, and S. Takenaka, *Analyst* **126** (2001) 1210.
[38]J. Wang and F. Zhou, *J. Electroanal. Chem.* **537** (2002) 95.
[39]F. Turcu, A. Schulte, G. Hartwich, and W. Schuhmann, *Angew. Chem. Int. Ed.* **43** (2004) 3482.
[40]F. Turcu, A. Schulte, G. Hartwich, and W. Schuhmann, *Biosens. Bioelectron*. **20** (2004) 925.

[41]P. M. Diakowski and H. B. Kraatz, *Chem. Commun.* **2009** (2009) 1189.
[42]A. J. Wain and F. Zhou, *Langmuir* **24** (2008) 5155.
[43]B. Liu, A.J. Bard, C. Z. Li, and H. B. Kraatz, *J. Phys. Chem. B* **109** (2005) 5193.
[44]W. S. Roberts, F. Davis, and S. P. Higson, *Analyst* **134** (2009) 1302.
[45]J. Wang, F. Song, and F. Zhou, *Langmuir* **18** (2002) 6653.
[46]A. A. Gorodetsky, W. J. Hammond, M. G. Hill, K. Slowinski, and J. K. Barton, *Langmuir* **24** (2008) 14282.
[47]K. Nakano, G. Hirayama, M. Toguchi, K. Nakamura, K. Iwamoto, N. Soh, and T Imato, *Sci. Technol. Adv. Mater*. **7** (2006) 718.
[48]K. Nakano, K. Nakamura, K. Iwamoto, N. Soh, and T. Imato, *J. Electroanal. Chem.* **628** (2009) 113.
[49]R. E. Gyurcsányi, G. Jágerszki, G. Kiss, and K. Tóth, *Bioelectrochemistry* **63** (2004) 207.
[50]E. Fortin, P. Mailley, L. Lacroix, and S. Szunerits, *Analyst* **131** (2006) 186.
[51]I. Palchetti, S. Laschi, G. Marrazza, and M. Maschni, *Anal. Chem*. **79** (2007) 7206.
[52]M. L. Metzker, *Genome Res.* **15** (2005) 1767.
[53]M. Margulies, M. Egholm, W. E. Altman, S. Attiya, J. S. Bader, L. A. Bemben, J. Berka, M. S. Braverman, Y.-J. Chen, Z. Chen, S. B. Dewell, L. Du, J. M. Fierro, X. V. Gomes, B. C. Godwin, W. He, S. Helgesen, C. H. Ho, G. P. Irzyk, S. C. Jando, M. L. I. Alenquer, T. P. Jarvie, K. B. Jirage, J.-B. Kim, J. R. Knight, J. R. Lanza, J. H. Leamon, S. M. Lefkowitz, M. Lei, J. Li, K. L. Lohman, H. Lu, V. B. Makhijani, K. E. McDade, M. P. McKenna, E. W. Myers, E. Nickerson, J. R. Nobile, R. Plant, B. P. Puc, M. T. Ronan, G. T. Roth, G. J. Sarkis, J. F. Simons, J. W. Simpson, M. Srinivasan, K. R. Tartaro, A. Tomasz, K. A. Vogt, G. A. Volkmer, S. H. Wang, Y. Wang, M. P. Weiner, P. Yu, R. F. Begley, and J. M. Rothberg, *Nature* **437** (2005) 376.
[54]E. Fortin, Y. Defontain, P. Milley, T. Livache, and S. Szunerits, *Electroanalysis* **17** (2005) 295.
[55]K. Eckhard, H. Shin, B. Mizaikoff, W. Schuhmann, C. Kranz, *Electrochem. Commun.* **9** (2007) 1311.
[56]K. Eckhard, M. Etienne, A. Schulte, W. Schuhmann, *Electrochem. Commun*. **9** (2007) 1793.

Professor Koji Nakano

Professor Koji Nakano is with the Faculty of Engineering at Kyushu University since 1994. He received his BSc and MSc degrees from Tohoku University, and his PhD from Kyushu University in 1993. In 1996 he received the Japan Society for Analytical Chemistry Commendation as Distinguished Young Chemists thanks to his pioneering work on chemical analysis using molecular organizates involving synthetic bilayer membrane, self-assembled monolayer, and DNA self-assembly. Currently, his scientific interest is focused on DNA nano-bio-technology, with a central focus on single-molecule measurements and molecular-chemical device developments.

4

Electrochemistry of Biomimetic Membranes

Rolando Guidelli and Lucia Becucci

Dept. of Chemistry, Florence University, Via della Lastruccia 3
50019 Sesto Fiorentino, Firenze, Italy

I. INTRODUCTION

Biological membranes are by far the most important electrified interfaces in living systems. They consist of a bimolecular layer of lipids (the lipid bilayer) incorporating proteins. Lipid molecules are *amphiphilic*, i.e., consist of a hydrophobic section (the hydrocarbon tail) and a hydrophilic section (the polar head). In biological membranes the two lipid monolayers are oriented with the hydrocarbon tails directed toward each other and the polar heads turned toward the aqueous solutions that bath the two sides of the membrane. The resulting lipid bilayer is a matrix that incorporates different proteins performing a variety of functions. Biomembranes form a highly selective barrier between the inside and the outside of living cells. They are highly insulating to inorganic ions, and large electrochemical potentialdifferences can be maintained across them. The permeability and structural properties of biological membranes are sensitive to the chemical nature of the mem-

N. Eliaz (ed.), *Applications of Electrochemistry and Nanotechnology in Biology and Medicine II*, Modern Aspects of Electrochemistry 53,
DOI 10.1007/978-1-4614-2137-5_4,

brane components and to events that occur at the interface or within the bilayer. For example, biomembranes provide the environmental matrix for proteins that specifically transport certain ions and other molecules, for receptor proteins and for signal transduction molecules. The lipid and protein portions of biomembranes are also sensitive to the presence of lipophilic perturbants. Anaesthetics, for example, readily partition into lipid membranes, altering their electrical and permeability characteristics, thus providing an indicator for these agents. The various responses observed in biomembranes are concentration-dependent, usually very rapid and reversible, and frequently voltage-dependent.

II. THE BIOMIMETIC MEMBRANES: SCOPE AND REQUIREMENTS

In view of the complexity and diversity of the functions performed by the different proteins embedded in a biomembrane (the integral proteins), it has been found convenient to incorporate single integral proteins or smaller lipophilic biomolecules into experimental models of biological membranes, so as to isolate and investigate their functions. This serves to reduce complex membrane processes to well-defined interactions between selected proteins, lipids and ligands. There is great potential for application of experimental models of biomembranes (the so-called biomimetic membranes) for the elucidation of structure-function relationships of many biologically important membrane proteins. These proteins are the key factors in cell metabolism, e.g., in cell-cell interactions, signal transduction, and transport of ions and nutrients. Thanks to this important function, membrane proteins are a preferred target for pharmaceuticals, with about 60% of consumed drugs addressing them. Biomimetic membranes are also useful for the investigation of phase stability (e.g., lipid-lipid phase separation, lipid raft formation, lateral diffusion), protein-membrane interactions (e.g., receptor clustering and co-localization), and membrane-membrane processes such as fusion, electroporation and intercellular recognitions. They are also relevant to the design of membrane-based biosensors and devices, and to analytical platforms for assaying membrane-based processes.

With only a few exceptions, biomimetic membranes consist of a more or less complex architecture that includes a lipid bilayer. In order of increasing complexity, they can be classified into: black lipid membranes (BLMs), solid-supported bilayer lipid membranes (sBLMs), tethered bilayer lipid membranes (tBLMs), polymer-cushioned bilayer lipid membranes (pBLMs), S-layer stabilized bilayer lipid membranes (ssBLMs), and protein-tethered bilayer lipid membranes (ptBLMs). Mercury-supported lipid monolayers and alkanethiol/lipid *hybrid bilayers* are particular biomimetic membranes that contain a single lipid monolayer.

The possibility of self-assembling monolayers and bilayers on metals with formation of rugged functionalized electrodes has stimulated a research aiming at exploiting self-assembly for the realization of biomembrane models capable of incorporating integral proteins in a functionally active state. To achieve this goal, biomembrane models consisting of lipid bilayers should meet a number of requirements:

(i) they should be robust enough for long-term stability, and be easily and reproducibly prepared;
(ii) they should have the lipid bilayer in the liquid crystalline state, and such as to allow lateral mobility;
(iii) they should have water (or, at least, a highly hydrated hydrophilic region) on both sides of the lipid bilayer;
(iv) they should be sufficiently free from pinholes and other defects that might provide preferential pathways for electron and ion transport across the lipid bilayer.

Requirements (ii) and (iii) are necessary for the incorporation of integral proteins into the lipid bilayer in a functionally active state. In fact, integral proteins have a hydrophobic domain buried inside the biomimetic membrane, which must be sufficiently fluid to accommodate this domain. Often, they also have hydrophilic domains protruding by over 6 nm outside the lipid bilayer. To avoid their denaturation and to promote their function, incorporation of integral proteins into biomimetic membranes must ensure that their extramembrane hydrophilic domains are accommodated in a hydrophilic medium on both sides of the lipid bilayer. Moreover, the transport of hydrophilic ions across a solid-supported lipid bilayer via ion channels or ion pumps is only possible if an aqueous or hydrophilic layer is interposed between the bilayer and the sup-

port. Requirement (iv) is needed to make the biomembrane model sufficiently blocking as to characterize ion channel or ion pump activity by electrochemical means without the disturbing presence of stray currents due to defects.

Apart from lipid molecules, the molecules that are most commonly employed for the fabrication of biomimetic membranes are *hydrophilic spacers* and *thiolipids*. Hydrophilic spacers consist of a hydrophilic chain (e.g., a polyethyleneoxy or oligopeptide chain) terminated at one end with an anchor group for tethering to a support and, at the other end, with a hydrophilic functional group (e.g., a hydroxyl group). Sulfhydryl or disulfide groups are employed as anchor groups for tethering to metals such as gold, silver or mercury (see Fig. 1B); methyl-, methyloxy- or chloride-substituted silane groups are used for tethering to glass, quartz, silica or mica. The latter supports are nonconducting and cannot be investigated by electrochemical techniques. Hydrophilic spacers serve to separate the lipid bilayer from a solid support, to compensate for surface roughness effects, to prevent any incorporated peptides or proteins from touching the support surface (thus avoiding loss of their functionality due to denaturation), and to provide an ionic reservoir underneath the lipid bilayer.

Thiolipids differ from hydrophilic spacers in that the hydrophilic chain is covalently linked to one or, more frequently, two alkyl chains at the opposite end with respect to the anchor group, as shown in Fig. 1A. The alkyl chains simulate the hydrocarbon tails of a lipid molecule and provide one half of the lipid bilayer to the biomimetic membrane. When tethered to a support, hydrophilic spacers expose to the bulk aqueous phase a hydrophilic surface, while thiolipids expose a hydrophobic surface. Clearly, lipid bilayers formed on top of hydrophilic spacers are noncovalently linked to them and can be regarded as *freely suspended*. Conversely, lipid monolayers assembled on top of thiolipid monolayers form lipid bilayers that are tethered to the support.

Before discussing advantages and disadvantages of these systems, we will describe in detail the electrochemical technique that is commonly employed for their investigation, namely electrochemical impedance spectroscopy (EIS), as well as some fabrication methodologies. In fact, our attention will be mainly focused on those biomimetic membranes that are amenable to investigation by electrochemical methods. Biomimetic membranes that are in-

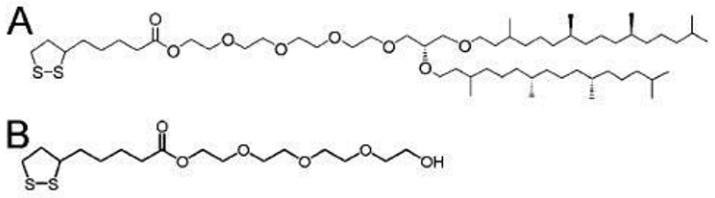

Figure 1. (A) Structure of a widely adopted thiolipid, called DPTL.[1] It consists of a tetraethyleneoxy chain terminated at one end with a lipoic acid residue and covalently linked at the other end to two phytanyl chains. (B) Structure of the corresponding hydrophilic spacer (TEGL), in which the two phytanyl chains are replaced by a hydroxyl group.

vestigated exclusively by non-electrochemical surface sensitive techniques, such as those formed on insulating supports (e.g., glass, mica, quartz, silica, etc.), will be considered only briefly.

III. ELECTROCHEMICAL IMPEDANCE SPECTROSCOPY

Many membrane proteins are *electrogenic*, i.e., translocate a net charge across the membrane. Consequently, it is possible to monitor their function directly by measuring the current flowing along an external electrical circuit upon their activation. Analogously, their deactivation by some antagonist can be monitored by a drop in current. The techniques of choice for these measurements are EIS and potential-step chronoamperometry or chronocoulometry, because the limited volume of the ionic reservoir created by a hydrophilic spacer in solid-supported biomimetic membranes cannot sustain a steady-state current.

Electrochemical impedance spectroscopy applies an a.c. voltage of given frequency to the system under study and measures the resulting current that flows with the same frequency. Both the amplitude of the a.c. current and its phase shift with respect to the a.c. voltage are measured. The frequency is normally varied gradually from 10^{-3} to 10^{5} Hz. To interpret measured impedance spectra, it is necessary to compare them with the electrical response of an equivalent circuit simulating the system under investigation. As a

rule, an equivalent circuit is assembled from resistors and capacitors, representing the electrically dominant components of biomimetic membranes. In general, a metal-supported self-assembled mono- or multilayer can be regarded as consisting of a series of slabs with different dielectric properties. When ions flow across each slab, they give rise to an ionic current $\boldsymbol{J}_{\text{ion}} = \sigma\boldsymbol{E}$, where $\boldsymbol{E}$ is the electric field and σ is the conductivity. Ions may also accumulate at the boundary between contiguous dielectric slabs, causing a discontinuity in the electric displacement vector $\boldsymbol{D} = \varepsilon\boldsymbol{E}$, where ε is the dielectric constant. Under a.c. conditions, the accumulation of ions at the boundary of the dielectric slabs varies in time, and so does the electric displacement vector, giving rise to a capacitive current $\boldsymbol{J}_{\text{c}} = \text{d}\boldsymbol{D}/\text{d}t$. The total current is, therefore, given by the sum of the ionic current and of the capacitive current. In this respect, each dielectric slab can be simulated by a parallel combination of a resistance, accounting for the ionic current, and of a capacitance, accounting for the capacitive current, namely by an *RC mesh*. Accordingly, the impedance spectrum of a self-assembled layer can be simulated by a series of RC meshes. It should be noted that lateral heterogeneities, such as defects or microdomains, cannot be accounted for by simulating them by RC meshes in parallel with each other. In fact, in view of Kirchhoff's laws for the combination of circuit elements, the parallel connection of RC meshes is reduced again to a single RC mesh, with averaged values for the resistance and the capacitance.

Application of an a.c. voltage of amplitude v and frequency f to a pure resistor of resistance R yields a current of equal frequency f and of amplitude v/R, in phase with the voltage. Conversely, application of the a.c. voltage to a pure capacitor of capacitance C yields a current of frequency f and amplitude $2\pi fC$, out of phase by $-\pi/2$ with respect to the voltage, i.e., in quadrature with it. This state of affairs can be expressed by stating that the admittance Y of a resistance element equals $1/R$, while that of a capacitance element equals $-\text{i}\omega C$, where $\omega = 2\pi f$ is the angular frequency and i is the imaginary unit. More generally, in an equivalent circuit consisting of resistances and capacitances, Y is a complex quantity, and the impedance Z is equal to $1/Y$, by definition. Hence, Z equals R for a resistance element, and $\text{i}/\omega C$ for a capacitance element. In analogy with the resistance in d.c. measurements, the overall im-

pedance of two circuit elements in series is equal to the sum of the impedances of the single circuit elements. Conversely, the overall impedance of two circuit elements in parallel is such that its reciprocal is equal to the sum of the reciprocals of the single circuit elements. Consequently, if two circuit elements have appreciably different impedances, their overall impedance is controlled by the circuit element of higher impedance if they are in series and by the circuit element of lower impedance if they are in parallel.

Bearing this in mind, let us consider a biomimetic membrane consisting of a thiolipid tethered to an electrode surface, with a lipid monolayer on top of it. As a first approximation, this tethered bilayer lipid membrane (tBLM) can be regarded as consisting of three adjacent slabs: the hydrophilic spacer moiety, the lipid bilayer moiety, and the aqueous solution bathing the lipid bilayer. A simple equivalent circuit commonly employed to interpret the impedance spectrum of a tBLM is shown in Fig. 2; R_Ω is the resistance of the aqueous electrolyte, R_m and C_m are the resistance and capacitance of the lipid bilayer, and C_s is the capacitance of the hydrophilic spacer. As an example, we will consider a tBLM that makes use of a convenient and widely used thiolipid called DPTL, first employed by Schiller et al.[1] (see Fig. 1A). It consists of a tetraethyleneoxy hydrophilic chain covalently linked at one end to a lipoic acid residue, for anchoring to the metal via a disulfide group, and bound at the other end via ether linkages to two phytanyl chains. Figure 2 shows the impedance spectrum of a tBLM consisting of a DPTL monolayer anchored to a mercury electrode, with a diphytanoylphosphatidylcholine (DPhyPC) monolayer on top of it. This tBLM incorporates gramicidin, a linear neutral pentadecapeptide that spans lipid bilayers by forming a N-terminus-to-N-terminus dimer.[2] The elements of the equivalent circuit are influenced by the movement of K^+ ions across the lipid bilayer, induced by the gramicidin channel. The spectrum is displayed on a Bode plot, namely a plot of $\log|Z|$ and phase angle ϕ against $\log f$, where $|Z|$ is the magnitude of the impedance.

As already stated, the impedance of circuit elements in series is determined by the element with the highest impedance; conversely, the impedance of circuit elements in parallel is determined by the element with the lowest impedance. Therefore, at the highest frequencies, $f=\omega/2\pi$, the overall impedance $|Z|$ is determined by the resistance R_Ω, because the impedance of the C_s element,

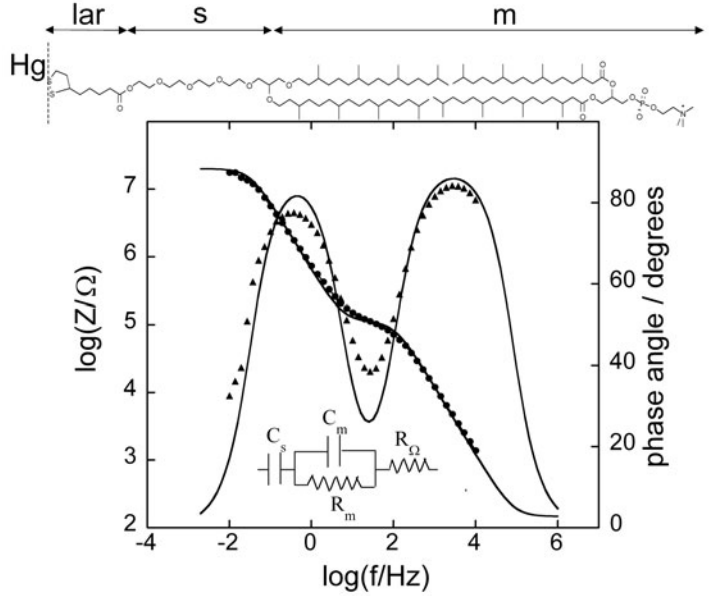

Figure 2. Plot of log|*Z*| (solid circles) and ϕ (solid triangles) against log *f* (Bode plot) for a mercury-supported DPTL|DPhyPC bilayer incorporating gramicidin from its 1×10^{-7} M solution in aqueous 0.1 M KCl at –0.600 V vs. Ag|AgCl(0.1M KCl).[2] The solid curve is the best fit of the equivalent circuit shown in the figure to the impedance spectrum, with C_s=0.25 μF, R_m=106 kΩ, C_m=14 nF, and R_Ω=146 Ω. Drop area = 2.2×10^{-2} cm^2. Top: structure of DPTL in tail-to-tail contact with a DPhyPC lipid molecule. The double-headed arrows mark the lipoic acid residue (lar), spacer (s) and lipid bilayer (m) sections of the tBLM.

$1/(\omega C_s)$, is $<<R_\Omega$; the same is true for the impedance of the R_mC_m mesh, which is determined by the lowest of the impedances of these two elements in parallel, i.e., $1/(\omega C_m)$. At the highest frequencies, |*Z*| is therefore controlled by R_Ω, which is independent of frequency and is characterized by a phase angle ϕ=0. With decreasing frequency, $1/(\omega C_m)$ becomes greater than R_Ω, while still remaining lower than R_m, and it is also > $1/(\omega C_s)$, because C_s is > C_m. Hence, |*Z*| coincides with $1/(\omega C_m)$, and the log|*Z*| vs. log *f* plot has a slope equal to –1, while the phase angle tends to 90°. With a further decrease in frequency, $1/(\omega C_m)$ becomes comparable with and ultimately less than R_m, and the Bode plot tends to become

independent of frequency, which would correspond to complete control by R_m. At the same time, ϕ decreases tending to zero. However, before this can occur, a further decrease in frequency makes $1/(\omega C_s) >> R_m$, causing $|Z|$ to coincide with $1/(\omega C_s)$. Hence, the slope of the Bode plot becomes once again equal to –1 and ϕ tends to 90°. The solid curve in Fig. 2 is the best fit of the $C_s(R_mC_m)R_\Omega$ equivalent circuit to the experimental plot. This Bode plot is rather featureless. A Bode plot richer in features is obtained by incorporating in the same tBLM the ion carrier valinomycin, a hydrophobic depsipeptide that cages a desolvated potassium ion shuttling it across the lipid bilayer.[3] In this case, the ϕ vs. log f plot exhibits an additional hump, as shown in Fig. 3. We will show in what follows that valinomycin allows an additional dielectric slab of the tBLM to be disclosed.

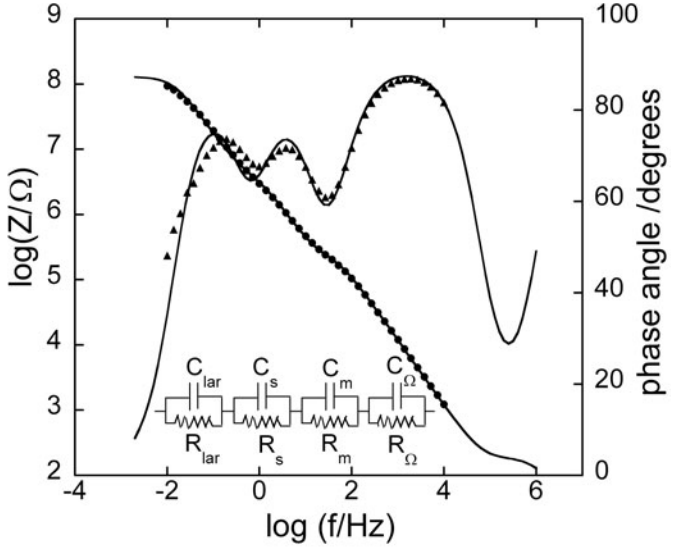

Figure 3. Plot of log$|Z|$ (solid circles) and ϕ (solid triangles) against log f (Bode plot) for a mercury-supported DPTL|DPhyPC bilayer incorporating valinomycin from its 1.5×10^{-7} M solution in aqueous 0.1 M KCl at –0.375 V vs. Ag|AgCl(0.1M KCl).[3] The solid curve is the best fit of the equivalent circuit shown in the figure to the impedance spectrum, with C_{lar}=92 nF, R_{lar}=0.126 GΩ, C_s=20 nF, R_s=0.155 MΩ, C_m=73 nF, R_m=2.2 MΩ, C_Ω=0.95 nF, R_Ω=170 Ω. Drop area= 2.2×10^{-2} cm^2.

Impedance spectra can also be displayed on other types of plots. To justify their use, we must consider that the impedance Z of a single RC mesh is given by:

$$Z^{-1} = R^{-1} - \mathrm{i}\omega C \tag{1}$$

Writing $Z \equiv Z' + \mathrm{i}Z''$, where Z' and Z'' are the in-phase and quadrature components of the impedance Z, and rearranging terms, we obtain:

$$Z' = R/\left(1 + \omega^2 R^2 C^2\right) \tag{2a}$$

$$Z'' = Z'\omega RC \tag{2b}$$

Eliminating ωRC from Eqs. (2a) and (2b) we get:

$$Z''^2 + Z'^2 - RZ' = 0 \rightarrow \left(Z' - R/2\right)^2 + Z''^2 = (R/2)^2 \tag{3}$$

Equation (3) yields a semicircle of diameter R and center of coordinates $(R/2,0)$ on a Z'' vs. Z' plot, called Nyquist plot. Noting that the maximum of this semicircle is characterized by the equality of Z' and Z'', from Eq. (2b) it follows that the angular frequency ω at this maximum equals the reciprocal of the time constant RC of the mesh. In the presence of a series of RC meshes, their time constants may be close enough to cause the corresponding semicircles to overlap partially. In this case, if the mesh of highest time constant has also the highest resistance, R_1, as is often the case, then the Nyquist plot of the whole impedance spectrum exhibits a single well-formed semicircle, R_1 in diameter. The semicircles of the remaining meshes are compressed in a very narrow area close to the origin of the Z'' vs. Z' plot, and can be visualized only by enlarging this area. Therefore, the Nyquist plot of the whole spectrum can be conveniently employed if one is interested in pointing out the resistance R_1 of the dielectric slab of highest resistance. This is apparent in Fig. 4, which shows the Nyquist plot for the tBLM incorporating valinomycin, whose Bode plot is reported in Fig. 3. The whole Nyquist plot displays a single semicircle. However, the enlargement of the initial portion of the plot in the inset

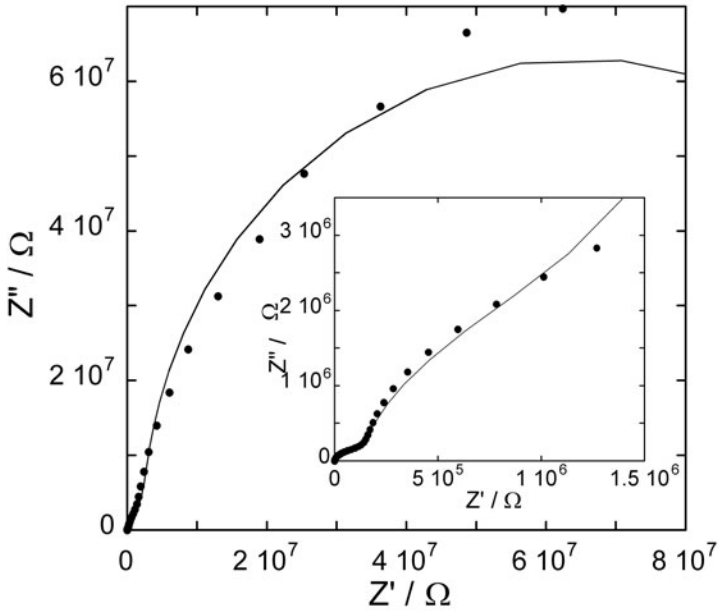

Figure 4. Plot of *Z*'' against *Z*' (Nyquist plot) for the same tBLM as in Fig. 3. The solid curve is the best fit of the equivalent circuit shown in Fig. 3 to the impedance spectrum, obtained by using the same *R* and *C* values. The semicircle in the figure corresponds to the RC mesh of highest time constant and highest resistance, ascribable to the lipoic acid residue. The inset shows an enlargement of the initial portion of the Nyquist plot.

of Fig. 4 reveals the presence of two additional partially fused semicircles.

The solid curve in Fig. 4 is the best fit of the equivalent circuit shown in Fig. 3 to the impedance spectrum. This equivalent circuit consists of a series of four RC meshes, simulating the lipoic acid residue, the tetraethyleneoxy hydrophilic spacer, the lipid bilayer and the aqueous phase bathing the lipid bilayer (see the structure on top of Fig. 2). Note that, in the present case, the combination (lipoic acid residue + hydrophilic spacer) is no longer simulated by a pure capacitance, and the aqueous phase is no longer simulated

by a pure resistance. In fact, even though the lipoic acid residue is the dielectric slab in direct contact with the metal, we cannot exclude a slight ionic flux across it and a resulting high (but not an infinitely high) resistance. Analogously, even though the capacitance of the aqueous phase interposed between the lipid bilayer and the auxiliary electrode is very low, it is not infinitely low, and its inclusion improves the fit.

To better visualize all semicircles, we have found it convenient to represent impedance spectra on a ωZ' vs. ωZ'' plot.[3] Henceforth, this plot will be briefly referred to as an *M plot*, since ωZ' and ωZ'' are the components of the modulus function M. A single RC mesh yields a semicircle even in this plot. Thus, if we multiply both members of Eq. (3) by ω^2 and we combine the resulting equation with Eq. (2b), after simple passages we obtain:

$$\omega^2 Z''^2+\omega^2 Z'^2-\omega Z''/C=0\rightarrow\left(\omega Z''-\frac{1}{2C}\right)^2+(\omega Z')^2=\left(\frac{1}{2C}\right)^2 \quad (4)$$

This is the equation of a semicircle of diameter C^{-1} and center of coordinates $(2/C,0)$ on a ωZ' vs. ωZ'' plot. Moreover, ω at the maximum of the semicircle is again equal to the reciprocal of the time constant RC of the mesh. While ω decreases along the positive direction of the abscissas on a Z'' vs. Z' plot, it increases on a M plot. Therefore, for a series of RC meshes, the last semicircle on the M plot is characterized by the lowest time constant. This is, unavoidably, the semicircle simulating the solution that baths the self-assembled film, due to its very low capacitance. Figure 5 shows the M plot relative to the same impedance spectrum that yields the Bode plot in Fig. 3 and the Nyquist plot in Fig. 4. The solid curve is the best fit of the equivalent circuit in Fig. 3, consisting of four RC meshes in series. Proceeding along the positive direction of the abscissas, the dashed curves express the contribution to ωZ' from each of the four different RC meshes, namely the quantity $\omega g_i/(g_i^2+\omega^2 C_i^2)$, where $g_i=1/R_i$ and C_i are the conductance and capacitance of the i-th mesh. The deviations of the dashed curves from a pure semicircle measure the extent of their overlapping with the neighboring semicircles. The four semicircles overlap only to a moderate extent, thus allowing their straightforward

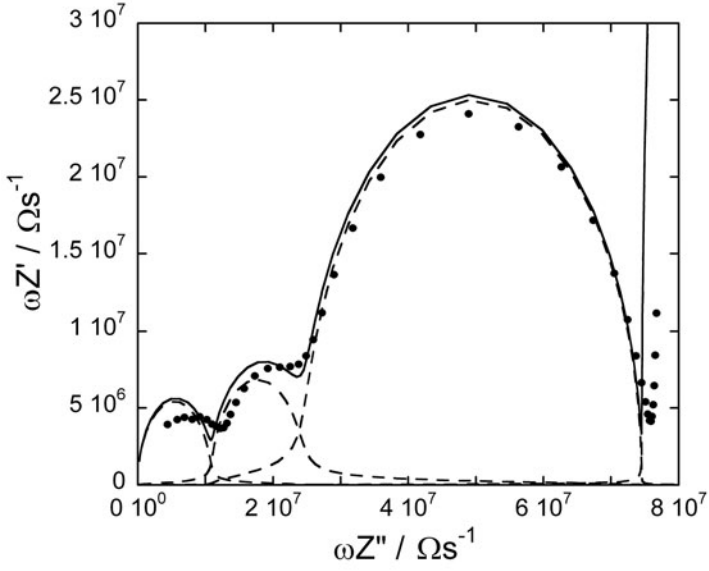

Figure 5. Plot of $\omega Z'$ against $\omega Z''$ (M plot) for the same tBLM as in Fig. 3. The solid curve is the best fit of the equivalent circuit shown in Fig. 3 to the impedance spectrum, using the same R and C values. The dashed curves are the contributions to $\omega Z'$ from the different RC meshes; proceeding along the positive direction of the abscissas, these curves are ascribed to the lipoic acid residue, the tetraethyleneoxy moiety, the lipid bilayer moiety, and the aqueous solution bathing the tBLM.[3]

deconvolution. This is due to an appreciable difference between the time constants of the four RC meshes, which are evenly distributed over a frequency range covering seven orders of magnitude. The capacitance of the solution interposed between the working and the counter electrode is of the order of 1 nF cm^{-2}. If it is disregarded by simulating the aqueous phase by a pure resistance, the contribution of the solution to the M plot is represented by a vertical straight line. As a matter of fact, the radius of the semicircle simulating the solution is not infinitely large, and its curvature is often clearly visible. The RC mesh of the aqueous solution does not depend on the architecture of the tBLM. Hence, the corresponding semicircle can be excluded, at least partially, from the M plot in order to better visualize the contribution from the other

meshes. The M plot permits the agreement between an experimental impedance spectrum and the corresponding fit to a series of RC meshes to be verified in detail. In this respect, it differs from the Bode plot, which is often almost featureless.

A plot that has been frequently adopted in the literature to display an impedance spectrum richer in features than the Bode plot is the Y'/ω vs. Y''/ω plot, sometimes called Cole-Cole plot.[4-6] Here Y' and Y'' are the in-phase and quadrature component of the electrode admittance. However, this plot yields a semicircle for a series combination of a resistance and a capacitance, and not for their parallel combination. Thus, the impedance Z of a RC series is given by:

$$Z = R + \mathrm{i}/(\omega C) \tag{5}$$

Noting that $Y \equiv Y' - \mathrm{i}Y'' = 1/Z$, rearrangement of Eq. (5) yields:

$$Y''/\omega = C/\left(\omega^2 R^2 C^2 + 1\right) \tag{6a}$$

$$Y'/\omega = \omega RC\left(Y''/\omega\right) \tag{6b}$$

Eliminating ωRC from Eqs. (6a) and (6b) we get:

$$\left(\frac{Y''}{\omega}\right)^2 + \left(\frac{Y'}{\omega}\right)^2 - C\left(\frac{Y''}{\omega}\right) = 0 \rightarrow \left(\frac{Y''}{\omega} - \frac{C}{2}\right)^2 + \left(\frac{Y'}{\omega}\right)^2 = \left(\frac{C}{2}\right)^2 \tag{7}$$

On a Cole-Cole plot, this equation yields a semicircle of diameter C and center of coordinates $(C/2,0)$. Here too, from Eq. (6b) it follows that ω at the maximum of the semicircle equals $1/RC$. Strictly speaking, a Cole-Cole plot is not suitable for verifying the fitting of a series of RC meshes to an experimental impedance spectrum. Thus, the admittance of a single RC mesh is given by:

$$\begin{gathered} Y = R^{-1} - \mathrm{i}\omega C \rightarrow Y'/\omega = (\omega R)^{-1} \\ Y''/\omega = C \end{gathered} \tag{8}$$

For a RC mesh to yield a semicircle on a Cole-Cole plot, an equation analogous to Eq. (7) should be satisfied:

$$\left(\frac{Y''}{\omega}-x\right)^2+\left(\frac{Y'}{\omega}\right)^2=x^2 \rightarrow (C-x)^2+\left(\frac{1}{\omega R}\right)^2=x^2 \tag{9}$$

where x is the radius of the semicircle on this plot. Solving this equation yields:

$$x=\frac{C}{2}\left(1+\frac{1}{\omega^2R^2C^2}\right) \tag{10}$$

Consequently, the Cole-Cole plot for a single RC mesh yields a semicircle of diameter C only for ω values high enough to make $\omega^2R^2C^2 >> 1$. Figure 6 shows the Cole-Cole plot for the same impedance spectrum displayed on the Bode, Nyquist and M plots in

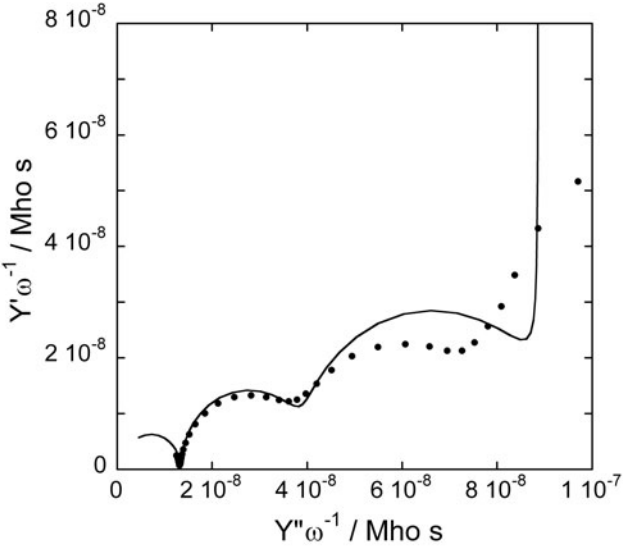

Figure 6. Plot of Y'/ω against Y''/ω (Cole-Cole plot) for the same tBLM as in Fig. 3. The solid curve is the best fit of the equivalent circuit shown in Fig. 3 to the impedance spectrum, using the same R and C values.

Figs. 3, 4 and 5. In a Cole-Cole plot, ω decreases along the positive direction of the Y''/ω axis. It is apparent that the fitting of a series of four RC meshes to the experimental spectrum shows appreciable deviations at the lower frequencies when the spectrum is displayed on a Cole-Cole plot.

An equivalent circuit consisting of a series of RC meshes with relatively close time constants yields calculated semicircles on Nyquist, M or Cole-Cole plots that overlap to an appreciable extent. Such an overlapping resembles a single depressed semicircular arc, namely an arc whose center lies below the horizontal axis. These arcs are often fitted to an equivalent circuit consisting of a parallel combination of a resistance R and of a *constant phase element* (CPE), whose empirical impedance function has the form: $Z_{CPE}=-(i\omega)^{-\alpha}/A$.[7] The hybrid CPE reduces to a pure capacitive impedance, $i/\omega A$, for $\alpha=1$, and finds its justification in a continuous distribution of time constants around a mean. The impedance of this parallel combination, called ZARC, is given by:

$$Z_{ZARC}^{-1} = R^{-1} - (i\omega)^{\alpha} A \rightarrow Z_{ZARC} = \frac{R}{1-(i\omega)^{\alpha} RA} \qquad (11)$$

For $\alpha = 1$, this expression reduces to the impedance of a RC mesh, and A coincides with the capacitance.

The use of ZARC elements for the fitting to impedance spectra of films deposited on satisfactorily smooth supports, such as mercury, seems redundant and difficult to relate to the structure of the film. In this case, a more significant approach is the following. The experimental spectra are fitted by an equivalent circuit consisting of a progressively increasing number of RC meshes in series.[8] The quality of the fitting is conveniently monitored on a M plot. Fitting errors less than 10% for the R and C values of the different RC meshes can be regarded as acceptable. When the addition of a further RC mesh does not determine a detectable improvement in the agreement between experimental and calculated M plots, the fitting error for the added RC mesh is normally found to be close to 100%. The last added RC mesh is, therefore, discarded from the fitting.

IV. FORMATION OF LIPID FILMS IN BIOMIMETIC MEMBRANES

Methodologies for the fabrication of biomimetic membranes vary somewhat from one biomimetic membrane to another. However, a number of experimental procedures for the formation of lipid monolayers and bilayers on solid supports are common to several biomimetic membranes. The most popular procedures are vesicle fusion, Langmuir-Blodgett and Langmuir-Schaefer transfers, and rapid solvent exchange. The formation of lipid monolayers and bilayers on gold and silver substrates is commonly monitored by surface plasmon resonance (SPR). Therefore, a brief description of this surface-sensitive technique seems appropriate.

1. Surface Plasmon Resonance

Surface plasmons are collective electronic oscillations in a metal layer, about 50 nm in thickness, excited by photons from a laser beam.[9] The beam is reflected by the back surface of the metal layer, while its front surface supports a dielectric film (e.g., a lipid bilayer), usually in contact with an aqueous solution. The evanescent electromagnetic field thereby generated in the metal layer can couple with the electronic motions in the dielectric film. The intensity of the electromagnetic field associated with surface plasmons has its maximum at the metal/(dielectric film) surface and decays exponentially into the space perpendicular to it, extending into the metal and the dielectric. This makes SPR a surface-sensitive technique particularly suitable for the measurement of the optical thickness of ultrathin films adsorbed on metals. As a rule, the incident angle of the laser beam is varied with respect to the back surface of the metal layer, and the reflected light intensity is measured. At a certain angle of incidence there exists a resonance condition for the excitation of surface plasmons, which causes the energy of the incident laser light to be absorbed by the surface plasmon modes and the reflectivity to attain a minimum (see Fig. 7).

The angular position of the minimum of the SPR reflectivity curves (i.e., the curves of reflectivity versus incident angle; see Fig. 7b) is critically dependent on the thickness of the layer adsorbed on the support surface. When macromolecules assemble

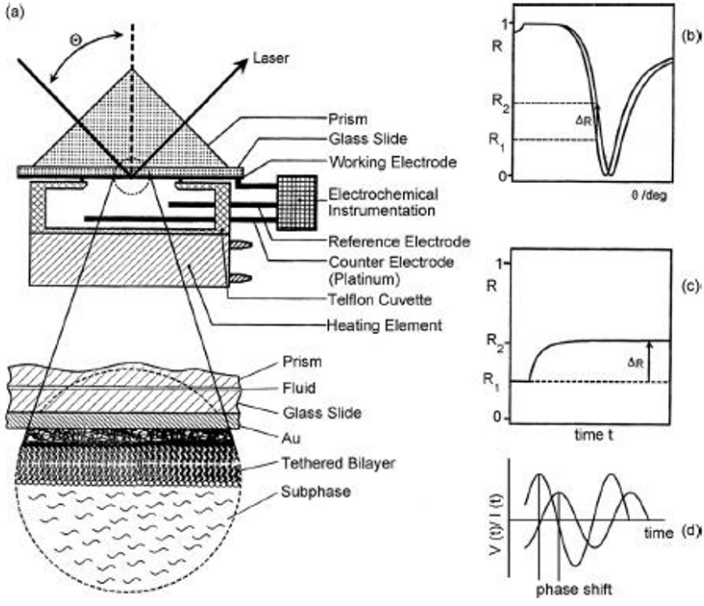

Figure 7. (a) Experimental set-up for surface plasmon resonance measurements, combined with an EIS module for simultaneous SPR and electrochemical measurements on tBLMs. The enlargement shows the solid/solution interface with the thin Au layer used for surface plasmon excitation, and the tethered lipid bilayer in contact with the aqueous phase; (b) typical SPR reflectivity curves before and after the formation of the distal lipid monolayer (on top of the self-assembled proximal tethered lipid monolayer) by vesicle fusion; (c) kinetics of the fusion process recorded by monitoring the change of reflectivity at a fixed angle of incidence as a function of time; (d) time dependence of the small-amplitude a.c. voltage used in EIS measurements and of the resulting a.c. current of equal frequency and different phase angle. (Reprinted from Ref.[9b] with kind permission from Elsevier.)

into a dielectric layer at the metal surface, the reflectivity minimum is shifted to a higher angle. Physical layer thicknesses can be calculated by quantitative modeling of the reflectivity curves using Fresnel's equations. This requires knowledge of the refractive index n and of the film thickness d of each dielectric slab of the multilayer system under investigation. The exact refractive index of the compound forming a layer on the metal surface is unknown; however, reasonable approximations for refractive indices are n=1.45 for proteins and n=1.5 for lipids. Once the refractive indices are established, the layer thickness can be extracted from a comparison between experimental and calculated reflectivity curves. By monitoring the reflectivity at a particular fixed angle of incidence close to resonance, the kinetics of adsorption at the interface can be monitored (see Fig. 7c). The reflectivity at the fixed angle increases in time from its value prior to the adsorption of the molecules, attaining a maximum limiting value when the adsorption process terminates.

At resonance, the interfacial evanescent field is enhanced by a factor of 16 (for a gold/water interface at λ = 633 nm) relative to the incoming light. Its strength is maximal at the metal surface, and decays exponentially normal to the surface with a penetration depth of 150 nm. Surface plasmon fluorescence spectroscopy (SPFS) exploits this large field enhancement to excite fluorophores located within the evanescent field.[10] This feature distinguishes SPFS from total internal reflection fluorescence (TIRF) microscopy, which basically utilizes the same optical excitation geometry but operates without a metal surface and thus with much lower field enhancement. Nonradiative energy transfer (quenching) from the excited fluorophore to a planar gold surface decays with the third power of the distance. In practice, the fluorescence intensity of the fluorophore increases gradually with increasing distance of the fluorophore from the gold layer, until it remains completely unquenched at a distance of about 30 nm.[11] Simultaneous SPR and SPFS analysis allows an estimate of both the thickness of a film and its separation from the substrate surface. Thus, when a lipid bilayer is formed on a gold support by vesicle fusion, this combined analysis may distinguish unambiguously whether vesicles or planar lipid films are adsorbed on the support surface.

Both SPR and EIS allow an evaluation of film thickness, based on a reasonable estimate of the refractive index of the film

in the case of SPR, or of its dielectric constant in the case of EIS. However, it must be borne in mind that the two techniques are sensitive to different features of a film.

2. Vesicle Fusion

Vesicles (or, more precisely, unilamellar vesicles) are spherical lipid bilayers that enclose an aqueous solution. To obtain vesicles, lipids are usually dissolved in an organic solvent. The solvent is then evaporated using a nitrogen stream or vacuum, so that a thin lipid film is produced on the glass surface of a vial. The lipid film is hydrated with an aqueous solution, whose temperature should be above the gel to liquid-crystalline transition temperature of the lipid with the highest transition temperature in the mixture. Giant unilamellar vesicles (GUVs) have a diameter ranging from 1 to 300 μm. They are usually produced by an electroformation approach. Multilamellar vesicles (MLVs) are quickly generated by the general protocol described above. Starting from MLVs, large unilamellar vesicles (LUVs, 100 to 1000 nm in diameter) with a narrow size distribution around a desired value are produced by freeze-thaw cycling the vesicles, followed by extrusion; this consists in pressing the vesicle suspension repeatedly through a membrane of defined pore size. Small unilamellar vesicles (SUVs, 20 to 50 nm in diameter) are prepared by extrusion through membranes with smaller pore size (about 30 nm) or by supplying ultrasound energy to the MLV suspension by using an ultrasonic bath or an ultrasonic probe (sonication).

The procedure for vesicle fusion consists of adsorbing and fusing SUVs on a suitable substrate from their aqueous dispersion. If the substrate is hydrophilic, vesicle fusion gives rise to a lipid bilayer by rupture of the vesicles and their *unrolling* and spreading onto the substrate. Conversely, if the substrate is hydrophobic, a lipid monolayer with the hydrocarbon tails directed toward the substrate is formed by rupture of the vesicles, splitting of the vesicular membrane into its two monomolecular leaflets and their spreading[12], as shown schematically in Fig. 8. This is confirmed by the different thickness change following vesicle fusion on a hydrophobic substrate (2–2.5 nm) with respect to a hydrophilic substrate (4.5–5 nm), as estimated by SPR.[13]

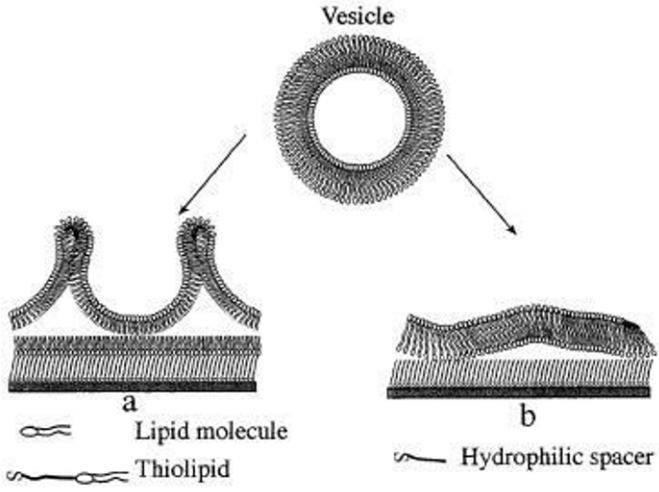

Figure 8. Schematic picture of: (a) splitting and spreading of a vesicle on a solid-supported thiolipid monolayer; (b) unrolling and spreading of a vesicle on a solid-supported hydrophilic spacer.

The kinetics of vesicle fusion, followed by monitoring the position of the minimum of the SPR reflectivity curves, depends on the composition and molecular shape of the vesicular lipids and on the nature of the substrate. As a rule, bilayer formation by vesicle unrolling onto a hydrophilic surface is faster than monolayer formation by vesicle fusion onto a hydrophobic surface. This is probably due to the fact that the processes involved in forming a planar bilayer starting from a vesicular bilayer are considerably less complex than those involved in forming a planar monolayer.[13,14]

The pathway of vesicle fusion on hydrophilic surfaces depends on several factors: the nature of the support (its surface charge, chemical composition and roughness), the nature of the lipid vesicles (their composition, charge, size and physical state), and the aqueous environment (its composition, pH and ionic strength). As a general trend, calcium ions are found to promote the adsorption and rupture of vesicles and lipid bilayer formation.[15] Effects are particularly strong on mica.[16] It has been suggested that the initial rapid stage of vesicle adsorption on hydrophilic surfaces

is controlled by vesicle adsorption at free sites of the surface, according to a Langmuirian type behavior. A second, lower stage is ascribed to vesicle unrolling and spreading processes. It has been proposed that the balance between the gain in adhesion energy (as given by the adhesion area) and the cost in the vesicle curvature energy (as given by the bilayer bending rigidity) is determinant for the adsorption, deformation and rupture of vesicles. Rupture occurs when strong adhesive forces cause the tension in the membrane of a partially fused vesicle to exceed the threshold for disruption of the membrane.[17]

Among hydrophilic substrates, those allowing the formation of lipid bilayers by vesicle fusion more easily are freshly oxidized surfaces of silica, glass, quartz and mica.[18] However, hydrophilicity is a necessary but not a sufficient condition to promote vesicle fusion. Surfaces of oxidized metals and metal oxides (e.g., TiO_2, Pt and Au) allow adsorption of intact vesicles but resist the formation of bilayers, presumably due to weak surface interactions.[19] Electrostatic, van der Waals, hydration and steric forces cause the noncovalently supported lipid bilayer to be separated from the solid surface by a nanometer layer of water.[20] This water layer prevents the support from interfering with the lipid bilayer structure, thus preserving its physical attributes, such as lateral mobility of the lipid molecules.

The quartz crystal microbalance with dissipation monitoring (QCM-D) has proved quite valuable to monitor the macroscopic features of vesicle deposition. A typical QCM sensor consists of a MHz piezoelectric quartz crystal sandwiched between two gold electrodes. The crystal can be brought to resonant oscillation by means of an a.c. current between the electrodes. Since the resonant frequency can be determined with very high precision (usually by less than 1 Hz), a mass adsorbed at the QCM surface can be detected down to a few ng cm^{-2}. At an ideal air/solid interface, there is a linear relationship between an increase in adsorbed rigid mass and a decrease in resonant frequency. The mass obtained from QCM-D measurements corresponds to the total mass coupled to the motion of the sensor crystal, including the mass of the adsorbed biomolecules and of the solvent bound or hydrodynamically coupled to the molecular film. This feature distinguishes mass measurements by QCM-D from those by SPR. In fact, the measured SPR signal originates from altered conditions for resonant

surface plasmon excitation due to changes in the interfacial refractive index. For a simple dielectric material there exists, as a first approximation, a nearly linear relationship between the change in refractive index caused by biomolecule adsorption and the number of biomolecules at the interface; on the other hand, SPR is practically insensitive to the presence of water molecules. Hence, the mass sensed by a QCM exceeds that estimated by SPR by the amount of water molecules bound or dynamically coupled to the adsorbed biomolecules. However, the dissipation monitoring of the QCM-D allows a distinction between lipid layers and loosely bound water molecules in adsorbed vesicles. In fact, under shear stress, lipid layers behave more elastically (or, differently stated, less viscously) than adsorbed vesicles, coupling strongly to the motion of the crystal surface. Conversely, adsorbed vesicles are substantially larger and less compact structures filled with water; moreover, water is also trapped between the vesicles and the surface. Consequently, vesicles are subject to larger deformations under shear stress. These viscoelastic features are invisible by simple resonance frequency determination. Viscoelasticity can, however, be visualized by measuring the energy loss, or dissipation (D) of the shear movement of the crystal in water. The dissipation D is measured by driving the crystal with a.c. current at the resonant frequency, followed by disconnection and analysis of the resulting damped sinusoidal oscillations. This dissipation parameter allows a distinction between intact, adsorbed vesicles (high dissipation) and lipid bilayer patches (low dissipation). Figure 9 shows the changes in resonance frequency (Δf) and in dissipation (ΔD) under different situations. If vesicles do not adsorb, no change in f or D takes place (Fig. 9A). If vesicles adsorb and remain intact, forming a supported vesicular layer, their high mass causes an appreciable frequency decrease, and also a high dissipation (Fig. 9B). If vesicles are initially adsorbed, but subsequently fuse forming a water-free lipid bilayer of lower mass, Δf shows a minimum before attaining a constant limiting value, while ΔD shows a maximum (Fig. 9C). Figure 9D exemplifies the case in which the vesicles adsorb and rupture instantaneously. Combined measurements by QCM-D and SPR have shown that isolated vesicles of egg-phosphatidylcholine (egg-PC) remain intact when bound to a silica support; a minimum critical vesicle coverage is required to initiate the conversion of surface-bound vesicles into

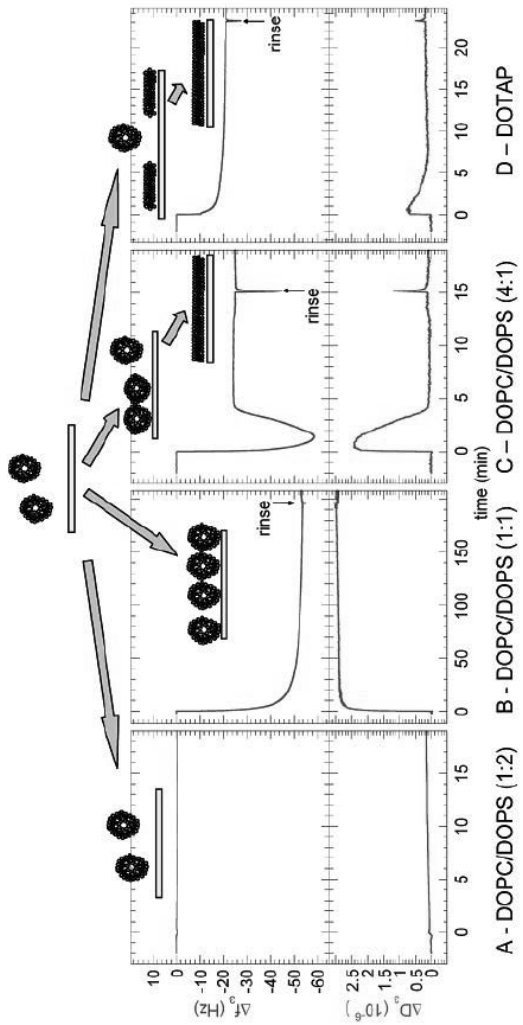

Figure 9. Lipid deposition pathways measured by QCM-D on silica. The legends indicate the lipids used: dioleoyltrimethylammonium-propane (DOTAP), dioleoylphosphatidylcholine (DOPC), and dioleoylphosphatidylserine (DOPS), with their molar mixing ratios. (Reprinted from Ref.[24] with kind permission from the American Chemical Society.)

lipid bilayer patches.[21] Use of the QCM-D permitted to confirm the formation of lipid bilayers on silica and of lipid monolayers on gold-supported alkanethiol monolayers by vesicle fusion, and the adsorption of intact vesicles on oxidized gold.[22]

Atomic force microscopy (AFM) has provided further direct evidence that silica can indeed be covered by isolated vesicles that remain stable for days.[23] Conversely, when adsorbing vesicles at low surface density on mica, they initially remain intact but rupture individually over a time interval ranging from minutes to hours.[16] The particularly smooth surface of mica imparts to vesicles and bilayer patches a certain lateral mobility, not to be confused with that of single lipid molecules. Thus, laterally mobile bilayer patches on mica tend to reshape into circular patches to minimize their line tension. Conversely, bilayer patches on silica frequently retain a strong irregular shape, providing evidence for lack of mobility. A satisfactory lateral mobility accelerates the formation of a complete lipid bilayer coating. In fact, the edges of lipid bilayer patches are thermodynamically unstable, and tend to interact with adjacent lipid material, e.g., by rupturing surface-bound vesicles or by coalescing with other bilayer patches.[24]

Initial adsorption of vesicles on hydrophobic surfaces is energetically disfavored, due to the presence of the hydrophilic polar heads on the outer surface of the vesicular membrane. Therefore, the vesicular membrane must split to allow its inner hydrophobic tails to get in contact with the hydrophobic surface. A possible pathway for vesicle fusion involves vesicle splitting, unrolling and spreading on the hydrophobic surface, as shown in Fig. 8a. The kinetics of vesicle fusion on the hydrophobic surface of gold-supported alkanethiol self-assembled monolayers was followed by SPR.[25] In the initial stage, the adsorbed layer thickness d increases linearly with the square root of time t, denoting control by vesicle diffusion to the surface according to Fick's first law. In a second stage, d increases roughly linearly with log t. Finally, the time dependence of d becomes typical of an adsorption process on an almost fully occupied surface. The curve of the surface coverage by vesicles against time was also monitored by SPR at different vesicle concentrations;[12] it was fitted to an equation practically identical with that derived for an electrode process controlled by diffusion and by a heterogeneous electron transfer step[26]. The resulting kinetic constant was ascribed to some surface reorganization of the

vesicles. The final increase in thickness following vesicle fusion amounts to 2.0–2.5 nm, as expected for a lipid monolayer, provided the vesicle concentration is not too high.[14]

When forming planar lipid monolayers and bilayers by vesicle fusion, the problem of vesicle mere adsorption or partial fusion on the substrate should be considered. When vesicles fuse spontaneously on a support, some of them may remain only partially fused, or even intact in the adsorbed state. When the surface density of vesicles is sufficiently high, their presence is revealed by an anomalously high thickness attained by the lipid film after vesicle fusion, as monitored by SPR. This phenomenon is particularly evident with supports consisting of mixtures, with comparable molar ratios, of two different molecules exposing to the bulk aqueous phase hydrophobic alkyl chains and hydrophilic functional groups, respectively.[6,27] With very high vesicle concentrations (5 mg/mL), monolayer thicknesses greater than 8 nm were reported on hydrophobic surfaces.[14] Thus, fusion of small unilamellar vesicles (SUVs) onto a binary mixture of hydrophobic cholesteryl-terminated molecules and hydrophilic 6-mercaptohexanol molecules yields AFM images showing heightened areas; their diameter being close to that of the SUVs denotes the presence of adsorbed vesicles.[4] The presence of a membrane protein, such as *cytochrome bo3*, in these vesicles increases the number density and the size of the heightened structures ascribable to adsorbed vesicles. Analogously, fusion of large unilamellar vesicles (LUVs) on a hydrophobic support exposing dipalmitoylphosphatidylethanolamine (DPPE) alkyl chains to the aqueous phase yields tapping-mode AFM (TM-AFM) images with a number of dome-shaped structures.[28] Some of these structures, whose diameter is close to that of the LUVs, tend to disappear after one hour, due to vesicle complete fusion. However, if the vesicles contain the membrane protein Na,K-ATPase, all the domelike structures are stable even after three hours. In general, adsorption of proteoliposomes (namely, vesicles incorporating membrane proteins) on hydrophobic surfaces prevents their complete spreading and fusion, due to the presence of protein molecules with extramembrane domains and to the hydrophilicity of the outer polar heads of the proteoliposomes.[15,29]

The presence of heightened areas in metal-supported lipid films formed by fusion of vesicles labeled with a fluorophore can

also be monitored by fluorescence microscopy. In fact, the energy of a photoexcited fluorophore is transferred nonradiatively to the metal support (quenching), if the fluorophore is at a distance from the metal surface shorter that a critical transfer distance (the Foerster radius). This critical distance amounts to about 20–30 nm for gold. Therefore, unquenched bright spots in the fluorescence microscopy images of gold-supported lipid films obtained by fusion of fluorophore-labeled vesicles mark the presence of heightened areas ascribable to adsorbed or hemifused vesicles.[30]

3. Langmuir-Blodgett and Langmuir Schaefer Transfer

Another procedure for forming a lipid monolayer on a hydrophobic substrate or a lipid bilayer on a hydrophilic substrate makes use of a Langmuir trough equipped with a movable barrier. By spreading a lipid dissolved in an organic solvent on the surface of the aqueous electrolyte contained in the trough and by allowing the solvent to evaporate, a lipid film is formed at the air/water interface. This film is compressed with the movable barrier until it is brought in proximity of the liquid crystalline state by adjusting the surface pressure. To form a lipid monolayer on a hydrophobic slab, this is immersed vertically through the lipid monolayer. This brings the hydrocarbon tails of the lipid monolayer, turned toward the air, in direct contact with the hydrophobic surface of the slab, which remains coated by a lipid monolayer (see Fig. 10A). This technique, called Langmuir-Blodgett (L-B) transfer, is also used to form a lipid bilayer on a hydrophilic slab.[31,32] In this case, the slab is initially immersed vertically through the lipid monolayer into the trough. No significant change in surface pressure is observed at this stage. The slab is then withdrawn at a speed slow enough to permit water to drain from the surface. During the withdrawal, the polar heads of the lipid monolayer are turned toward the surface of the hydrophilic slab, giving rise to noncovalent self-assembly (see Fig. 10B). The resulting decrease in the surface pressure of the lipid monolayer at the air/water interface is prevented by reducing its area with the moving barrier. A further lipid monolayer is then self-assembled on top of the first one by the so-called Langmuir-Schaefer (L-S) transfer. In practice, the lipid-coated slab is brought into horizontal contact with the lipid monolayer at the air/water interface, after compressing it at a preset surface pressure. Finally,

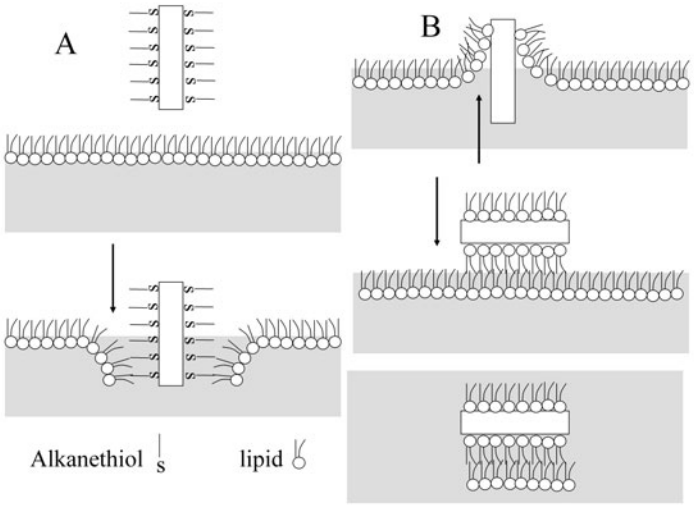

Figure 10. (A) Formation of a lipid monolayer on a hydrophobic alkanethiol-coated slab by Langmuir-Blodgett transfer; (B) Formation of a lipid bilayer on a hydrophilic slab by Langmuir-Blodgett transfer and subsequent Langmuir-Schaefer transfer.

the slab covered by the lipid bilayer is detached from the aqueous subphase. The combination of the L-B and L-S transfers is used principally for lipid bilayer deposition on hydrophilic surfaces of glass, mica, quartz, polymeric materials, graphite and, to a minor extent, on metals such as gold.[33]

An advantage of L-B and L-S transfers over vesicle fusion is that the strict composition of a mixed lipid monolayer on the trough surface is maintained after its transfer. Conversely, the composition of a mixed lipid layer on a substrate does not necessarily correspond to that of the vesicles used to form it, and varies strongly with the history of the sample preparation. On the other hand, an advantage of vesicle fusion over L-B and L-S transfers is that vesicles may easily incorporate membrane proteins, forming proteoliposomes. To this end, membrane proteins are usually stabilized in detergent micelles and then incorporated into the lipid vesicles upon removing the detergent molecules by dialysis. Fusion of proteoliposomes on a metal-supported thiolipid monolayer may

then cause the insertion of the membrane proteins in the resulting lipid bilayer.

4. Rapid Solvent Exchange

A further procedure for depositing a lipid monolayer is the *rapid solvent exchange*. This method is usually employed to self-assemble a lipid monolayer onto a hydrophobic surface exposing alkyl chains to the bulk aqueous phase. The method involves placing a small amount of lipid dissolved in a water miscible solvent, such as ethanol, onto the hydrophobic substrate and incubating it for a few minutes.[34,35] The ethanol solution is, then, vigorously displaced in a few seconds by a large excess of an aqueous buffer solution, taking care to avoid the formation of air bubbles at the surface. During the lipid addition and the subsequent rinsing with the aqueous solution, the lipid self-assembles to form a lipid monolayer and the lipid in excess is rinsed away.

5. Fluidity in Biomimetic Membranes

A fundamental property of biological membranes is the long-range lateral mobility of the lipid molecules. The fluidity of the plasma membrane, interposed between the cytosol and the extracellular space, should be preserved in supported biomimetic membranes. Free movement of lipid molecules enables the biomimetic membrane to react to the presence of proteins, charges and physical forces in a dynamic and responsive manner. A satisfactory fluidity allows biomimetic membranes to reorganize upon interaction with external perturbations, mimicking the functionality of living cell membranes. In particular, lateral mobility enables a biomimetic membrane to incorporate large membrane proteins from their detergent solutions by making space for them; it also determines the spontaneous separation of the components of a lipid mixture (demixing), giving rise to the formation of important lipid microdomains, called lipid rafts.

The fluidity and lateral mobility of biomimetic membranes can be characterized quantitatively by AFM[23] and fluorescence microscopy. Fluorescence recovery after photobleaching (FRAP) is one of the most popular ways of measuring molecular diffusion in membranes.[36] It relies on introducing a small amount of fluores-

cent probe molecules, usually covalently bound to lipids, into the membrane. A short burst of intense excitation light is projected onto the membrane, destroying the fluorescence of the fluorophore molecules in a well defined spot, a photochemical process called photobleaching. The gradual fluorescence recovery within the given spot is followed as a function of time, thus permitting an estimate of the lipid diffusion coefficient. In supported membranes, this coefficient typically ranges from 1 to 10 $\mu m^2\ s^{-1}$. When applied to lipid bilayers self-assembled on smooth supports such as silica, glass, quartz, mica or indium tin oxide (ITO), FRAP usually confirms a satisfactory lateral mobility of lipid molecules.[18,37] Conversely, biomimetic membranes consisting of a thiolipid monolayer tethered to a gold electrode, with a self-assembled lipid monolayer on top of it, does not exhibit lateral mobility. This is also true for the distal lipid monolayer noncovalently linked to the thiolipid monolayer, no matter if obtained by vesicle fusion or by Langmuir-Schaefer transfer.[6,30] A biomimetic membrane consisting of a hydrophilic spacer tethered to gold, with a lipid bilayer formed on top of it, was reported to exhibit fluorescence recovery after photobleaching, if the noncovalently bound lipid bilayer was formed by Langmuir-Blodgett and Langmuir-Scheafer transfers.[6] Fluorescence recovery in the gold-supported biomimetic membrane could only be observed for a short period of time, due to the gradual energy transfer from the fluorophore molecules to gold (quenching). No fluorescence recovery could be observed by forming the lipid bilayer on top of the hydrophilic spacer by vesicle fusion. Evidently, the unavoidable presence of adsorbed and hemifused vesicles prevents lateral mobility of the lipid molecules of the distal monolayer. The strict connection between the presence of adsorbed vesicles and the lack of lateral mobility allows conclusions on lateral mobility to be drawn by monitoring the presence of adsorbed vesicles by a QCM-D.

Electrostatic interactions between vesicles and support play an important role in vesicle fusion. Thus, variously charged gold-supported mixed monolayers of alkanethiols ω-functionalized with the neutral -OH group, the positive $-NH_3^+$ group or the negative $-COO^-$ group induce the fusion of oppositely charged vesicles, as monitored by FRAP.[38] Conversely, the fusion of vesicles made of neutral, zwitterionic lipids takes place only if the charge of the mixed functionalized alkanethiols exceeds a minimum value; this

is explained by electrostatic attraction between the charge of the mixed thiols and the oppositely charged end of the dipole of the zwitterionic lipid molecules.

As distinct from solid supports, such as gold or silver, mercury imparts lateral mobility to lipid monolayers directly self-assembled on its surface, thanks to its liquid nature. This is demonstrated by rapid spontaneous phase separation, with microdomain formation, in a lipid monolayer self-assembled on top of a DPTL thiolipid monolayer tethered to a mercury microelectrode.[39] The presence of microdomains was directly verified from the images of the distal lipid monolayer by using two-photon fluorescence lifetime imaging microscopy (2P-FLIM).

V. THE VARIOUS TYPES OF BIOMIMETIC MEMBRANES

In examining the various types of biomimetic membranes, we will first consider simple experimental models consisting of a single lipid monolayer, self-assembled either on mercury or on an alkanethiol monolayer tethered to a metal electrode. Subsequently, biomimetic membranes comprising a lipid bilayer will be examined, in the order of approximately increasing complexity.

1. Mercury Supported Lipid Monolayers

A simple and easily prepared biomembrane model obtained by noncovalent self-assembly consists of a phospholipid monolayer supported by a hanging mercury drop electrode. The use of a lipid-coated mercury electrode as a biomimetic membrane was introduced by Miller[40] and subsequently adopted in a modified version by Nelson.[41] The lipid coating is obtained by spreading a solution of the lipid in pentane on the surface of an aqueous electrolyte, allowing the pentane to evaporate and immersing a hanging mercury drop electrode in the electrolyte. This procedure gives rise to a lipid monolayer, with the hydrocarbon tails directed toward the hydrophobic mercury surface and the polar heads directed toward the solution. The defect-free support provided by liquid mercury to the lipid monolayer and the complete absence of pentane in the film impart high mechanical stability, resistance to electric fields

and reproducibility to the monolayer. This self-assembly procedure exploits the fact that mercury is the most hydrophobic metal. This by no means implies that mercury has no affinity for the oxygen of water; in fact, at the potential of zero charge, the water molecules adsorbed on bare mercury are slightly oriented with the oxygen turned toward mercury, although less than on all other metals.[42] However, as the adsorbing lipid molecules have to decide where to turn their hydrophilic polar head to attain a minimum in their adsorption free energy, they choose to turn it toward the aqueous phase, where the polar head can form hydrogen bonds with the adjacent water molecules.

Thanks to the liquid state of the mercury support, this simple biomembrane model is fluid and allows lateral mobility of the lipid molecules. However, it has no hydrophilic ionic reservoir on the metal side of the lipid film, and consists of a single lipid monolayer. Consequently, it is not suitable for the study of the function of integral proteins. It can be used to investigate the behavior of the polar heads of the lipid monolayer with varying pH, the behavior of small lipophilic biomolecules incorporated in the lipid film and that of peripheral redox proteins adsorbed on the film surface.

Over the potential region of minimum capacitance, which ranges from –0.15 to –0.75 V/SCE, the film is impermeable to inorganic metal ions, whereas it becomes permeable outside this region. The differential capacitance C of a lipid monolayer on mercury over this region is about 1.7–1.8 μF cm^{-2}, namely twice the value for a solvent-free black lipid membrane (BLM). At positive potentials the region of minimum capacitance is delimited by a capacitance increase that precedes mercury oxidation; at negative potentials it is delimited by two sharp peaks that lie at about –0.9 and –1.0 V/SCE (peaks 1 and 2 in Fig. 11) and by a third peak at about –1.35 V/SCE in the case of DOPC. Peaks 1 and 2 of DOPC are capacitive in nature and are due to field induced two-dimensional phase transitions. The third peak in Fig. 11 exhibits hysteresis in the reverse potential scan[41,43] and is due to partial desorption of the lipid. Complete desorption takes place at potentials negative enough to cause a merging of the curve of the differential capacitance C against the applied potential E recorded on lipid-coated mercury with that obtained on bare mercury, under otherwise identical conditions.

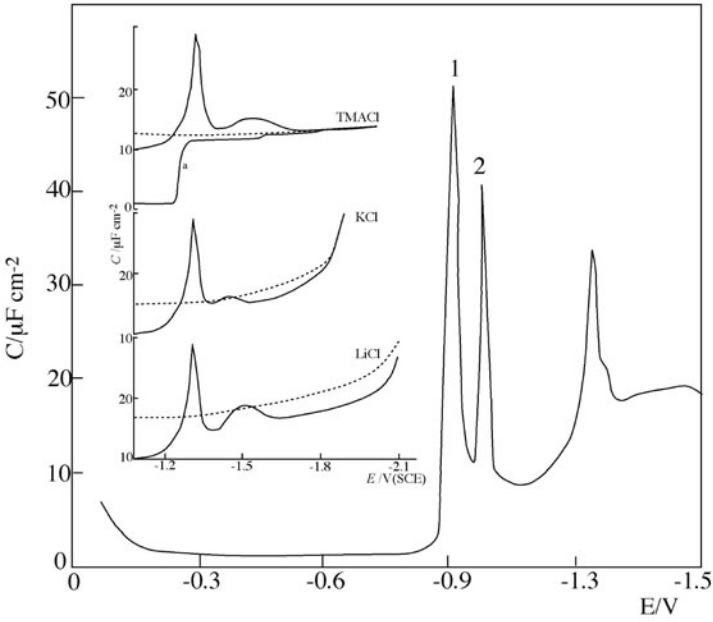

Figure 11. Curve of the differential capacitance *C* against potential *E vs.* SCE for DOPC-coated mercury in aqueous 0.1 M KCl. The inset shows *C* vs. *E* curves for bare (dashed line) and DOPC-coated (solid line) mercury in 0.1M solutions of tetramethylammonium (TMA) chloride, KCl and LiCl.[44]

At the far negative potentials at which lipid desorption is complete, the lipid molecules remain in close proximity of the mercury surface for hours in the form of positively charged micellar aggregates, and spread back readily on the electrode surface with a positive shift in potential.[44,45] This desorption/re-adsorption process was imaged by using epi-fluorescence microscopy and including a small amount of an amphiphilic fluorescent dye molecule in the lipid monolayer.[46] On a Hg electrode, as distinct from a Au electrode, fluorescence can be detected even if the fluorophore is at a small distance from the electrode. In fact, the fluorescence quenching efficiency, due to nonradiative energy transfer to the electrode, is by two to three orders of magnitude lower on Hg than on Au. Upon scanning the potential progressively in the negative

direction up to film desorption, the fluorescence intensity maintains a constant low level along the flat capacitance minimum; a large increase in fluorescence is observed at far negative potentials, indicating a separation of the lipid monolayer from the electrode surface. By scanning back the potential, the fluorescence decreases slowly down to the positive potential limit; however, neither the fluorescence nor the capacitance recovers the pristine value, denoting a defective reformed monolayer. In contrast to a similar system on gold[47], the fluorescent particles or aggregates on Hg are freely mobile, preventing an image analysis yielding their number density and size.

As a rule, incorporation of neutral hydrophobic organic compounds, such as polynuclear aromatic hydrocarbons,[48] polychlorinated biphenyls and phenothiazine,[49] into DOPC monolayers on Hg causes a negative shift and a depression of peaks 1 and 2; this is often accompanied by a slight decrease in the differential capacitance minimum. This effect becomes more pronounced with an increase in the aromaticity and hydrophobicity of the compound. Thus, while the effect of benzene and naphthalene is negligible, it becomes appreciable with hydrocarbons with three, four or five aromatic rings.[50] Hydrophobicity alone, as measured, say, by the octanol/water partition coefficient, is not sufficient to explain this effect; thus, undecane and dodecane have a high partition coefficient but no observable effect on lipid monolayers. The slight decrease in the flat capacitance minimum which is often observed with an increase in the bulk concentration of these compounds is probably to be ascribed to a thickening of the film following their incorporation in the lipid monolayer; this should more than compensate for the expected increase in capacitance stemming from the higher dielectric constant of aromatic compounds compared to that, $\cong 2$, of the lipid tails. The concomitant decrease in the height of the reorientation peaks 1 and 2 and their broadening is due to a decrease in the cooperativity of the reorientation of the lipid molecules, caused by the intercalation of the foreign molecules.

Phospholipid-coated mercury electrodes have been used to measure the intrinsic protonation constants of DOPC, dioleoylphosphatidylethanolamine (DOPE), dioleoylphosphatidylserine (DOPS)[51] and dioleoylphosphatidic acid (DOPA),[52] the surface dipole potential of DOPC, DOPS and DOPA,[53] as well as the change in the dipole potential of DOPS and DOPA with a change

in the charge density of the polar heads of these phospholipids[54] and upon adsorption of certain anti-tumor drugs.[55] These investigations were conducted by measuring the differential capacitance C and the charge density $\sigma_M$of lipid-coated mercury at a special homemade hanging mercury drop electrode.[56] In particular, σ_M was measured by contracting a lipid-coated mercury drop while keeping its neck in contact with the lipid reservoir spread at the water/argon interface, so as to allow a free exchange of lipid material between the lipid monolayer that coats the mercury drop and the lipid film spread on the aqueous solution.[57] This procedure ensures that the thickness and all other properties of the lipid monolayer remain unaltered during the contraction. The charge following the contraction divided by the decrease in drop area yields directly the charge density σ_M on the mercury surface. The experimental data were analyzed on the basis of a model of the membrane/solution interphase that accounts for the presence of charged ionizable groups either exposed to the aqueous phase or buried well inside the polar head region.[51] The behavior of DOPS was found to be particularly involved, with its phosphate group buried somewhere inside the polar head region, and the carboxyl and ammonium groups exposed to the aqueous phase. It was concluded that the overall charge density of a DOPS monolayer varies from slightly negative to slightly positive values as the bulk pH of the bathing solution is varied from 7 to 4.[54] Generalizing this model to account for the expansion of a lipid-coated Hg drop completely immersed in an aqueous solution and for the resulting tilt in the self-assembled phospholipid molecules, the dipole potentials of DOPS and DOPC monolayers were estimated at +140 – +150 mV, positive toward the interior of the film. The fact that these monolayers have very similar dipole potentials indicates that this dipole potential is not to be ascribed to the serine or choline group of their polar heads, but rather to a group common to these two lipids and buried deeper inside the polar head region. This can be reasonably identified with the glycerol backbone.

The effect of lipophilic ions on the capacitance minimum of lipid-coated mercury may be summarized as follows. If the compound is simply *adsorbed* on top of the lipid monolayer or intercalated between the polar heads, it does not affect the tail region, whose capacitance C_t is much less than that of the head region and close to that, C_m, of the whole lipid monolayer. In this case the

capacitance, C_c, of the film of the compound will be in series with C_m, causing a decrease in the overall capacitance $C \cong (C_m^{-1} + C_c^{-1})^{-1}$. In general, this decrease is low, because the polarizability of the compound (and, hence, its C_c value) is higher than that of the lipid tails. While remaining merely adsorbed in the polar head region, the compound may also determine a condensation and an increase in the alignment of the lipid monolayer, resulting in its thickening and in a decrease in capacitance. On the other hand, if the compound penetrates the hydrocarbon tail region, the fraction θ of the electrode surface covered by the compound will have a capacitance C_c higher than that, C_m, of the pure lipid domains. As a rough approximation and disregarding any edge effects at the boundary between the two different domains, the overall capacitance is given by $C = \theta C_c + (1 - \theta)C_m$ and is, therefore, higher than that of the pure lipid film. The cationic phenothiazine derivatives cause a moderate increase in the capacitance minimum.[49,58] The anionic diuretic furosemide causes an initial slight decrease in the capacitance minimum at low bulk concentrations[59] and then an increase at higher concentrations.[58,59] This may indicate that these anions start interacting with the polar heads at low concentrations, before penetrating the tail region at higher concentrations. All these ions depress and broaden peaks 1 and 2, just as neutral compounds. The cationic antibiotic polymyxin narrows the minimum capacitance region on the negative side and decreases the capacitance minimum by about 0.35 μF cm^{-2}.[60] This indicates that this peptide does not penetrate the hydrocarbon tail region.

Lipoproteins are molecular aggregates that transport water-insoluble lipids in the blood plasma: they contain a core of neutral lipids, coated with a monolayer of phospholipids in which special proteins (apolipoproteins) and cholesterol are embedded. The interaction of apolipoprotein A-I with DOPC-coated mercury proceeds in steps when increasing progressively its bulk concentration, $c_{A\text{-}I}$.[61] For $c_{A\text{-}I} \leq 4$ μg cm^{-3} the differential capacitance minimum C is not affected, but the concomitant decrease in the orientation peaks of DOPC points to an interaction of apoA-I with the polar heads of the lipid, possibly electrostatic, through its hydrophilic amino acids. With a further increase in $c_{A\text{-}I}$ the plot of C versus $c_{A\text{-}I}$ shows a first sigmoidal step, with a plateau at ~ 4 μF cm^{-2},

which is then followed by a further sigmoidal step, with a plateau at ~ 7.5 μF cm^{-2}. These C versus $c_{A\text{-}I}$ steps correspond to two consecutive penetration steps into the hydrocarbon tail region, probably associated with two different conformational changes of apoA-I. 10 mol % cholesterol in the DOPC monolayer suppresses the second penetration step, while 25 mol % suppresses both steps. This may be explained by the cholesterol molecules rigidifying the lipid monolayer, thereby preventing it from associating with some penetrating domains of apoA-I.

Small lipophilic ions such as tetraphenylphosphonium ($TPhP^+$) and tetraphenylborate ($TPhB^-$) prefer to be located in the polar head region ($x = \beta$) and in direct contact with the electrode surface ($x = 0$) rather than in the much less polarizable intermediate hydrocarbon tail region. We can therefore envisage two potential energy wells for these ions at $x = 0$ and $x = \beta$, with a potential energy barrier in between.[62] The charge involved in a potential step from a value negative (positive) enough for the anion (the cation) to be entirely located at $x = \beta$ to a value positive (negative) enough to induce a complete translocation of the ion to $x = 0$, once decreased by the charge involved in the same potential step in the absence of the incorporated ion, yields directly the opposite of the charge density of the ion in the lipid film. This procedure allowed the determination of the adsorption isotherms of the $TPhP^+$ and $TPhB^-$ ions in DOPC and DOPS monolayers.[62] In interpreting these isotherms, discreteness-of-charge effects were considered.

6-Ketocholestanol (KC), a steroid that differs from cholesterol mainly by the presence of a carbonyl group, was reported to form pores inside a mercury-supported DOPC monolayer by a mechanism of nucleation and growth similar to that of a number of channel-forming peptides.[63] The potential steps responsible for pore formation by KC molecules give rise to the potentiostatic charge vs. time curves shown in Fig. 12, whose sigmoidal shape reveals two consecutive two-dimensional phase transitions. The first phase transition is ascribed to an increase in the alignment of the KC dipoles along the direction of the interfacial electric field, with the oxygen of the carbonyl group more fully turned toward the aqueous solution. The increase in differential capacitance from 1.2 to 6.5 μF cm^{-2} observed over the potential range between the two phase transitions is ascribed to the first phase transition giving rise

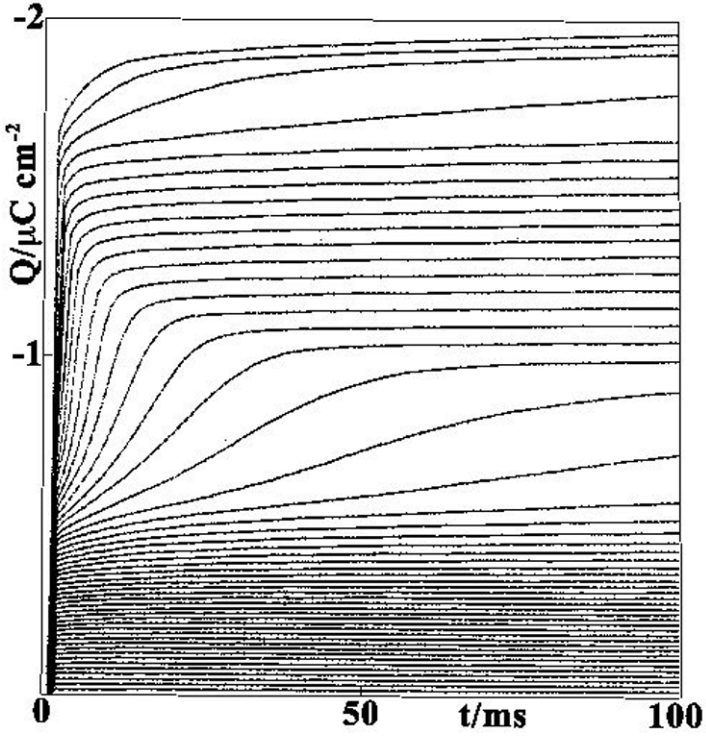

Figure 12. Charge vs. time curves following a series of potential steps from a fixed initial potential E_i= –0.250 V/SCE to final potentials E varying by –10 mV increments from –0.250 to –0.750 V on a mercury electrode coated with a lipid monolayer consisting of 67 mol% DOPC + 33 mol% 6-ketocholestanol and immersed in aqueous 0.1 M KCl.[63]

to bundles of KC molecules, with the oxygens turned toward the interior of the bundles. In these hydrophilic pores the inorganic ions can move back and forth following the a.c. signal, causing an increase in differential capacitance. The decrease in differential capacitance from 6.5 to 1.8 μF cm^{-2} after the second phase transition suggests that this transition involves the disruption of the pores and a return to a random distribution of DOPC and KC molecules within the mixed monolayer. The permeability of the lipid film to Tl^+ ions induced by the first phase transition, and its abrupt decrease induced by the second phase transition, support the formation and subsequent disruption of pores across the lipid monolayer.

Ubiquinone-10 (UQ) is an important, ubiquitous biomolecule that is present in many membranes and acts as a proton and electron carrier in the respiratory chain of the mitochondrial membrane. It consists of a quinone ring, which can be reduced to the corresponding quinol, and is provided with a long, rigid isoprenoid chain imparting a high affinity for lipids. The mechanism of its reduction inside a phospholipid monolayer supported by mercury was investigated by carrying out a series of consecutive potential steps from a fixed initial value E_i, where UQ is still electroinactive, to progressively more negative potentials, E_f, and by measuring the charge $Q(t,E_f)$ following each step, as a function of both time t and potential E_f.[64] The faradaic charge, $Q_f(t,E_f)$, was obtained by subtracting the capacitive charge measured in the absence of UQ from $Q(t,E_f)$. From the linear dependence of E_f upon log t, at constant $Q_f(t,E_f)$ and pH, and upon pH, at constant $Q_f(t,E_f)$ and t, it was concluded that UQ electroreduction to ubiquinol, UQH_2, takes place via a one-electron transfer in quasi equilibrium, followed by the rate-determining uptake of a proton; this rate determining step is followed by the rapid uptake of a further electron and a further proton, yielding UQH_2. The generic chronocoulometric procedure employed for UQ was also adopted to study the electrochemical behavior of dioactadecylviologen[65] and of vitamine K_1,[66] an essential constituent for blood coagulation, upon incorporating these molecules in a self-assembled DOPC monolayer supported by mercury.

Ion channels are responsible for the flow of hydrophilic ions across biomembranes along their electrochemical potential gradient, namely from the membrane side where the electrochemical

potential of the ion is higher to that where it is lower (passive transport). A widely investigated ion channel is gramicidin, a linear pentadecapeptide with helical structure that turns its hydrophobic groups toward the exterior of the helix and its hydrophilic carboxyl groups toward the interior. The length of a gramicidin channel is of 1.3 nm, about one half the thickness of a biomembrane. To span a biomembrane, two helical monomers of gramicidin form a helical dimer, with the N-terminuses of the dimer interacting in the center of the membrane. The resulting hydrophilic pore allows the transport of monovalent cations, such as alkali metal ions, across the membrane. The monomer of gramicidin incorporated in a mercury-supported phospholipid monolayer was reported by Nelson to act as an ion channel toward Tl^+ ion, thus allowing its penetration across the monolayer and its electroreduction to thallium amalgam.[67-71] From a cyclic voltammetric and a chronoamperometric investigation of Tl^+ ion electroreduction through the gramicidin channel, Nelson proposed a Chemical-Electrochemical (CE) mechanism, in which the rate-determining step is a preceding homogeneous chemical step associated with Tl^+ entry into the channel, prior to Tl^+ electroreduction.[69,70] This electrode process at a mercury-supported phospholipid monolayer incorporating gramicidin was employed by Nelson as a model system to probe the effect of lipid charge, solution composition and incorporation of biologically active compounds on ion channel transport. Thus, it was shown that a negatively charged DOPS monolayer increases the rate of Tl^+ transport with respect to a neutral DOPC monolayer, while polyvalent cations, such as Mg^{2+} and Dy^{3+}, have an opposite effect.[70] This is ascribed to the electrostatic interaction of this charge with Tl^+ ions in the immediate vicinity of the lipid film, with a resulting influence on their local concentration. The behavior of the same system by potential-step chronocoulometry was interpreted by Becucci et al.[72] on the basis of a mechanism that includes the diffusion of thallous ions toward the lipid film and a potential-independent heterogeneous step consisting of the dehydration of the ion and its binding to a site located at the mouth of the ion channel. The further step involving the surmounting of a potential energy barrier located somewhere in the middle of the channel is considered to be in quasi-equilibrium, and hence its potential dependence is of the Nernstian type. Rueda and coworkers[73], by investigating this system by EIS, postulated an additional

homogeneous chemical step mimicking the deactivation and release of a Tl^+-gramicidin intermediate from the electrode surface, in competition with the surmounting of the potential energy barrier located within the channel.

Two lipophilic neutral molecules are commonly incorporated into membranes with the aim of altering their dipole potential, namely phloretin, which creates a dipole potential negative toward the interior of the lipid film, and 6-ketocholestanol, which creates a dipole potential positive toward the interior, due to the presence of a carbonyl group.[74,75] As expected, incorporation of phloretin in the lipid monolayer containing gramicidin has no effect on the kinetics for thallous ion reduction.[72] In fact, the favorable dipole potential created by phloretin, negative toward the interior of the film, cannot accelerate the overcoming of the potential energy barrier more than predicted by a Nernstian-type behavior. Conversely, the unfavorable dipole potential, positive toward the interior of the film, created by incorporating 23 mol % 6-ketocholestanol in the DOPC monolayer, slows down this intermediate step by increasing the height of the potential energy barrier within the ion channel. This leads to a decrease in the rate constant for the surmounting of the barrier, which has the typical Butler-Volmer dependence upon the applied potential.[72]

2. Alkanethiol-Lipid Hybrid Bilayers

Great interest has been focused on self-assembled films that are attached to a solid support by formation of a covalent linkage between the self-assembled molecules and the solid support, yielding structures of long-term, mechanical stability. Monolayers of alkanethiols on gold are probably the most widely used and best characterized of all self-assembled films to date. Self-assembly involves the anchoring of the thiol to the gold surface through the sulfhydryl group, often accompanied by its deprotonation and electron transfer from the sulfur atom to the metal. The hydrocarbon chains are, therefore, directed toward the aqueous solution. The self-assembly is normally carried out by keeping the electrode immersed in an ethanol solution of the thiol from 12 to 24 hr for Au or Ag and from 5 to 20 min for Hg.

The deposition of a phospholipid monolayer on top of an alkanethiol monolayer tethered to gold can be accomplished by sev-

eral different preparation techniques, by exploiting the attractive hydrophobic interactions between the hydrocarbon tails of the alkanethiol and those of the phospholipid. The most common procedure for lipid deposition onto alkanethiol monolayers is vesicle fusion. The architecture of the mixed alkanethiol/lipid bilayer, in which the lipid forms a well-ordered, non-interdigitated monolayer on the alkanethiol, with its polar heads directed toward the aqueous solution, was confirmed by surface enhanced Raman spectroscopy (SERS), reflection absorption infrared spectroscopy (RAIRS), neutron reflectivity and EIS. A dipalmitoylphosphatidylcholine (DPPC) monolayer on top of a gold-supported alkanethiol monolayer in air was found by RAIRS to be highly ordered, with 95% of all-trans conformers.[76] SERS indicates that short chain alkanethiols, which are relatively disordered, are more affected by addition of a phospholipid monolayer than longer chain alkanethiols. Neutron reflectivity in D_2O of a DPPC/octadecanethiol bilayer on Au yields a scattering length density (SLD) profile that was fitted to a model of three layers: the sulfur layer, a hydrocarbon layer consisting of the alkyl chains of both the alkanethiol and DPPC, and the polar head region of DPPC.[77] At 60°C, where DPPC is in the liquid crystalline state, the thickness of the hydrocarbon layer region equals 3.3 nm, and that of the polar head region equals 1.0 nm. However, the flat minimum of the SLD profile, corresponding to a totally unhydrated region, is only about 2.2 nm wide, because the polar head region, which is estimated to contain 10 water molecules per DPPC molecule, is also significantly hydrated. AFM images of the gold-supported hybrid bilayer provide clear evidence that the phospholipid monolayer on top of the alkanethiol monolayer is substantially complete and homogeneous. Electrochemical impedance spectra of alkanethiol/phospholipid bilayers on gold have been analyzed with an equivalent circuit consisting of a capacitance C_{hb}, simulating the hybrid bilayer, with in series the resistance R_Ω of the aqueous solution.[25,78] By considering the capacitance C_t of the thiol monolayer in series with that, C_m, of the phospholipid monolayer, C_{hb} is given by $C_tC_m/(C_t + C_m)$. Upon measuring independently the differential capacitance C_t of the sole thiol monolayer on gold, the above equation allows an estimate of C_m. For a palmitoyloleoylphosphatidylcholine (POPC) monolayer on top of an octadecanethiol monolayer tethered to gold, C_m amounts to about

1.8 μF cm^{-2}, in good agreement with values obtained both at solvent-free black lipid membranes (BLM) and at an octadecanethiol/DOPC bilayer self-assembled on a hanging mercury drop electrode.[79] The latter hybrid bilayer is readily prepared by first immersing the mercury drop for one or two minutes in a thiol solution in ethanol; the phospholipid monolayer on top of the alkanethiol monolayer is then obtained by immersing the thiol-coated mercury drop into an aqueous solution on whose surface a phospholipid film has been previously spread.

Solid-supported alkanethiol/phospholipid bilayers are unsuitable for incorporation of channel-forming peptides and membrane proteins, because they do not fulfill the requirements listed in Section II. Thus, no hydrophilic layer is interposed between the hybrid bilayer and the electrode surface, thus excluding the space and water required for the proper folding of the extramembrane domains of integral proteins. Moreover, the flexibility and fluidity of the chemisorbed alkanethiol monolayer in direct contact with the electrode is much less than that of BLMs; this lack of flexibility and fluidity makes these mixed bilayers practically impermeable to lipophilic molecules of biological importance, such as ubiquinone-10 and vitamin K_1, and to lipophilic ions.[79] The kinetics of inorganic redox couples exhibiting a Nernstian behavior on bare gold is almost completely suppressed by hybrid alkanethiol/lipid bilayers for alkanethiol chains with more than eight carbon atoms, pointing to an assembly that provides a substantial barrier to electron transfer and to hydrophilic ions.[79,80] Electron tunneling across these films takes place only at very high overpotentials.

The polypeptide melittin is the major component of the venom of the honey bee. This peptide carries five positive charges. From its aqueous solutions, melittin binds spontaneously to biomembranes and BLMs. At low concentrations, it induces voltage-gated channels in BLMs, while at concentrations higher than 1.2 μg/mL it causes their disruption.[81-84] When bound to lipid bilayers, melittin adopts a highly α-helical conformation, with most hydrophobic residues on one side and most hydrophilic residues on the opposite side of the helix long axis. At zero transmembrane potential, these amphipathic helices accumulate on the surface of the membrane, parallel to the plane of the bilayer. As the transmembrane potential is made negative on the opposite side of the membrane with respect to melittin, the helices form membrane-spanning aggregates

that induce pore conductance. Addition of melittin to a gold-supported alkanethiol/phospholipid bilayer increases the faradaic current for ferricyanide electroreduction, rendering it practically identical with that observed across the sole alkanethiol monolayer;[78,84] this suggests that melittin may permeate the fluid lipid monolayer, but not the underlying alkanethiol monolayer.

The integral protein cytochrome *c* oxidase (COX) spans the inner mitochondrial membrane and is the terminal component of the respiratory electron-transport chain. It catalyzes the redox reaction between the small peripheral protein cytochrome *c* in its reduced form, i.e., ferro-cytochrome *c*, and oxygen, with formation of ferri-cytochrome *c* and water; it also pumps protons from the matrix to the intermembrane space, where it interacts with ferro-cytochrome *c*. COX was reported to retain its functional redox activity after incorporation in a gold-supported hybrid octadecanethiol/lipid bilayer from its detergent solution.[85] Thus, the cyclic voltammogram of COX in this hybrid bilayer yields an oxidation and a reduction peak whose peak potentials are practically equidistant from the known standard potential of the cytochrome a_3 redox site of this enzyme. However, this result was obtained by choosing thiol concentrations and experimental conditions allowing the formation of large uncovered areas of the gold electrode, where COX could partition into the hybrid bilayer during the dialysis procedure. This system was subsequently improved by monitoring the exact amount of octadecanethiol required for the formation of a thiol submonolayer, using a quartz crystal microbalance.[86] Moreover, gold was replaced by silver as the substrate. The Ag-S bond being stronger than the Au-S bond was considered to increase the stability of the membrane. In addition, the fact that the alkyl chains of the tethered thiol molecules are less tilted on silver than on gold was believed to favor a closer approach of the enzyme to the electrode surface. The cyclic voltammogram of COX incorporated in the silver-supported hybrid bilayer shows an oxidation peak much higher than the reduction one. This was ascribed to a nonfaradaic charge flowing during the positive voltage scan, as a consequence of a conformational transition allowing ion movement into and out of the hybrid bilayer.

Alkanethiol-coated electrodes may be usefully employed for adsorbing membrane fragments whose proteins retain their normal activity. Thus, erythrocyte ghosts, i.e., fragments of the plasma

membrane obtained by osmotic lysis of erythrocyte cells, are readily adsorbed on alkanethiol-coated gold.[87] The thickness of the adsorbed erythrocyte membrane, as measured by ellipsometry, SPR and AFM, ranges from 3 to 4 nm. This is not an unreasonable estimate for the thickness of a single leaflet of the erythrocyte membrane, in view of the presence of transmembrane proteins, which are expected to contribute to the total thickness of the layer. Acetylcholinesterase, an erytrocyte marker enzyme associated with the outer leaflet of erythrocyte cells, retains its activity on this alkanethiol/erythrocyte hybrid bilayer for at least eight days. The fact that the enzyme binds to the outer leaflet of the erythrocyte membrane supports the view that the ghost membrane splits and spreads onto the thiol SAM exposing the outer leaflet to the bulk solution, as depicted in Fig. 8a. Alkanethiol-coated gold was also used to adsorb antigens for screening antibody production.[88,89] Usually, epitopes, i.e., peptide sequences representing the major antigenic sites of the antigen, are adsorbed onto the alkanethiol monolayer by vesicle fusion or by Langmuir-Blodgett transfer, thus creating a structured antigen-bearing surface. Antibodies raised against the peptide sequence show notable preferential binding to the peptide-covered part of the surface. The resulting increase in the thickness of the gold-supported film is followed by SPR. This procedure can also be used for studying receptor-ligand binding events. Thus, for instance, the enzyme pyruvate carboxylase, which catalyzes the carboxylation of pyruvate, requires the coenzyme biotin for catalytic activity. Biotin is a small molecule covalently bound to a lysine residue at the active site of the enzyme. Avidin is a protein that can bind biotin very tightly, making it unavailable for its function as a coenzyme. Lipid vesicles containing a biotinylated phospholipid are fused onto alkanethiol-coated gold. Injection of neutravidin gives rise to specific biotin-neutravidin interactions. The resulting increase in film thickness is again followed by SPR.[89]

Annexin A1 is a protein that reversibly binds to cellular membranes in a Ca^{2+}-dependent manner. It was adsorbed on a POPC:(palmitoyloleoylphosphatidylserine = POPS) (4:1) lipid monolayer assembled by vesicle fusion on an octanethiol monolayer tethered to the gold surface of a QCM.[91] Adsorption of annexin A1 to this hybrid bilayer in the presence of Ca^{2+} ions was monitored by the decrease in resonance frequency. No adsorption

was observed in the absence of Ca^{2+} ions, nor even in their presence, if the POPC-POPS mixture was replaced by pure POPC. This indicates that annexin A1 requires the simultaneous presence of a negatively charged membrane and Ca^{2+} ions to interact with membranes. The adsorption isotherm of annexin A1 to POPC:POPS (4:1) was found to satisfy the Langmuir isotherm and its association constant was determined at different Ca^{2+} ion concentrations.

3. Bilayer Lipid Membranes (BLMs)

An important advance in biomembrane methodology was established when Mueller et al.[92] reported a method for forming planar bilayer lipid membranes separating two aqueous phases. According to this method, a lipid solution in a nonpolar solvent such as decane is spread beneath an aqueous phase across an aperture several millimeters in diameter drilled through a partition (septum) of some hydrophobic material such as Teflon. This procedure for forming the lipid bilayer is called the *painting method*. The spontaneous organization of the amphiphilic lipid molecules into a bilayer is driven by the strong self-association of water molecules, which inhibits the mixing of water and amphiphile. Strong lateral intermolecular forces between the long hydrocarbon tails of the lipid molecules also contribute to this self-assembly. The layer of the lipid solution in the nonpolar solvent becomes gradually thinner, with rainbow interference colors appearing on it, followed by black spots; finally, the whole layer becomes completely black. The blackening marks the transition of the lipid layer from a multimolecular to a bimolecular film, called bilayer (or black) lipid membrane (BLM), which is a non-reflecting optically black film. The resulting system consists of a lipid bilayer in quasi equilibrium with an annulus of lipid solution in the nonpolar solvent, called torus or Plateau-Gibbs border, which forms a transition zone between the bilayer and the septum. This system has been studied extensively as a model for the lipid bilayer of cell membranes. Nonetheless, its usefulness has been questioned, because the thin lipid film contains solvent molecules dispersed within the bilayer and in the form of microlenses floating in the bilayer.[93-97] To what extent the presence of the organic solvent limits the usefulness of

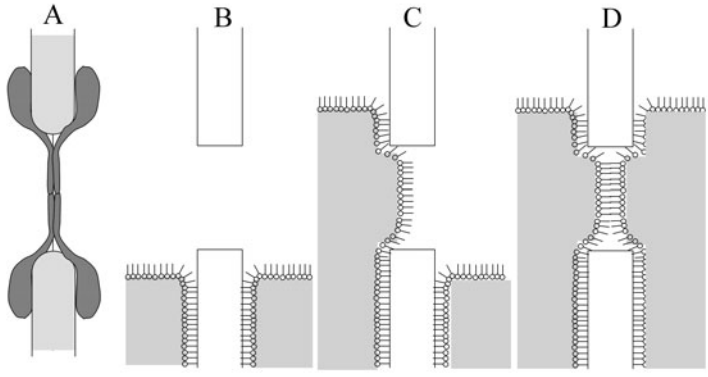

Figure 13. (A) Schematic picture of the cross-section of a black lipid membrane obtained by the painting method, with the Plateau-Gibbs border. (B-D) Preparation of the Montal-Mueller bilayer lipid membrane by raising the solution level on the left hand side of the aperture and, then, on its right hand side.

these BLMs has not been established, but it is clearly important to be able to form solvent-free planar bilayers.

A method for forming bilayers from lipid monolayers that eliminates solvent was developed by Montal and Mueller.[98]. Two polytetrafluoroethylene troughs containing an aqueous solution are separated by a thin (6.5–25 μm) septum through which a hole, 0.1–0.5 mm in diameter, is punched above the solution level. A lipid monolayer is spread from a pentane or hexane solution on each aqueous solution. After the solvent has evaporated, the water level is raised above the aperture first in one trough, and then in the other, bringing the alkyl chains of the monolayers into apposition (see Fig. 13). The Montal-Mueller technique is a particularly significant achievement because asymmetric bilayers can be formed[99] and proteins can be incorporated by first introducing them into the lipid monolayers.[100] The differential capacitance of this solvent-free BLM amounts to 0.8÷0.9 μF cm^{-2},[98] and it is higher than that, about 0.3÷0.4 μF cm^{-2}, of a BLM obtained by the painting method.[101] Evidently, the presence of organic solvent in the latter BLM decreases its differential capacitance.

BLMs have been extensively employed as matrixes for the incorporation of integral proteins, photoactive pigments and biomolecules involved in biophysical, biochemical and physiological studies. A major drawback of BLMs is their fragility, high sensitivity toward vibrations and mechanical shocks, and low resistance to electric fields; thus, they hardly last more than eight hours and collapse under potential differences (transmembrane potentials) greater than 100–150 mV between the solutions that bath the two sides of the BLM; moreover, they do not lend themselves to investigations with surface-sensitive techniques.

A simple procedure for forming BLMs was recently described by Poulos et al.[102] A squalene:decane (2:1) mixture containing 1% DPhyPC is added to a 1 M KCl aqueous solution in a small glass vial. Thanks to its immiscibility with water and its lower density, the organic solvent floats on the aqueous phase. In half an hour, a lipid monolayer is spontaneously formed at the organic/aqueous interface, with the polar heads turned toward the aqueous phase. A 1 μL droplet of an aqueous solution is then dropped into the organic phase, reaching by gravity the organic/aqueous interface without fusing with the aqueous phase. The lower, flattened portion of the droplet surface in contact with the lipid monolayer becomes rapidly coated by a lipid bilayer. Finally, an Ag/AgCl wire is immersed into the droplet, allowing the closure of the electric circuit via a further reference electrode immersed in the aqueous phase. This system allowed the recording of single channel currents of gramicidin, alamethicin and α-hemolysin.

Recently, attempts have been made to form more robust lipid bilayers (often referred to as *planar free-standing bilayers*) by spanning them over nanopores interposed between two aqueous and/or hydrogel phases. These free-standing bilayers have a fluidity probably comparable with that of biological membranes, thus imparting lateral mobility to lipid molecules and membrane proteins. The observed thirty times increase in stability by reducing the pore size by a factor of four demonstrates the benefit from using nanopores. Besides stabilizing lipid bilayers, small apertures increase the signal-to-noise ratio to an appreciable extent. Peptides and small channel-forming proteins insert spontaneously into these preformed bilayers. Bulky membrane proteins are incorporated either by fusion of proteoliposomes to preformed bilayers or by direct fusion of proteoliposomes to nanopores. Little is known

about the influence of nanopores on the fusion of proteoliposomes of similar size.

By comparing free-standing bilayers on Teflon chips with pore diameters ranging from 25 to 250 μm, the capacitance was found to be about equal to 0.6 μF cm^{-2}, a value typical of solvent-containing BLMs.[103] These bilayers were stable for many hours even at applied voltages up to 400 mV. The ion-channel activity of alamethicin and α-hemolysin could be recorded with a high signal-to-noise ratio, by using low-noise patch-clamp amplifier technology. Evans' group reported a device consisting of a 100 μm micromachined hole in a gold surface suspended over an aqueous reservoir. An octadecanethiol[104] or perfluorothiol monolayer[105] was tethered to the gold surface, to impart a hydrophobicity similar to that of the bilayer-forming solution to the hole rim. A lipid bilayer was then painted across the aperture with a plastic stick. Incorporation of the channel-forming peptides gramicidin and alamethicin allowed the recording of their single-channel activities.

Polycarbonate membranes commercially used for ultrafiltration are a porous material, with irregularly arranged pores of uniform size of about 1 μm. Favero et al.[106] covered one side of the membrane with a gold layer that was subsequently hydrophobized by tethering an alkanethiol monolayer on top of it. After gently dropping an egg-PC solution in *n*-hexane on the gold-coated side of the polycarbonate membrane, free-standing bilayers were spontaneously formed in the pores. By incorporating gramicidin D, the following order of increasing conductance, $NH_4^+ > K^+ >> Li^+$ was verified, in accordance with the known selectivity coefficients of this peptide. By setting up an apparatus allowing continuous conductance measurements under flowing conditions, the same authors[107] tested the functional activity of an ionotropic glutamate receptor incorporated in this microarray of BLMs. By injecting 0.1 μM glutamate in the flowing solution and by then removing it with pure buffer, a notable increase in conductance was recorded, followed by a return to the initial low value. Enhancement in conductance by injecting the coagonist glycine, and conductance suppression by injecting the antagonist Mg^{2+} ions, were verified. Although the feasibility of functional assays for membrane proteins was demonstrated, ultrafiltration membranes have a number of limitations. Thus, the stability of these membranes is about 10 h

with 25% cholesterol; the achieved sealing of about 10 MΩ cm^2 is too low for sensitive measurements;[108] the pore distribution is random, resulting in merged pores that may affect the bilayer stability; the membrane is about 10 nm thick, with a resulting high *aspect ratio* (i.e., pore size to membrane thickness); the stability of coated gold on polymer carbonate may be too low for continuous use.

Nanoporous alumina membranes with highly ordered pores of 60 and 280 nm in diameter have been frequently used by Steinem and coworkers to support free-standing lipid bilayers. In their earlier work, a differential capacitance of about 1 μF cm^{-2} was obtained for bilayers formed by fusing giant vesicles on nanopores of 30 and 50 nm diameter.[109] In a further development, the nanoporous alumina supports were coated with gold, and 1,2-dipalmitoyl-*sn*-glycero-3-phosphothioethanol was tethered to its surface via its thiol group.[110] The gold surface so hydrophobized favors the spanning of lipid bilayers across the nanopores of the alumina membrane, upon painting its gold-coated side with a DPhyPC solution in *n*-decane. The membrane was clamped between two Teflon half-cells. The formation of lipid bilayers in this *nano-bilayer lipid membrane* (nano-BLM) was followed by measuring the differential capacitance of the membrane by EIS up to the attainment of its maximum limiting value. The impedance spectra were fitted to an RC mesh, simulating the lipid bilayer, with the solution resistance R_Ω in series with it. Upon regarding the resistance of the thiol-coated gold much higher and its capacitance much lower than those of the pores, the resistance and capacitance of the whole membrane were referred exclusively to the active area of the pores, yielding a specific capacitance of 0.5–0.6 μF cm^{-2} and a specific resistance of up to 0.16 GΩ cm^2. As opposed to the membrane capacitance, the membrane resistance strongly depends on the quality of the preparation and the age of the nano-BLM. What is important for recording single channel currents by a low-noise patch-clamp amplifier is the resistance R_m of the whole nano-BLM, which must be higher than 1 GΩ to reduce the background electrical noise to the order of 1–2 pA. R_m decreases gradually in time, due to the progressive rupture of the individual lipid bilayers spanning the single pores. This gradual decrease in resistance causes a progressive increase in the current baseline, but the back-

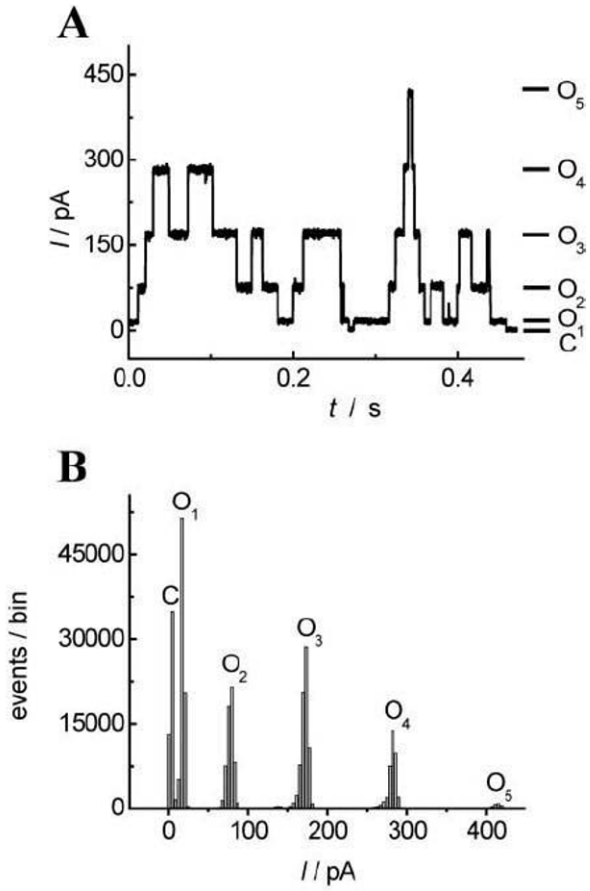

Figure 14. (A) Representative current trace showing single pore fluctuations induced by alamethicin. The nano-BLM was symmetrically bathed in 0.5 M KCl and a holding potential of 70 mV was applied. Data were filtered at 1 kHz. The whole burst of fluctuations is due to a single pore event, fluctuating between conductance levels O_1–O_5. O_1 = 16.4 pA; O_2 = 79.1 pA; O_3 = 171.7 pA; O_4 = 281.6 pA; O_5 = 415.2 pA. C = 3.0 pA reflects the current baseline with the channel closed. (B) Corresponding current amplitude histogram. (Reprinted from Ref. [110] with kind permission from Elsevier.)

ground noise remains low enough to allow the monitoring of single channel currents, provided R_m is maintained above 1 GΩ. From a statistical analysis, the lifetime of nano-BLMs with resistance higher than 1 GΩ was estimated at 1.5 days. Single channel currents of gramicidin, alamethicin[110] (see Fig. 14) and OmpF porin[111] were recorded, and the corresponding current amplitude histograms were reported.

OmpF porin is an integral membrane protein located in the outer membrane of *Escherichia coli.* It is a non-specific transport channel that allows the diffusion of small, polar molecules (600–700 Da in size) through the cell outer membrane, where it forms a trimer. The characteristic conductance states of the three OmpF monomers could be observed with the nano-BLM. Fast openings and closures of a single monomer, superimposed on the slow kinetics of the channel, was also recorded. Moreover, the blockade of the ion flow as a result of interaction of the antibiotic ampicillin with OmpF porin was verified. These experiments show that single channel currents of bulky proteins, such as OmpF porin, whose cross-sectional area amounts to about 80 nm^2, can be monitored using nano-BLMs with highly ordered pores of 60 nm in diameter. These nano-BLMs were also used to record the photocurrents generated by purple membrane fragments adsorbed on the lipid bilayers spanning the micropores.[112] Purple membranes from *Halobacterium salinarium* are very rich in the proton pump bacteriorhodopsin, which pumps protons from the cytoplasmic to the extracellular side of the bacterium membrane upon photoactivation by green light. The purple membrane fragments were added to the compartment exposing the gold-coated side of the alumina membrane. After their adsorption on the lipid bilayers spanning the nanopores and their illumination, the purple membrane fragments with the extracellular side facing the lipid bilayers cause protons to translocate through the proton pump. This movement generates a current transient that decays with a characteristic decay time; the current tends to a nonzero stationary value, revealing a small permeability of the nano-BLM to protons. Addition of the lipophilic proton ionophore CCCP increases the level of the stationary current by facilitating the diffusion of protons pumped by bacteriorhodopsin across the lipid bilayer.

Silicon nitride membranes with 800 nm pores arranged in regular arrays were hydrophobically functionalized, and bilayers were

then formed in the pores by the painting method.[113,114] The stability of these free-standing bilayers was found to depend on the nature of the lipid. Bilayers formed from the cylindrically shaped phosphatidylethanolamine exhibit a membrane resistance higher than 1 GΩ for more than one week, while those formed from DPhyPC remain above this threshold value for two days. Bilayers of the naturally occurring soy PC mixtures are stable for only about 2 h, but a reduction of the pore size from 800 to 200 nm increases their stability by a factor of 30. Membrane sheets with a well-defined orientation were transferred onto a regular array of holes, 50-600 nm in diameter, in a silicon nitride chip, 100–500 nm thick.[115] By pressing the chip against a supported layer of cultured cells and by then removing it, the cells rupture and membrane fragments remain attached to the chip, spanning the holes. The chip was integrated into a microfluidic chamber suitable for optical imaging.

Tien et al.[116] devised a biomimetic membrane formed at the end of a salt-bridge tubing. Briefly, a freshly cut salt-bridge tubing attached to the end of a Ag/AgCl(KCl) reference electrode is firstly dipped into an alkane solution of the lipid and then transferred into an aqueous solution, so as to form a lipid bilayer. In this case, the hydrophilic surface required for bilayer formation is provided by the freshly cut agar gel containing KCl. The resistance of these supported BLMs is usually irreproducible from one membrane to another. More recently, replacing water by a hydrogel as a hydrophilic medium has permitted to achieve a notable increase in stability of lipid bilayers in micropores. Thus, for instance, a lipid bilayer formed across a Teflon aperture was protected with a layer of photopolymerized poly(ethylene glycol) dimethacrylate, and proteins were incorporated by allowing them to diffuse slowly through the previously formed gel.[117] Covalent conjugation of the lipid bilayer to the encapsulating hydrogel was found to increase preservation of the lipid-containing solvent reservoir (the Plateau-Gibbs border) surrounding the membrane, thereby extending the membrane lifetime. To further reduce the flow of organic solvent away from the Plateau-Gibbs border, the Teflon septum was replaced by a glass cover slide where a 500 μm hole was drilled.[118] The hydrophilic glass surface was made hydrophobic by functionalizing it with 3–methacryloxypropyltrimethoxysilane, to provide cross-linkable vinyl groups on the glass surface. In this way, the hydrogel precursor could covalently bind to the vinyl groups of the

silane-coated glass substrate during the process of hydrogel polymerization, sealing the solvent annulus. This allowed the capacitance of the membrane to maintain its value of about 0.4 μF cm^{-2}, typical of a solvent-containing bilayer, for 12 days. In a different approach, a lipid bilayer was protected on both sides by precast gel slabs, and the electrical properties of nicotinic acetylcholine receptor[119] and of the peptides valinomycin and gramicidin[120] were examined, upon incorporating them in the bilayer. An appreciable decrease in the noise level was achieved by Kang et al.[121] by fabricating a chip in which a bilayer containing a single α-hemolysin channel was incapsulated by forming an agarose gel around it. A Teflon septum with a 100 μm diameter aperture was clamped between the cis and trans compartments of a chamber. A buffer solution in liquid agarose at 45°C was added to both compartments, maintaining the liquid level below the orifice of the septum. After spreading a DPhPC solution in pentane on the surface of the liquid agarose and allowing pentane to evaporate, the agarose level in the two compartments was raised by adding further warm agarose solution. By adopting this Montal and Mueller procedure (cf. Fig. 13), a lipid bilayer was obtained with a capacitance of 0.8-1 μF cm^2, typical of a solvent-free bilayer. The subsequent insertion of a preformed heptameric α-hemolysin channel into the lipid bilayer was monitored by an abrupt current jump. The chamber was then cooled to allow the agarose to form a gel, and the single nanopore chip was cut away from the chamber. The chip was stable and storable for at least three weeks at 4°C and endured mechanical disturbance.

With BLMs, the transmembrane potential can be readily adjusted and varied by applying a given potential difference across two identical reference electrodes (say, two Ag/AgCl electrodes) immersed in the bulk solutions bathing the two sides of the membrane. This procedure is not usually applicable to vesicles, due to their small size. However, a sophisticated and elegant electrophysiological technique, called *patch-clamping*, allows an ultramicropipette, whose tip has an inner diameter of a few micrometers, to penetrate both cells[122] and giant unilamellar vesicles (GUVs). The ultramicropipette contains an electrolyte solution with a reference Ag/AgCl electrode inside, while an identical reference electrode is immersed in the external solution. This allows the trans-

membrane potential to be measured and varied at will. Other widely employed biomembrane models are unilamellar lipid vesicles (also called liposomes). Due to their small size, they cannot be studied by electrochemical techniques. Rather, they can be investigated by spectroscopic techniques using fluorescent or spin labeled molecular probes. Electrical methods are used to apply square wave electric field pulses to cell suspensions, for the investigation of pore formation in biomembranes induced by electric fields (electroporation).[123]

In an effort to overcome the drawbacks of BLMs, more robust biomimetic membranes have been fabricated, by immobilizing lipid bilayers on solid surfaces. They are normally obtained by self-assembly, which can be driven exclusively by noncovalent, hydrophobic interactions or with the additional contribution of covalent linkages. In spite of notable improvements in this direction, some major problems of solid supported membranes arise when attempting to use them for analytical applications; the very small space between the bilayer and the support (from 2 to 10 nm) is rapidly saturated by the transported species. This makes quantitative dynamic measurements difficult.

4. Solid Supported Bilayer Lipid Membranes (sBLMs)

The term *solid supported bilayer lipid membrane* (sBLM) or, simply, *solid supported membrane*, is commonly used to denote a biomimetic membrane consisting of a lipid bilayer in direct contact with a solid support. These biomimatic membranes are typically formed on a hydrophilic solid support by immersing it in an aqueous dispersion of small unilamellar vesicles (SUVs), which slowly rupture and spread on the surface of the support. Alternatively, they can be formed by Langmuir-Blodgett and Langmuir-Schaefer transfers. When appropriately formed, these sBLMs are separated from the support surface through a water layer, estimated between 6 and 15 Å thick.[124,125] Several theoretical and experimental investigations of water near polar hydrophilic surfaces suggest that it is more ordered than bulk water, with higher viscosity and lower dielectric constant.[126,127] In accordance with these predictions, the characteristics of the lipid bilayer have been found to be structurally coupled with the support properties, such as its charge[128], wettability[129] and topography[130]. Frictional or electrostatic coupling be-

tween the support and at least the proximal leaflet of the lipid bilayer may induce undesirable asymmetries in compositional, structural, mechanical and dynamic properties of the lipid bilayer.[131] The lubrification effect of the water layer imparts a significant long-range lateral mobility to the lipid bilayer. However, significant frictional coupling between the bilayer and the underlying substrate slows down lateral diffusion, which may be accompanied by a breakdown of the two-dimensional fluid nature of the membrane.

The above biomembrane models are not suitable for studying the function of integral proteins. In fact, these proteins have hydrophilic domains protruding outside the lipid bilayer. To avoid their denaturation and to promote their function, the incorporation of integral proteins into biomembrane models must ensure that their protruding hydrophilic domains are accommodated in a hydrophilic medium on both sides of the lipid bilayer. Not surprisingly, embedded membrane-spanning proteins usually show no lateral diffusion, because of their interaction with the substrate[132], even though some of them maintain their function if their active site is far from the solid substrate.

The majority of sBLMs are formed on nonconducting supports such as silica, glass or mica.[18,32,37] Consequently, they are not amenable to electrochemical measurements. Thus, for instance, sBLMs on silica were recently formed from mixtures of native *Escherichia coli* bacterial inner membrane (IM) vesicles, which contain membrane proteins, diluted with egg-PC vesicles.[132] These sBLMs were investigated by QCM, AFM, attenuated total internal-reflection Fourier-transform infrared spectroscopy (ATR-FTIR) and FRAP. Samples with less than 40% IM were found to form sBLMs by vesicle fusion. They were fluid, as shown by FRAP, and those with 30% IM contained the protein, as confirmed by ATR-FTIR. Conversely, the samples with more than 40% IM were dominated by vesicle adsorption. By forming a sBLM on silica, side by side with an alkanethiol/lipid hybrid bilayer on gold, it was found by FRAP that the lipid molecules of the distal monolayer of the sBLM could move laterally, mixing freely with those of the hybrid bilayer.[133] Moreover, the distal and proximal monolayers of the sBLM on silica could also mix by flip-flop.

In what follows, a few examples of sBLMs investigated by electrochemical techniques will be examined. Phospholipid bi-

layers on Au(111) single crystal faces have been prepared by Lipkowski and coworkers either by vesicle fusion[134] or by Langmuir-Blodgett and Langmuir-Schaefer transfers.[33] The latter procedure yields bilayers with a higher packing density and with smaller tilt angles of the alkyl chains with respect to the surface normal. These bilayers have been characterized by charge density measurements, photon polarization modulation infrared reflection absorption spectroscopy (PM IRRAS)[134,33] and neutron reflectivity.[135] The minimum differential capacitance of these bilayers is about equal to 2 $\mu F\ cm^{-2}$, and is attained at charge densities σ_M on the metal higher than $-8\ \mu C\ cm^{-2}$. The differential capacitance being greater than that of a solvent-free BLM denotes the presence of a number of defects, while neutron reflectivity reveals the presence of water molecules within the lipid bilayer. As σ_M becomes negative of $-8\ \mu C\ cm^{-2}$, the lipid bilayer starts to detach from the electrode, but remains in close proximity to the electrode surface. In fact, neutron reflectivity indicates that the lipid bilayer is suspended on a thin cushion of the aqueous electrolyte, which screens the metal charge and contains a large fraction of the overall interfacial potential difference; consequently, the electric field across the lipid bilayer becomes weak. This suspended lipid bilayer is essentially defect-free and its structure resembles that of lipid bilayers supported by a quartz surface. The IR data demonstrate that the carbonyl and phosphate groups are more hydrated when the bilayer is adsorbed on the electrode surface at $\sigma_M > -8\ \mu C\ cm^{-2}$ than when it is detached from the electrode at more negative charge densities.[134] Neutron reflectivity shows that a significant amount of water enters the polar head region of the lipid bilayer when it is in contact with the metal surface. The detachment of the lipid bilayer from the electrode surface is accompanied by a decrease in the tilt angle of the alkyl chains with respect to the surface normal from about 55° to 35°, with a resulting increase in bilayer thickness. The PM IRRAS measurements indicate that, as long as the lipid bilayer remains attached to the metal surface, changes in the local electric field by several orders of magnitude have only a small effect on the orientation of the phospholipid molecules.[136] Electrochemical scanning tunneling microscopy (EC-STM) images of adsorption of dimyristoylphosphatidylcholine (DMPC) on Au(111) show that the lipid molecules are initially adsorbed flat, with the alkyl chains

oriented parallel to the surface;[137] the resulting ordered monolayer resembles that formed by alkanes. With time, the molecules reorient and the monolayer is transformed into a hemimicellar film. In the presence of a high vesicle concentration in solution, the hemimicellar state is transformed further into a bilayer.

A sBLM formed by fusing vesicles consisting of a mixture of 50 mol% cholesterol and 50 mol% dihexadecyl-dimethyl-ammonium bromide on boron doped (p-type) silicon covered with native oxide was investigated by EIS.[138] The positively charged lipid was chosen to favor vesicle spreading on the negatively charged Si/SiO_2 surface. The impedance spectrum was simulated by an equivalent circuit consisting of two RC meshes in series, with the resistance R_Ω of the aqueous solution in series with them. One RC mesh simulates the electrode, regarded as a combination of the Si space-charge region, the SiO_2 oxide and the thin water layer interposed between the semiconductor surface and the lipid bilayer; the other RC mesh simulates the lipid bilayer. The resistance and capacitance of the electrode amount to about 19 MΩ cm^2 and 2.2 μF cm^{-2}, respectively, those of the lipid bilayer to 0.98 MΩ cm^2 and 0.75 μF cm^{-2}. Values of the two capacitances are close, but the resistance of the electrode is much greater than that of the lipid bilayer, due to the 1.3–1.4 nm thick silicon oxide. The time constants of the two RC meshes are, therefore, appreciably different and the corresponding frequency ranges are sufficiently apart to allow an accurate estimate of the corresponding parameters. Incorporation of gramicidin from an aqueous solution decreases the resistance of the lipid bilayer by more than one order of magnitude in the presence of Na^+ ions, and even more in the presence of K^+ ions. This agrees with the cation selectivity scale of gramicidin. When the Si/SiO_2 substrate was coated with a lipid bilayer consisting of a mixture of 1,2-dioleoyl-3-trimethyl-ammonium propane (DOTAP) and DOPC, the resistance R_m of the bilayer was found to attain a maximum value for 10 mol% of the positively charged lipid.[8] Electrostatic forces are those of longest range between a lipid bilayer and a substrate, but other forces are also operative, such as attractive van der Waals forces and repulsive hydration and steric forces. In view of the major role played by electrostatic forces, the rapid decrease of R_m for DOTAP mole fractions greater than 10% can be tentatively explained by electrostatic repulsion between the partially formed SiO_2-supported lipid

bilayer and the fusing vesicles. The repulsion among the charged lipid molecules of the SiO_2-supported bilayer may also favor the entrapment of inorganic ions in the polar head region and their subsequent movement along small fluctuating membrane-spanning pores, with a resulting decrease in R_m.

A sBLM formed by fusing DMPC-cholesterol vesicles on the optically transparent semiconductor indium tin oxide (ITO) was investigated by EIS.[139] The vesicles also contained 10 mol% of a positively charged lipid to favor their interaction with the negatively charged ITO surface. The impedance spectrum was analyzed with the same equivalent circuit used for the Si/SiO_2 substrate. In this case, gramicidin was incorporated in the ITO-supported lipid bilayer by incubating it with gramicidin-containing vesicles. Upon incorporating gramicidin, the resistance R_m of the lipid bilayer was strongly reduced in the presence of a Na^+ salt with an organic anion not permeating membranes, whereas its capacitance did not change remarkably. Conversely, R_m was practically unaffected in the presence of a Cl^- salt with an organic cation not permeating membranes. This experiment confirms the functional activity and ion selectivity of gramicidin, which is known to be highly selective toward monovalent inorganic cations. The outer membrane proteins OmpF and OmpA from *Escherichia coli* were reconstituted in vesicles that were fused on ITO.[139] In an aqueous solution of NaCl, the resistance of the ITO-supported lipid bilayer was strongly reduced by incorporating OmpF, whereas it was only slightly decreased by incorporating OmpA. Such a behavior was explained by the fact that only OmpF is a pore-forming protein, whereas OmpA does not form pores. Note that the functional activity of OmpF was preserved because, on the cytosolic side of the bacterial membrane, it has no extramembrane domain that might be endangered by direct contact with the ITO surface.

Freshly formed surfaces of Pt, Au, Ag, Cu, Ni or stainless steel are hydrophilic. Self-assembly of a lipid bilayer on these surfaces is realized by cutting the end of a Teflon-coated hydrophilic metal wire while keeping it dipped in a decane or squalene solution of the lipid, and by then immersing the freshly cut metal surface in an aqueous solution for 5–10 min.[140] During this period, the lipid solution in excess creeps between the metal wire and its Teflon coating, leaving a self-assembled lipid bilayer on the metal surface. The differential capacitance of this film, 0.3–0.5 μF cm^{-2},

is lower than that, about 0.8–0.9 μF cm^{-2}, of solvent-free BLMs, thus denoting the incorporation of alkane molecules, and its resistance (~0.5 MΩ cm^2) is also lower. The potential range covered by this solid-supported bilayer before its breakdown is appreciably wider than that at conventional BLMs, attaining values as high as 1.5 V. Since the metal surface can be rough after cutting, it can induce defects in the overlying lipid bilayer. These sBLMs, devised by Tien, were used by this author and coworkers[141] to carry out a feasibility study of an antigen-antibody reaction. The hepatitis B surface antigen was incorporated into the bilayer and was then allowed to interact with the corresponding monoclonal antibody in the bathing solution. The antigen-antibody interaction results in a notable linear decrease in the bilayer resistance with an increase in the antibody concentration, up to 50 ng mL^{-1}. These sBLMs were also used with the aim of realizing electrodes for biosensor applications.[141] In this connection, nonbiological liposoluble molecules such as ferrocene, tetracyanoquinodimethane (TCNQ) and tetrathiafulvalene (TFF) were incorporated in the bilayer and employed as electron carriers between the electrode and a hydrophilic redox couple present in the aqueous solution.[142] As an example, vinyl-ferrocene incorporated in a platinum-supported lipid bilayer acts as an electron carrier between the electrode and the peripheral, water-soluble protein ferri-cytochrome *c*.[143] The lipid bilayer provides a natural, biocompatible, surface for cytochrome *c* binding, with a resulting enhancement both in the equilibrium constant for cytocrome *c* adsorption on the bilayer and in the electron transfer rate between electrode and protein, with respect to a gold electrode in the presence of bipyridyl.[144] Fullerene C_{60} incorporated in a lipid bilayer supported by ITO was shown to facilitate electroreduction of ferricyanide ion and, upon illumination, to accelerate the photoinduced electron transfer from electron donors in solutions, (e.g., water, EDTA), to the electrode.[145]

In general, two possible mechanisms may be responsible for transmembrane electron transport between the electrode and a hydrophilic, lipid insoluble, redox couple present in the aqueous solution:

(1) a redox reaction at the bilayer/water boundary between the hydrophilic redox couple and a lipophilic redox couple pre-

sent in the bilayer, which shuttles electrons to or from the electrode surface;

(2) an electron tunneling across the bilayer, possibly assisted by some lipophilic molecule possessing conjugate π-bonds, and therefore capable of providing an electron-conductive pathway across the lipid bilayer.

The latter view, uphold by Tien and some other authors[146], is inspired by the existence in natural membranes of sites, small in extent, where electron transfer between hemes occurs as a result of the overlapping of the orbitals of neighboring molecules. However, the probability of electron tunneling through the entire thickness of a lipid bilayer, even in the presence of molecules with conjugated double bonds such as ferrocene, TCNQ or TFF[142], seems doubtful. In fact, it would require overpotentials higher than those observed experimentally.

A different procedure for the realization of a lipid bilayer noncovalently attached to a silver surface was adopted by Salamon, Tollin et al.[147] It consists of spreading a small amount of a solution of a lipid in a suitable solvent across a small orifice in a Teflon sheet sandwiched between a thin silver film, deposited on the external surface of a prism, and an aqueous solution. The hydrophilic surface of silver attracts the polar heads of the lipid molecules, thus forming a lipid monolayer with the hydrocarbon tails directed toward the bulk lipid phase. This phase becomes progressively thinner through the accumulation of the excess lipid and its solvent at the edge of the Teflon orifice, with formation of an annulus (the Plateau-Gibbs border), until the orifice is covered by a lipid bilayer enclosed between the silver surface and the aqueous solution. The authors claim that a water layer remains in contact with the silver electrode during this process, thus favoring the incorporation of integral proteins into the bilayer. The above sBLMs, noncovalently attached to the metal support, are reported to be stable for 25–35 h. However, the capacitance C of these bilayers, measured by EIS, is about one order of magnitude greater than that of a conventional BLM, denoting an appreciable amount of defects.[148] By a detailed analysis of the minimum, depth and half-width of the SPR reflectivity curves of these silver-supported lipid bilayers, Salamon and Tollin studied the structural changes following the incorporation of a number of integral proteins into the bilayer and the interaction of

these proteins with their associated water-soluble proteins (e.g., incorporation of rhodopsin and its interaction with the G-protein transducin[149], incorporation of cytochrome *c* oxidase and its interaction with cytochrome c.)[150] This allowed the authors to distinguish conditions under which nonspecific electrostatic interactions prevail over those characterized by the predominance of specific hydrophobic interactions. Salamon and Tollin have subsequently improved the technique by interposing a thin dielectric layer of SiO_2, acting as a waveguide, between the silver layer and the lipid bilayer, which was now self-assembled on the hydrophilic SiO_2 surface.[151] This system allows an estimate of the refractive index and the extinction coefficient of the composite film not only with *p*-polarized light (i.e., in the direction perpendicular to the bilayer plane), as in conventional SPR, but also with *s*-polarized light, i.e., in the direction parallel to the bilayer plane. These parameters measure the anisotropic character of the lipid membrane structure. This technique, called *coupled plasmon-waveguide resonance spectroscopy* (PWR), has provided useful pieces of information on the structural changes accompanying the incorporation in a lipid bilayer of the integral protein cytochrome b_6f and its interaction with the peripheral, water-soluble protein plastocyanin;[152] the structural changes involved in the incorporation of different receptors and in their ligand binding have also been investigated. The PWR spectroscopy has also been used to monitor the formation of microdomains in mixed sphingomyelin-DOPC mixtures (called lipid rafts) and the sorting of receptors into each microdomain.[153] The microdomain size evaluated from the lateral resolution of the PWR sensor is very high (100–300 μm). While providing useful structural information on (lipid bilayer) - (integral protein) - (peripheral protein) systems, this technique cannot provide direct evidence for the functional activity of these systems and a verification that the differential capacitance of the lipid film is that expected for a well-behaved lipid bilayer.

5. Tethered Bilayer Lipid Membranes (tBLMs)

As a rule, tethered bilayer lipid membranes refer to architectures in which the lipid bilayer is separated from the support through a monomolecular layer tethered to the support via a sulfhydryl or disulfide group (for gold, silver or mercury supports) or via a

silane group (for silica and glass supports). The monolayer interposed between the support surface and the lipid bilayer should have a well-defined composition and geometrical arrangement, as distinct from polymer-cushioned bilayer lipid membranes. TBLMs will be classified on the basis of the nature of the molecules composing the tethered monolayer, as follows:

(1) spacer-based tBLMs;
(2) thiolipid-based tBLMs;
(3) (thiolipid-spacer)-based tBLMs.

We will examine these three types separately.

(*i*) *Spacer-Based tBLMs*

The spacer may consist of an alkanethiol, functionalized with a hydrophilic group (e.g., a hydroxyl, carboxyl or amino group) at the apposite end of the alkyl chain with respect to the sulfhydryl group. More frequently, it consists of a thiolated or disulfidated hydrophilic chain. The spacer is tethered to a support via its sulfhydryl or disulfide group and a lipid bilayer is self-assembled on top of it, often by vesicle fusion. The interior of ω-functionalized alkanethiol monolayers is hydrophobic, as opposed to that of thiolated hydrophilic chains. However, even the latter spacers do not necessarily ensure a satisfactory hydration if they are too closed packed. In both cases, a thin water layer, about 1 nm thick, is normally interposed between the spacer monolayer and the lipid bilayer, as in the case of sBLMs; this provides a small ionic reservoir for channel-forming peptides incorporated in the lipid bilayer moiety. Since the lipid bilayer is not covalently linked to the support, it is expected to be sufficiently fluid to accommodate relatively bulky membrane proteins, unless they have large extramembrane domains on both the cytosolic and the extracellular side. The lateral mobility of lipid molecules on a hydrophilic spacer was verified by FRAP in about 10 min on very smooth gold surfaces[6], but a sufficient fluidity may probably be verified at longer times even on rougher surfaces. The capacitance of the lipid bilayer in these tBLMs is close to 1 $\mu F\ cm^{-2}$, but its resistance assumes relatively low values, of the order of 0.5 $M\Omega\ cm^2$.

A tBLM consisting of a 3-mercaptopropionic acid (MPA) tethered to gold, with a bilayer of the positively charged lipid dimethyldioctadecylammonium bromide (DODAB) on top, was used to incorporate gramicidin.[154] The lipid bilayer was stabilized by electrostatic interactions with the spacer. To this end, a pH of 8.6 was used to completely deprotonate the MPA monolayer, and the ionic strength of the solution was kept sufficiently low by using 1,1-valent electrolytes of concentration less than 50 mM. The ion-channel activity of gramicidin was verified by EIS upon simulating the lipid bilayer by a resistance and a Warburg impedance in series, and by a capacitance in parallel with the first two elements. The Warburg impedance was introduced to account for cation diffusion in the bulk aqueous phase. The same tBLM was used to incorporate the 25 kDa *Clavibacter* ion channel (CAC), which exhibits anion selectivity.[155] CAC incorporation decreases the resistance of the lipid bilayer from 3 to 5 times. The conductivity induced by CAC increases exponentially with potential, and linearly with chloride or with CAC concentration. Lipid bilayers formed on gold-supported alkanethiol monolayers ω-functionalized with an amino group were found to exhibit a film thickness more than twice that on alkanethiol monolayers ω-functionalized with a carboxyl group, by using SPR.[11] Combining surface plasmon fluorescence spectroscopy (SPFS) with SPR by fluorescently labeling the lipid films, the fluorescence intensity of the lipid bilayer on the $-NH_2$ surface was found to be almost three orders of magnitude higher than that on the –COOH surface. It was concluded that many adsorbed vesicles were present on the $-NH_2$ surface.

Another procedure for preparing spacer-bilayer assembies on electrodes consists of anchoring a polyethyleneoxy hydrophilic spacer to a hanging mercury drop electrode via a terminal sulfhydryl anchoring group by immersing the mercury drop in an ethanol solution of the spacer for about 20 min.[156] After extracting the spacer-coated mercury drop from the ethanol solution, it is slowly brought into contact with a lipid film previously spread on the surface of an aqueous electrolyte, by taking care to keep the drop neck in contact with the lipid reservoir. This disposition allows a free exchange of lipid material between the lipid reservoir on the surface of the aqueous electrolyte and the spacer-coated drop. This procedure gives rise to the formation of a lipid bilayer in contact

with the spacer-coated drop, by exploiting the spontaneous tendency of a lipid film to form a bilayer when interposed between two hydrophilic phases. The fluidity of the tBLM was tested by recording the cyclic voltammogram for the electroreduction of ubiquinone-10 incorporated in the lipid bilayer. The voltage-dependent ion channel activity of melittin incorporated in the tBLM was verified by EIS. A similar mercury-supported tBLM was fabricated by using a thiolated hexapeptide molecule with a high tendency to form a 3_{10}-helical structure as a spacer.[157] This thiopeptide had two triethylenoxy side chains to impart it a satisfactory hydrophilicity. The resulting tBLM was characterized by chronocoulometry and EIS and its suitability as a biomimetic membrane was tested by incorporating ubiquinone-10 and valinomycin.

(*ii*) *Thiolipid-based tBLMs*

A *thiolipid* molecule consists of a hydrophilic polyethyleneoxy or oligopeptide hydrophilic chain terminated at one end with a sulfhydryl or disulfide group for anchoring to the support and covalently linked at the other end to two alkyl chains simulating the hydrocarbon tails of a lipid (see Fig. 1A). A tethered thiolipid monolayer exposes a hydrophobic surface to the bulk aqueous phase and provides one half of the lipid bilayer. The other half is obtained by forming a lipid monolayer on top of the thiolipid monolayer, usually by vesicle fusion. Aqueous solutions of lipids, solubilized with a detergent in the form of micelles, have also been employed for this purpose, upon diluting the solution with an electrolyte below the critical micelle concentration of the detergent.[158]

(*a*) *Gold-supported thiolipid-based tBLMs*

Polyethyleneoxy-based thiolipid monolayers and (polyethyleneoxy-based thiolipid)/phospholipid bilayers tethered to gold have been characterized by SPR, EIS and cyclic voltammetry, and the synthesis of the thiolipids has been described.[158-160] The cross-sectional area of a hydrophilic polyethyleneoxy chain is smaller than that of the two alkyl chains, if it is in its fully extended conformation, but not if it is coiled. In the former case it is sufficiently hydrated to provide a satisfactory ionic reservoir; conversely, in the latter case it may accommodate only a limited amount of water

molecules. Whether the conformation is extended or coiled depends both on the interfacial electric field and on the nature of the metal support. TBLMs fabricated with polyethyleneoxy-base thiolipids exhibit capacitances in the range from 0.5 to 0.7 μF cm^{-2} and resistances in the range from 5 to 10 MΩ cm^2, which are comparable with the values found for conventional BLMs; however, somewhat higher capacitance values (1 μF cm^{-2}) have been reported for long spacers.[161] A particularly convenient tBLM of this type, called DPTL, was synthesized in the Max Planck Institute of Polymer Science in Mainz.[1] It consists of a hydrophilic tetraethyleneoxy chain covalently linked to a lipoic acid residue for anchoring to the metal at one end, and bound via ether linkages to two phytanyl chains at the other end (see Fig. 1A). Its cross-sectional area is of about 55 $Å^2$.

Thiolipopeptides consist of an oligopeptide chain terminated at one end with a sulfhydryl group and covalently linked at the other end to the polar head of a phospholipid. They are considered to assume a helical structure, rather than a β-sheet structure.[162] In this case, their cross-sectional area amounts to about 75 $Å^2$. They are usually obtained by tethering to a gold electrode a *thiopeptide* consisting of an oligopeptide chain terminated with a sulfhydryl group at one end and with a carboxyl group at the other end. This thiopeptide monolayer is then coupled *in situ* with dimyristoylphosphatidylethanolamine (DMPE).[163] TBLMs fabricated with thiolipopeptides have been employed for the incorporation of a number of integral proteins; they exhibit high capacitances (from 2 to 10 μF cm^{-2}) and low resistances, of the order of 10^4 Ω cm^2, which are more than three orders of magnitude lower than those of conventional BLMs.[164-166] The low resistance is ascribed to a not perfectly homogeneous coverage of the thiolipid monolayer by the distal lipid monolayer; this coverage is estimated at about 70% of full coverage and makes the tBLMs insufficiently insulating.[163] This is indicative of the presence of an appreciable number of pinholes and other defects in the bilayer, as well as of a certain disorder of the hydrocarbon chains. It was suggested that the thiolipopeptide monolayer actually consists of a mixture of the thiolipopeptide and of the corresponding uncoupled thiopeptide. This conclusion was based on the observation that gold-supported tBLMs formed from a presynthesized thiolipopeptide did not per-

mit the functional activity of incorporated proteins.[30] Such a functionality was recovered only by mixing the thiolipopeptide with a hydrophilic thiol, such as mercaptohexanol.

A structural and functional characterization of a DPTL monolayer tethered to gold was recently reported by Vockenroth et al.[167] using neutron reflectivity (NR) and EIS. The tetraethyleneoxy moiety was found to be only partly hydrated at the more positive potentials. However, at –0.600 V vs. Ag/AgCl(0.1 M KCl) a pronounced increase in the neutron scattering length density of the spacer was observed, denoting an increased amount of water transferred into this region. Leitch et al.[168] drew similar conclusions using polarization modulation infrared reflection absorption spectroscopy (PM-IRRAS). Thus, the fraction of nonhydrated C=O of the lipoic acid ester group was found to be about 50% at the more positive potentials and to attain a value of about 30% at –0.600 V, which denotes an increasing hydration of the spacer at these negative potentials. Analogous conclusions were also drawn by McGillivray et al.[35] by using NR, EIS and Fourier-transform IRRAS (FT-IRRAS) to investigate a gold-supported thiolipid monolayer similar to DPTL, with a hydrophilic spacer moiety consisting of a hexaethyleneoxy chain directly bound to a sulfhydryl group. FT-IRRAS revealed a significant disorder in the spacer region and a substantial order in the hydrocarbon tail region. Moreover, NR showed that the spacer region had a thickness smaller than its fully extended length and only 5 vol% exchangeable water, despite its significant disorder. Since the incorporation of proteins with extramembrane domains requires a significant hydration of the spacer, the thiolipid monolayer was then diluted with short β-mercaptoethanol (βME) molecules. This permitted water molecules to be accommodated in the more spacious thiolipid-βME mixture. By self-assembling a lipid monolayer on top of this mixed monolayer, McGillivray et al.[35] obtained a tBLM with a differential capacitance comparable with that of conventional BLMs. Moreover, NR data revealed the presence of an appreciable amount of exchangeable water in the spacer moiety of this tBLM.

Thiolipid-based tBLMs, when anchored to solid supports such as gold or silver, do not meet the requirement of fluidity and lateral mobility. The thiolipid molecules are rigidly bound to the metal surface atoms. In principle, the lipid molecules on top of the thiolipid monolayer may be free to move laterally. In practice, howev-

er, their lateral mobility is hindered by the presence of adsorbed or hemifused vesicles and by the roughness of the metal support (see Section IV.5). Moreover, the hydration of the polyethyleneoxy moiety of thiolipids anchored to gold is low, while the incorporation of proteins with extramembrane domains requires a significant hydration of the spacer. Only small peptides and ionophores can be accommodated in the lipid bilayer moiety of polyethyleneoxy-based tBLMs, via incorporation from their aqueous solutions.

A typical example is the depsipeptide valinomicin, an ion carrier that complexes a potassium ion with its carbonyl groups. Valinomycin cages potassium ions and shuttles them across the bilayer from the aqueous solution to the hydrophilic polyethyleneoxy chain, moving back and forth. Upon incorporating valinomycin in the tBLM, the impedance spectrum was fitted to an equivalent circuit consisting of three circuit elements in series: a capacitance C_s simulating the spacer, a R_mC_m mesh simulating the lipid bilayer, and a resistance R_Ω, simulating the aqueous solution.[161,169] In a KCl solution, the conductance, $1/R_m$, of the lipid bilayer moiety was found to increase proportionally to the bulk valinomycin concentration, c_v. The lipid bilayer capacitance, C_m, remained practically constant with varying c_v using the DPTL thiolipid[169], but increased linearly with c_v using a different thiolipid.[161] The high selectivity of valinomycin toward potassium ion with respect to sodium ion was verified. The impedance spectra of a gold-supported DPTL/DPhyPC tBLM incorporating valinomycin were also interpreted with a SPICE computer program designed to simulate processes across membranes with an electrical network;[169] this amounts to solving the Nernst-Planck equation for field-assisted diffusion of permeating ions across a membrane with the appropriate boundary conditions. However, in doing so, the potential difference across the tBLM, measured with respect to an Ag/AgCl(sat. NaCl) reference electrode, was identified with its extrathermodynamic absolute potential difference (see also Ref. 170). A gold-supported DPTL/DPhyPC tBLM was also used to incorporate the M2 peptide, which forms a straight α-helix spanning lipid bilayers.[171] Bundles of M2 α-helixes form a hydrophilic pore in the membrane, by turning their polar residues toward the interior of the pore and their nonpolar residues toward its exterior. M2 is one of the four membrane-spanning segments composing each of the five subunits that constitute the nicotinic acetylcholine

receptor. As distinct from valinomycin and gramicidin, the M2 peptide does not insert spontaneously into a lipid bilayer from the bulk solution. Therefore, its incorporation was achieved by preloading the vesicles used for the formation of the distal leaflet of the tBLM with it. The M2 pore allows the passage of small monovalent cations such as Na^+ and K^+, but not larger cations such as tetramethylammonium (TMA). Upon incorporating M2, the resistance of the lipid bilayer is reduced to one fifth of its value in KCl solution, but increases again by exchanging the KCl solution with a TMACl solution.

In spite of the lack of lateral mobility and low hydration of these tBLMs, attempts have been made to incorporate the exotoxin α-hemolysin from *Staphylococcus aureus*, a water soluble, monomeric, 293-residue polypeptide that forms heptameric pores in lipid bilayers. Three different polyethyleneoxy-based tBLMs have been employed: $HS(CH_2CH_2O)_6(CH_2)_{17}CH_3$ (THEO-C_{18}),[172] DPTL and DPHDL,[173] which differs from DPTL by the presence of six ethyleneoxy units, instead of four, and of two lipoic acid residues, instead of one. With all thiolipids, incorporation of *α*-hemolysin causes a decrease in resistance and an increase in capacitance of the tBLM. The effect of *α*-hemolysin on the tBLM obtained by self-assembling an egg-PC monolayer on the THEO-C_{18} thiolipid is bimodal and poorly reproducible. In some experiments, the fitting of two RC meshes in series to the impedance spectra indicates that the parameters ascribed to the hexaethyleneoxy moiety are practically unaffected. This suggests that the protein penetrates only the distal monolayer of the tBLM. In a second group of experiments, the resistance ascribed to the hexaethyleneoxy moiety decreases by two orders of magnitude. As a whole, the changes in the hexaethyleneoxy and hydrocarbon moieties induced by *α*-hemolysin suggest that this toxin penetrates the tBLM partially or totally. The resistance of the DPHDL monolayer was very low (0.33 kΩ cm^2) when compared with that, 9.9 MΩ cm^2, of the DPTL monolayer. This denotes a loosely packed DPHDL monolayer. However, the formation of a DPhyPC monolayer on top of it by vesicle fusion seems to heal some of its defects. Upon incorporating *α*-hemolysin, the resistance of the lipid bilayer moiety of the DPHDL/DPhyPC tBLM decreases by three orders of magnitude, and that of the DPTL/DPhyPC tBLM by one order of magnitude.

In view of the well-known lysing effect of α-hemolysin on biomembranes, we cannot exclude a similar effect on these tBLMs, with membrane breakdown.

By replacing the lipoic acid residue of DPTL with a trichloropropyl-silane group, a supramolecule (DPTTC) was obtained, which was self-assembled on a SiO_2 surface via the trichlorosilane tether.[174] The SiO_2 layer was very thin (about 0.2 nm), being the native oxide layer of a highly p-doped silicon wafer. Consequently, a tBLM obtained by forming a lipid monolayer on top of the DPTTC monolayer tethered to the silicon wafer could be investigated by EIS. The impedance spectrum of the resulting tBLM was simulated by two RC meshes in series, with the omnipresent solution resistance R_Ω in series with them. The two RC meshes simulated the oxide layer and the lipid bilayer tethered to it, respectively. The functionality of this tBLM was tested by verifying the ion-channel activity and ion selectivity of valinomycin and gramicidin. Valinomycin decreases the resistance of the lipid bilayer in the presence of KCl by three orders of magnitude, while the corresponding capacitance remains practically unaltered. The highly insulating properties of this tBLM have potential for biosensing applications on semiconductor chips. A tBLM was also formed on aluminum oxide (AlO_x) sputtered on template-stripped gold.[175] An *anchor-lipid* was immobilized on the AlO_x film, about 2.7 nm thick, via Langmuir-Blodgett transfer. The anchor-lipid differs from DPTL by the replacement of the lipoic acid residue with a $-P{=}O(OEt)_2$ group for anchoring to the AlO_x surface. A DPhyPC monolayer was deposited on top of the anchor-lipid monolayer by vesicle fusion. The natural porosity of the AlO_x film, not visible at AFM, was intended to enlarge the ionic reservoir beneath this tBLM. The thin AlO_x film on gold allowed an EIS and SPR characterization of the system. The impedance spectrum of the tBLM was fitted by a parallel combination of a resistance and a constant phase element (instead of a capacitance), in series with the electrolyte resistance, R_Ω. The lipid bilayer had a resistance of about 17 $M\Omega\ cm^2$ and a capacitance of 10 $\mu F\ cm^{-2}$. The resistance is similar to that of gold-supported tBLMs, but the capacitance is one order of magnitude higher. This suggests that the tBLM adheres to some extent to the pores of the AlO_x layer. Incorporation of valinomycin in the lipid bilayer decreases its resistance by more than one order

of magnitude in the presence of K^+ ions, but not in that of Na^+ ions, confirming the ion selectivity of this ionophore.

Au-supported thiolipopeptide-based tBLMs have been reported to incorporate a few bulky proton pumps. Thus, Naumann et al. incorporated the proton pump ATPase CF_0F_1 from chloroplasts and that, ATPase EF_0F_1, from *Escherichia coli*, in a tBLM fabricated with a hydrophilic oligopeptide spacer.[164,165] SPR yields a thickness of about 5 nm for the lipid bilayer in the absence of the proton pump and of 7 to 9 nm in its presence.[163] The square-wave voltammogram of the lipid film incorporating the ATPase, as recorded at pH 7.4 in the absence of the activating compound ATP, shows a small reduction peak at -0.7 V vs. Ag/AgCl(sat. KCl), due to hydrogen evolution. Progressive additions of ATP to the aqueous solution bathing the biomimetic membrane cause a gradual increase in the reduction peak; this was ascribed to an increase in the proton concentration within the hydrophilic oligopeptide spacer adjacent to the electrode surface, due to proton pumping from the aqueous solution by the activated ATPase. A confirmation comes from the suppression of the reduction peak by tentoxin, an extremely specific inhibitor of the ATPase from chloroplasts. In a subsequent work, Naumann et al.[30] verified by FRAP that the distal lipid leaflet, obtained by fusion of egg-PC liposomes mixed with a fluorescence labeled lipid, did not show lateral mobility. They also confirmed the functional activity of the H-ATPase by monitoring by EIS a decrease in the membrane resistance upon addition of ATP. This decrease was observed at potentials much more positive than those at which hydrogen ion electroreduction on gold takes place. Since a decrease in resistance monitored by EIS involves a back-and-forth movement of protons across the membrane and the H-ATPase is not an ion channel, we may hypothesize that the protons, after being translocated by the proton pump toward the electrode, move rapidly backward by nonspecific diffusion across a leaky membrane.

Cytochrome *c* oxidase (COX) was incorporated in an analogous Au-supported, thiolipopeptide-based tBLM.[166] The integral protein COX is the terminal component of the respiratory electron-transport chain and spans the inner mitochondrial membrane. It catalyzes the redox reaction between the small peripheral protein cytochrome *c* in its reduced form, i.e., ferro-cytochrome *c*, and oxygen, with formation of ferri-cytochrome *c* and water; it also

pumps protons from the matrix to the intermembrane space, where it interacts with ferro-cytochrome *c*. In the absence of ferro-cytochrome *c*, the square-wave voltammogram of the tBLM incorporating COX shows a reduction peak due to the electroreduction of protons on the gold surface at –0.70 V, as usual; increasing additions of ferro-cytochrome *c* cause a progressive decrease of this peak; this decrease was ascribed to a decrease in the proton concentration within the thiopeptide spacer, due to proton pumping from the spacer to the aqueous solution. This direction of the proton flux was explained by the fact that ferro-cytocrome *c* can only interact with the COX protein molecules that turn their intermembrane-space side toward the aqueous phase, which is also the direction of COX proton pumping in biomembranes. The addition of cyanide, which is known to inhibit proton transport by binding to the binuclear center of COX, eliminates the effect of ferro-cytochrome *c*. As already stated, thiolipopeptide-based tBLMs have a differential capacitance much higher and a resistance much lower than those of conventional BLMs, thus denoting poor electrical properties and an appreciable field-assisted permeability to protons. The lipid monolayer on top of the thiolipopeptide monolayer shows no detectable mobility. This was demonstrated by fusing lipid vesicles labeled with a fluorescent probe, photobleaching a spot of the resulting tBLM with a laser beam and monitoring any fluorescence recovery after photobleaching (FRAP) in this spot; no recovery was observed after ten minutes.

The above conclusions as to proton pump incorporation in thiolipopeptide-based tBLMs should be examined in light of the observation that vesicles have a low propensity to fuse on the hydrophobic surface exposed to the aqueous solution by a thiolipid monolayer, especially if they incorporate an integral protein; rather, they are adsorbed or partially fused (cf. Section IV.2). Incorporation of the above proton pumps from their solutions in detergent may easily take place in the membrane of adsorbed or partially fused vesicles, since the vesicular membrane is clearly interposed between two aqueous phases. An analogous situation may be envisaged with proteoliposomes that are adsorbed or partially fused on the thiolipid monolayer from their suspending solution. In this respect, the functional activity of the above proton pumps might well be successfully verified even with vesicles or proteoliposomes adsorbed and/or partially fused on a thiolipid mono-

layer, without the need for a spacious ionic reservoir beneath a well-behaved lipid bilayer. In fact, their activation would cause an increase in the proton concentration on top of the thiolipid monolayer (in the case of F_0F_1 ATPase activated by ATP) or its decrease (in the case of COX activated by ferrocytocrome *c*). In view of the relative permeability of the leaky thiolipopeptide monolayers to protons, this would determine an increase or a decrease in the proton electroreduction current on gold, as actually observed.

A tBLM consisting of a gold-supported thiolipopeptide, with a soybean-PC monolayer on top, was used to incorporate the odorant receptor OR5 from *Rattus norvegicus* during its *in vitro* synthesis.[176] The vectorial insertion of the protein into the tBLM in a functional and oriented form was verified. The incorporation and orientation of the protein were shown by immunolabeling in combination with surface plasmon enhanced fluorescence spectroscopy (SPFS). Reversible ligand binding was demonstrated by surface-enhanced infrared reflection absorption spectroscopy (SEIRAS). Total internal fluorescence (TIRF) imaging, confocal fluorescence correlation spectroscopy (FCS) and FRAP allowed the incorporation density and the translational mobility of OR5 to be quantified.[177]

A gold-supported thiolipopeptide-based tBLM was also employed to incorporate the acetylcholine receptor (AChR), a ligand-gated channel protein present in the postsynaptic membrane of the muscle cell. The binding of acetylcholine to the receptor protein causes a conformational change in the protein that allows the influx of Na^+ ions into the muscle cell. The venoms of certain snakes contain peptide neurotoxins (e.g., α-bungarotoxin) that are competitive inhibitors of the AChR. The thickness of the lipid bilayer of the tBLM, as estimated by SPR, increases from about 4.5 to about 6.5 nm upon AchR incorporation.[178] This suggests a relatively high packing density of the AchR molecules arranged perpendicular to the bilayer. Addition of α-bungarotoxin causes a slow but appreciable increase in thickness, thus denoting the binding of this toxin to the binding sites of AChR, possibly accompanied by major conformational changes. This test confirms that at least a portion of the AchR protein is oriented with the extracellular domain pointing outside of the lipid bilayer, since α-bungarotoxin binds to this domain. The inhibitory effect of α–bungarotoxin on the ion-channel activity of AchR was not verified.

Gold-supported DPTL/DPhyPC tBLMs on microchips have recently been employed to measure single channel currents of peptides and proteins. To this end, a microelectrode array device consisting of many (100×100 μm^2) *sensor* pads was employed (see Fig. 15).[179-181] A DPTL monolayer was tethered to the gold-coated sensor pads from a DPTL solution in ethanol; then, a lipid monolayer was formed on top of it by vesicle fusion. In view of the very small surface area of the pad, the resistance of the resulting tBLM ranged from 1.5 to 17 GΩ. This resistance was high enough to reduce the background electrical noise to the low level required for the use of the patch-clamp technique. A droplet of a buffered aqueous solution was applied to a given tBLM-coated gold pad. Then, a conventional patch pipette containing an Ag/AgCl electrode and filled with the same buffer solution was inserted into the droplet. The electrical circuit of the patch-clamp amplifier was closed with a tungsten-tipped electrode that was positioned onto a gold-coated *probe* pad electrically wired to the given sensor pad.

This devise has allowed the recording of single channel currents of gramicin A,[179] the high-conducting Ca^{2+}-activated K^+ (BK or Maxi-K) channel, the synthetic M2δ ion channel[180] and the mechanosensitive channel of large conductance (MscL) from *Escherichia coli*.[181] All these peptides and proteins were incorporated into lipid vesicles, before fusing them onto the DPTL-coated sensor pad. With the exclusion of the gramicidin channel, the unitary conductance of the remaining ion channels was found to be from one third to one tenth of that obtained with conventional BLMs. In this connection, one cannot exclude the possibility that, even in this case, the channels responsible for single channel currents are located in the membrane of adsorbed or partially fused vesicles. In fact, if this is the case, then the capacitive coupling between the vesicular membrane and the tBLM is expected to decrease the unitary conductance of the channels. The channel lifetimes for both open and closed states were normally found in good agreement with those obtained under similar conditions in conventional patch-clamp experiments. Plots of the current against the applied voltage are roughly linear and pass through the origin of the coordinate system, with the only exception of gramicidin. However, it is not clear whether the voltage is referred to the Ag/AgCl reference electrode or whether the curves were forced to pass through the origin.

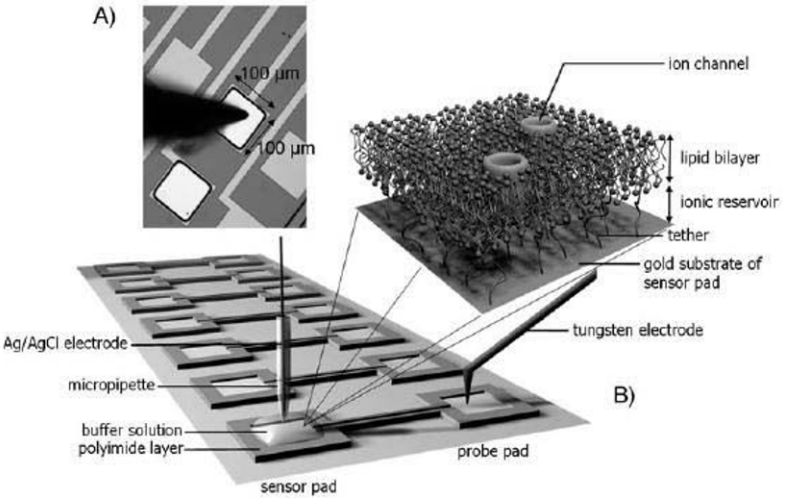

Figure 15. The tethered bilayer membrane array. A) An optical microscope image of the probe pad and the tungsten electrode tip. B) Graphical representation of the tethered bilayer membrane array. The lower left corner shows the gold sensor pad covered with a tBLMs that incorporates ion channels. An Ag/AgCl electrode situated in a patch micropipette was used as an electrode and was inserted into the buffer drop. The gold substrate of the sensor pad was connected by a thin gold line to the probe pad onto which a tungsten tip was lowered as a counter electrode. The inset shows the tBLM formed at the gold surface of the sensor pad. (Reprinted from Ref. [181] with kind permission from Elsevier.)

The capacitance and resistance of DPTL/DPhyPC tBLMs on gold microelectrodes of circular shape, with diameters ranging from 4000 to 8 μm, was examined as a function of the electrode size.[182] For the larger electrodes, the capacitance is directly proportional to the electrode area, while the resistance is inversely proportional to it. For the smaller electrodes, the capacitance decreases linearly and the resistance increases linearly with a decrease in the electrode diameter. This indicates that the capacitance and resistance of the larger electrodes are dominated by the electrode area, while the circumference seems to have the dominant role at smaller electrodes. Consequently, for small electrode sizes, a slight disorder of the bilayer structure at the edge of the electrode has a major influence on the electrical properties of the membrane. This conclusion is supported by the consideration that the micro-tBLMs used for the recording of single channel currents have resistances ranging from 1.5 to 15 GΩ. These resistances are high enough to reduce the level of the background noise down to the range of a few pA. However, the corresponding specific resistances are much less than those attained with identical tBLMs anchored to macroscopic gold electrodes of areas of the order of 1×10^{-2} cm^2. In fact, the specific resistance of the latter tBLMs amounts to about 15 MΩ cm^2. If a 100×100 μm^2 micro-tBLM had such a specific resistance, it should have a resistance of 150 GΩ. The loose packing of micro-tBLMs may explain why they may incorporate relatively bulky proteins much more easily than macro-tBLMs, without having to dilute the thiolipid with a short spacer.

(*b*) *Mercury-supported thiolipid-based tBLMs*

As distinct from Au-supported thiolipid-based tBLMs, Hg-supported thiolipid-based tBLMs do not require the use of thiolipid-spacer mixtures to incorporate channel-forming proteins. Thanks to the fluidity imparted to the thiolipid monolayer by the liquid mercury surface, these tBLMs may incorporate bulky proteins, such as OmpF porin from *Escherichia coli*[183] and the HERG potassium channel,[184] in a functionally active state. Upon incorporating gramicidin[2] or valinomicin,[3] the tetraethyleneoxy (TEO) moiety of DPTL in aqueous KCl solution undergoes a conformational change ascribable to its elongation, as the applied potential

is stepped from a fixed initial value of –0.200 V/SCE to a final value of –0.500 V/SCE.[3] As the final value of this potential step becomes progressively more negative, the charge of K^+ ions accommodated in the TEO spacer increases rapidly, attaining a maximum limiting value of about 45 μC cm^{-2} at –0.8 V/SCE.[185] This corresponds to three potassium ions per DPTL molecule, denoting an appreciable hydration of the spacer. Moreover, EIS measurements of the surface dipole potential of the TEO spacer tethered to mercury yield values that compare favorably with the dipole moment of TEO molecules measured in organic solvents;[186] this suggests a substantial order of the TEO chains in Hg-supported tBLMs. Incidentally, tBLMs supported by Au[165] or Ag[187] do not allow ionic charge measurements carried out by stepping the applied potential to final values negative of ~ –0.650 V. In fact, the resulting charge vs. time curves show a linear section with a relatively high and constant slope that is maintained for an indefinitely long time.[165,187] The constant current responsible for this linear increase in charge is ascribed to a slight water electroreduction with hydrogen formation. The high hydrogen overpotential of mercury avoids this inconvenience. When comparing interfacial phenomena on different metals, rational potentials should be used, namely potentials referred to the potential of zero charge (pzc) of the given metal in contact with a nonspecifically adsorbed 1,1-valent electrolyte. The pzc equals –0.435 V/SCE for Hg[188] and –0.040 V/SCE for polycrystalline Au.[189] Therefore, an appreciable hydration of the TEO moiety, possibly accompanied by its elongation[3], takes place in the proximity of a rational potential of about zero on Hg, but at a much more negative rational potential of about –0.600 V on Au,[167,168] close to the DPTL desorption from this metal. A drawback in the use of mercury-supported tBLMs is represented by the notable difficulty in using surface sensitive techniques for their structural characterization.

With respect to solid metal supports, mercury has the advantage of providing a defect free, fluid and readily renewable surface to the self-assembling thiolipid/lipid bilayer. Moreover, it imparts lateral mobility to the whole mixed bilayer. In addition, the self-assembly of a lipid monolayer on top of a thiolipid monolayer is readily carried out by simply immersing a thiolipid-coated mercury drop in an aqueous electrolyte on whose surface a lipid film has been previously spread.[3] Thanks to the hydrophobic inter-

actions between the alkyl chains of the thiolipid and those of the lipid, this simple procedure gives rise to a lipid bilayer anchored to the mercury surface via the hydrophilic spacer moiety of the thiolipid. By avoiding the use of vesicles, this procedure excludes any artifacts due to partially fused vesicles. These advantageous features make the incorporation of membrane proteins in mercury-supported thiolipid-based tBLMs easier and safer than in solid-supported tBLMs.

A tBLM obtained by self-assembling a DPhyPC monolayer on top of a DPTL-coated mercury electrode was investigated by impedance spectroscopy over a frequency range from 1×10^{-2} to 1×10^{5} Hz and over a potential range of 0.8 V, both in the absence and in the presence of the ion carrier valinomycin.[3] The impedance spectra obtained upon incorporating valinomycin in this tBLM from aqueous 0.1 M KCl are particularly rich of characteristic features, especially when reported in a ωZ' versus ωZ" plot (the M plot; cf. Section III). This plot shows four partially fused semicircles (see Fig. 5), which can be straightforwardly fitted by an equivalent circuit consisting of a series of four RC meshes. Each semicircle corresponds to a RC mesh; the diameter of the semicircle measures the reciprocal, $1/C$, of the capacitance of the RC mesh, while the angular frequency ω at the maximum of the semicircle measures the reciprocal of its time constant, $\tau = RC$. The angular frequency increases in the direction of increasing ωZ". The R and C values relative to the four RC meshes vary appreciably with the applied potential. To this end, a generic approximate approach was developed, which applies the concepts of impedance spectroscopy to a model of the electrified interface and to the kinetics of potassium ion transport assisted by valinomycin across the tBLM.[3] This permits the four RC meshes to be ascribed to four different slabs composing the tBLM. Proceeding in the positive direction of the abscissas, the first semicircle has the highest resistance and was ascribed to the lipoic acid residue, in direct contact with the electrode surface. The second semicircle has a capacitance of about 7 $\mu F\ cm^{-2}$, close to that of a monolayer of tetraethyleneoxythiol self-assembled on mercury, and was ascribed to the TEO moiety. The third semicircle in the absence of valinomycin has a capacitance close to 1 $\mu F\ cm^{-2}$, a value typical of a conventional solvent-free BLM, and was reasonably ascribed to the lipid bilayer moiety.

Finally, the last semicircle has the same resistance as the electrolyte solution and a very low capacitance, of the order of 1 nF cm^{-2}, and was ascribed to the electrolyte solution adjacent to the tBLM.

The same tBLM was used to incorporate the peptide melittin, whose α-helical monomers aggregate in the lipid bilayer to form an ion channel.[190] The impedance spectrum was again fitted to an equivalent circuit consisting of four RC meshes, and the capacitance C_m and resistance R_m of the mesh ascribed to the lipid bilayer moiety were examined as a function of the applied potential and of the lipid composition of the bilayer. The bilayer conductance, $1/C_m$, was found to increase abruptly above the background level at a sufficiently negative applied potential, attaining a maximum value, in agreement with the voltage-gated nature of the melittin channel. In fact, it is known that the melittin molecules lie flat on the surface of biomembranes and penetrate them only when the transmembrane potential on the opposite side of the biomembrane becomes sufficiently negative. The conductance increases with the composition of the distal monolayer of the tBLM in the order DOPC:cholesterol (60:40) < DOPC < DOPC:sphingomyelin:cholesterol (59:15:26) < DOPS. When using the ternary mixture, which may form lipid rafts, a fifth RC mesh of high capacitance and low resistance is clearly visible in the M plot; it disappears at the same applied potential at which the conductance increases abruptly. This behavior was tentatively ascribed to the formation of a melittin layer on top of the lipid rafts of the distal mixed lipid monolayer: at the applied potential at which the melittin molecules penetrate the lipid bilayer, this melittin layer is disrupted. The sigmoidal charge vs. time curves following a potential step from a value at which melittin channels are not formed to one at which they are formed was interpreted on the basis of a generic kinetic model.[191] This model accounts for the potential-independent disruption of melittin clusters adsorbed flat on the lipid bilayer, induced by the potential-dependent penetration of the resulting monomers into the lipid bilayer; the potential-independent aggregation of the monomers inside the bilayer with channel formation is then treated on the basis of a mechanism of nucleation and growth. This explains the initial induction period responsible for the sigmoidal shape of charge vs. time curves.

The channel-forming protein OmpF porin from *Escherichia coli* was incorporated in a mercury-supported DPTL/DPhyPC bi-

layer, and the resulting impedance spectrum in aqueous KCl was fitted by an equivalent circuit consisting of four RC meshes.[183] The dependence of the resulting circuit elements upon the applied potential was interpreted on the basis of an approximate approach based on a model of the electrified interface and on the kinetics of the translocation of potassium and chloride ions across the lipid bilayer. Incorporation of OmpF porin increased the conductivity of the lipid bilayer moiety of the tBLM over a narrow potential range straddling the zero value of the potential difference across the lipid bilayer moiety.

Gramicidin is a peculiar channel-forming peptide whose helical structure differs from the α-helix of common peptides and membrane proteins by the fact that it has a lumen large enough to allow the passage of simple desolvated monovalent cations. Since its length is about one half that of a biomembrane, it spans the membrane by forming a dimeric channel. The C-terminuses of the two gramicidin monomers composing a dimer contain three tryptophan residues that form hydrogen bonds with the polar heads of the lipid bilayer. Consequently, the corresponding N-terminuses are directed toward each other, in the middle of the lipid bilayer, just as the dipole moments of the two monomeric units. A transmembrane potential different from zero is, therefore, expected to favor electrostatically one monomeric orientation at the expense of the other, thus destabilizing the dimer. Nonetheless, the stationary current due to the flow of potassium ions along gramicidin channels incorporated in a conventional BLM increases with an increase in the transmembrane potential, exhibiting an almost quadratic dependence.[192] This behavior was confirmed by incorporating gramicidin in a mercury-supported DPTL/DPhyPC bilayer and by carrying out a series of potential steps from a potential positive enough to repel potassium ions from the TEO spacer to progressively more negative potentials and by recording the resulting charge vs. potential curves.[2] The slope of the initial portion of these curves measures the stationary current due to the ionic flux. Plotting this current against the transmembrane potential yields a curve in good agreement with that obtained with conventional BLMs. To explain this behavior, it was assumed that the rate constant for dimer formation increases in parallel with an increase in the ionic flux. In fact, when the time elapsed between the passage of two consecutive cations through the junction between the two

monomers forming the conducting dimer starts to become comparable with, and ultimately shorter than, the time required for the dissociation of the two monomers, such a dissociation becomes increasingly less probable. The curve calculated on the basis of this assumption was in good agreement with experiment.

The HERG K^+ channel is present in the plasma membrane and consists of four identical subunits, each spanning the membrane with six α-helixes. It may exist in one of three conformations: a closed (C), an open (O) and an inactive (I) conformation.[193] At the rest potential, the transmembrane potential (measured with respect to the potential on the extracellular side of the plasma membrane, taken conventionally equal to zero) is negative, and the HERG channel is in the C conformation. If we carry out a positive potential step that annihilates the transmembrane potential (a process called depolarization) the channel passes slowly from the C to the O conformation, but very rapidly from the O to the I conformation; consequently, the resulting outward flux of potassium ions is small and lasts for about one millisecond. If we then carry out a subsequent potential step to a value more negative than the rest potential (a process called hyperpolarization), the channel passes rapidly from the I to the O conformation and slowly from the O to the C conformation. Consequently, the inward flux of potassium ions is much higher than the outward flux, and lasts for more that 100 ms. The HERG K^+ channel was incorporated in a mercury-supported DPTL/DPhyPC bilayer from its aqueous solution in the detergent Triton X-100.[184] At a potential of –300 mV/SCE, corresponding to a transmembrane potential of +150 mV, the channel is in the I conformation. By stepping the applied potential to –720 mV/SCE, corresponding to a transmembane potential of about –270 mV, the HERG channel passes rapidly from the I to the O conformation, and then slowly to the C conformation. Figure 16 shows the charge vs. time curve following this potential step. The charge first increases rapidly due to the charging of the double layer, and then more slowly, due both to the flux of potassium ions induced by the opening of the HERG channel and to the nonspecific ionic flux across the membrane. To extract the charge ascribed exclusively to the opening of the HERG channel, the same potential step was repeated after adding WEY, a specific inhibitor of the HERG channel. By subtracting the charge transient in the presence of WAY from that in its absence, the

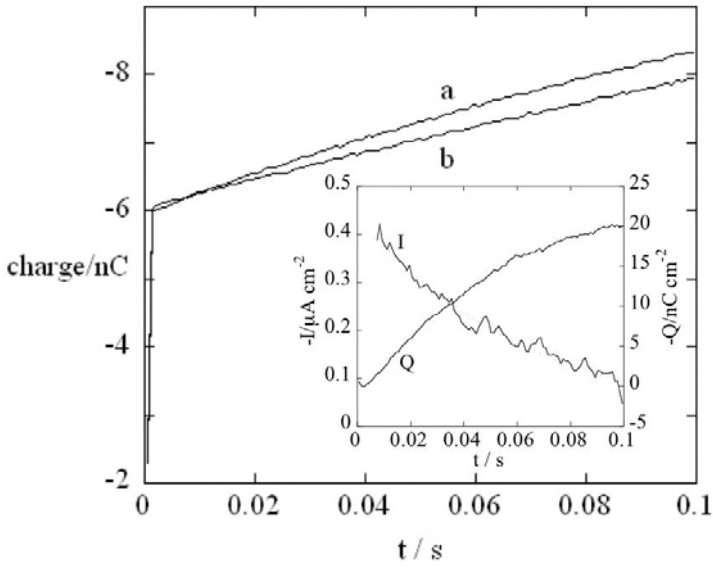

Figure 16. Charge vs. time *t* curves following a potential step from –0.300 to –0.720 V/SCE at a tBLM incorporating the HERG channel in 0.1 M KCl, both before (*a*) and after addition (*b*) of 5 μM WAY. The inset shows the curve of the charge *Q* against time t, obtained by subtracting curve (*b*) from curve (a), and the corresponding curve of the current *I* against *t*; both *Q* and *I* are ascribable to the HERG channel activation.[184]

charge vs. time curve due exclusively to the opening of the HERG channel was obtained, as shown by the inset of Fig. 16. The same procedure was followed to obtain the corresponding current versus time curve; this curve shows a monoexponential decay with time, with a time constant in good agreement with that obtained by the patch-clamp technique with conventional BLMs.

Sarcolipin (SLN) and phospholamban (PLN) are two small membrane proteins that modulate the function of Ca-ATPase of the sarcoplasmic reticulum. They were incorporated in a mercury-supported DPTL/DPhyPC bilayer to verify whether these two proteins may form ion-selective pores in biomembranes.[194-196] SLN inhibits the Ca-ATPase activity at low Ca^{2+} concentrations. However, it is also reported to increase the level of Ca^{2+} accumulation

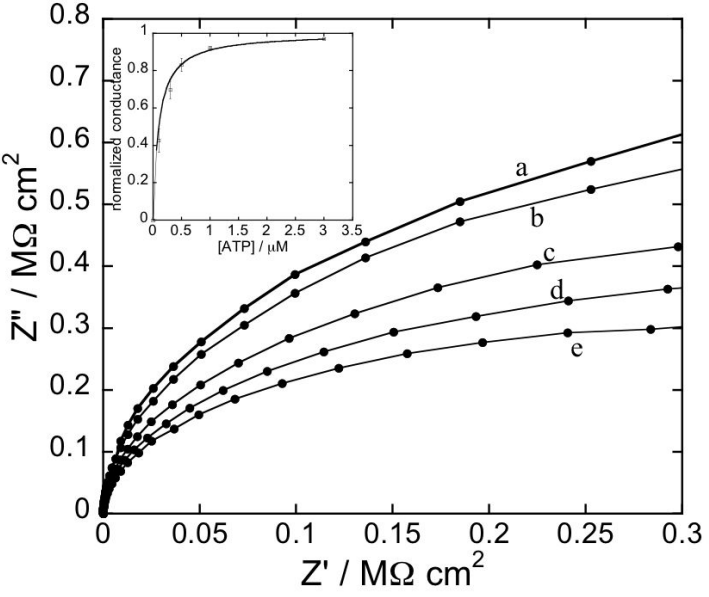

Figure 17. The solid circles are experimental points on a Z″ vs. Z′ plot for a tBLM in a pH 5.3 aqueous solution of 0.05 M NaH_2PO_4 at -0.500 V vs. Ag/AgCl(0.1M KCl) in the absence of SLN (*a*), after incorporation of SLN from its 0.7 μM solution (*b*), and after subsequent additions of 0.1 (*c*), 0.3 (*d*) and 3 μM ATP (*e*). The solid curves are fits of a series of four RC meshes to the solid circles. The values of the resistance, R_m, of the lipid bilayer moiety resulting from the fits are: 0.90 (*a*), 0.70 (*b*), 0.53 (*c*), 0.42 (*d*) and 0.35 (*e*) MΩ cm^2. The corresponding C_m values are all close to 1 μF cm^{-2}. Inset: Conductance, $1/R_m$, normalized to its maximum value equated to unity, as a function of the ATP concentration. The error bars denote standard deviations. The solid curve is a fit of the Michaelis-Menten equation to the experimental points.[195]

in the lumen of the SR at high calcium ion concentrations. It consists of a single α-helix that spans the whole membrane. It was shown that SLN forms channels highly selective toward small inorganic anions, such as chloride ion.[194] The resistance of the tBLM immersed in a 0.05 M aqueous solution of the sodium salt of the tetravalent anion adenosyntriphosphate (ATP), which does not permeate biomembranes, does not change upon incorporating SLN. This indicates that SLN does not allow the translocation of

simple monovalent cations such as sodium ion. On the other hand, if the sodium salt of ATP is diluted with an equal volume of a NaCl solution containing the same concentration of Na^+ ions, the resistance decreases by about one order of magnitude, indicating that SLN allows the translocation of the small chloride anion across the lipid bilayer. Incorporation of SLN in a tBLM immersed in a pH 5.3 aqueous solution of 0.05 M NaH_2PO_4 causes only a slight decrease in the resistance of the lipid bilayer, as measured by the diameter of a Z' vs. Z' plot (Nyquist plot; cf. Section III); however, submicromolar additions of ATP decrease the resistance of the tBLM to an appreciable extent, as shown in Fig. 17.[195] Plotting the conductance against the ATP concentration yields a curve that tends asymptotically to a limiting value and can be satisfactorily fitted by the Michaelis-Menten equation, with an association constant for the SLN-ATP complex of about 0.1 μM (see the inset of Fig. 17).

This behavior was explained by regarding a SLN channel as consisting of a bundle of four or five SLN α-helixes that turn their hydrophilic side, containing two hydrophilic threonine residues, toward the interior of the bundle; this provides a hydrophilic pathway for small desolvated inorganic anions, such as chloride ion. Phosphate ion is somewhat bulkier than chloride ion. However, SLN contains a positively charged arginine residue (Arg6) just outside the lipid bilayer, on its cytoplasmic side. ATP was assumed to bind electrostatically to this arginine residue. The repulsion among the highly negatively charged ATP molecules bound to Arg6 should widen the lumen of the SLN channel, thus allowing the passage of phosphate ions. On the basis of this and other features of SLN, it was proposed that SLN is just the P_i *transporter* described by Lee and coworkers[197] on 1991 and whose nature was not known up to now. The role of SLN is that of translocating phosphate ions from the cytoplasm to the lumen of the sarcoplasmic reticulum, thus causing the precipitation of calcium phosphate and increasing the level of Ca^{2+} accumulation in the lumen.

Phospholamban (PLN) exists in equilibrium between the pentameric and monomeric forms. The pentamer releases to Ca-APTase a monomer, which forms a 1:1 complex inhibiting the affinity of Ca-ATPase for Ca^{2+}.[198] Phosphorylation of the monomer by ATP removes the inhibition. Both SLN and the PLN monomer have a single α-helix that spans the membrane. As distinct

from SLN, PLN has a large cytoplasmic domain. The two α-helixes are quite similar, having several identical residues. The main difference between the SLN and the PLN helix is represented by the presence of two hydrophilic threonines in the SLN helix, which occupy positions analogous to those of two hydrophobic cysteines, C41 and C46, in the PLN helix; the two cysteines play a fundamental role in the stabilization of the PLN pentamer, by forming hydrogen bonds. Incorporation of PLN in a mercury-supported DPTL/DPhyPC bilayer does not affect its resistance over the physiological range of transmembrane potentials.[196] It was concluded that the absence of the two threonine residues prevents the PLN pentamer from forming a hydrophilic pore. An analogous lack of ion channel activity was exhibited by the T18A mutant of SLN, where the Thr18 hydrophilic residue is replaced by a hydrophobic alanine residue.[195] This confirms the role played by the threonine residues in the ion channel activity of SLN.

A mercury-supported tBLM was formed at the tip of a microelectrode for measuring single-channel activity.[199] To this end, use was made of a platinum wire embedded in a thin glass capillary and terminated with a platinum microdisk, about 20 μm in diameter. Mercury was electrodeposited on this microdisk from a pH 1 mercurous nitrate aqueous solution, giving rise to a mercury spherical cap that was coated with a DPTL/DPhyPC bilayer. The resistance of this *tethered bilayer lipid micromembrane* ranged from 5 to 30 GΩ and was, therefore, high enough to decrease the electrical noise to the very low level required for the recording of single-channel currents by the patch-clamp technique. Its differential capacitance amounted to 1.0 μF cm^{-2}, denoting the formation of a well-behaved solvent-free lipid bilayer. The channel protein OmpF porin from the outer membrane of *Escherichia coli* was incorporated in this micromembrane from its aqueous solution in the detergent Triton X-100. Figure 18 shows the single channel currents due to the opening of the OmpF porin channel as a function of time at different applied potentials. A burst of single channel currents is observed at –400 mV/SCE, and to a minor extent at –500 mV, which corresponds to a zero transmembrane potential. This behavior is consistent with the well known property of OmpF porin, according to which this channel protein undergoes inactivation on both sides of the zero transmembrane potential.

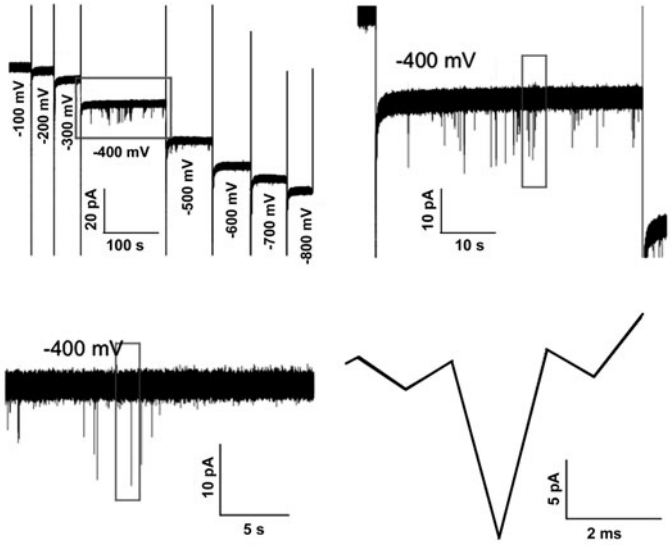

Figure 18. Single-channel traces of OmpF porin from *Escherichia coli* incorporated in a mercury-supported tethered bilayer lipid micromembrane immersed in aqueous 0.1 M KCl, at different applied potentials measured vs. a Ag/AgCl(3M KCl) reference electrode. Potentials must be decreased by 50 mV to refer them to the SCE.[199]

This micromembrane was also used to investigate the spontaneous formation of microdomains, when the distal monolayer is made up of a lipid mixture. Microdomains are in the gel state when they consist primarily of a lipid with a transition temperature from the gel to the liquid crystalline state (also called melting temperature, T_m) higher than room temperature, such as sphingomyelin. When these microdomains also contain cholesterol to an appreciable extent, they become fluid, albeit more ordered and tightly packed than the surrounding lipid matrix, consisting primarily of lipids with T_m lower than room temperature, such as DOPC. The latter microdomains, called *lipid rafts*, are qualified as *liquid-ordered*, to distinguish them from the *liquid-disordered* lipid matrix. Lipid rafts are microdomains, composed of glycolipids,

sphingolipids and cholesterol, which are present in the outer leaflet of plasma membranes. Rafts are receiving increasing attention since they are considered to regulate the membrane function in eukaryotic cells. The presence of microdomains was directly visualized from the image of the distal lipid monolayer, by using two-photon fluorescence lifetime imaging microscopy (2P-FLIM).[39] The distal monolayer consisted of a sphingomyelin:DOPC:cholesterol (47:47:6) mixture, with the addition of 1 mol% laurdan. Laurdan is a fluorophore that is known to distribute uniformly in coexisting gel, liquid-ordered and liquid-disordered phases. It emits in the blue region of the optical spectrum and has a longer lifetime in the gel phase, while it emits in the green region and has a shorter lifetime in the liquid-disordered phase. The fluorescence lifetime image of the distal lipid mixture shows a high degree of heterogeneity and is characterized by the coexistence of gel, liquid-ordered and liquid-disordered phases. Microdomains with an irregular percolative-like shape and lifetimes of 3450±50 ps are ascribed to the gel phase. Small roundish microdomains immersed in the surrounding matrix have lifetimes of 2830±50 ps and are attributed to the liquid-ordered phase. Finally, the matrix, with intermediate fluorescence lifetimes, is ascribed to the coexistence of the liquid–disordered phase and of liquid-ordered microdomains of size below the resolution of the microscope (about 0.4 μm radial).

(*iii*) (*Thiolipid-Spacer*)-*Based tBLMs*

A mixture of a short hydrophilic spacer anchored to gold via a sulfhydryl or disulfide group (e.g., mercaptoethanol or dithiodiglycolic acid) and of a thiolipid with its terminal hydrophobic group (e.g., a cholesteryl[13,14] or a phytanyl group[34]) capable of pinning a lipid bilayer gives rise to a practically aqueous region sandwiched between the short spacer and the lipid bilayer (see Fig. 19); this may favor the accommodation of the extramembrane domains of relatively bulky membrane proteins. Deposition of a lipid bilayer onto such a mixture of a short spacer and of a thiolipid is usually carried out by vesicle fusion or by rapid solution exchange. The resulting lipid bilayer has a capacitance of about 0.5–0.6 μF cm^{-2} and a resistance higher than 5 MΩ cm^2. These values com-

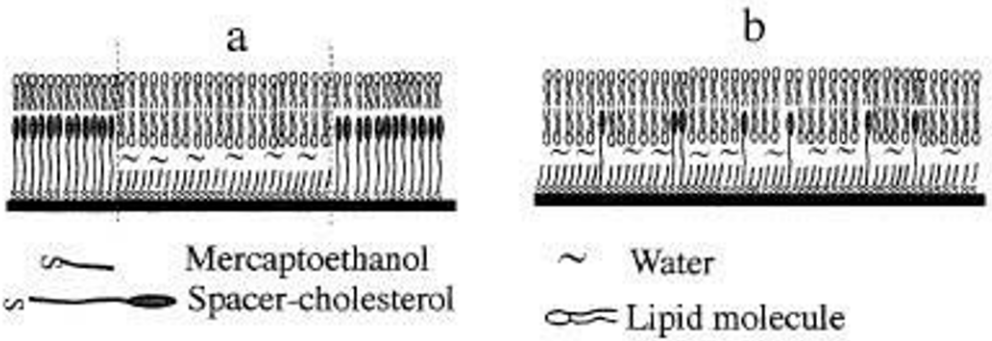

Figure 19. (a) Schematic picture of a micropatterned film consisting of distinct areas covered by a mercaptoethanol monolayer with a lipid bilayer on top, and by a monolayer of a hydrophilic spacer covalently bound to a cholesteryl group with a lipid monolayer on top. (b) Schematic picture of a mixed monolayer of mercaptoethanol and spacer-cholesterol molecules with a lipid bilayer on top.

pare favorably with those of conventional BLMs. Ion-channel activity of gramicidin and melittin incorporated in such a tBLM and ion-selectivity of gramicidin were verified by EIS.[34] However, here too, the lateral mobility of the lipid bilayer is hindered by the hydrophobic group of the thiolipid molecules, which provides a fraction of the proximal leaflet of the lipid bilayer.

The ability of the volume enclosed between the gold electrode and the lipid bilayer moiety of (thiolipid-spacer)-based tBLMs to accommodate water molecules and inorganic ions was estimated from the level of conductance induced by the incorporation of a given amount of the ionophore valinomycin. This ionic reservoir was simulated by a capacitance C_s and the lipid bilayer by an R_mC_m mesh. By using a number of thiolipids and spacers of variable length, Cornell and coworkers[34] found that the conductance, $1/R_m$, of the lipid bilayer increases with an increase in the length of the thiolipid and with a decrease in that of the spacer. In a subsequent paper, the same authors used a long thiolipid terminated with a benzyl disulfide anchor in order to increase the separation among the thiolipid molecules, and mixed it with different proportions of the short mercaptoacetic acid disulfide. The capacitance, C_s, of the ionic reservoir of the resulting tBLMs was regarded as consisting of the capacitance, C_H, of tightly bound inorganic ions in series with the capacitance, C_d, of diffuse layer ions, in analogy with the Helmholtz layer and diffuse layer capacitances at a bare gold electrode.[200] The separation between the C_H and C_d capacitances was estimated from the dependence of the overall capacitance C_s of the ionic reservoir on the bulk ionic concentration and on the applied potential. As a matter of fact, the situation within the ionic reservoir is somewhat different from that at a bare electrode because the inorganic ions are prevented from coming in direct contact with the electrode surface, due to the presence of the short spacer and of the benzyl ring.

Relatively bulky membrane proteins with extramembrane domains can be accommodated in the bilayer if the areas covered by the short thiolated spacer are sufficiently large. Differences in chain length[201] and chemistry[202] between thiolipids and spacers may hopefully favor the formation of phase-demixed domains on the nanoscale, facilitating protein incorporation. This seems to be the case with mixed monolayers of cholesteryl-based thiolipids and short thioalcohol spacers on gold.[203] Reductive desorption

peaks of these mixtures yield well-formed single peaks at mole fractions close to 100% of any of the two pure components, whereas two partially overlapping peaks are observed at intermediate mole fractions. This indicates that phase separation takes place over an intermediate mole fraction range. No tBLMs were observed by EIS when trying to fuse vesicles on tethered mixed monolayers with thiolipid mole fractions below this intermediate mole fraction range. These results were confirmed by friction AFM images in air, recorded with a hydrophilic cantilever tip. Hydrophobic heightened domains due to repulsion between the tip and the hydrophobic thiolipid were observed at intermediate mole fractions.

A relatively high resistance of 0.1 MΩ cm^2 was attained by fabricating a micropatterned monolayer of a thiolated triethyleneoxy chain covalently bound to a cholesteryl group, whose hydrophobic surface was covered by a lipid monolayer formed by vesicle splitting and spreading;[5] this micropatterned film had 15 μm × 15 μm square holes filled with a mercaptoethanol monolayer, whose hydrophilic surface was covered by a lipid bilayer formed by vesicle unrolling and spreading. The square holes filled with the short mercaptoethanol molecules and the lipid bilayer on top are believed to be preferential sites for the incorporation of integral proteins. In fact, the rigidity of the cholesteryl groups and their anchorage to the electrode via the thiolated triethyleneoxy chain make the mixed cholesteryl/lipid bilayer less suitable for protein incorporation than the liquid-crystalline lipid bilayer on top of the mercaptoethanol monolayer. Biofunctionality of this tBLM was confirmed by incorporation of the ionophore valinomycin and the channel-forming peptide gramicidin, which exhibited the expected ion selectivity. Instead of using a microcontact printing on gold, an alternative approach consisted in transferring a mixture of a thiolipid and of palmitic acid to a gold substrate by the Langmuir-Blodgett technique. The regularly distributed domains of palmitic acid on gold were then washed away in a suitable solvent, while the covalently bound thiolipid was not removed; the resulting domains of bare gold were then filled with a mercaptoethanol monolayer.[89] Besides microcontact printing and Langmuir-Blodgett transfer of phase-separated thiolipid monolayers, deep-UV photolithography was employed for patterning thiol layers on gold surfaces.[204]

Vesicle unrolling was facilitated by using a gold-supported monolayer consisting of a mixture of short-chain polyethyleneoxythiol hydrophilic spacers and of thiolipid molecules consisting of the same spacer covalently bound to a cholesteryl group.[13] These cholesterol derivatives serve as *anchoring units* that penetrate into the outer monolayer of unilamellar vesicles and increase both the fluidity of gel-phase bilayers and the rigidity of liquid-crystalline-phase bilayers. Vesicle fusion on monolayers of mixtures of these colesteryl-based thiolipids and spacers takes place only for fractional surface coverages of the thiolipid exceeding a minimum value. *In situ* investigation of these tBLMs by ATR-FTIR spectroscopy indicates that the distal leaflet of these tBLMs is comprised of pure lipid and the proximal one is comprised of a mixture of cholesteryl and lipid.[205] A particular tBLM was fabricated by anchoring to a smooth template-stripped gold surface a mixture of DPTL and of a spacer (TEGL) in which the two phytanyl chains of the DPTL molecules were replaced by a terminal hydroxyl group (see Fig. 1);[27] a lipid bilayer was then formed on top of this mixture by vesicle fusion. Contact mode and friction mode AFM images of the mixed DPTL-TEGL monolayer seem to exclude phase segregation. Ion-channel activity of gramicidin and melittin incorporated in this tBLM and ion selectivity of gramicidin were verified by EIS.

A gold-supported mixture of a triethyleneoxythiol covalently linked to a cholesteryl group, with a lipid monolayer on top, and of 6-mercaptohexanol, with a lipid bilayer on top, was used to incorporate cytochrome *bo3* (*cbo3*).[4] This is the primary membrane-bound terminal oxidase of *Escherichia coli*, which catalyzes the oxidation of ubiquinol-8 and the reduction of oxygen to water in a process coupled to proton translocation across the cell membrane. Upon incorporating *bo3* and ubiquinone-8 into this tBLM in the presence of oxygen, a reduction cyclic voltammogram was recorded at potentials negative enough to cause ubiquinone-8 electroreduction to ubiquinol-8 on gold. In this way, ubiquinol-8 transfers electrons continuously from the gold electrode to *cbo3*, where it is reoxidized by oxygen to ubiquinone-8, which moves back to the electrode surface. The height of the sigmoidal-shaped catalytic cyclic voltammograms increased with an increase in oxygen concentration, whereas it was completely suppressed upon addition of 1 mM cyanide ion.

A micropatterned layer, consisting of regions of thiolipid molecules with a lipid monolayer on top alternated with regions of mercaptoundecanoic acid with a lipid bilayer on top, was used to incorporate rhodopsin.[204,206] This integral protein contributes to the closing of the Na^+ channels of the plasma membrane of the outer segment of the vertebrate rod cell. When rhodopsin is photoactivated, it starts an enzyme cascade that amplifies the absorption of light by a factor of one million. The first step of this cascade is the interaction of the photoactivated rhodopsin with transducin, a peripheral protein that binds to guanosine-5'-diphosphate (GDP) in its inactive state, and to guanosine-5'-triphosphate (GTP) in its active state, as schematically depicted in Fig. 20. Transducin is

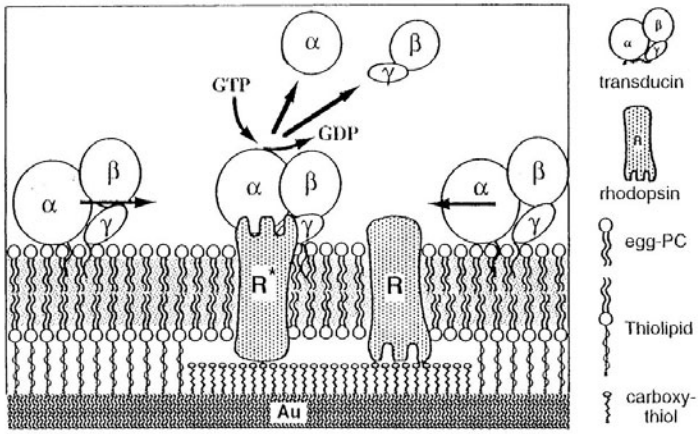

Figure 20. Schematic picture of rhodopsin–transducin coupling on patterned gold-supported bilayers, as described in the text. Rhodopsin is preferentially incorporated in the freely suspended bilayer domains, while transducin is adsorbed indifferently on anchored and freely suspended bilayer regions of the tBLM. When rhodopsin is photoactivated, transducin is depleted only in the freely suspended bilayer regions, and therefore diffuses from anchored to freely suspended bilayer domains. This lateral displacement of transducin and its release from defined domains are observed by one-dimensional imaging SPR. (Reprinted from Ref. [204] with kind permission from the American Chemical Society.)

composed of three subunits, designated α, β and γ. The GDP/GTP binding site is associated with the α subunit. Photoactivated rhodopsin (R*) interacts with the α subunit of transducin by catalyzing the replacement of bound GDP with GTP, which results in the dissociation of the α subunit from the β and γ subunits. Scanning the micropatterned film by SPR shows that rhodopsin is preferentially incorporated into the lipid bilayer on top of the mercaptoundecanoic acid, which is more fluid and has a more water-rich reservoir than the lipid bilayer consisting of the anchored thiolipid with a lipid monolayer on top. On the other hand, the peripheral protein transducin cannot distinguish between the two different lipid-coated regions and is equally adsorbed on both. The progressive increase in film thickness due to transducin binding to the micropatterned film is monitored by SPR, just as the rapid decrease in film thickness due to transducin desorption following rhodopsin photoactivation in the presence of GTP. After interrupting illumination, a slow increase in film thickness is observed, due to transducin rebinding.

The OmpF porin, a pore forming protein present in the outer membrane of *Escherichia coli*, was incorporated in a tBLM consisting of a mixture of a diethyleneoxy-based thiolipid and of a sulphanylpropionic acid spacer.[206,207] This ligand-gated channel acts as a receptor for the antibacterial toxin colicin N, which blocks the channel by binding to its mouth. The conductance of the lipid bilayer incorporating OmpF porin, as measured by EIS, amounts to 1.54 mS cm^{-2}. Progressive additions of colicin N cause a gradual decrease in conductance up to a minimum limiting value of 1.35 mS cm^{-2}. Setting the conductance value in the absence of colicin equal to unity and its limiting value in the presence of colicin equal to zero, the sigmoidal plot of the resulting *normalized* conductance against the logarithm of colicin concentration is practically identical to that obtained at a conventional BLM. However, the limiting value of the conductance at a conventional BLM is more than three orders of magnitude less than the initial value, while at the gold-supported tBLM it is only 15% less. This is due to the poor electrical properties of the lipid bilayer, which allows an appreciable nonspecific ionic flux.

6. Polymer-Cushioned Bilayer Lipid Membranes (pBLMs)

The spaciousness of the ionic reservoir of tBLMs may not be sufficient to accommodate bulky extramembrane domains of membrane proteins. The problem is particularly serious with cell-adhesion receptors, whose functional extracellular domains can extend to several tens of nanometers. Thus, the spreading of proteoliposomes doped with human platelet integrin $\alpha_{IIb}\beta_3$ and ATP synthase on quartz or glass substrates results in inhomogeneous patches of pinned proteins.[208,209] This problem can be circumvented by separating the lipid bilayer from the solid substrate using soft polymeric materials of typically less than 100 nm thickness, which rest on the substrate and support the bilayer. These stratified films are often referred to as polymer-cushioned or polymer-supported bilayer lipid membranes (for a review, see Ref. 210). This approach reduces the non-specific binding of proteins to the solid support and the frictional coupling between proteins and the support, preventing the risk of protein denaturation due to direct contact between protein subunits and the bare support surface. In some cases, the cushion may assist self-healing of local defects in lipid bilayers deposited on macroscopically large supports.

To form a thermodynamically stable polymer-lipid composite film on a solid support in aqueous solution and to avoid the formation of polymer blisters, several requirements should be fulfilled. Specifically, the spreading pressures should be positive for the lipid bilayer on the polymer and for the polymer on the solid support.[211] From a thermodynamic viewpoint, a stratified structure is only stable if each additional layer results in a gain in the total surface free energy. Moreover, the interaction between the lipid bilayer and the substrate surface must be repulsive. In fact, if the net force acting per unit area (disjoining pressure) is negative, continuous thinning of the interlayer results in the film collapse, i.e., dewetting, giving rise to regions of tight local contact between the lipid bilayer and the substrate surface (the so-called pinning centers). Polymer-cushioned membranes are fairly unstable if the attractive interfacial forces between the polymer and the lipid bilayer are relatively weak. In this case, the bilayer can easily detach from the polymer cushion. On the other hand, too strong attractive forces may decrease the lateral mobility of the bilayer. A compromise should, therefore, be found between a sufficient stability of the

polymer/lipid interface and lateral mobility. A possible strategy consists of enhancing the stability of polymer-cushioned membranes via attractive electrostatic interactions.[212] A different approach to stabilization of polymer-cushioned membranes was adopted by Naumann et al. [213] by tethering the polymer both to the substrate and to the membrane. To this end, a benzophenone silane photocoupling agent was tethered to a glass surface via the silane group. A lipopolymer-phospholipid mixture preorganized at the air/water interface was transferred to the benzophenone silane funtionalized glass surface by the Langmuir-Blodgett technique. The benzophenone moiety was then covalently linked to the C-H groups of the polymer chains by UV irradiation. Finally, a DMPC monolayer was transferred by the Langmuir-Schaefer technique from the air/water interface to the cushion, thus adding the distal leaflet of the bilayer to the polymer-cushioned membrane. Long-range lateral mobility within the bilayer was verified by FRAP at 40°C, when DMPC is in the liquid-crystalline state. However, a notable decrease in the lateral mobility of the distal lipid monolayer was observed by increasing the lipopolymer tethering density beyond a certain limit. A similar approach was used by Wagner and Tamm,[214] who prepared lipid bilayers supported by a linear polyethyleneoxy chain derivatized at one end with a triethoxysilane group, for anchoring to a quartz support, and at the other end with DMPE for anchoring to the lipid bilayer. By reconstituting annexin V and cytochrome b_5 in the lipid bilayer, the lateral diffusion of these proteins was measured.

The advantage of using polymer supports can be appreciated when studying biological functions of incorporated cell receptors. Membranes supported by 5-nm thick cellulose films have been used to incorporate cell receptors of the integrin family. When probing the interaction between these pBLMs and giant vesicles exposing integrin-specific ligands, the adhesion free energy for the interaction was comparable with the value inferred from the integrin-ligand dissociation constant.[208] This strongly suggests that integrins fully retain their mobility and native functionality when incorporated in these pBLMs.

Polymer cushions have also been conveniently employed as supports of cellular membranes. Human erythrocyte *ghosts* (i.e., red blood cells after removal of their cytoplasm) were adsorbed over cellulose cushions.[215,216] After incubation of the ghosts for 60

min, the orientation of the erythrocyte membrane was identified with two immune-fluorescence labels. This labeling proved that polymer-supported human erythrocyte membranes are almost free from local defects and expose the cytoplasmic domain to the bulk aqueous phase. The success of this deposition suggests that cellulose cushions fulfill the conditions of complete wetting of cellular membranes and finely tune the cell-surface interactions. However, FRAP experiments showed no sign of lateral diffusion, probably due to the presence of spectrine cytoskeletons.

Usually, polymer cushions are anchored to supports such as glass, silica and mica, by using polymers derivatized with alkyl silanes[20] or triethoxysilane for covalent linkage to silanols at the surface of the silicate substrates.[225] More rarely, they are anchored to gold or to semiconductors such as GaAs via thiolated polymers. Covalent coupling of polymers to silane or thiol anchors can be achieved through epoxy groups, photoactive groups and so-called active esters.[217] A variety of polymeric materials have been employed. These include polyacrylamide,[218] polyethyleneimine, dextran,[219] trimethylsilylcellulose,[220] chitosan[221] and hyaluronic acid[222].

Wong et al.[223,224] characterized lipid bilayers supported by a polyethyleneimine cushion on a quartz substrate by neutron reflectometry and found that thickness, surface roughness and coverage of the polymer depend strongly on the method of preparation. Kühner et al.[218] prepared 30–40 μm thick polyacrylamide gels on glass and coated them with monolayers and bilayers, using Langmuir-Blodgett techniques. When examined by epifluorescence microscopy, these bilayers exhibited residual domain structure. Lateral mobility of a lipid-linked 20-residue peptide antigen was verified in these bilayers. In an extension of this work, the electrophoretic mobility of charged lipids was determined in monolayers that were supported by agarose gels;[225] bilayers did not form on these substrates. In another study, bilayers were formed on a polyvinyl substrate that had functionalized diethylene amino groups for reaction with lipid head groups.[226] Although homogeneous bilayers with high lateral mobility were obtained under some conditions, the hydrophilic linkers were too short to accommodate membrane proteins in this system. Elender et al.[219] were able to form uniformly fluorescent bilayers of DMPC and 20 mol% cholesterol on 600-800 nm cushions of dextran supported by Si/SiO_2 and glass. The

lateral diffusion coefficient and mobile fraction of the lipids were high in this system, which, however, was very unstable in the absence of cholesterol. All above polymer-supported lipid bilayers were deposited on non-conducting supports and, consequently, they are not amenable to electrochemical measurements. These bilayers were often patchy and with several defects.

Polymer-cushioned lipid bilayers on conducting supports have been investigated only rarely. Spinke et al.[227,228] described a polymer-supported lipid bilayer anchored to gold. These authors used a methacrylic terpolymer consisting of a hydrophilic main chain that acts as a spacer, a disulfide unit that anchors the polymer to the gold surface, and a hydrophobic lipid-like part that forms a first lipid monolayer upon self-assembly. A second lipid monolayer was formed on top of the first by fusion with DMPC vesicles. The fusion was followed by SPR, which revealed a maximum increase in film thickness by about 2 nm after 4 h.

Polymer-cushioned lipid bilayers have frequently been investigated on the indium-tin-oxide (ITO) semiconductor. In case of a lipid bilayer deposited on a regenerated (and thus hydrophilic) cellulose cushion, the swollen polymer film behaves like an aqueous electrolyte. Selective ion transport via ion channels and carrier proteins incorporated in the membrane was, therefore, quantitatively evaluated by determining the electric resistance of the membrane.[229] On ITO electrodes, the presence of polymer cushions significantly reduces local defect densities and results in an electric resistance from 5 to 50 times higher than that of a lipid bilayer directly deposited on ITO. [8,138,139]

A hydrophobic cellulose derivative provides not only an environment to a lipid monolayer, but also acts as an electric insulator with an electric resistance as high as 20 MΩ cm^2. When a lipid monolayer is deposited on a semiconductor surface pre-coated with such a polymer insulator, the whole system consists of a conductor-insulator-semiconductor set-up. As the film thickness can be controlled with nm accuracy, the potential drop across the polymer insulator can be controlled precisely. The system can be tuned so as to detect the charging and discharging of the polar heads of the lipid monolayer by monitoring changes in the semiconductor space charge capacitance. When optimized, this simple device should reach a sensitivity of about 1 e/30 nm^2.[230]

7. S-Layer Stabilized Bilayer Lipid Membranes (ssBLMs)

Monomolecular crystalline arrays of protein subunits, called S-layers, are common surface structures of archea and bacteria.[233-237] They constitute the outermost component of the cell envelope of these procaryotic organisms. S-layer subunits can be aligned in lattices with oblique, square or hexagonal symmetry. Since S-layers are monomolecular assemblies of identical protein subunits, they exhibit pores of identical size and morphology. Most S-layers have a rather smooth outer surface and a more corrugated inner surface. In gram-negative archea, S-layers are the only component external to the cytoplasmic membrane; pillar-like extensions of the subunits of the S-layers may even penetrate into the polar head region of the membrane. Conversely, in gram-positive bacteria, the rigid wall component in direct contact with the cytoplasmic membrane is primarily composed of peptidoglycan, a polymer consisting of sugars and amino acids that forms a mesh-like layer. A group of non classical cell wall polymers, called *secondary cell wall polymers* (SCWPs), are covalently bound to muramic acid residues of peptidoglycan and attached non-covalently, presumably by a lectin-type interaction, to the S-layer proteins. SCWPs are composed of disaccharide repeating units and contain pyruvate ketals that provide a negative charge. In gram-negative bacteria, a thin peptidoglycan layer is interposed between an inner membrane and an outer membrane, with an S-layer non-covalently bound to the latter.

Since S-layer subunits of most bacteria interact with each other through non-covalent forces, they can be set free with high concentrations of agents that break hydrogen bonds, such as guanidine hydrochloride or urea. Once the S-layer lattice of a bacterial cell is completely disintegrated and the disintegrating agent is removed by dialysis, the S-layer subunits have the unique capability to reassemble spontaneously in suspension, at the liquid/air interface, on solid surfaces, on spread lipid monolayers and on liposomes. Recrystallization starts at several distant nucleation points on the surface and proceeds until neighboring crystalline areas meet. It this way, a closed mosaic of differently oriented monocrystalline domains is formed. Recrystallization of isolated S-layer proteins on differently charged solid supports reveals an electroneutral outer and a net negative or net positive inner S-layer surface.

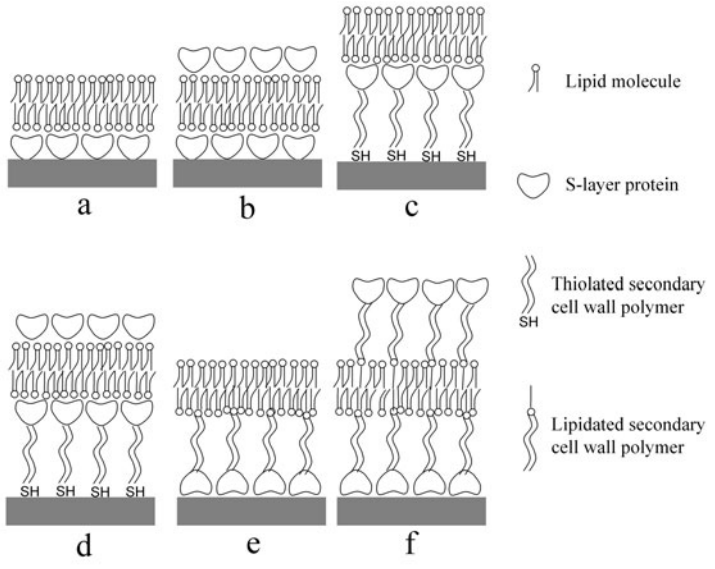

Figure 21. Schematic picture of S-layer stabilized solid supported lipid membranes. (a) S-layer directly recrystallized on gold, with a lipid bilayer on top. (b) Same as (a), with an additional S-layer recrystallized on top of the lipid bilayer. (c) Thiolated secondary cell wall polymers (SCWPs) directly bound to gold and interacting with a S-layer, with a lipid bilayer on top. (d) Same as (c), with an additional S-layer recrystallized on top of the lipid bilayer. (e) S-layer directly recrystallized on gold and interacting with lipidated SCWPs, which anchor a lipid bilayer. (f) Same as (e), with lipidated SCWPs inserted into the distal lipid monolayer and interacting with an additional S-layer.

The natural tendency of S-layers to interact with membranes has been exploited to insert them as an intermediate layer between a lipid bilayer and a substrate, giving rise to the so-called *S-layer stabilized bilayer lipid membranes* (ssBLMs). Thus, in the case of bacterial S-layer proteins, it has been demonstrated that protein domains or functional groups of the S-layer lattice interact via electrostatic forces with some head groups of lipid molecules. In addition, the affinity of S-layer proteins for the corresponding SCWPs, which are recognized as specific binding sites, can be used to fabricate complex architectures (see Fig. 21). Thus, a mon-

olayer of SCWPs, suitably thiolated at one end, can be anchored to a gold support, and a S-layer can be spontaneously recrystallized on top of it; finally, a lipid bilayer can be self-assembled on top of the S-layer. Optionally, the lipid bilayer so formed can be further stabilized by recrystallizing an additional S-layer on top of it. Alternatively, a loose monolayer of lipidated SCWP molecules can be bound to a S-layer previously recrystallized on a substrate; a lipid bilayer self-assembled on top of the SCWP monolayer is then firmly anchored by the lipid moieties of the SCWPs, which penetrate the proximal lipid leaflet. Optionally, the lipidated SCWP molecules present on the outer lipid leaflet can be bound to a further S-layer. All these architectures have a stabilizing effect on the associated lipid bilayer, leading to an improvement in its lifetime and robustness. The assembly of S-layer structures from solution to a solid substrate, such as an Au-coated glass slide, can be followed by SPR or by a QCM-D.[233] The self-assembling process is completed after approximately 45 min. The mass increase followed by QCM-D corresponds to a thickness of about 8-9 nm, in agreement with the value estimated by SPR.

A well-characterized S-layer protein, SbqA from *Bacillus sphaericus* CCM 2177, was used as an ultrathin crystalline, water containing hydrophilic layer between a gold electrode and a lipid bilayer.[234] The SbqA protein recrystallizes in monomolecular square lattices with the neutral outer surface exposed to the aqueous phase and the negatively charged inner surface attached to the gold electrode. A morphological unit, about 170 nm in diameter, consists of four protein monomers. The pores are of identical size and morphology, with a diameter of about 3.5 nm. A SqbA-coated gold substrate was pressed against a polyethylene plastic sheet attached vertically to the open side of a chamber, as shown in Fig. 22a. An orifice, about 1×10^{-3} cm^2 in area, was made through the plastic sheet by punching it with a perforating tool. Alternatively, a piece of SUM was interposed between the gold surface and the plastic sheet (Fig. 22b). SUM (S-layer ultrafiltration membrane) is an isoporous structure with very sharp molecular exclusion limits, manufactured by depositing under pressure up to three stacked S-layer-carrying cell wall fragments on a commercial polyamide microfiltration membrane (MFMs), with an average pore size of approximately 0.4 μm. The 1–4 μm sized S-layer fragments are deposited on the microfiltration membrane as shingles on a roof.

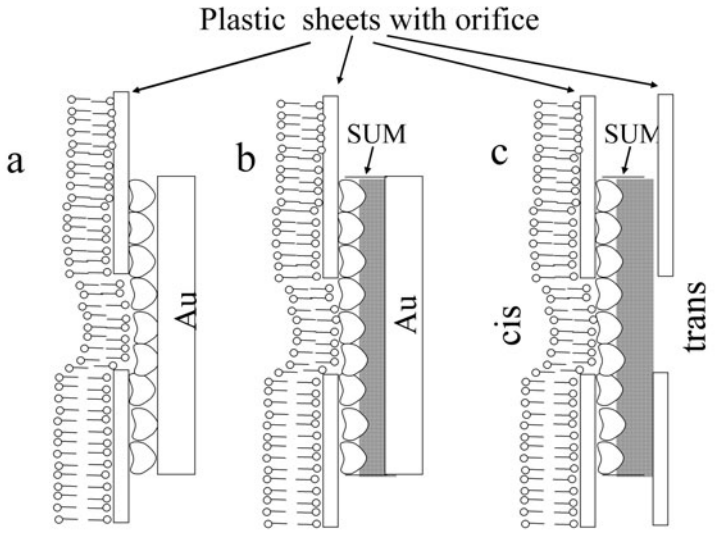

Figure 22. (a) Gold-supported SbpA layer pressed against a perforated plastic sheet, with a lipid bilayer transferred onto the SbpA layer by the Langmuir-Blodgett technique. (b) Same as (a), apart from the replacement of the SbpA layer by SUM. (c) Lipid bilayer supported by SUM and interposed between two bulk aqueous phases.

The side of the SUM with attached the S-layer lattices was turned toward the chamber. A DPhyPC lipid bilayer on top of the SqbA- or SUM-coated gold was formed by a modified Langmir-Blodgett technique. To this end, the chamber was filled with an aqueous electrolyte above the orifice level, a DPhyPC solution is *n*-hexane was spread on the electrolyte surface and the organic solvent was allowed to evaporate. By lowering the electrolyte level below the orifice, a first lipid monolayer was deposited on the coated gold, and a second monolayer was deposited by raising again the electrolyte level.

A tetraetherlipid (TEL) was also used in place of DPhyPC. This is a bipolar, membrane-spanning phospholipid consisting of a 72 member microcycle formed by two glycerol units that are bridged by two biphytanoyl chains. While in phospholipids the alkyl chains are connected to the glycerol moieties by ester bonds, in tetraetherlipids they are connected by four ether bonds, provid-

ing an enhanced robustness under acidic conditions and at high temperatures (up to 100°C). To self-assemble a TEL monolayer (which corresponds to a phospholipid bilayer) on the surface of the coated gold, it is just sufficient to raise the level of the electrolyte, on whose surface a TEL has been previously spread, above the orifice level. The electrochemical properties and the stabilities of the DPhyPC bilayers and of the TEL monolayers were verified by EIS, upon fitting the data by a simple RC mesh. In fact, for practical purposes, the resistance R_Ω of the electrolyte could be neglected. The specific capacitances were 0.53 and 0.69 μF cm^{-2} for DPhyPC bilayers and 0.75 and 0.77 μF cm^{-2} for TEL monolayers resting on SbpA and SUM, respectively. Membrane resistances of up to 80 MΩ cm^2 were observed for DPhyPC bilayers on SbpA. In addition, lipid bilayers supported by SbpA exhibited a long-term robustness of up to two days. Upon incorporating the voltage-gated ion channel alamethicin at open circuit, the membrane resistance dropped from about 80 MΩ cm^2 to about 950 Ω cm^2, whereas the capacitance did not change. Subsequent addition of the inhibitor amiloride caused a modest increase in resistance. The ion-channel activity of the ion carrier valinomycin and its selectivity toward K^+ ions with respect to Na^+ ions were also verified.

In a different approach, the gold support was replaced by an aqueous electrolyte.[235] In this case, the polyethylene plastic sheet was folded in half and interposed between two compartments. An orifice was punched in the two adjacent plastic sheets and a piece of SUM was placed over the aperture, between the two sheets, with the S-layer covered side turned toward the cis compartment (Fig. 22c). Both compartments were filled to just above the aperture with an aqueous electrolyte; a DPhyPC-(dipalmitoylphosphatidic acid) lipid bilayer was then formed on the cis side of the SUM by the same modified Langmuir-Blodgett procedure previously described. For comparison, an unsupported, conventional BLM was also formed across the aperture using the same lipid mixture and the same Langmuir-Blodgett technique. Conventional BLMs and SUM-supported lipid bilayers showed a specific capacitance of 0.6–0.7 μF cm^{-2}. The S-layer produced a stabilizing effect on the lipid bilayer. Thus, the dielectric breakdown voltage of the conventional BLM was 220 mV, whereas the SUM-supported lipid bilayer did not rupture upon application of three

voltage ramps of up to 500 mV, and had lifetimes of up to 8 h. In such a comparison, the potential difference across the SUM was regarded as negligible in view of its very low resistance of about 5 mΩ. Incorporation of α-hemolysin in the SUM-supported lipid bilayer allowed the recording of single channel currents, which were of comparable height with those on conventional BLMs. TEL monolayers were also deposited by the modified Langmuir-Blodgett technique on a SUM interposed between two aqueous phases, in place of phospholipid bilayers.[236] Recrystallization of a S-layer on top of SUM-supported TEL monolayers increased the lifetime of the membrane from about 7 to about 21 h, while leaving the specific conductance unaltered. Gramicidin was incorporated in SUM-supported membranes composed of DPhyPC, TEL and mixtures of DPhyPC and TEL, and single-channel currents were recorded. The selectivity toward K^+ ions was found to be higher than that toward Na^+ ions, in accordance with the behavior at conventional BLMs. However, the conductivity at SUM-supported membranes was significantly lower than that at conventional BLMs. Attempts to span a pure TEL monolayer across the aperture in a plastic sheet without a SUM support by the modified Langmuir-Blodgett technique were unsuccessful.

8. Protein-Tethered Bilayer Lipid Membranes (ptBLMs)

In all the biomimetic membranes previously described and allowing the incorporation of proteins, the protein orientation in the membrane is purely casual. At most, if one of the two extremembrane domains of the protein is much bulkier than the other, incorporation in a tBLM occurs preferentially with the bulkier domain turned toward the aqueous phase, in view of the limited spaciousness of the hydrophilic moiety of the tBLM. Moreover, the packing density of the reconstituted proteins in the lipid bilayer is not well controlled. The need for a well-defined protein orientation with respect to the electrode surface is particularly felt with redox membrane proteins, in which the electrons involved in a chain of redox centers are conveyed across the membrane in a well-defined direction.

To overcome this problem, Knoll, Naumann and coworkers have developed a novel methodology based on tethering proteins, rather than lipids, to the electrode surface; the lipids are then al-

lowed to self-assemble around the tethered proteins.[237] To this end, a recombinant membrane protein is engineered to bear a stretch of six consecutive histidine residues. A gold surface is then functionalized by attaching a molecule terminated with a nitrilotriacetic (NTA) moiety at one end and with a sulfhydryl group for anchoring to gold at the other end. Complexation of Ni^{2+} ions to both the NTA functionality and the histidines of the stretch causes the protein to be anchored to the gold surface from its solution in detergent, as shown in Fig. 23. To retain full functional integrity, the membrane protein is incorporated into a lipid bilayer. For this purpose, the protein layer tethered to gold is mixed with detergent-destabilized lipid vesicles of DMPC. By removing the detergent

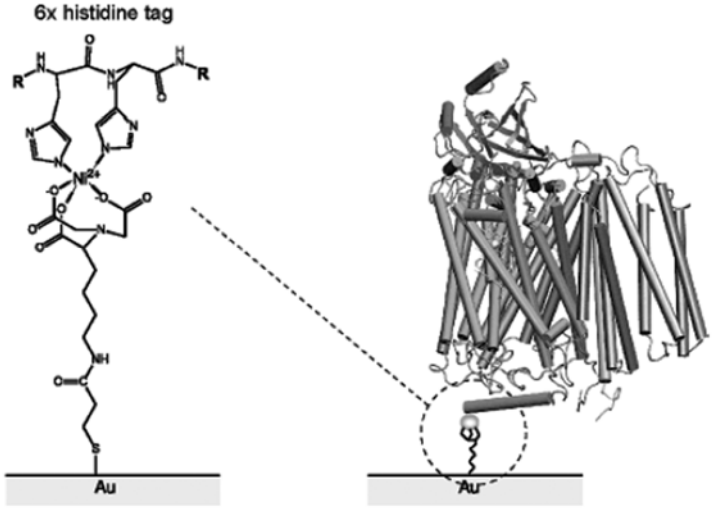

Figure 23. Adsorption of cytochrome *c* oxidase on the Ni-NTA modified Au surface via the His-tag at the C-terminus of subunit I. Two nitrogen atoms of the imidazole rings from two of the histidines of the His stretch coordinate the Ni^{2+} ion. The coordinating histidines residues are not necessarily adjacent in the primary sequence, as drawn in the figure. (Reprinted from Ref. [237] with kind permission from the American Chemical Society.)

with microporous biobeads, the tethered proteins are surrounded by lipid molecules that form a lipid bilayer around them, as verified by SPR and EIS; a water layer remains interposed between the lipid bilayer and the NTA moiety, acting as an ionic reservoir.

This approach has been adopted to investigate the function of cytochrome *c* oxidase (COX) from the proteobacterium *Rhodobacter sphaeroides*.[237] COX is the last enzyme in the respiratory electron transport chain of bacteria, located in the bacterial inner membrane. It receives one electron from each of four ferrocytochrome *c* molecules, located on the periplasmic side of the membrane, and transfers them to one oxygen molecule, converting it into two water molecules. In the process, it binds four protons from the cytoplasm to make water, and in addition translocates four protons from the cytoplasm to the periplasm, to establish a proton electrochemical potential difference across the membrane.

In this protein-tethered bilayer lipid membrane (ptBLM), the orientation of the protein with respect to the membrane normal depends on the location of the histidine stretch (his tag) within the protein. Two opposite orientations of the protein were investigated, either with the cytochrome *c* binding side pointing away from the electrode surface or directed toward the electrode, simply by engineering the his tag on the C terminus of subunit SU I or SU II, respectively. The individual steps of functionalization of the gold support, adsorption of the engineered protein and its reconstitution in the lipid bilayer were followed in situ by means of surface-enhanced infrared absorption spectroscopy (SEIRAS).[237] The functional activity of COX was verified by cyclic voltammetry with both protein orientations. In this connection, it should be noted that electron transfer in COX occurs sequentially through the four redox centers Cu_A, heme a, heme a_3 and Cu_B, in the direction from the binding site of cytochrome *c*, located on the outer side of the bacterial membrane, to its inner side. With the cytochrome *c* binding side pointing away from the electrode surface, the primary electron acceptor, Cu_A, is far from the electrode surface. Hence, in the absence of cytochrome *c*, the cyclic voltammogarm exhibits only a capacitive current. This indicates that COX is not electrically coupled to the electrode, and direct electron transfer does not take place. Under these conditions, the electrochemical impedance spectra were fitted to an equivalent circuit consisting of a capacitance C_s, with in series an R_mC_m mesh and the solution resistance

R_Ω; the capacitance C_s simulates the ionic reservoir and the R_mC_m mesh simulates the lipid bilayer.[238] The capacitance C_m and resistance R_m of the bilayer amount to about 6 μF cm^{-2} and 800 kΩ cm^2. This high capacitance and low resistance denote a loosely packed lipid bilayer, partly ascribable to the presence of a high protein content. As ferri-cytochrome *c* is added in the presence of oxygen, at potentials negative of 270 mV/NHE it starts to be electroreduced to ferro-cytochrome *c*. This triggers an electrocatalytic process whereby, in the enzymatic cavity of COX, ferro-cytochrome *c* is oxidized by oxygen to ferri-cytochrome *c*, which can be continuously electroreduced to ferro-cytochrome *c*. This gives rise to a reduction current in the negative potential region.

When the COX is oriented with the cytochrome *c* binding side pointing toward the electrode surface, the primary electron acceptor, Cu_A, is also oriented toward the electrode. In this case, the cyclic voltammogram in the absence of oxygen shows a single reduction peak at about –274 mV/NHE, due to the electroreduction of the enzyme, and a corresponding oxidation peak at about –209 mV/NHE.[239,240] The peak currents increase linearly with the scan rate, denoting a surface confined process. Moreover, scan rates < 1 V s^{-1} leave the peak potentials unaltered, indicating that the electron transfer is reversible (i.e., in quasi-equilibrium) at these scan rates. The fact that the reduction and oxidation peak potentials do not coincide was ascribed to some purely chemical protonation step within the protein. The midpoint potential is shifted by about -450 mV with respect to the standard potential of +230 mV/NHE, determined for the Cu_A redox center in isolated COX. This was explained by assuming that the first transient electron acceptor in the reduction process is not the Cu_A center, but rather the Ni(II) ion of the Ni(II)/Ni(I) redox couple of the Ni-NTA complex. At scan rates < 1 V s^{-1}, oxidation and reduction peaks are slightly asymmetric. A further increase in scan rate enhances this asymmetry, leading to the appearance of a second peak at scan rates > 20 V s^{-1}, as shown in Fig. 24. The resulting complex voltammogram of the four-redox-site COX protein was deconvoluted into four Gaussian components. Kinetic parameters of the four one-electron transfer steps, one for each redox center, were extracted from the plots of the four deconvoluted peak potentials against the logarithm of the scan rate (the so-called *trumpet* plot).

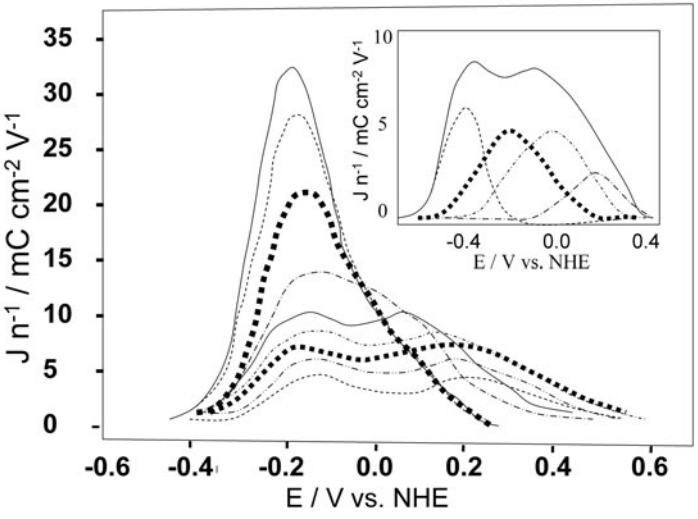

Figure 24. Oxidative branches (baseline-corrected) of the cyclic voltammograms of COX with the his tag attached to subunit II in the absence of oxygen, at scan rates between 1 and 600 V s^{-1} (current densities normalized by the scan rate, ≅ 1 V s^{-1}). Proceeding downwards, the scan rate increases in the order: 1, 3, 7.5, 20, 40, 300, 400, 500, and 600 V s^{-1}. Inset: Example of a deconvolution into four Gaussian components. (Reprinted from Ref. [239] with kind permission from Elsevier.)

Strong evidence that the electron transfer observed by cyclic voltammetry takes place directly within the enzyme was derived from Soret band excited surface-enhanced resonance Raman spectroscopy (SERRS) taken as a function of potential.[240,241] The cyclic voltammogram of COX oriented with the cytochrome *c* binding side directed toward the electrode was used to determine the functional activity of the enzyme as a function of its surface density.[242] This density was varied by diluting the thiol functionalized with the chelator nitrilotriacetic (NTA) moiety with a non-functionalized thiol that did not bind to the enzyme. At low COX surface densities, the bilayer does not effectively form, and protein aggregates are observed; on the other hand, at very high surface densities, very little lipid is able to intrude between the closely packed protein molecules. In both cases, redox activity is low. Redox activity is preserved in the biomimetic membrane only at

moderate surface coverages, in which a continuous lipid bilayer is present and the protein molecules are not forced to aggregate.

In the presence of oxygen, electrons transferred from the electrode to the redox centers of COX are irreversibly transferred to oxygen, leading to a notable increase of the reduction peak, which now lies at –202 mV/NHE, and to a continuous electron transfer. The cyclic voltammogram also shows a further reduction peak at –422 mV/NHE. This is due to the catalytic turnover of COX, which reduces oxygen to water and pumps protons into the interstitial space between the electrode and the lipid bilayer. Proton electroreduction at the electrode surface determines the second reduction peak. The absence of direct electron transfer and of proton electroreduction when COX is oriented with the cytochrome *c* binding site turned toward the solution confirms the orientation dependence both of direct electron transfer and of transmembrane proton transport.

VI. CONCLUSIONS

The use of electrochemical techniques such as cyclic voltammetry, EIS and charge transient recordings for the investigation of biological systems is becoming increasingly popular, just as the application of the concepts of electrochemical kinetics and of the structure of electrified interfaces to the interpretation of the electrochemical response.

Several efforts are presently made to realize biomembrane models consisting of a lipid bilayer anchored to a solid electrode through a hydrophilic spacer and satisfying those requirements of ruggedness, fluidity and high electrical resistance that are necessary for the incorporation of integral proteins in a functionally active state. A unique feature of these biomembrane models is the achievement of the maximum possible vicinity of a functionally active integral protein to an electrode surface (the electrical transducer). The capacitive currents resulting from the activation of ion pumps, transporters, channel proteins and channel-forming peptides incorporated in these biomembrane models can be analyzed over a broad potential range by electrochemical techniques, which are by far less expensive than other techniques presently adopted.

The realization of these biomembrane models allows fundamental studies of the function of integral proteins. Biomimetic membranes are ideally suited to elucidate many problems in molecular membrane biology, by permitting a reliable and rapid functional screening of a large number of mutant receptor proteins. This will open the way to the elucidation of structure-function relationships in ligand-receptor and protein-protein interactions. Moreover, the development of biomimetic systems that incorporate therapeutically or diagnostically important natural proteins will open the door to the realization of sensors targeting biological analytes. Making biomembrane models sufficiently insulating and free from pinholes and other defects that might provide preferential pathways for electron and ionic transfer across the lipid bilayer is a particularly challenging goal in the characterization of ion channel activity. It can be tackled by making the solid support as smooth as possible, by using micropatterned solid-supported lipid bilayers formed via microcontact printing on gold, or by synthesizing hydrophilic and amphiphilic spacers with an architecture that may favor highly compact monolayers.

Many practical applications are foreseen for these sensors, such as the detection of drug candidates modulating the function of ion channels and pumps or targeting membrane receptors. In this respect, there is strong need to develop novel, rapid and highly sensitive methods for drug screening, capable of selecting and analyzing a huge number of compounds. At present, screening of pharmacologically active compounds follows traditional procedures that apply time-consuming ligand-binding studies and receptor-function tests separately. Thus, for instance, the function of ion channels and transporters is traditionally characterized in detail by patch clamp studies, which investigate the proteins in their natural environment, the cellular membrane. These assays are tedious to perform and difficult to automate at high throughput, making the investigation of many samples difficult. The lack of knowledge about the different functions of these channels is due to a lack of specific inhibitors, which are unavailable due to the lack of efficient measuring systems. Present ligand-binding experiments identify only ligands to already known binding sites on the protein(s) of interest and neglect other potentially more interesting sites. Moreover, they cannot easily differentiate between agonists and antagonists. Thus, the direct, predominantly electrochemical de-

termination of the function of ion channels and pumps in biomembrane models reconstituted from purified components addresses a strongly felt need for the development of new drug candidates or diagnostic test systems.

ACKNOWLEDGMENTS

Thanks are due to Ente Cassa di Risparmio di Firenze for financial support to the authors' research on metal-supported biomimetic membranes. The technical support by Dr. Giovanni Aloisi in the preparation of the manuscript is gratefully acknowledged.

ACRONYMS

AFM	Atomic force microscopy
ATR-FTIR	Attenuated total internal-reflection Fourier-transform infrared spectroscopy
BLM	Bilayer lipid membrane
COX	Cytochrome *c* oxidase
DMPC	Dimyristoylphosphatidylcholine
DMPE	Dimyristoylphosphatidylethanolamine
DOPA	Dioleoylphosphatidic acid
DOPC	Dioleoylphosphatidylcholine
DOPE	Dioleoylphosphatidylethanolamine
DOPS	Dioleoylphosphatidylserine
DPhyPC	Diphytanoylphosphatidylcholine
DPPC	Dipalmitoylphosphatidylcholine
DPPE	Dipalmitoylphosphatidylethanolamine
DPTL	2,3-Di-*O*-phytanyl-sn-glycerol-1-tetraoxyethylene glycol-D,L-α-lipoic ester
Egg-PC	Egg-phosphatidylcholine
EIS	Electrochemical impedance spectroscopy
FRAP	Fluorescence recovery after photobleaching
GUV	Giant unilamellar vesicle
ITO	Indium tin oxide
NR	Neutron reflectivity
PBLM	Polymer-cushioned bilayer lipid membrane

POPC	Palmitoyloleoylphosphatidylcholine
PtBLM	Protein-tethered bilayer lipid membrane
QCM	Quartz crystal microbalance
QCM-D	Quartz crystal microbalance with dissipation monitoring
SBLM	Solid-supported bilayer lipid membrane
SEIRAS	Surface-enhanced infrared absorption spectroscopy
SERRS	Surface-enhanced resonance Raman spectroscopy
SPR	Surface plasmon resonance
SsBLM	S-layer stabilized bilayer lipid membrane
SUV	Small unilamellar vesicle
TBLM	Tethered bilayer lipid membrane
TEGL	Tetraoxyethylene glycol-D,L-α-lipoic acid ester
TEO	Tetraethyleneoxy

REFERENCES

[1]S. M. Schiller, R. Naumann, K. Lovejoy, H. Kunz, and W. Knoll, *Angew. Chem. Int. Ed. Engl.* **42** (2003) 208.

[2]L. Becucci, A. Santucci, and R. Guidelli *J. Phys. Chem. B* **111** (2007) 9814.

[3]L. Becucci, M. R. Moncelli, R. Naumann, and R. Guidelli, *J. Am. Chem. Soc*. **127** (2005) 13316.

[4]L. J. C. Jeuken, S. D. Connell, P. J. F. Henderson, R. B. Gennis, S. D. Evans, and R. J. Bushby, *J. Am. Chem. Soc.* **128** (2006) 1711.

[5]A. Toby, A. Jenkins, R. J. Bushby, N. Boden, S. D. Evans, P. F. Knowles, Q. Liu, R. E. Miles, and S. D. Ogier, *Langmuir* **14** (1998) 4675.

[6]M. Baumgart, M. Kreiter, H. Lauer, R. Naumann, G. Jung, A. Jonczyk, A. Offenhäusser, and W. Knoll, *J. Colloid Interf. Sci.* **258** (2003) 298.

[7]J. R. Macdonald and W. B. Johnson in *Impedance Spectroscopy. Emphasizing solid materials and systems*, Ed. by J. R. Macdonald, J. Wiley & Sons, New York, 1987, p.1.

[8]G. Wiegand, N. Arribas-Layton, H. Hillebrandt, E. Sackmann, and P. Wagner, *J. Phys. Chem. B* **106** (2002) 4245.

[9] (a) W. Knoll, *Annu. Rev. Phys. Chem.* **49** (1998) 569; (b) W. Knoll, I. Köper, R. Naumann, and E.-K. Sinner, *Electrochim. Acta* **53** (2008) 6680.

[10]B. Wiltschi, W. Knoll, and E.-K. Sinner, *Methods* **39** (2006) 134.

[11]K. Tawa, and K. Morigaki, *Biophys J*. **89** (2005) 2750.

[12]A. L. Plant, *Langmuir* **15** (1999) 5128.

[13]L. M. Williams, S. D. Evans, T. M. Flynn, A. Marsh, P. F. Knowles, R. J. Bushby, and N. Boden, *Langmuir* **13** (1997) 751.

[14]L. M. Williams, S. D. Evans, T. M. Flynn, A. Marsh, P. F. Knowles, R. J. Bushby, and N. Boden, *Supramol. Sci.* **4** (1997) 513.

[15]G. Puu and I. Gustafson, *Biochim. Biophys. Acta* **1327** (1997) 149.

[16]R. P. Richter and A. Brisson, *Biophys. J.* **88** (2005) 3422.

[17]R. Lipowsky and U. Seifert, *Mol. Crystals* **202** (1991) 17.
[18]E. Kalb, S. Frey, and L. K. Tamm, *Biochim. Biophys. Acta* **1103** (1992) 307.
[19]E. Reimhult, F. Hook, and B. Kasemo, *Langmuir* **19** (2003) 1681.
[20]E. Sackmann, *Science* **271** (1996) 43.
[21]C. A. Keller, K. Glasmästar, V. P. Zhdanov, and B. Kasemo, *Phys. Rev. Lett*. **84** (2000) 5443.
[22]C. A. Keller and B. Kasemo, *Biophys. J.* **75** (1998) 1397.
[23]R. P. Richter A. Mukhopadhyay, and A. Brisson, *Biophys. J.* **85** (2003) 3035.
[24]R. P. Richter, R. Bérat, and A. R. Brisson, *Langmuir* **22** (2006) 3497.
[25]S. Lingler, I. Rubinstein, W. Knoll, and A. Offenhäusser, *Langmuir* **13** (1997) 7085.
[26]P. Delahay and J. E. Strassner, *J. Am. Chem. Soc.* **73** (1951) 5219.
[27]L. He, J. W. F. Robertson, J. Li, I. Kärcher, S. M. Schiller, W. Knoll, and R. Naumann, *Langmuir* **21** (2005) 11666.
[28]A. Zebrowska and P. Krysinski, *Langmuir* **20** (2004) 11127.
[29] J. Jass, T. Tjärnhage, and G. Puu, *Biophys. J.* **79** (2000) 3153.
[30]R. Naumann, T. Baumgart, R. Gräber, A. Jonczyk, A. Offenhäusser, and W. Knoll, *Biosens. Bioelectr.* **17** (2002) 25.
[31]L. K. Tamm and H. M. McConnell, *Biophys. J.* **47** (1985) 105.
[32]H. M. McConnell, T. H. Watts, R.M. Weis, and A. A. Brian, *Biochim. Biophys. Acta* **864** (1986) 95.
[33]I. Zawisza, X. Bin, and J. Lipkowski, *Langmuir* **23** (2007) 5180.
[34]B. Raguse, V. Braach-Maksvytis, B. A. Cornell, L. G. King, P. D. J. Osman, R. J. Pace, and L. Wieczorek, *Langmuir* **14** (1998) 648.
[35]D. J. McGillivray, G. Valincius, D. J. Vanderah, W. Febo-Ayala, J. T. Woodward, F. Heinrich, J. J. Kasianowicz, and M. Lösche, *Biointerphases* **2** (2007) 21.
[36]D. Axelrod, D. E. Koppel, J. Schlessinger, E. Elson, and W.W. Webb, *Biophys. J.* **16** (1976) 1055.
[37]A. N. Parikh, *Biointerphases* **3** (2008) FA22.
[38]T. W. Cha, A. Guo, and X.-Y. Zhu, *Biophys. J.* **90** (2006) 1270.
[39]L. Becucci, S. Martinuzzi, E. Monetti, R. Mercatelli, F. Quercioli, S. Battistel, and R. Guidelli, *Soft Matter*, accepted.
[40]I. R. Miller, in *Topics in Bioelectrochemistry and Bioenergetics*, Ed. By G. Milazzo, Wiley, Chichester, 1981, p. 194.
[41]A. Nelson and A. Benton, *J. Electroanal. Chem.* **202** (1986) 253.
[42]S. Trasatti, in *Modern Aspects of Electrochemistry*, Ed. by B. E. Conway and J.O'M. Bockris, Vol. 13, Plenum, New York, 1979, p. 81.
43, A. Nelson and N. Auffret, *J. Electroanal. Chem*. **248** (1988) 167.
[44]F. Tadini Buoninsegni, L. Becucci, M. R. Moncelli, and R. Guidelli, *J. Electroanal. Chem*. **500** (2001) 395.
[45]D. Bizzotto and A. Nelson, *Langmuir* **14** (1998) 6269.
[46]D. Bizzotto, Y. Yang, J. L. Shepherd, R. Stoodley, J. Agak, V. Stauffer, M. Lathuillière, A. S. Akhtar, and E. Chung, *J. Electroanal. Chem*. **574** (2004) 167.
[47] J. Shepherd, Y. Yang, and D. Bizzotto, *J. Electroanal. Chem*. **524-525** (2002) 54.
[48]A. Nelson, *Anal. Chim. Acta* **194** (1987) 139.
[49]A. Nelson, N. Auffret, and J. Borlakoglu, *Biochim. Biophys. Acta* **1021** (1990) 205.
[50]A. Nelson, N. Auffret, and J. Readman, *Anal. Chim. Acta* **207** (1988) 47.
[51]M. R. Moncelli, L. Becucci, and R. Guidelli, *Biophys. J.* **66** (1994) 1969.
[52]M. R. Moncelli and L. Becucci, *J. Electroanal. Chem.* **385** (1995) 183.

[53]L. Becucci, M. R. Moncelli, R. Herrero, and R. Guidelli, *Langmuir* **16** (2000) 7694.
[54]M. R. Moncelli, L. Becucci, F. Tadini Buoninsegni, and R. Guidelli, *Biophys. J.* **74** (1998) 2388.
[55]R. Herrero, M. R. Moncelli, R. Guidelli, M. Carla', A. Arcangeli, and M. Olivotto, *Biochim. Biophys. Acta* **1466** (2000) 278.
[56]M. R. Moncelli and L. Becucci, *J. Electroanal. Chem.* **433** (1997) 91.
[57]L. Becucci, M. R. Moncelli, and R. Guidelli, *J. Electroanal. Chem.* **413** (1996) 187.
[58]M. R. Moncelli and L. Becucci, *Bioelectrochem. Bioenerg.* **39** (1996) 227.
[59]I. R. Miller, *J. Membrane Biol.* **101** (1988) 113.
[60]I. R. Miller, D. Bach, and M. Teuber, *J. Membrane Biol*. **39** (1978) 49.
[61]M-F. Lecompte, A.-C. Bras, N. Dousset, I. Portas, R. Salvayre, and M. Ayrault-Jarrier, *Biochemistry* **37** (1998) 16165.
[62]M. R. Moncelli, R. Herrero, L. Becucci, and R. Guidelli, *J. Phys. Chem.* **99** (1995) 9940.
[63]L. Becucci, M. R. Moncelli, and R. Guidelli, *J. Am. Chem. Soc*. **125** (2003) 3785.
[64]M. R. Moncelli, L. Becucci, A. Nelson, and R. Guidelli, Biophys. J. **70** (1996) 2716.
[65]R. Herrero, M. R. Moncelli, L. Becucci, and R. Guidelli, *J. Phys. Chem. B* **101** (1997) 2815.
[66]R. Herrero, F.Tadini Buoninsegni, L. Becucci, and M.R. Moncelli, *J. Electroanal. Chem.* **445** (1998) 71.
[67]A. Nelson, *J. Electroanal. Chem.* **303** (1991) 221.
[68]A. Nelson, *J. Chem. Soc. Faraday Trans.* **89** (1993) 2799.
[69]A. Nelson, *Langmuir* **12** (1996) 2058.
[70]A. Nelson, *Langmuir* **13** (1997) 5644 .
[71]M. Rueda, I. Navarro, G. Ramirez, F. Prieto, C. Prado, and A. Nelson, *Langmuir* **15** (1999) 3672.
[72]L. Becucci, M. R. Moncelli, and R. Guidelli, *Biophys. J*. **82** (2002) 852.
[73]F. Prieto, I. Navarro, and M. Rueda, *J. Electroanal. Chem.* **550-551** (2003) 253.
[74]J. C. Franklin and D. S. Cafiso, *Biophys. J.* **65** (1993) 289.
[75]E. Gross, R. S. Bedlack, Jr., and L. M. Loew, *Biophys. J.* **67** (1994) 208.
[76]C. W. Meuse, G. Niaura, M. L. Lewis, and A. L. Plant, *Langmuir* **14** (1998) 1604.
[77]C. W. Meuse, S. Krueger, C. F. Majkrzak, J. A. Dura, J. Fu, J. T. Connor, and A. L. Plant, *Biophys. J.* **74** (1998) 1388.
[78]A. L. Plant, *Langmuir* **9** (1993) 2764.
[79]F. Tadini Buoninsegni, R. Herrero, and M. R. Moncelli, *J. Electroanal. Chem*. **452** (1998) 33.
[80]A. L. Plant, M. Gueguetchkeri, and W. Yap, *Biophys. J.* **67** (1994) 1126.
[81]M. Pawlak, S. Stankowski, and G. Schwarz, *Biochim. Biophys. Acta*. **1062** (1991) 94.
[82]M. T. Tosteson, D. C. Tosteson, *Biophys. J.* **36** (1981) 109.
[83]C. Kempf, R. D. Klausner, J. N. Weinstein, J. Van Renswoude, M. Pincus, and R. Blumenthal, *J. Biol. Chem*. **257** (1982) 2469.
[84]W. Hanke, C. Metfessel, H.-U. Wilmsen, E. Katz, J. Jung, and G. Boheim, *Biochim. Biophys. Acta* **727** (1983) 108.
[85]J. K. Cullison, F. M. Hawkridge, N. Nakashima, and S. Yoshikawa, *Langmuir* **10** (1994) 877.
[86]J. D. Burgess, M. C. Rhoten, and F. M. Hawkridge, *Langmuir* **14** (1998) 2467.

[87]N. M. Rao. A. L. Plant, V. Silin, S. Wight, and S. W. Hui, *Biophys. J.* **73** (1997) 3066.
[88]M. Boncheva, C. Duschl, W. Beck, G. Jung, and H. Vogel, *Langmuir* **12** (1996) 5636.
[89]B. Duschl, M. Liley, G. Corradin, and H. Vogel, *Biophys. J.* **67** (1994) 1229.
[90]A. L. Plant, M. Brigham-Burke, E. C. Petrella, and D. J. O'Shannessy, *Anal. Biochem.* **226** (1995) 342.
[91]K. Kastl, M. Ross, V. Gerke, and C. Steinem, *Biochemistry* **41** (2002) 10087.
[92]P. Mueller, D. O. Rudin, H. T. Tien, and W. C. Wescott, *Circulation* **26** (1962) 1167.
[93]F. A. Henn and T. E. Thompson, *J. Mol. Biol.* **31** (1968) 227.
[94]D. M. Andrews and D. A. Haydon, *J. Mol. Biol.* **32** (1968) 149.
[95]R. E. Pagano, J. M. Ruysschaert, and I. R. Miller, *J. Membr. Biol.* **10** (1972) 11.
[96]S. H. White and T. E. Thompson, *Biochim. Biophys. Acta* **323** (1973) 7.
[97]S. H. White, D. C. Petersen, S. Simon, and M. Yafuso, *Biophys. J.* **16** (1976) 481.
[98]M. Montal and P. Mueller, *Proc. Natl. Acad. Sci. U.S.A.* **69** (1972) 3561.
[99]M. Montal, *Biochim. Biophys. Acta* **298** (1973) 750.
[100]M. Montal and J. I. Korenbrot, *Nature (Lond.)* **246** (1973) 219.
[101]K. Janko and R. Benz, *Biochim. Biophys. Acta* **470** (1977) 8.
[102]J. L. Poulos, T.-J. Jeon, R. Damoiseaux, E. J. Gillespie, K. A. Bradley, and J. J. Schmidt, *Biosens. Bioelectron.* **24** (2009) 1806.
[103]M. C. Peterman, J. M. Ziebarth, O. Braha, H. Bayley, H. A. Fishman, and D. M. Bloom, *Biomed. Devices* **4** (2002) 231.
[104]S. D. Ogier, R. J. Bushby, Y. Cheng, S. D. Evans, S. W. Evans, A. T. A. Jenkins, P. F. Knowles, and R. E. Miles, *Langmuir* **16** (2000) 5696.
[105]Y. Cheng, R. J. Bushby, S. D. Evans, P. F. Knowles, R. E. Miles, and S. D. Ogier, *Langmuir* **17** (2001) 1240.
[106]G. Favero, A. D'Annibale, L. Campanella, R. Santucci, and T. Ferri, *Anal. Chim. Acta* **460** (2002) 23.
[107]G. Favero, L. Campanella, S. Cavallo, A. D'Annibale, M. Perella, E. Mattei, and T. Ferri, *J. Am. Chem. Soc.* **127** (2005) 8103.
[108]A. Janshoff and C. Steinem, *Anal. Bioanal. Chem.* **385** (2006) 433.
[109]J. Drexler and C. Steinem, *J. Phys. Chem. B* **107** (2003) 11245.
[110]W. Römer and C. Steinem, *Biophys. J.* **86** (2004) 955.
[111]E. K. Schmitt, M. Vrouenraets, and C. Steinem, *Biophys. J.* **91** (2006) 2163.
[112]C. Horn and C. Steinem, *Biophys. J.* **89 (**2005) 1046.
[113]X. Han, A. Studer, H. Sehr, I. Geissbühler, M. Di Berardino, F. K. Winkler, and L. Tiefenauer, *Adv. Mater.* **19** (2007) 4466.
[114] L. X. Tiefenauer and A. Studer, *Biointerphases* **3** (2008) FA74.
[115]C. Danelon, J.-B. Perez, C. Santschi. J. Brugger, and H. Vogel, *Langmuir* **22** (2006) 22.
[116]X. Lu, A. Leitmannova Ottova, and H. T. Tien, *Bioelectrochem. Bioenerg.* **39** (1996) 285.
[117]T. J. Jeon, N. Malmstadt, and J. J. Schmidt, *J. Am. Chem, Soc.* **128** (2006) 42.
[118]T.-J. Jeon, N. Malmstadt, J. L. Poulos, and J. J. Schmidt, *Biointerphases* **3** (2008) FA96.
[119]J. A. Beddow, I. R. Peterson, J. Heptinstall, and D. J. Walton, *Anal. Chem.* **76** (2004) 2261.

[120]R. F. Costello, I. R. Peterson, J. Heptinstall, and D. J. Walton, *Biosens. Bioelectron.* **14** (1999) 265.
[121]X.-F. Kang, S. Cheley, A. C. Rice-Ficht, and H. Bayley, *J. Am. Chem. Soc.* **129** (2007) 4701.
[122]E. Neher, B. Sakmann, and J. H. Steinbach, *Pflügers Arch.* **375** (1978) 219.
[123]J. Teissié, in *Bioelectrochemistry of Membranes*, Ed. by D. Walz, J. Teissié, and G. Milazzo, Birkhäuser Verlag, Basel, Switzerland, 2004, p. 205.
[124]A. A. Brian and H. M. McConnel, *Proc. Natl. Acad. Sci. U.S.A.* **81** (1984) 6159.
[125]K. D. Mossman, G. Campi, J. T. Groves, and M. L. Dustin, *Science* **310** (2005) 1191.
[126]C. Boissiere, J. B. Brubach, A. Mermet, G. de Marzi, C. Bourgaux, E. Prouzet, and P. Roy, *J. Phys. Chem. B* **106** (2002) 1032.
[127]R. J. Mashl, S. Joseph, N. R. Aluru, and E. Jakobsson, *Nano Lett.* **3** (2003) 589.
[128]R. P. Richter, N. Maury, and A. R. Brisson, *Langmuir* **21** (2005) 299.
[129]P. Lenz, C. M. Ajo-Franklin, and S. G. Boxer, *Langmuir* **20** (2004) 11092.
[130]J. Schmitt, B. Danner, and T. M. Bayerl, *Langmuir* **17** (2001) 244.
[131]M. Hetzer, S. Heinz, S. Grage, and T. M. Bayerl, *Langmuir* **14** (1998) 982.
[132]C. E. Dodd, B. R. G. Johnson, L. J. C. Jeuken, T. D. H. Bugg, R. J. Bushby, and S. D. Evans, *Biointerphases* **3** (2008) FA59.
[133]B. L. Jackson, J. A. Nye, and J. T. Groves, *Langmuir* **24** (2008) 6189.
[134]I. Zawisza, A. Lachenwitzer, V. Zamlynny, S. L. Horswell, J. P. Goddard, and J. Lipkowski, *Biophys. J.* **85** (2003) 4055.
[135]L. Burgess, M. Li, S. L. Horswell, G. Szymanski, J. Lipkowski, J. Majewski, and S. Satija, *Biophys. J.* **86** (2004) 1763.
[136]X. Bin, S. L. Horswell, and J. Lipkowski, *Biophys. J.* **89** (2005) 592.
[137]S. Xu, G. Szymanski, and J. Lipkowsky, *J. Am. Chem. Soc.* **126** (2004) 12276.
[138]O. Purrucker, H. Hillebrandt, K. Adlkofer and M. Tanaka, *Electrochim. Acta* **47** (2001) 791.
[139]S. Gritsch, P. Nollert, F. Jähnig, and E. Sackmann, *Langmuir* **14** (1998) 3118.
[140]L-G. Wang, Y-H. Li, and H. T. Tien, *Bioelectrochem. Bioenerg.* **36** (1995) 145.
[141]H. T. Tien, S. H. Wurster, and A. L. Ottova, *Bioelectrochem. Bioenerg.* **42** (1997) 77.
[142]A. Ottova-Leitmannova and H.T. Tien, *Progr. Surf. Sci.* **41** (1992) 337.
[143]Z. Salamon and G. Tollin, *Bioelectrochem. Bioenerg.* **25** (1991) 447.
[144]W. J. Albery, H. A .O. Hill, and A. R. Hillman, *J. Am. Chem. Soc.* **103** (1981) 3904.
[145]H. Gao, G.-A. Luo, J. Feng, A. L. Ottova, and H. T. Tien, *J. Photochem. Photobiol. B: Biology* **59** (2000) 87.
[146]H. T. Tien and J. R. Zon, in *Mechanistic approaches to interactions of electric and electromagnetic fields with living systems*, Ed. by M. Blank and E. Findl, Plenum Press, New York, 1987, p. 301.
[147]Z. Salamon, Y. Wang, G. Tollin, H. A. Macleod, *Biochim. Biophys. Acta* **1195** (1994) 267.
[148]Z. Salamon, G. Lindblom, and G. Tollin, *Biophys. J.* **84** (2003) 1796.
[149]Z. Salamon, Y. Wang, J. L. Soulages, M. F. Brown, and G. Tollin, *Biophys. J.* **71** (1996) 283.
[150]Z. Salamon and G. Tollin, *Biophys. J.* **71** (1996) 848.
[151]Z. Salamon, H. A. Macleod, and G. Tollin, *Biophys. J.* **73** (1997) 2791.
[152]Z. Salamon, D. Huang, W. A. Cramer, and G. Tollin, *Biophys. J.* **75** (1998) 1874.

[153]Z. Salamon, S. Davanathan, I. D. Alves, and G. Tollin, *J. Biol. Chem*. **280** (2005) 11175.
[154]C. Steinem, A. Janshoff, H.-J. Galla, and M. Sieber, *Bioelectr. Bioenerg.* **42** (1997) 213.
[155]A. Michalke, T. Schürholz, H.-J. Galla, and C. Steinem, *Langmuir* **17** (2001) 2251.
[156]L. Becucci, R. Guidelli, Q. Liu, R. J. Bushby, and S. D. Evans, *J. Phys. Chem B* **106** (2002) 10410.
[157]C. Peggion, F. Formaggio, C. Toniolo, L. Becucci, M. R. Moncelli, and R. Guidelli, *Langmuir* **17** (2001) 6585.
[158]H. Lang, C. Duschl, and H. Vogel, *Langmuir* **10** (1994) 197.
[159]H. Lang, C. Duschl, M. Grätzel, and H. Vogel, *Thin Solid Films* **210/211** (1992) 818.
[160]N. Boden, R. J. Bushby, Q. Liu, S. D. Evans, A. T. A Jenkins, P. Knowles, and R. E. Miles, *Tetrahedron* **54** (1998) 11537.
[161]C. Steinem, A. Janshoff, K. von dem Bruch, K. Reihs, J. Goossens, and H-J. Galla, *Bioelectrochem. Bioenerg.* **45** (1998) 17.
[162]J. D. Lear, Z. D. Wassermann, and W. D. De Grado, *Science* **240** (1988) 1179.
[163]N. Bunjes, E. K. Schmidt, A. Jonczyk, F. Rippmann, D. Beyer, H. Ringsdorf, P. Gräber, W. Knoll, and R. Naumann, *Langmuir* **13** (1997) 6188.
[164]R. Naumann, A. Jonczyk, R. Kopp, J. van Esch, H. Ringsdorf, W. Knoll, and P. Gräber, *Angew. Chem. Int. Ed. Engl.* **34** (1995) 2056.
[165]R. Naumann, A. Jonczyk, C. Hampel, H. Ringsdorf, W. Knoll, N. Bunjes, and P. Gräber, *Bioelectrochem. Bioenerg.* **42** (1997) 241.
[166]R. Naumann, E. K. Schmidt, A. Jonczyk, K. Fendler, B. Kadenbach, T. Liebermann, A. Offenhäusser, and W. Knoll, *Biosens. Bioelectron.* **14** (1999) 651.
[167]I. K. Vockenroth, C. Ohm, J. W. F. Robertson, D. J. McGillivray, M. Lösche, and I. Köper, *Biointerphases* **3** (2008) FA68.
[168]J. Leitch, J. Kunze, J. D. Goddard, A. L. Schwan, R. J. Faragher, R. Naumann, W. Knoll, J. R. Dutcher, and J. Lipkowski, *Langmuir* 25 (2009) 10354.
[169]R. Naumann, D. Walz, S. M. Schiller, and W. Knoll, *J. Electroanal. Chem.* **550-551** (2003) 241.
[170] J. W. F. Robertson, M. G. Friedrich, A. Kibrom, W. Knoll, R. L. C. Naumann, and D. Walz, *J. Phys. Chem. B* **112** (2008) 10475.
[171]I. K. Vockenroth, P. P. Atanasova, J. R. Long, A. T. A. Jenkins, W. Knoll, and I. Köper, *Biochim. Biophys. Acta* **1768** (2007)1114.
[172]S. A. Glazier, D. J. Vanderah, A. L. Plant, H. Bayley, G. Valincius, and J. J. Kasianowicz, *Langmuir* **16** (2000) 10428.
[173]I. K. Vockenroth, P. P. Atanasova, A. T. A. Jenkins, and I. Köper, *Langmuir* **24** (2008) 496.
[174]V. Atanasov, N. Knorr, R. S. Duran, S. Ingebrandt, A. Offenhäusser, W. Knoll, and I. Koper, *Biophys. J.* **89** (2005) 1780.
[175]R. F. Roskamp, I. K. Vockenroth, N. Eisenmenger, J. Braunagel, and I. Köper, *ChemPhysChem.* **9** (2008) 1920.
[176]R. Robelek, E. S. Lemker, B. Wiltschi, V. Kirste, R. Naumann, D. Oesterhelt, and E.-K. Sinner, *Angew. Chem. Int. Ed.* **46** (2007) 605.
[177]M. Leutenegger, T. Lasser, E.-K. Sinner, and R. Robelek, *Biointerphases* **3** (2008) FA136.

[178]E. K. Schmidt, T. Liebermann, M. Kreiter, A. Jonczyk, R. Naumann, A. Offenhäusser, E. Neumann, A. Kukol, A. Maelicke, and W. Knoll, *Biosens. Bioelectron.* **13** (1998) 585.
[179]M. Andersson, H. K. Keizer, C. Zhu, D. Fine, A. Dodabalapur, and R. S. Duran, *Langmuir* **23** (2007) 2924.
[180]H. M. Keizer, B. R. Dorvel, M. Andersson, D. Fine, R. B. Price, J. R. Long, A. Dodabalapur, I. Köper, W. Knoll, P. A. V. Anderson, and R. S. Duran, *ChemBioChem* **8** (2007) 1246.
[181]M. Andersson, G. Okeyo, D. Wilson, H. Keizer, P. Moe, P. Blouunt, D. Fine, A. Dodabalapur, and R. S. Duran *Biosen. Bioelectron.* **23** (2008) 919.
[182]I. K. Vockenroth, D. Fine, A. Dodobalapur, A. T. A. Jenkins, and I. Köper, *Electrochem. Commun*. **10** (2008) 323.
[183]L. Becucci, M. R. Moncelli, and R. Guidelli Langmuir **22** (2006) 1341.
[184]L. Becucci, M.V. Carbone, T. Biagiotti, M. D'Amico, M. Olivotto and R. Guidelli, *J. Phys. Chem. B* **112** (2008) 1315.
[185]L. Becucci and R. Guidelli, *Soft Matter* **5** (2009) 2294.
[186]L. Becucci, A. L. Schwan, E. E. Sheepwash and R. Guidelli, *Langmuir* **25** (2009) 1828.
[187]L. Becucci, M. Innocenti, E. Salvietti, A. Rindi, I. Pasquini, M. Vassalli, M. L. Foresti, and R. Guidelli, *Electrochim. Acta* **53** (2008) 6372.
[188] D. C. Grahame, *J. Am. Chem. Soc.* **76** (1954) 4819.
[189]J. Clavilier and C. Nguyen Van Huong, *J. Electroanal. Chem.* **41** (1973) 193.
[190]L. Becucci, R. Romero León, M. R. Moncelli, P. Rovero and R. Guidelli. *Langmuir* **22** (2006) 6644.
[191]L. Becucci and R. Guidelli, *Langmuir* **23** (2007) 5601.
[192]E. Bamberg and R. Benz, *Biochim. Biophys. Acta* **426** (1976) 570.
[193]M. C. Trudeau, J. W. Warmke, B. Ganetzky, and G. A. Robertson, *Science* **269**, (1995) 92; A. Arcangeli, L. Bianchi, A. Becchetti, L. Faravelli, M. Coronnello, E. Mini, M. Olivotto, and E. Wanke, *J. Physiol.* **489** (1995) 455.
[194]L. Becucci, R. Guidelli, C. B. Karim, D. D. Thomas, and G. Veglia, *Biophys. J.* **93** (2007) 1.
[195]L. Becucci, R. Guidelli, C. B. Karim, D. D. Thomas, and G. Veglia, *Biophys. J.* **97** (2009) 2693.
[196]L. Becucci, A. Cembran, C. B. Karim, D. D. Thomas, R. Guidelli, J. Gao and G. Veglia, *Biophys. J.* **96** (2009) L60.
[197]H. I. Stefanova, J. M. East, and A. G. Lee, *Biochim. Biophys. Acta* **1064** (1991) 321; H. I. Stefanova, S. D. Jane, J. M. East, and A. G. Lee, *Biochim. Biophys. Acta* **1064** (1991) 329.
[198]S. L. Robia, K. S. Campbell, E. M. Kelly, Z. Hou, D. L. Winters, and D. D. Thomas, *Circ. Res.* **101** (2007) 1123; Z. Hou, E. M. Kelly, and S. L. Robia, *J. Biol. Chem.* **283** (2008**)** 28996.
[199]L. Becucci, M. D'Amico, S. Daniele, M. Olivotto, A. Pozzi, and R. Guidelli Bioelectrochemistry, doi:10.1016/j.bioelechem.2009.08.007.
[200]G. Krishna, J. Schulte, B. A. Cornell, R. Pace, L. Wieczorek, and P. D. Osman, *Langmuir* **17** (2001) 4858.
[201]Y.-S. Shon, S. Lee, S. S. Perry, and T. R. Lee, *J. Am. Chem. Soc.* **122** (2000) 1278.
[202]R. C. Chambers, C. E. Inman, and J. E. Hutchison, *Langmuir* **21** (2005) 4615.
[203]L. J. C. Jeuken, N. N. Daskalakis, X. Han, K. Sheikh, A. Erbe, R. J. Bushby, and S. D. Evans, *Sen. Actuat. B* **124** (2007) 501.

[204]S. Heyse, O. P. Ernst, Z. Dienes, K. P. Hofmann, and H. Vogel, *Biochemistry* **37** (1998) 507.
[205]Y. Cheng, N. Boden, R. J. Bushby, S. Clarkson, S. D. Evans, P. F. Knowles, A. Marsh, and R. E. Miles, *Langmuir* **14** (1998) 839.
[206]S. Heyse, T. Stora, E. Schmid, J. H. Lakey, and H. Vogel, *Biochim. Biophys. Acta* **1376** (1998) 319.
[207]T. Stora, J. H. Lakey, and H. Vogel, *Angew. Chem. Int. Ed.* **38** (1999) 389.
[208]S. Goennenwein, M. Tanaka, B. Hu, L. Moroder, and E. Sackmann, *Biophys. J.* **85** (2003) 646.
[209]O. Purrucker, S. Gonnenwein, A. Fortig, R. Jordan, M. Rusp, M. Bärmann, L. Moroder, E. Sackmann, and M. Tanaka, *Soft Matter* **3** (2007) 333.
[210]M. Tanaka and E. Sackmann, *Nature* **437** (2005) 656; *Phys. Stat. Sol.* **203** (2006) 3452.
[211]M. Kühner and E. Sackmann *Langmuir* **12** (1996) 4866; G. Elender, and E. Sackmann, *J. Phys. II* **4** (1994) 455.
[212]J. Y. Wong, C. K. Park, M. Seitz, and J. N. Israelachvili, *Biophys. J.* **77** (1999) 1458.
[213]C. A. Naumann, O. Prucker, T. Lehmann, J. Ruhe, W. Knoll, and C. W. Frank, *Biomacromolecules* **3** (2002) 27.
[214]M. L. Wagner and L. K. Tamm, *Biophys. J.* **79** (2000) 1400.
[215]M. Tanaka, S. Kaufmann, J. Nissen, and M. Hochrein, *Phys. Chem. Chem. Phys.* **3** (2001) 4091.
[216]M. Tanaka, F. F. Rossetti, and S. Kaufmann, *Biointerphases* **3** (2008) FA12.
[217]E. Sackmann and M. Tanaka, *Trends Biotechnol.* **18** (2000) 58.
[218]M. Kühner, R. Tampé, and E. Sackmann, *Biophys. J.* **67** (1994) 217.
[219]G. Elender, M. Kühner, and E. Sackmann, *Biosens. Bioelectron.* **11** (1996) 565.
[220]F. Rehfeldt and M. Tanaka, *Langmuir* **19** (2003) 1467.
[221]T. Baumgart and A. Offenhäusser, *Langmuir* **19** (2003) 1730.
[222]K. Sengupta, J. Schilling, S. Marx, M. Fischer, A. Bacher, and E. Sackmann, *Langmuir* **19** (2003) 1775.
[223]J. Majewski, J. Y. Wong, C. K. Park, M. Seitz, J. N. Israelachvili, and G. S. Smith, *Biophys. J.* **75** (1998) 2363.
[224]J. Y. Wong, J. Majewski, M. Seitz, C.K. Park, J.N. Israelachvili, and G.S. Smith, *Biophys. J.* **77** (1999) 1445.
[225]C. Dietrich and R. Tampé, *Biochim. Biophys. Acta* **1238** (1995) 183.
[226]D. Beyer, G. Elender, W. Knoll, M. Kühner, S. Maus, H. Ringsdorf, and E. Sackmann, *Angew. Chem. Int. Ed. Engl.* **35** (1996) 1682.
[227]J. Spinke, J. Yang, H. Wolf, M. Liley, H. Ringsdorf, and W. Knoll, *Biophys. J.* **63** (1992) 1667.
[228]C. Erdelen, L. Häussling, R. Naumann, H. Ringdorf, H. Wolf, and J. Yang, *Langmuir* **10** (1994) 1246.
[229]H. Hillebrandt, G. Wiegand, M. Tanaka, and E. Sackmann, *Langmuir* **15** (1999) 8451.
[230]H. Hillebrandt, M. Tanaka, and E. Sackmann, *J. Phys. Chem. B* **106** (2002) 477.
[231]B. Wetzer, D. Pum, and U. B. Sleytr, *J. Struct. Biol.* **119** (1997) 123.
[232]B. Schuster, D. Pum, and U. B. Sleytr, *Biointerphases* **3** (2008) FA3.
[233]W. Knoll, R. Naumann, M. Friedrich, J. W. F. Robertson, M. Lösche, F. Heinrich, D. J. McGillivray, B. Schuster, P. C. Gufler, D. Pum, and U. B. Sleytr, *Biointerphases* **3** (2008) FA125.

[234]P. C. Gufter, D. Pum, U. B. Sleytr, and B. Schuster, *Biochim. Biophys. Acta* **1661** (2004) 154.
[235]B. Schuster, D. Pum, M. Sára, O. Braha, H. Bayley, and U. B. Sleytr, *Langmuir* **17** (2001) 499.
[236]B. Schuster, S. Weigert, D. Pum, M. Sára, and U. B. Sleytr, *Langmuir* **19** (2003) 2392.
[237]K. Ataka, F. Giess, W. Knoll, R. Naumann, S. Haber-Pohlmeier, B. Richter, and J. Heberle, *J. Am. Chem. Soc.* 126 (2004) 16199.
[238]F. Giess, M. G. Friedrich, J. Heberle, R. L. Naumann, and W. Knoll, *Biophys. J.* **87** (2004) 3213.
[239]M. G. Friedrich, J. W. F. Robertson, D. Walz, W. Knoll, and R. L. C. Naumann, *Biophys. J.* **94** (2008) 3698.
[240]R. L. C. Naumann and W. Knoll, *Biointerphases* **3** (2008) FA101.
[241]M. G. Friedrich, F. Giess, R. Naumann, W. Knoll, K. Ataka, J. Heberle, J. Hrabakova, D. H. Murgida, and P. Hildebrandt, *Chem. Commun. (Cambridge)* **21** (2004) 2376.
[242]M. G. Friedrich, V. U. Kirste, J. Zhu, R. B. Gennis, W. Knoll, and R. L. C. Naumann, *J. Phys. Chem. B* **112** (2008) 3193.

Rolando Guidelli

Rolando Guidelli was born in Florence on December 27, 1938. He was promoted to full professor of Electrochemistry at Florence University in 1971. His scientific interests have been focused to electrode kinetics, structure of the metal/water interface and bioelectrochemistry. Professor Guidelli is the recipient of the 2005 "Katsumi Niki" Prize for Bioelectrochemistry of the International Society of Electrochemistry (ISE), of the 2009 "Giulio Milazzo" Prize of the Bioelectrochemical Society, and of the "Sigillo d'oro" of the Italian Chemical Society. He is a fellow of the ISE, honorary member of the Bioelectrochemical Society, and associate editor of the journal *Bioelectrochemistry*.

5

Electrochemical Analysis of Ion Channels and Transporters in Pore-Suspending Membranes

Eva K. Schmitt[*] and Claudia Steinem[**]

[*]*Nuffield Department of Clinical Laboratory Science, John Radcliffe Hospital, University of Oxford, Oxford OX3 9DU, United Kingdom*
[**]*Institute of Organic and Biomolecular Chemistry, University of Göttingen, Tammannstr. 2, 37077 Göttingen, Germany*

I. INTRODUCTION

Ion channels represent a class of membrane spanning protein pores that mediate the flux of ions in a variety of cell types. They reside virtually in all the cell membranes in mammals, insects and fungi, and are essential for life, serving as key components in inter- and intracellular communication.[1] They are also of major importance for the human physiology and, thus, are highly attractive molecular drug targets.[2] However, investigation of ion channels and their pharmacological modulation is by no means an easy task, as their function relies on a laterally mobile and highly insulating lipid bilayer. Functionality of an ion channel is synonymous with the detection of ion currents. Upon the opening of one channel, typically 10^7–10^8 charges are transferred across the membrane per second and per channel, which gives rise to a current of around 2–20 pA

N. Eliaz (ed.), *Applications of Electrochemistry and Nanotechnology in Biology and Medicine II*, Modern Aspects of Electrochemistry 53,
DOI 10.1007/978-1-4614-2137-5_5,

that can only be monitored with high gain amplifiers. The patch clamp technique is the state-of-the-art technology for the study of ion channels,[3] but patch clamping is a laborious process requiring skilled and highly trained scientists. Owing to its ultra-low throughput, conventional patch clamp is frequently applied only in the later stages of drug discovery and development. To be able to search for new drug candidates at an earlier stage of drug development, high throughput screening assays are required. In recent years, new methods have been developed, which are a trade-off between high throughput and high information content. These so-called automated patch clamp systems[4-6] provide a platform, which allows for the investigation of ion channels from a functional perspective, i.e., the electrical characteristics of ion channels and their modulation by drugs can be monitored in great detail. Automated patch clamp, however, relies on currents in the picoampere regime, which are generated by a single ion channel, and data workup of these single events is rather tedious.

Hence, integral methods such as impedance spectroscopy, cyclovoltammetry or chronoamperometry are in some cases advantageous. For example, electrogenic transporter proteins exhibit transport rates of only 10–1000 s^{-1} and, thus, the electrical activity of a single protein cannot be detected. To obtain a detectable electrical current in the range of picoamperes, at least 10^4 transporters have to work in concert. Some of the most profitable drugs are inhibitors for transport proteins, and many transporters are possible targets for new drug developments. For example, ouabain and digoxin act on the cardiac muscle cell Na^+/K^+-ATPase in patients with congestive heart failure, while fluoxetine and imipramine are inhibitors of the sodium coupled serotonin transporter that are used as antidepressants. The gastric proton pump of the stomach mucosa is a drug target to treat ulcers and gastric reflux, which is medicated with omeprazole, lanosprazole, pantoprazole, and pariprazole. It is obvious that new approaches are necessary to develop bioanalytical devices and drug screening techniques for the pharmaceutical industry, targeting transport proteins as well as ion channels in an integral manner.

A number of approaches are based on lipid membranes that are attached to a conducting solid substrate such as gold, platinum or indium tin oxide. To establish solid supported membranes, either two separate monolayers can be deposited on the material by

means of the Langmuir-Blodgett and/or Langmuir-Schäfer technique, or, more easily, self-assembly processes are exploited. While Langmuir-Blodgett films offer the control over the composition and lateral pressure of both leaflets, self-assembly techniques are more versatile and the bilayers are easier to prepare. In the latter case, lipids are attached via covalent or quasi-covalent linkage, which appears to be an attractive solution to the problem of membrane immobilization. However, at the same time, the lateral mobility and a sufficient distance between solid support and the surface-facing membrane leaflet needs to be maintained, which is a prerequisite for a functional reconstitution of membrane proteins. Only few examples are given that demonstrate the feasibility of incorporating transmembrane proteins in solid supported membranes owing to the close proximity of the membrane to the solid substrate.[7-9] To overcome these difficulties, other strategies comprising the separation of a solid supported membrane by a thin, water-swollen polymer cushion or anchoring of lipids to the support by spacer units (tethered bilayers) to increase the distance between the membrane and the substrate have been developed,[10,11] which allowed monitoring of ion flows through reconstituted channels.[7,12-15] However, the ion currents are hampered by the capacitive coupling of the membrane to the substrate and, thus, single channel ion currents cannot be detected.

To combine the merits of robustness of membranes attached to a support with the advantage of freestanding bilayers, which allow an easy insertion of transmembrane proteins without a capacitive coupling, substrates with pore arrays or even porous materials have been introduced as membrane supports.[16-19] Membranes spanning these holes with diameters between 50 nanometres and several tens of micrometres take advantage of the natural properties of a cell membrane, where integrated ion channels are mobile, and transport of ions from one side of the membrane to the other is not hindered by the vicinity of a substrate.

Here, we give an overview of the potential of pore-suspending membranes for electrical monitoring of ion channel and transporter activities. We will focus on our established pore-suspending membrane systems based on functionalized porous alumina substrates with pore diameters of only 60 nm. The presented systems exhibit membrane resistances which allow for integral electrical readouts

by impedance spectroscopy and, in part, voltage clamp experiments on single ion channel forming peptides and proteins.

II. ELECTROCHEMICAL CHARACTERISATION OF PORE-SUSPENDING MEMBRANES

1. Nano-BLMs

A couple of years ago, we developed an artificial membrane system based on porous alumina substrates that can be considered as a hybrid between a solid supported membrane and a freestanding lipid bilayer. As each of the bilayers spanning the pores of the substrate resembles a black lipid membrane (BLM), a membrane that was first invented by Müller and Rudin in the 1970's, but of nanometre size, the system was called nano-BLMs.

To investigate the electrical properties, such as capacitance and resistance of lipid membranes, electrochemical impedance spectroscopy (EIS) is a powerful technique.[12,20,21] In general, this method is well suited to elucidate the electrochemical properties of sensitive biological interfaces in a non-invasive manner by the application of an alternating voltage of small amplitude.

(*i*) *Formation and Impedance Analysis of Nano-BLMs*

Porous alumina can be prepared easily, reproducibly and rather cheaply in almost arbitrary lateral dimensions, making this material well suited for routine applications as well as for biosensor devices. The substrates are formed by anodisation in the presence of acids.[22,23] To use them as an underlying substrate for nano-BLMs, the pore-bottoms need to be removed, which results in a sieve-like structure.[24] For the formation of nano-BLMs we adapted a method, which was originally established to prepare solid supported membranes on gold electrodes.[9] The strategy is to utilize the strong, quasi-covalent interaction between gold and sulfur to chemisorb alkane thiols or thiol-functionalized lipids such as the phospholipid 1,2-dipalmitoyl-*sn*-glycero-3-phosphothioethanol (DPPTE) on gold surfaces. Thus, the upper part of the alumina substrates is covered with a 60 nm gold layer followed by the chemisorption of a thiol compound that renders the upper surface

hydrophobic. In order to allow for nano-BLM formation in an aqueous environment, the substrate is fixed in a Teflon cell consisting of two identical compartments separated by the porous alumina substrate with an area of 7 mm^2 sealed by two O-rings (Fig. 1A).

For impedance analysis, platinised platinum electrodes, immersed in the electrolyte solution on both sides, serve as working (*cis* compartment) and counter electrode (*trans* compartment) and are connected to an impedance/gain-phase analyser SI 1260 from Solartron Instruments (Farnborough, UK). Owing to the sieve-like alumina structure, solely the electrolyte resistance R_{el} is monitored in impedance measurements, with the capacitance of the platinum electrode occurring at low frequencies (Fig. 2 A/B, filled squares). In a theoretical approach, we previously addressed the problem of the conducting or so-called "active" area of the porous substrates.[25] We concluded that only the electrolyte-filled pores contribute to the electrical characteristics of the material, and only the porous area of the substrate needs to be taken into account when area dependent parameters are calculated.

Nano-BLMs are established on the functionalized porous alumina substrates by applying a droplet of a lipid dissolved in a non-volatile solvent such as *n*-decane. Owing to the hydrophobicity of the functionalized porous alumina the droplet spreads evenly, leading to an insulating layer. The formation of lipid bilayers can then be followed by means of impedance spectroscopy in a frequency regime of 10^{-2}–10^6 Hz. In Fig. 2A/B, typical impedance spectra of a functionalized porous alumina substrate before (filled squares) and after nano-BLM formation (open squares) are shown. Figure 2A depicts the absolute value of the impedance |Z|, whereas Fig. 2B presents the phase angle ϕ as a function of the applied frequency. The absolute value of the impedance of a fully established bilayer is determined by the electrolyte resistance at 10^6 Hz, whereas immediately after lipid-solvent application a capacitance is predominant and, thus, a phase shift of around –90° is detected. By measuring ϕ at a frequency of 10^6 Hz, the kinetics of the thinning process, a process that is known from classical BLMs, can be monitored with high time resolution. Figure 2C illustrates the shift of the phase angle ϕ(10^6 Hz) from –85° after the lipid-solvent droplet has been applied to almost 0° after 150 s, indicating the

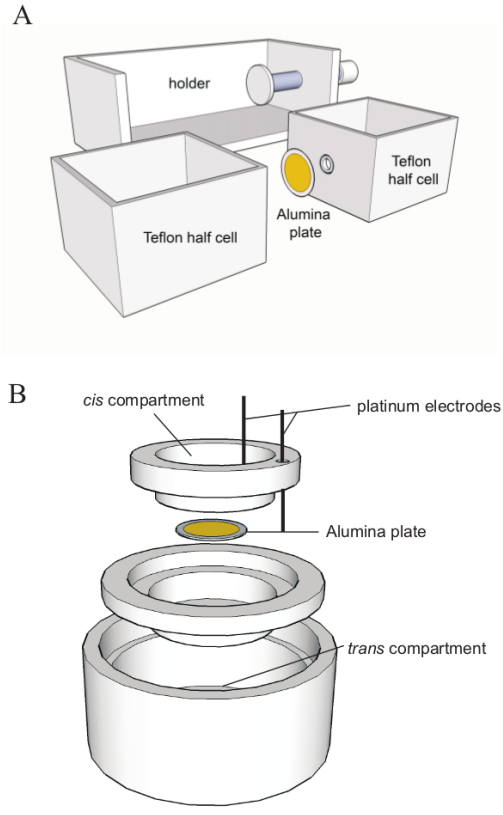

Figure 1. A) Teflon cell that is used for impedance analysis and voltage clamp experiments on nano-BLMs. The porous alumina substrate is clamped between two O-rings, which define the active area. An electrode is placed in each compartment (two-electrode configuration), which are connected to either an impedance analyser or the headstage of the patch clamp amplifier. B) Setup used for electrical measurements on pore-spanning membranes obtained from vesicle spreading. The porous substrate is located between the two upper parts of the Teflon chamber by means of sealing rings. The single pieces of the setup are tightly secured via the third part of the setup, which serves as the *trans* compartment, whereas the chamber on top is the *cis* compartment. Platinised platinum electrodes in the *cis* and *trans* compartment (two-electrode configuration) serve to detect the signal in impedance and photocurrent measurements.

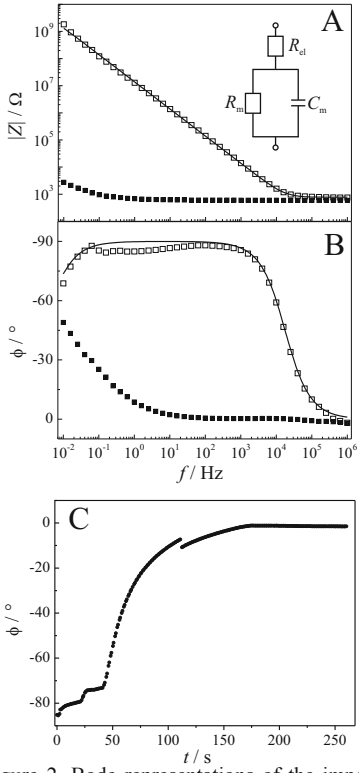

Figure 2. Bode representations of the impedance data [A) Magnitude of the impedance, B) phase angle between current and voltage] of gold-covered porous alumina membranes functionalized with a DPPTE-monolayer before (■) and one day after (□) the application of DPhPC dissolved in *n*-decane on the porous alumina substrate to form a nano-BLM. The solid lines are the results of the fitting procedure to (□) using the equivalent circuit shown in the inset: C_m = 11.7 nF, R_m = 4.7 GΩ. Inset: Equivalent circuit composed of a parallel *RC*-element (R_m and C_m) representing the electrical behaviour of a lipid bilayer in series to an Ohmic resistance R_{el} that represents the electrolyte solution and the wire connections.[24] C) Time-resolved increase in ϕ(10^6 Hz) during the membrane formation process, allowing to follow the kinetics and success of the thinning process. Electrolyte: 1 M KCl, 1 mM $CaCl_2$, pH 6.0.[26]

removal of the solvent, leaving an about 5 nm thin bilayer behind. This procedure allows to quickly assess whether a nano-BLM has been successfully formed.[26]

In order to elucidate if a lipid bilayer is fully covering the porous substrate, characteristic membrane parameters are extracted from the impedance spectra. The data analysis is based on an electrical model (Fig. 2 A, inset). The very simple equivalent circuit comprises three elements, which represent the different components of the electrochemical system. It is composed of a parallel *RC*-element, namely an Ohmic resistor R_m and a capacitor C_m, which represent the electrical behaviour of a lipid bilayer, in series to another Ohmic resistor R_{el} that represents the electrolyte solution and the wire connections. The obtained impedance spectra are characterized by the electrolyte resistance R_{el} in the high frequency regime ($5 \cdot 10^4$–10^6 Hz), and the capacitance C_m at frequencies below $5 \cdot 10^4$ Hz. At frequencies below $3 \cdot 10^{-1}$ Hz a second Ohmic resistance is discernable, which is attributed to the membrane resistance R_m. Fitting the parameters of the equivalent circuit to the data results in good agreement between data and fit with a membrane capacitance of C_m = 11.7 nF and a membrane resistance of R_m = 4.7 GΩ. Taking the porosity of the alumina substrate of 33 % into account, which was determined by scanning electron microscopy,[24] an active area of A = 2.3 mm^2 is calculated. Thus, the mean capacitance of C_m = (14.9 ± 3.3) nF (n > 50) translates into a specific capacitance of $C_{m,sp}$ = (0.65 ± 0.2) µF cm^{-2}. $C_{m,sp}$ is defined as $C_m A^{-1}$. This value agrees well with those obtained for classical BLMs[27] and supports the idea that single lipid bilayers have been formed across the pores.

(*ii*) *Long-Term Stability of Nano-BLMs*

The achieved membrane resistances of the nano-BLMs are similar to those of traditional BLMs and are obviously sufficient to perform single channel recordings. However, the suitability of classical BLMs in biosensor applications is limited, as the BLM ruptures at a certain point, i.e., owing to mechanical distortion, leading to the loss of the insulating membrane in one single event. In contrast, in nano-BLMs each bilayer, suspending a single pore, is decoupled from the others and can therefore rupture separately, as proven by visualizing the process by fluorescence microscopy[28]

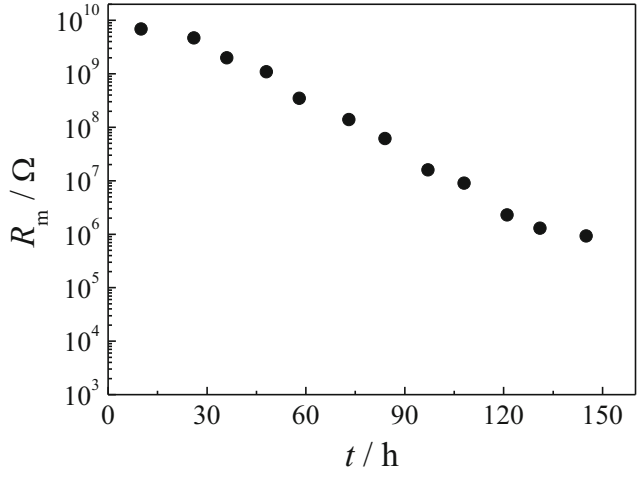

Figure 3. Time course of the membrane resistance R_m obtained by EIS analysis of a nano-BLM in a frequency range of 10^{-2}-10^{6} Hz. The membrane resistance was extracted from the impedance data by fitting the parameters of the equivalent circuit shown in the inset of Fig. 2A to the data.[24]

and scanning ion conductance microscopy (SICM).[29] Monitoring this process by EIS results in a decreasing membrane resistance R_m over time as shown in Fig. 3.

In the first 48 hours after membrane formation, R_m drops from 7 GΩ to 1 GΩ. During this time period, the membrane is well suited for single channel measurements. Then, the membrane resistance decreases further leading to membrane resistances of around 150 MΩ after 72 hours and 2 MΩ after 120 hours. After 132 hours, the membrane resistance has reached 1 MΩ. From a statistical analysis, the lifetime of the nano-BLM with membrane resistances larger than 1 GΩ was calculated to be (1.5 ± 0.5) days (n > 30). These data prove that the long-term stability of nano-BLMs is by far greater than the one of classical BLMs. Notably, in some cases it happened during the time course of the experiment that the membrane resistance increased again, which indicates that a self-healing process might occur within the membrane. This implies that nano-BLMs underlie permanent fluctuations affecting the resistance and capacitance of the membrane.

These data show that nano-BLMs are a powerful membrane system that overcomes the disadvantage of poor long-term stability of classical BLMs. However, classical BLMs have also been developed further in recent years in order to diminish their drawbacks such as long-term stability and applicability in chip based assays. Glass supports with a single pore of 100-400 nm in diameter served as supports for BLMs, which are stable for up to two weeks.[30] In another approach, giant unilamellar vesicles are sucked on a single hole by means of low pressure, which ruptures the vesicle and generates a bilayer within seconds.[31] Nevertheless, these systems still only provide a bilayer covering one single hole, whereas nano-BLMs are composed of more than 10^9 individual bilayers.

2. Pore-Suspending Membranes on CPEO3

(*i*) *Impedance Analysis of Pore-Suspending Membranes on Porous Alumina with Fully Opened Pore Bottoms*

Nano-BLMs proved to be a robust system for the investigation of ion channels on a single channel level (see Section III). Due to the method of preparation, nano-BLMs still contain some organic solvent, which is reflected in the mentioned fluctuations in membrane resistance and the obtained lateral diffusion coefficients.[28] Several membrane proteins lose activity in the presence of organic solvents such as *n*-decane and hence bilayers prepared without addition of solvent are highly desirable. For BLMs this has been realized by the method of Montal and Mueller, who established solvent-free lipid bilayers by the membrane folding method.[32]

Already some years ago, we followed a strategy to form pore-suspending bilayers starting from large unilamellar vesicles (LUVs).[22,33,34] With this method, it is not only possible to gain solvent-free pore-spanning membranes, but in addition it holds the potential for establishing lipid bilayers with high protein density. As a starting point, porous substrates were functionalized with a thiol-component to chemically distinguish between the upper surface and the inner pore walls, which should prevent the fusion of vesicles within the pores. Yet, these membranes proved to be rather leaky, as shown by EIS.[34] To achieve highly insulating pore-

suspending membranes, it turned out to be advantageous to functionalize the gold-covered porous substrate with cholesterylpolyethylenoxy thiol (CPEO3), a cholesterol derivative with a hydrophilic linker terminated with a thiol group, which renders the upper surface hydrophobic.[35] CPEO3 was already successfully used by others to establish solid supported membranes on gold electrodes.[36,37] To generate pore-suspending membranes, LUVs composed of 1,2-diphytanoyl-*sn*-glycero-3-phosphocholine (DPhPC)/ 1,2-dioleoyl-*sn*-glycero-3-phosphocholine (DOPC) (6:4) were spread and fused on CPEO3-functionalized porous alumina, leading to a pore-suspending membrane, whose electrical characteristics could be monitored by EIS. The setup was a three-piece Teflon chamber with the porous substrate horizontally fixed between the two upper parts (Fig. 1B). Sealing rings allow insulating the substrate area from its environment. However, to prevent leak currents, a small amount of *n*-decane was applied in the sealing ring region prior to the addition of liposomes. The organic solvent did not alter the electrical properties of the sample. A characteristic course of the absolute value of the impedance $|Z|(f)$ after 30 hours of incubation with LUVs is depicted in Fig. 4 A (open squares). To extract the electrical parameters of the membrane system, again the equivalent circuit depicted in Fig. 2 A (inset) was used.

Good accordance between model and experimental data is found with a membrane capacitance of $C_m = 4$ nF and a membrane resistance $R_m = 82$ MΩ. Taking the porous area into account, the absolute capacitance value translates into a specific capacitance of 0.4 μF cm^{-2}. From independent experiments, a mean specific membrane capacitance of (0.5 ± 0.1) μF cm^{-2} ($n = 5$) was determined. This is in agreement with values found for solvent-free BLMs, which are 0.5–1.0 μF cm^{-2}.[27] The membrane resistance R_m, which varied between 10^6–10^8 Ω, is still lower than those obtained for nano-BLMs. However, it is already sufficiently high to monitor channel activities in an integral manner,[38] as will be shown in detail in Section IV.

Pore-spanning membranes feature a high degree of mechanical and long-term stability. The membrane resistance R_m was extracted by impedance data analysis and given as a function of time (Fig. 4 B). Up to 50 hours after preparation, R_m remains almost constant followed by a decrease, which is attributed to the rupture of single pore-suspending membranes. It turned out that adding

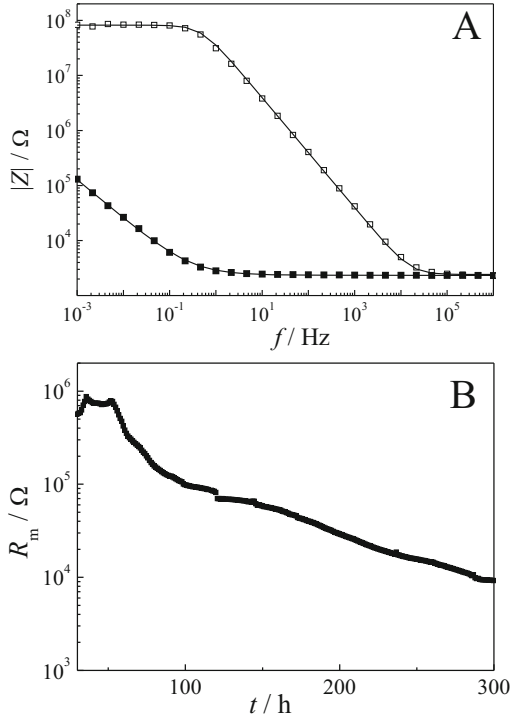

Figure 4. A) Absolute value of the impedance $|Z|(f)$ of a functionalized porous alumina substrate prior the addition of the vesicle suspension (■). (□) depicts the impedance data obtained 30 hours after vesicle addition. The solid line is the result of a fitting routine using the equivalent circuit shown in Fig. 2 A (inset) with $C_m = 4$ nF and $R_m = 82$ MΩ. B) Change in membrane resistance R_m as a function of time as a measure of long-term stability of a pore-suspending bilayer preparation. After the pore-suspending membrane had been established, impedance spectra were taken every hour and the membrane resistance was extracted from the impedance data. Around 50 hours after vesicle addition, rupturing of the membranes becomes discernable as a decrease in membrane resistance. Electrolyte: 0.1 M NaCl.[35]

LUVs to established pore-spanning membranes, which are partially ruptured and thus leaky, refurbished the insulating properties. We demonstrated that the absolute value of the impedance of pore-spanning lipid bilayers increased by one order of magnitude four hours after LUVs were added.[35]

Interestingly, not all pore-spanning membrane preparations resulted in an impedance spectrum as shown in Fig. 4 A. In many cases, two dispersions were monitored that changed during the vesicle incubation process, as observed in the impedance spectra shown in Fig. 5 A.

To analyse these data, three degenerate networks are conceivable (Fig. 5 C). Two Ohmic resistors and capacitors, respectively, account for the two observed dispersions in series to a resistor that reflects the electrolyte resistance R_{el}. Data analysis based on the three networks provided very similar values for each parameter and, hence, they cannot be distinguished. Over the course of an incubation period of 22 hours, as indicated by the arrow in Fig. 5 A, the two dispersions merge into one. We hypothesize that, within the first stage of bilayer formation, the LUVs fuse only partially (Fig. 5 B). This intermediate state of hemi-fused liposomes could be modelled by two *RC*-elements in series to each other (Fig. 5 B), characterising the electrical properties of the membrane interfaces.

(*ii*) Impedance Analysis of Pore-Suspending Membranes on Porous Alumina with Partially Opened Pore Bottoms

Despite the promising electrical properties and long-term stability of these pore-spanning membranes, they suffered from very long formation times of up to 24 hours. Especially when proteoliposomes are applied, a fast preparation is desired, as some proteins denature, thus losing their function within a few hours. We assumed that the area where the sealing ring contacts the porous substrate is crucial for current leakage. Thus, we altered the surface of the porous substrates with a total area of 0.314 cm^2 in a way that only a small fraction of the barrier oxide within the sealing ring area is fully removed (0.079 cm^2), while the rest of the pores remain sealed with alumina (Fig. 6).

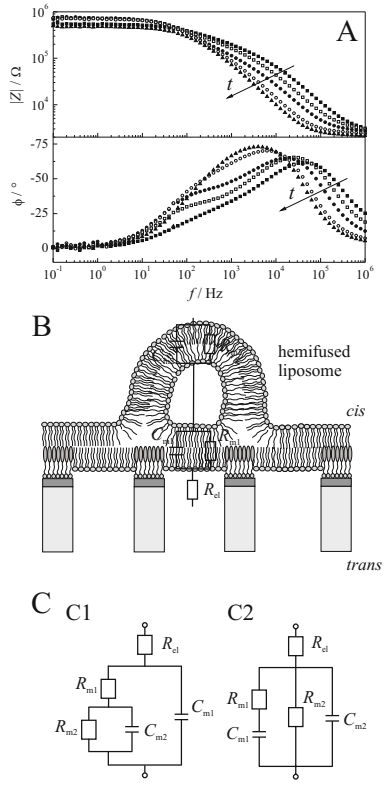

Figure 5. A) Absolute value of the impedance $|Z|(f)$ and phase angle $\phi(f)$ of a pore-spanning membrane on CPEO3-functionalized porous alumina in the presence of a vesicle suspension composed of DPhPC/DOPC 6:4 (■) 4 hours, (□) 9 hours, (●) 12 hours, (○) 15 hours and (▲) 22 hours after the addition of LUVs. The arrow indicates the time course of the experiment. Of the two discernable dispersions at the beginning, only one dispersion is found at the end of the incubation period. Electrolyte: 0.1 M NaCl.[35] B) Scheme depicting the hypothesized intermediate state during pore-spanning membrane formation, which leads to two dispersions in the impedance spectra together with an equivalent circuit representing the two membranes (R_{m1}, C_{m1} and R_{m2}, C_{m2}) and the electrolyte resistance R_{el}. C) Alternative equivalent circuits to model the impedance data, which feature two discernable dispersions with R_{m1}, R_{m2}, C_{m1} and C_{m2} and the electrolyte resistance R_{el}.

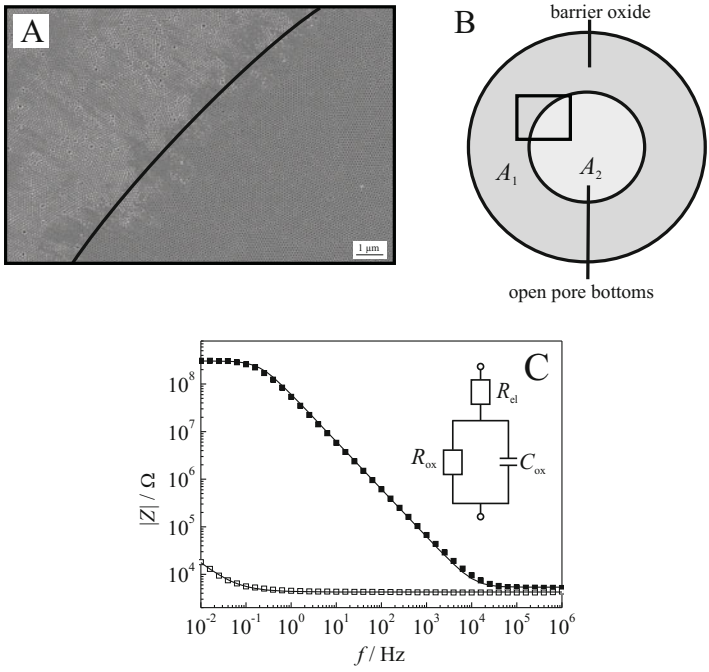

Figure 6. A) Scanning electron microscopy image of the porous alumina substrate after partial opening of the pores, and B) schematic drawing of the substrate. C) Impedance spectra of a porous alumina layer (■) before and (□) after pore bottom opening. The solid lines are the results of the fitting procedures. For (■), the equivalent circuit shown in the inset was used with the following results: R_{ox} = 0.3 GΩ, C_{ox} = 2.6 nF and R_{el} = 5400 Ω. For (□), an equivalent circuit comprising the electrolyte resistance R_{el} in series to a CPE-element, representing the non-ideal capacitive properties of the platinised platinum electrodes, was used with the following results: R_{el} = 4300 Ω, A = 0.6 mF $s^{\alpha-1}$ and α = 0.80. Inset: Equivalent circuit composed of a parallel connection of a resistance R_{ox} and a capacitance C_{ox} representing the aluminium oxide in series to the electrolyte resistance R_{el}.[38]

As only the porous area fraction of the substrate (p = 33 ± 3 %) is considered electrically active,[25] these areas translate into A_1 = 0.0026 cm^2 and A_2 = 0.0078 cm^2, respectively. However, alumina is not an ideal insulator, as shown by EIS. The mean specific capacitive values $C_{ox,sp}$ of the remaining barrier oxide is (1.1 ± 0.3) µF cm^{-2} (n = 16), the specific resistance $R_{ox,sp}$ varies from 10^4–10^7

Ω cm^2. Hence, the electrical properties of the partially remaining barrier oxide need to be considered in data analysis.

On these particular alumina substrates that were again functionalized with CPEO3, the fusion process of LUVs leading to insulating lipid bilayers was finished after 3 hours, which is significantly faster. Also the success rate of the preparation increased to 80 %. We suggest that the process is driven by the bilayer that is formed on the solid part of the alumina substrate, which then acts as a nucleation site for membrane formation in the adjacent region. It was shown by others that the border of a lipid bilayer catalyzes the growth of bilayers in adjacent regions when liposomes are added.[39,40]

To analyse the impedance data, an equivalent circuit was developed that takes the two different areas (A_1 and A_2) of the porous substrate into account (Fig. 7).

The barrier oxide layer is represented by a resistance R_{ox} and a capacitance C_{ox}, on which a lipid bilayer characterized by a membrane resistance $R_{m,c}$ and capacitance $C_{m,c}$ is deposited. To get access to R_{ox} and C_{ox}, the electrical response of the substrate prior to the selective removal of the barrier oxide layer was measured by EIS for each individual substrate. To account for the electrical properties of the lipid bilayer covering the open-pore array, a parallel *RC*-element with the membrane resistance $R_{m,o}$ and capacitance $C_{m,o}$ is added in series, whereas R_{el} represents the Ohmic behaviour of the electrolyte in the bulk and the open-pore array. This equivalent circuit, however, contains too may parameters to be able to fit all of them independently. Two approaches were followed to simplify the equivalent circuit and reduce the number of parameters. For both, prior to the fitting routine, R_{ox} and C_{ox} were individually determined and kept constant during the following fitting routine. In approach (1), we assumed that the area related values $R_{m,sp}$ and $C_{m,sp}$ obtained from lipid bilayers on gold electrodes are similar to those of membranes attached to the barrier oxide. This approach implies that the barrier oxide is fully covered by a lipid bilayer, whereas the coverage of the open pores is not defined, thus the parameters $R_{m,o}$ and $C_{m,o}$ as well as R_{el} are free in the fit routine. In approach (2), the specific membrane capacitance and membrane resistance were assumed to be equal on the open-pore array and on the barrier oxide. This was rationalized by the electrical properties of CPEO3-DPhPC/DOPC bilayers on planar

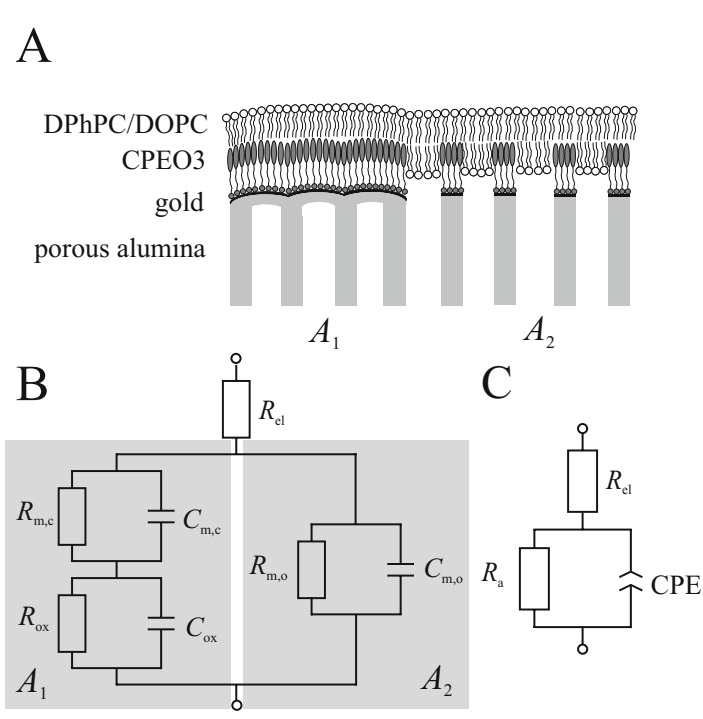

Figure 7. A) Schematic drawing of the pore-suspending membrane on the porous alumina substrate. B) Equivalent circuit representing the different elements of the membrane system. R_{ox} and C_{ox} were independently determined by impedance analysis and kept constant during the fitting routine. C) Simplified equivalent circuit according to the procedure described in the text.[38]

non-porous gold electrodes. Approach (2) results in Eqs. (1) and (2):

$$\frac{C_{m,o}}{A_2} = \frac{C_{m,c}}{A_1} \tag{1}$$

$$R_{m,o} \cdot A_2 = R_{m,c} \cdot A_1 , \tag{2}$$

which allow to replace $R_{m,o}$ and $C_{m,o}$. Based on these considerations, the equivalent circuit shown in Fig. 7B contains only three free parameters (R_{el}, $R_{m,c}$ and $C_{m,c}$).

If active ion channels are incorporated in pore-suspending membranes, solely the resistance of the bilayer covering the open pores, $R_{m,o}$ changes significantly. In this case, approach (2) is already too elaborate for data analysis and a more simple equivalent circuit can be applied (approach 2'), which is depicted in Fig. 7 C. Here, the resistance R_a represents the overall resistance at the limit of low frequencies, which reads:

$$\lim_{\omega \to 0} Z^{Re}(\omega) = R_a = R_{m,o} \frac{R_{ox} + R_{m,c}}{R_{m,o} + R_{ox} + R_{m,c}} \tag{3}$$

$$\lim_{\omega \to 0} Z^{Im}(\omega) = 0 \tag{4}$$

In the model shown in Fig. 7C, R_a is in parallel to a constant phase element (CPE). The constant phase element was chosen instead of a capacitor to account for the non-ideal capacitive behaviour of the system. With the known parameter R_{ox}, $R_{m,c}$ and $R_{m,o}$ can be calculated from Eq. (3). In Fig. 8, the results of the two different approaches (2) and (2') are compared.

The fitting results demonstrate that approach (2) (---) and (2') (—) reflect the course of the impedance data slightly better than approach 1 (not shown). For approach (1), the parameter $R_{m,c}$ is three orders of magnitude larger than those determined by approach (2) and (2'), which is a result of the assumption of an ideal membrane coverage on the solid area. However, this does not necessarily imply that approaches (2) and (2') are more valid models than (1). All of them are a compromise to minimize the number of free parameters in data analysis. From four independent experiments we determined $C_{m,o,sp}$ as 0.75-1.80 μF cm^{-2} and $R_{m,sp}$ as $(2.3–6.9)\cdot 10^3$ Ω cm^2. The differing area dependent values may reflect the error in the porous area, which was not individually determined for each substrate. Furthermore, hemifused vesicles could still be present, although not resolved in impedance spectra as a second dispersion. While for approach (2') no information about

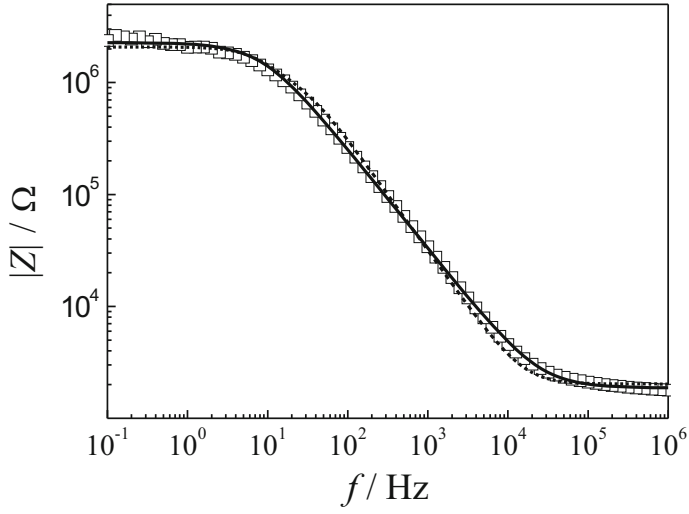

Figure 8. Absolute value of the impedance $|Z|$ of a pore-spanning bilayer from LUVs (DPhPC/DOPC 6:4) on CPEO3-functionalized porous alumina with selectively opened pore-bottoms with R_{ox} = 8.9 MΩ und C_{ox} = 6.7 nF, previously determined by EIS. The dashed line is the result of fitting the parameters of the equivalent circuit shown in Fig. 7 B following approach (2): R_{el} = 2000 Ω, $R_{m,o}$ = 2.6 MΩ, $C_{m,o}$ = 1.9 nF, $R_{m,c}$ = 0.89 MΩ and $C_{m,c}$ = 5.8 nF. The solid line is the result of fitting the equivalent circuit shown in Fig. 7 C: R_{el} = 2000 Ω, R_a = 2.3 MΩ, C_a = 8.2 nF. Buffer: 10 mM TRIS, 100 mM TMA, pH 8.6.[38]

the capacitive properties of the membrane itself are obtained, the overall resistance R_a and, after applying Eq. (3), $R_{m,c}$ and $R_{m,o}$ can be accurately determined in a simple fit routine. This is a prerequisite for the analysis of impedance data obtained in the presence of active ion channels, as further discussed in Section IV.

III. RECONSTITUTION OF PEPTIDES IN NANO-BLMS

As outlined in Section II, nano-BLMs are clearly advantageous over classical BLMs, as they exhibit similar high membrane resistances, but are at the same time attached to a substrate, which makes these membranes long-term and mechanically stable. In the following paragraphs, several examples will be given to demon-

strate the applicability of nano-BLMs to monitor the activity of ion channel peptides even down to the single channel level by voltage clamp experiments.

1. Peptidic Carriers and Ion Channels

To electrically monitor the activity of carriers and ion channel forming peptides, the setup depicted in Fig. 1 A is routinely used. For single channel recordings, two Ag/AgCl electrodes in the *cis* and *trans* compartment were connected to an Axopatch 200B patch clamp amplifier (Axon Instruments, Foster City, CA, USA) in capacitive or resistive feedback configuration. The *trans* compartment was connected to ground and all potentials in the *cis* compartment are given relative to ground. Data were collected with a sampling rate of 10 kHz and filtered with a 4-pole low pass Bessel filter with a cut-off frequency of 500 Hz-1 kHz.

(*i*) *Reconstitution of the Ion Carrier Valinomycin*

As a first example, the ion carrier valinomycin was investigated in nano-BLMs. Valinomycin is a cyclic depsipeptide from *Streptomyces fulvissimus* consisting of three identical units. It mediates the transport of many alkali and alkaline earth cations in organic films or solvents of low polarity. It is highly selective for K^+ and Rb^+ over Li^+, Na^+, and alkaline earth cations by forming a three-dimensional complex around the cation in order to increase its solubility in nonpolar organic solvents or the interior of a biological membrane. In solid supported membranes, the transport characteristics of valinomycin has been investigated in an integral manner by means of impedance spectroscopy.[41,42] However, the ion transport is always hampered by the underlying capacitance of the substrate. Impedance analysis of nano-BLMs doped with valinomycin should, however, allow an immediate extraction of the change in membrane resistance as a result of the valinomycin transport activity. To reconstitute a nano-BLM system with valinomycin, first a 1,2-diphythanoyl-*sn*-glycero-3-phosphocholine (DPhPC) nano-BLM on an octadecanethiol submonolayer was prepared and then valinomycin dissolved in dimethylsulfoxide was added in front of the membrane, which results in the spontaneous insertion of the depsipeptide. Impedance spectra were rec-

orded in an alkali cation-free buffer (10 mM TRIS, 50 mM $N(CH_3)_4Cl$, pH 7.4, further referred to as tetramethylammonium chloride (TMA) buffer). The membrane resistance of the nano-BLM should remain constant even after insertion of the carrier, as TMA cannot be complexed by valinomycin and, thus, no transport activity should be monitored. If, however, different potassium ion concentrations were added to both compartments, the impedance spectra changed considerably (Fig. 9 A).

The equivalent circuit shown in Fig. 2 A can be applied to extract the membrane resistance. The membrane resistance can also readily be approximated from the magnitude of the impedance at low frequencies, where $|Z|$ becomes independent of the frequency and equals the sum of R_{el} and R_m (Fig. 9 A). In pure TMA buffer, a specific membrane resistance of $R_{m,sp}$ = 4.4 MΩ cm^2 was monitored. After exchanging the solution with TMA buffer containing 500 mM K^+, the resistance decreased considerably to $R_{m,sp}$ = 0.3 MΩ cm^2. By varying the potassium ion concentration in a range of 50-500 mM, a linear relation of the membrane conductance as a function of c_K was obtained (Fig. 9 B). The same holds for the sodium ion dependency. A linear dependence of the membrane conductance as a function of c_{Na} was found in a concentration range of 50-500 mM (Fig. 9 B). Obviously, the conductance increase in the presence of potassium ions is significantly larger than in the presence of sodium ions, if valinomycin is embedded in the nano-BLM. The slope, which is a measure of the transport of the cation mediated by valinomycin, is approximately 20 times larger for K^+ than for Na^+. This result is in good accordance with the known selectivity of valinomycin for potassium over sodium ions found in different membrane systems.[12,43-46] A parameter that cannot be controlled is, however, the valinomycin concentration in the membrane, which also determines the macroscopic transport efficiency. Thus, a direct comparison between different cation transport efficiencies can only be performed on one nano-BLM after insertion of valinomycin. As a nano-BLM lasts various buffer exchanges, even in a continuous flow system,[47] experiments on one nano-BLM can be easily performed. To verify that a nano-BLM without valinomycin is not conducting for potassium cations, it was immersed in a TMA buffer containing either 500 mM KCl or 500 mM NaCl. Impedance analysis revealed no significant change in membrane resistance in the presence of high salt.

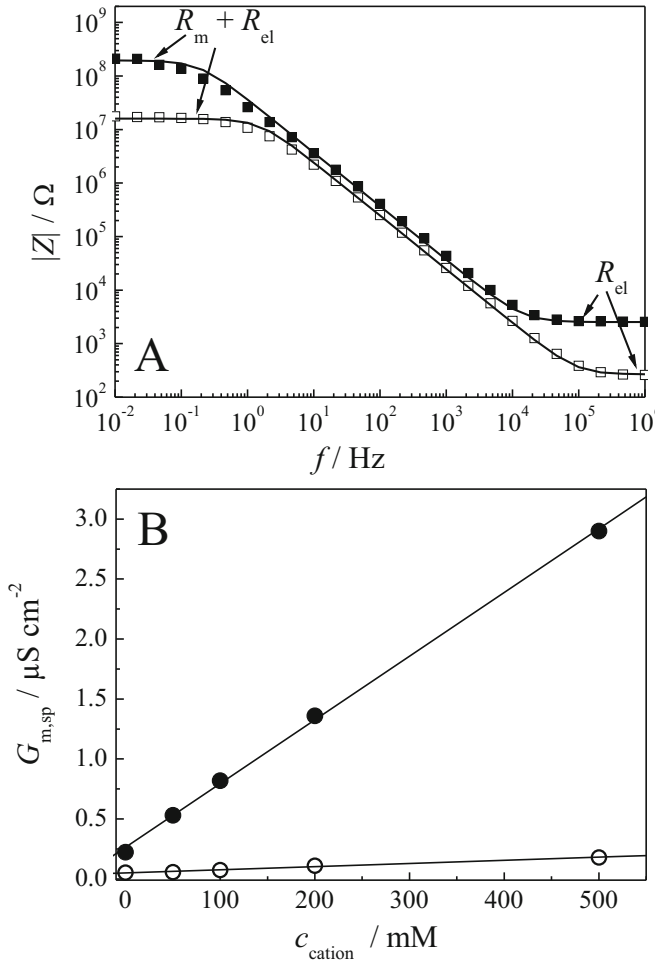

Figure 9. A) Impedance spectra ($|Z|(f)$) in the frequency range of 10^6-10^{-2} Hz after addition of valinomycin in (■) TMA buffer and in the presence of (□) TMA buffer containing 500 mM KCl. The membrane capacitance slightly changed in the range of (0.23 ± 0.04) µF cm^{-2}. B) Conductance plotted vs. increasing concentrations of KCl (●) and NaCl (○) in the bulk phase. The solid lines are the results of linear regressions.[47]

(*ii*) *Reconstitution of Channel Forming Peptides*

As nano-BLMs exhibit very similar membrane resistances as classical BLMs and are accessible from both sides, they are well suited for the reconstitution of channel forming peptides. In the next paragraphs, we describe several examples of peptide reconstitution from the aqueous phase, resulting in the insertion of single peptides, which allow the investigation of their channel conductance.

(*a*) *Gramicidin*

One of the most well-known model systems for ion transport through peptide-based channels is gramicidin A. This linear pentadecapeptide is synthesized by *Bacillus brevis*[48,49] forming a channel in lipid bilayers consisting of two antiparallel oriented monomers bound to each other by six hydrogen bonds. The resulting dimer has a length of only 26 Å, which is sufficient to span the hydrophobic part of a membrane. Owing to the given length, a functional gramicidin channel is only formed in a single lipid bilayer and this fact can be used to verify that nano-BLMs are indeed single lipid bilayers. The transmembrane ion channel selectively facilitates the permeation of alkali cations. The ion selectivity following $K^+ > Na^+ > Li^+$ as well as the partial blockade by Ca^{2+} are well understood.[50,51] Thus, it has been widely used together with novel lipid bilayer systems such as solid supported membranes to investigate their integrity for membrane transport functions.[52,53] For single channel recordings, nano-BLMs were bathed in 500 mM KCl solution. Application of a holding potential of V_h = +70 mV across the bilayer allowed the voltage-driven ion current induced by gramicidin upon its bilayer partition to be measured. Gramicidin dissolved in ethanol was added to the nano-BLM in a 10 nM concentration. After insertion of two half channels, single conductance states as well as multiples of those with distinct conductance states were recorded.[23] A single open state exhibits a current flow of (4.2 ± 0.2) pA, which translates in a gated conductance state of (60 ± 2) pS. Voltage-clamp experiments were also carried out in 500 mM CsCl solution, resulting in a conductance of (76 ± 5) pS. In 500 mM LiCl, only single channel openings were observed, which occurred rather rarely with a mean conductance

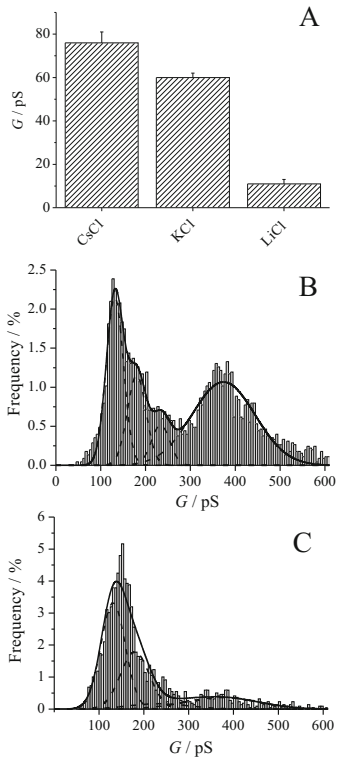

Figure 10. A) Single channel conductance values *G* of gramicidin D in a DPhPC nano-BLM on a porous alumina substrate with a mean pore diameter of 280 nm. Three different cations with a concentration of 500 mM were added to both sides of the porous substrate. B) Histogram analysis of the observed conductance states of the 2,2'-bipyridine-functionalized peptidic ion channel in nano-BLMs up to 1000 pS (3556 events, bin width: 5 pS, normalized to all events (4524)) in the absence of $NiCl_2$. C. Histogram analysis of the conductance states of the 2,2'-bipyridine-functionalized peptidic ion channel in the presence of 2.5-5 µM $NiCl_2$ up to a conductance of 1000 pS (2029 events, bin width: 5 pS, normalized to all events (2189)). The solid lines are the results of fitting four Gaussian distributions (dotted lines) to the histograms.[58]

of (11 ± 2) pS (Fig. 10 A). The observed conductivities for the different alkali cations are in good agreement with the selectivity series of gramicidin, which is known to be $Cs^+ > K^+ > Li^+$.

(*b*) *Alamethicin*

Full functionality of a membrane system is only given if the lateral mobility of the components is proven. Gramicidin can be observed in a functional state even in a solid supported membrane system, in which one leaflet is attached to the substrate as demonstrated by Cornell and coworkers.[54,55] In contrast, one alamethicin helix, a peptaibol from *Trichoderma viridae*, spans the entire lipid bilayer and forms voltage gated ion channels with multiple conductance levels. This behaviour can be explained by the formation of transmembrane aggregates according to the barrel stave mechanism.[56] The uptake and release of alamethicin helical monomers from a channel aggregate accounts for the observed multi-state conductance levels.[57] The formation of such helix bundles requires the lateral movement of the individual helices. We analyzed whether such helix bundles are formed, if alamethicin is reconstituted into nano-BLMs. The nano-BLMs were bathed in 500 mM KCl and alamethicin was added only to the *cis* side from an ethanolic solution, resulting in a final concentration of about 100 nM, while applying a holding potential of V_h = +70 mV. The voltage-dependent activation of single alamethicin channels with up to five conductance states was observed.[23] The different conductance states are defined by the number of monomers making up the pore forming aggregate. Hence, from the results one can conclude that, indeed, monomeric alamethicin helices can move laterally within the nano-BLM to form conducting oligomers.

(*c*) *2,2'-Bipyridine-Functionalized Peptidic Ion Channels*

Based on this knowledge, it was the idea to control the helix bundle formation of amphipathic helices in nano-BLMs. Thus, we synthesized an α-helical amphipathic peptide with the sequence H_2N-(LeuSerSerLeuLeuSerLeu)$_3$$CONH_2$, to which a bipyridine moiety with a spacer of 7 carbon atoms was attached to the N-terminus,[58] in order to answer the question if it is possible to control the conductance behaviour of the peptide by complexation of

the bipyridine residues with Ni^{2+}. The peptide sequence itself[59] had already been shown to insert into lipid bilayers as an amphipathic α-helix, forming cation selective ion channels with an effective diameter of 0.8 nm under voltage control.[59-61] From the effective diameter and computer simulations it was concluded that a hexameric bundle is formed in lipid bilayers.[60,62] The synthetic peptide was inserted into nano-BLMs from an ethanolic solution and its channel properties were characterized by single channel recordings under voltage clamp conditions in the absence and presence of $NiCl_2$. Characteristic rectangular current traces were observed either in the absence or in the presence of Ni^{2+}.[58] We attribute this step-like current increase and decrease to the assembly and disassembly of a helix bundle composed of a defined number of amphipathic peptide helices. Altogether, four different opening levels were discernable in the current range of around 25 pA (O_1), 35 pA (O_2), 45 pA (O_3) and 70 pA (O_4). Channel events of one opening level were often observed in bursts, which lasted several seconds. Event histograms were used to determine the conductance states (Fig. 10 B), resulting in four Gaussian distributions with G_1 = (131 ± 19) pS, G_2 = (181 ± 20) pS, G_3 = (234 ± 20) pS, and G_4 = (374 ± 70) pS. Twenty one percent of all events did not fall into these conductance levels but were larger than 600 pS. Taking the fact that the lowest conductance state is attributed to six peptide monomers forming a helix bundle, as proposed by DeGrado and coworkers,[59,60] the higher conductance states would be a result of a continuous increase in the number of helices participating in the bundle, up to nine helices.

In the presence of Ni^{2+}, the analysis of the conductance states indeed revealed a considerable change. $NiCl_2$ was added in a concentration of 2.5-5 μM to both sides of the membrane and voltage clamp experiments were again performed. The majority of events were found in a current range of 15-110 pA. A histogram analysis demonstrated that the conductance states are in the same range as those observed in the absence of Ni^{2+} (Fig. 10C). However, their distribution is significantly different. Four Gaussian functions were fitted to the data with the assumption that the mean conductance states do not change in the presence of Ni^{2+}, thus keeping these four parameters constant. It is obvious that the first and second conductance levels are very prominent, while the third and fourth ones are greatly diminished. The relative area of the first and se-

cond conductance states equals 78 % in the presence, and only 43 % in the absence, of $NiCl_2$. Only 7 % of all events were found with a conductance level above 600 pS. From these findings, it can be concluded that the complexation of bipyridine by Ni^{2+} indeed results in a considerable confinement of the observed multiple conductance states. Assuming that the lowest conductance state is a result of the formation of a six helix bundle, helix bundles with six and seven helices are preferentially formed in the presence of Ni^{2+}, while higher-order aggregates become less likely.

2. Protein Channels

Relatively large transmembrane proteins such as α-hemolysin[63] and the glutamate receptor[19] have been reconstituted into membranes on orifices in either polycarbonates or silicon, with diameters greater than 1 μm. We raised the question of how the pore size of the porous material limits the incorporation and the functionality of complex integral membrane proteins in nano-BLMs. To address this question, the functional insertion of the outer membrane protein F (OmpF) from *E. coli* and of the eukaryotic protein connexon 26 (Cx26) was investigated in nano-BLMs on porous alumina with pore diameters of 60 nm by observing the ion channel activity in voltage clamp experiments, as detailed below.

(*i*) *Outer Membrane Protein F*

The porin OmpF is a well characterized protein in terms of structure[64,65] and channel activity. It is composed of 16 antiparallel aligned β-sheets (β-barrel), connected by amino acid sequences building up a water-filled pore. Three of these monomeric units with a molecular weight of 37.1 kDa and a length of 5 nm are arranged around a three-fold molecular axis. One protein covers an area of roughly 80 nm^2. In a nano-BLM, it is surrounded by just a few thousand lipids. Ion selectivity and conductivity of the channel is assumed to be a result of the constriction zone[66] that is formed by loop 3, which folds into the barrel at approximately half the height of the channel. By voltage clamp experiments, we were able to prove that the protein is fully functional in nano-BLMs. The insertion of the porin results in a three-step increase and decrease in current due to the stepwise opening and closing of each subunit

pore.[26] Point histogram analysis of the current traces allowed for the determination of the three different conductance levels with G_1 = (1700 ± 80) pS, G_2 = (3360 ± 80) pS and G_3 = (5060 ± 50) pS. In addition, we investigated whether we are also able to monitor the reported fast kinetics and subconductance states. Also, these characteristics of the porin pore were found in nano-BLMs, indicating that the close proximity of immobilized lipid bilayers on the pore rims does not influence the ion channel activity.[26] Nestorovich et al.[67] reported that the β-lactam antibiotic ampicillin is capable of blocking the OmpF channel by moving in and out of the channel. This process takes place on a rather fast time scale. It turned out that the time resolution of our system is not sufficient to fully resolve every single ampicillin blockade as was demonstrated in the work of Nestorovich et al.[67] However, blockades of ampicillin were clearly detected as downward spikes of the ion flow during the opening of one monomer.[26] These results indicate that the porous substrate underneath the membrane does not prevent the full functionality of a large transmembrane protein, even though one membrane, spanning a 60 nm pore of the porous alumina substrate, is composed of only roughly 4000 lipids.

(*ii*) *Connexon 26*

Connexins are members of a multigene family of membrane-spanning proteins that form intercellular channels, which are composed of two hexameric hemichannels, called connexons (Cx). These intercellular channels organize into gap junctional plaques and span the extracellular space/matrix of adjacent cells, thus allowing a passive exchange of small molecules up to about 1 kDa.[68] By the formation of gap junctions, two membranes can be electrically connected. As a prerequisite for the electrical coupling, connexons need to be reconstituted into a membrane system that is accessible from both sides. Nano-BLMs can provide the required accessibility and, at the same time, the stability to connect a membrane such as the plasma membrane of a cell via the formation of gap junctions. To elucidate the functionality of a connexon in nano-BLMs, connexon 26 (Cx26) isolated from baculovirus-infected Sf9 cells was reconstituted. This was achieved by adding Cx26 dissolved in a 1 % (*v/v)* octyl-polyoxyethylene (*o*-POE) detergent solution to the *cis* side of the Teflon cell, leading to a final

concentration of 0.7-2.7 ng mL^{-1}. Since the insertion of a Cx26 oligomer is a random process, activity is observed sometimes already after several minutes, but in other cases only after hours. By means of voltage clamp experiments, information about the conductance states of Cx26 can then be gathered. If a hemichannel was inserted, current traces were recorded and different holding potentials ranging between V_h = +150 mV and -150 mV were applied. It turned out that the hemichannels exhibit a pure Ohmic behaviour with a mean conductance of (33 ± 3) pS (Fig. 11 A).

This result is in good agreement with conductance values obtained from the same hemichannel inserted into planar bilayers on microstructured glass supports, a method provided by the company Nanion (Munich, Germany).[69] A statistical analysis of all single channel events reveals one prominent conductance state with a mean conductance of G_1 = (34 ± 8) pS. In addition, but less frequently, larger conductance states were observed with two distributions at G_2 = (70 ± 8) pS and G_3 = (165 ± 19) pS. Other groups found similar single channel conductance values for reconstituted hemichannels, being in the range of 35-316 pS.[70,71] This result indicates that even Cx26 hemichannels can be inserted into nano-BLMs in a functional manner.

IV. IMPEDANCE ANALYSES ON PORE-SPANNING MEMBRANES

Nano-BLMs with membrane resistances in the range of gigaohms prove to be a suitable model system for the investigation of peptides and large transmembrane proteins on a single channel level, as outlined in Section III. In contrast, pore-spanning lipids bilayers generated by vesicle fusion on porous alumina exhibit resistances two to three orders of magnitude lower than those of nano-BLMs. Still, ion channel activity can be measured by using EIS. This technique allows detecting conducting channel proteins in pore-spanning bilayers in an integral manner and, thus, overcomes the need for gigaohm seals. Here, we present the monitoring of ion channel activity, namely of OmpF and gramicidin, by means of EIS.

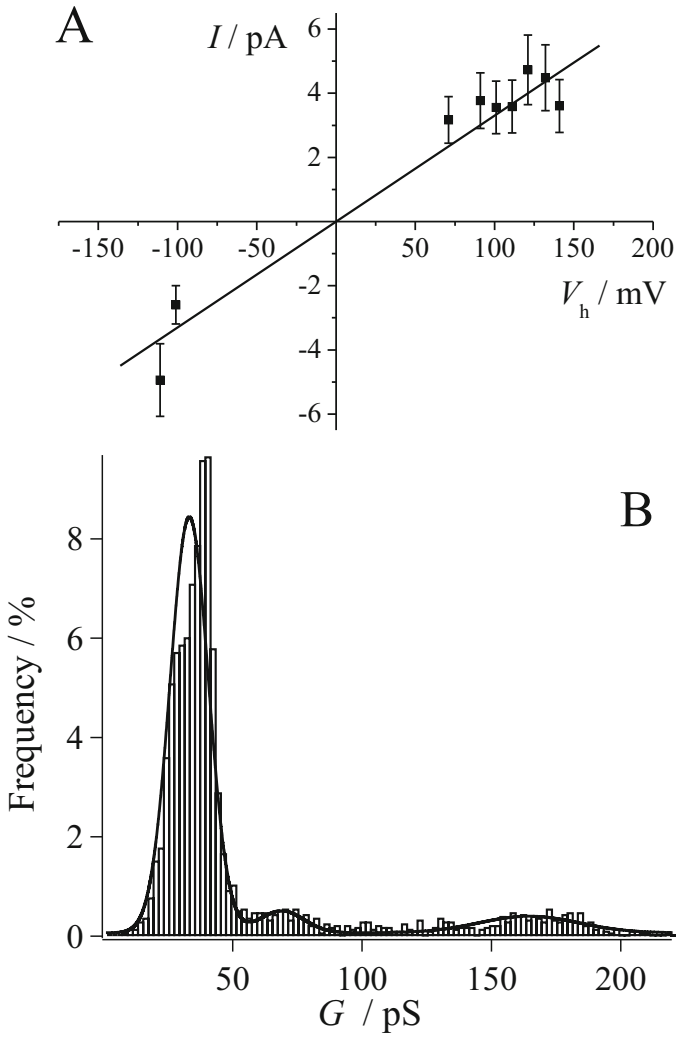

Figure 11. A) Cx26 current-voltage relationship of averaged current steps ranging between 0-63 pS (2169 events). The hemichannel shows a linear I-V_h-dependence with a main conductance of (33 ± 3) pS. B) Event-histogram of the observed conductance states of Cx26 in nano-BLMs (2691 events, bin width: 2 pS). The solid line is the results of fitting three Gaussian distributions to the histogram. Three main conductance states are assigned to G_1 = (34 ± 8) pS, G_2 = (70 ± 8) pS, and G_3 = (165 ± 19) pS.[69]

1. Reconstitution of OmpF

In Section II, the electrochemical characteristics of pore-spanning membranes investigated by EIS were discussed in detail. The data reveal that the absolute value of the impedance $|Z|$ at frequencies $< 10^1$ Hz is solely governed by the resistive properties of the bilayer and is thus frequency independent. Thereby, performing EIS experiments at a fixed frequency of 10 Hz or less allows following the membrane resistance R_m without taking the capacitive properties into account. Membrane-integrated, active ion channels produce a change in membrane conductivity, which is readily detected as a change in the absolute value of the impedance $|Z|$ at the chosen frequency as a function of time. Prior to this time resolved experiment, impedance spectra need to be recorded to determine the frequency range in which the membrane resistance R_m is well defined.

As mentioned in Section III, reconstitution of transmembrane proteins from an aqueous solution requires that the molecules are solubilised in and added from a detergent solution. Detergents are amphiphiles and known to interact with lipid bilayers. Studies on liposomes revealed that detergents at concentrations considerably below their critical micellar concentration (CMC) partition into the bilayers and permeabilise them.[72,73] Hence, prior to protein addition, we first investigated the influence of the detergent *o*-POE on R_m, which is widely used to solubilise membrane proteins. Figure 12 represents $|Z|$(1 Hz) of a pore-spanning bilayer as a function of time monitored in 0.1 M NaCl. It is obvious that a final concentration of 0.0002% (*v*/*v*) *o*-POE, which is four orders of magnitude below its CMC, is sufficient to permeabilise the bilayer such that $|Z|$(1 Hz) decreases by two orders of magnitude. However, by exchanging for detergent-free electrolyte solution, the original membrane resistance is recovered. Thus, the interaction of *o*-POE in sub-CMC concentrations with pore-spanning membranes is fully reversible. Then, OmpF in *o*-POE (0.0002% (*v*/*v*) *o*-POE, 0.5 nM OmpF) was added to the pore-spanning lipid bilayers, again resulting in a significant decrease in membrane resistance. Yet, rinsing with electrolyte solution resulted in only partial recovery of the membrane resistance. The net drop in bilayer resistance R_m is a result of the formation of OmpF pores in the pore-suspending

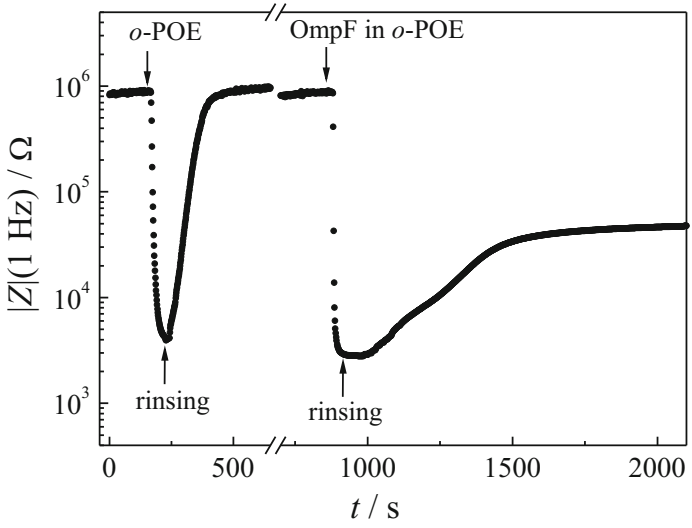

Figure 12. Time-resolved change of the magnitude of the impedance $|Z|$ at a fixed frequency of 1 Hz of a pore-suspending membrane after the addition of *o*-POE with a final concentration of 0.0002 % (*v/v*) and rinsing with buffer, followed by the addition of OmpF dissolved in *o*-POE to the *cis* side, leading to a final protein concentration of 0.5 nM in 0.0002 % (*v/v*) *o*-POE. Electrolyte: 0.1 M NaCl.[35]

membrane, demonstrating that the proteins are functionally inserted.

Based on this result, we raised the question of how many OmpF molecules contribute to the decrease in membrane resistance. In order to quantify this, the change in conductivity ΔG is calculated from the bilayer resistance before (R_0) and after (R_m) the insertion of OmpF. According to Eq. (5):

$$\Delta G = \frac{1}{R_m} - \frac{1}{R_0} = G_m - G_0 \tag{5}$$

ΔG equals 19.7 µS. Taking the conductivity of 535 pS of a single OmpF trimer in 0.1 M NaCl into account,[18] approximately 10^6 proteins cause the monitored decrease in bilayer resistance. This calculation demonstrates that a significant number of mole-

cules need to be incorporated in order to detect active ion channels in pore-spanning membranes.

These facts raise the question, why only one or a few protein molecules insert into nano-BLMs, whereas 10^6 are incorporated into pore-suspending lipid bilayers. Both the total membrane area and the final protein concentration in the measuring chamber cannot explain the observed difference. On the one hand, the total membrane area of pore-spanning membranes is approximately twofold smaller, which in theory decreases the probability of an insertion event. On the other hand, even though the concentration of OmpF added to pore-spanning membranes is at most 300-fold higher, it cannot explain the incorporation of 10^6 times more molecules compared to nano-BLMs. Thus, another parameter seems to limit the insertion of protein molecules and detergents into nano-BLMs. Presumably, detergent molecules and proteins dissolve in the residues of the organic solvent, which is required for preparing nano-BLMs and is known to remain in the membrane.[29] Thus, the molecules might lose their functionality in these membrane areas. In contrast, pore-suspending membranes are nominally free of organic solvent and all incorporated molecules are fully functional.

The comparison of the insertion of OmpF in nano-BLMs versus pore-spanning membranes reveals that these two membrane systems address different experimental needs. While pore-spanning membranes cannot be used for single channel recordings, they are suited for monitoring membrane resistances by EIS and prove to be highly sensitive to the incorporation of vast numbers of membrane soluble molecules. Indeed, the use of this high insertion efficiency could be envisioned to be applied for monitoring lipid bilayer interactions of membrane modulators, which cause permeabilisation. Furthermore, these insertion rates in pore-spanning bilayers hold the advantage of introducing membrane proteins in such numbers that allow for integral measurements of their channel activity. However, the interactions of detergent molecules that are always present when working with solubilised membrane proteins are considerable, and their impact on the electric properties of the bilayers is significantly disrupting. An alternative route to reconstitute ion channels in pore-spanning membranes prevents the use of detergents and involves the use of proteoliposomes as described in detail in the following paragraph.

2. Analysis of Gramicidin D Activity

We aimed to reconstitute ion channels in pore-spanning membranes by fusion of proteoliposomes on functionalized porous substrates. Gramicidin D turned out to be a good test case for the development of the principle strategy.

(*i*) *Channel Activity of Gramicidin D Reconstituted into Pore-Spanning Membranes*

Large unilamellar vesicles composed of DOPC doped with 2 mol% gramicidin D were prepared and the conformation of gramicidin D was analyzed by circular dichroism (CD) spectroscopy, verifying that it forms the conducting conformation.[29] To generate pore-suspending membranes with reconstituted active gramicidin channels, we followed the strategy of first generating a pore-suspending bilayer composed of DPhPC/DOPC (6:4) from vesicle spreading before adding gramicidin D-doped DOPC vesicles to the system for 8–12 hours. Porous alumina substrates with partially opened pore bottoms were used, as the lipid membranes form considerably faster on these substrates (see Section II). If the alumina oxide resistance R_{ox} is known, model (2') can be applied for analysis. For large R_{ox}, the overall resistance R_a resembles $R_{m,o}$ (Eq. 3). This allows to directly link the change in overall resistance to a change in $R_{m,o}$ generated by a conducting ion channel. Throughout the preparation steps, a buffer solution containing TMA was used. TMA is too large to diffuse through the gramicidin channel[74] and, thus, the membrane resistance is supposed to remain unaffected upon insertion of the channel active peptide. To verify the functional transfer of gramicidin D into the pore-spanning membranes, its channel activity was monitored by adding monovalent cations (LiCl, NaCl, and KCl) to the TMA-containing buffer solution into the upper *cis* compartment of the liquid cell (Fig. 1 B). The distinct selectivity for alkali cations and its concentration dependence are the main characteristics of the gramicidin channel. Impedance spectra were recorded before and after increasing the ion concentration to follow the electrical response of the membrane system. The entire experiment with various cations was performed on one membrane preparation, as the electrical properties of pore-spanning membranes depend on the underlying alumina substrate,

the membrane properties and the number of incorporated ion channels.

Figure 13 shows impedance spectra in the absence and after addition of LiCl, NaCl and KCl, respectively, at concentrations of 1-10 mM. The decrease of the overall Ohmic resistance upon addition of alkali cations is clearly discernable in the Nyquist plots by a decrease of the radius of the semicircle. If the alkali cations are removed by rinsing with alkali cation-free buffer, the initial membrane resistance is almost fully regained. Only a slight decrease in the initial membrane resistance is observed, indicating the formation of some additional defects in the bilayer induced by the numerous buffer exchanges. In order to quantify the membrane parameters, the equivalent circuit shown in Fig. 13 D was fitted to the data. It is composed of electrical elements presented in Fig. 7 C, with the difference of an additional component, Z_W. This Warburg-element accounts for the mass transport processes at the membrane interface:

$$Z_w = \frac{\sigma_W}{\sqrt{\omega}}(1-i)\,. \tag{6}$$

The parameter σ_W is the concentration resistance and ω – the applied frequency. The Warburg-element is commonly used by electrochemists to model the diffusion-limited mass transport towards electrodes upon redox reactions.[75] It has, however, also been used to model the diffusion limited transport of ions across free-standing lipid membranes.[76] In case of an ideal diffusion behaviour, the data points comprise an angle of 45° with Z^{Re} at low frequencies, the typical frequency dependence of Z_W (Fig. 13 D).

Upon cation addition to the gramicidin D doped membranes, the overall resistance R_a decreases up to two orders of magnitude. In order to translate the decrease in membrane resistance into a change in conductance ΔG, Eq. (5) was used. According to Hladky and Haydon,[48] a linear relationship of $\Delta G(c)$ in the concentration range of 0-100 mM is expected, which is found in the experiments (Fig. 14 A, closed symbols). A unit conductance for all three different alkali cations can be deduced from the slope m of a linear regression to the data with $m_{Li} = (1.29 \pm 0.05)$ µS mM^{-1}, m_{Na} (3.3 ± 0.2) µS mM^{-1} and $m_K = (6.3 \pm 0.3)$ µS mM^{-1}. To compare different

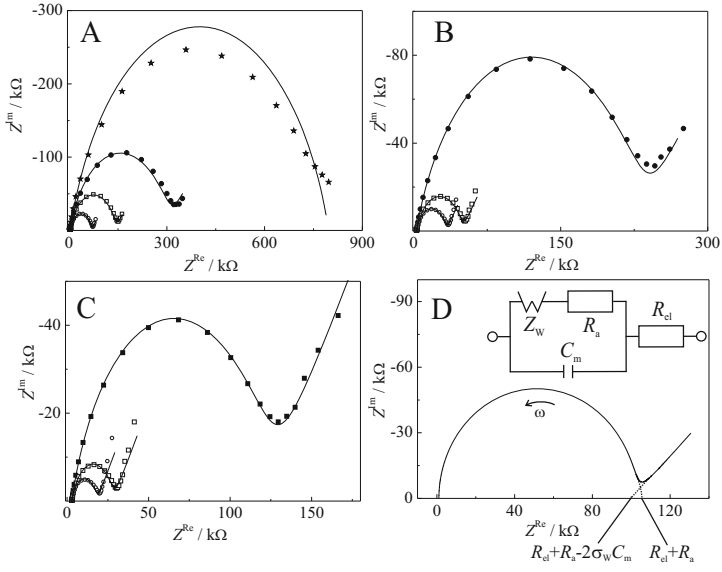

Figure 13. Impedance spectra (Nyquist plots) of a pore-spanning membrane 12 hours after incubation with DOPC vesicles containing 2 mol% gramicidin D obtained in various alkali cation concentrations: 0 mM (★), 1 mM (●), 5 mM (□) and 10 mM (○). A. LiCl, B. NaCl, and C. KCl. Buffer: 10 mM TRIS, 100 mM TMA, pH 8.6. D. Simulated impedance spectrum (Nyquist plot) based on the equivalent circuit shown in the inset. Electrolyte resistance R_{el} = 100 Ω, overall resistance R_a = 10^5 Ω, membrane capacitance C_m = 10^{-7} F, Warburg impedance Z_W with σ_W = 23570 Ω $s^{-0.5}$.[38]

membrane preparations doped with gramicidin, the ratio m_K/m_{Na} was calculated from three independent experiments to be 1.7 ± 0.2, which is in good agreement with the value of 1.8 found for classical BLMs.[77]

Ion selectivity and conductance ratios are reliable indicators of the functionality of an ion channel. However, from the view of pharmacologists, only the characteristic interaction with a modulator, which blocks or activates the channel, unambiguously defines its functionality. It is well known that divalent cations are capable of reducing the conductance of gramicidin.[50] Thus, the same experiments of cation transport were performed in the presence of

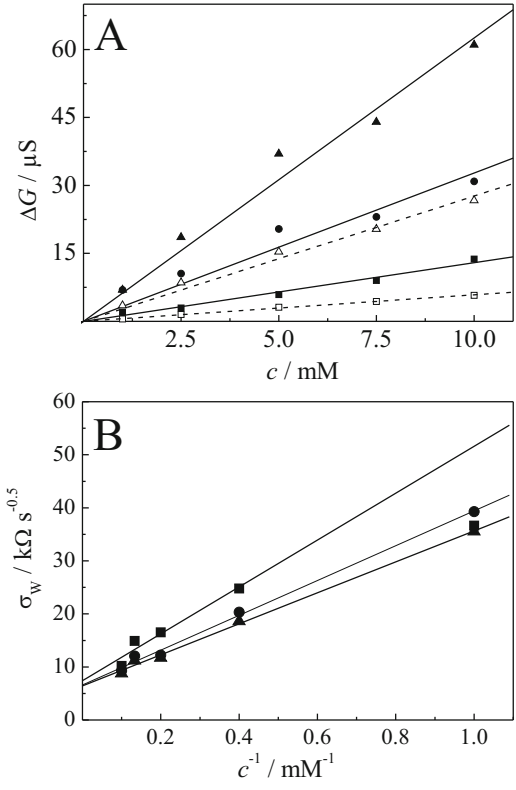

Figure 14. A) Conductance change ΔG of a gramicidin D-doped pore-spanning membrane in the absence (filled symbols) and presence of 20 mM $CaCl_2$ (open symbols). LiCl (■), LiCl + 20 mM $CaCl_2$ (□), NaCl (●), KCl (▲), KCl + 20 mM $CaCl_2$ (Δ). The solid lines are linear regressions yielding slopes for the mean conductance per concentration unit in the absence of Ca^{2+}. m_{Li} = (1.29 ± 0.05) μS mM^{-1}, m_{Na} = (3.3 ± 0.2) μS mM^{-1}, m_K = (6.3 ± 0.3) μS mM^{-1}. The dashed lines are linear regressions in the presence of $CaCl_2$ with the following slopes: $m_{Li,Ca}$ = (0.585 ± 0.008) μS mM^{-1} and $m_{K,Ca}$ = (2.76 ± 0.09) μS mM^{-1}. Buffer: 10 mM TRIS, 100 mM TMA, pH 8.6.[38] B) Concentration resistance σ_W as a function of c^{-1} in the presence of (■) LiCl, (●) NaCl und (▲) KCl. Linear regressions result in the slope s and the intercept $\sigma_{W,0}$. s_{Li} = 44.2 kΩ $s^{-0.5}$ mM, $\sigma_{W,0,Li}$ = 7.4 kΩ $s^{-0.5}$, s_{Na} = 32.8 kΩ $s^{-0.5}$ mM, $\sigma_{W,0,Na}$ = 6.6 kΩ $s^{-0.5}$, s_K = 29.2 kΩ $s^{-0.5}$ mM, $\sigma_{W,0,K}$ = 6.4 kΩ $s^{-0.5}$. Buffer: 10 mM TRIS, 100 mM TMA, pH 8.6.

$CaCl_2$. The alkali cations K^+ (best conducting cation) and Li^+ (worst conducting cation) were chosen for this set of experiments. In the presence of Ca^{2+}, ΔG also changes linearly with increasing cation concentration and the slope is steeper for K^+ than for Li^+ (Fig. 14 A, open symbols). Linear regressions to the data in the presence of $CaCl_2$ reveal a slope of $m_{Li,Ca}$ = (0.585 ± 0.008) µS mM^{-1} and $m_{K,Ca}$ (2.76 ± 0.09) µS mM^{-1}. The observed conductance in the presence of Ca^{2+} is approximately 2-fold lower than in its absence, independent of the conducting alkali cation. Bamberg and Läuger[50] studied the influence of Ca^{2+} in detail and showed that the gramicidin channel is not partially blocked by divalent ions, but its open probability is reduced. Interestingly, the open probability is a function of the lipid composition of the membrane. For DPhPC-bilayers, they observed a reduction in conductance of approximately 70 %, while we monitored a decrease of about 45 % in pore-spanning membranes composed of DPhPC/DOPC.

We raised the question of how many active gramicidin channels contribute to the observed change in conductance. Thus, the conductance for one gramicidin A channel at 10 mM KCl was taken into account (G = 2.15 pS), which was obtained from planar lipid bilayer experiments.[78] The number of active ion channels incorporated into the pore-suspending membrane was calculated from the obtained ΔG value at 10 mM KCl. According to this calculation, roughly $3 \cdot 10^7$ conducting gramicidin dimers are inserted into the pore-suspending membrane. With the area of one gramicidin D channel of 0.4 nm^2, and the total substrate area of 0.0104 cm^2, an area fraction of 0.001 % is occupied by active ion channels. A theoretical maximum area fraction of 0.6 % of gramicidin D in the pore-spanning membrane would be possible, assuming a 100 % peptide transfer from the vesicles into the pore-suspending membranes. However, as only conducting dimers are electrically monitored, the number is significantly lower. This result shows that a large number of peptides can be transferred into the pore-suspending membranes, rendering the protocol promising for studies that involve the activity of transporters with small turnover numbers of one molecule or less per second.

There are several publications dealing with the electrical recording of gramicidin in freestanding BLMs as well as SSMs or tethered lipid membranes (tBLMs). Hence, the question arises what is the advantage of using pore-spanning membranes. One ob-

vious advantage is that pore-spanning membranes overcome the problem of an underlying substrate, as it is required for SSMs[22,79] or tBLMs,[9,13] which serves at the same time as the electrode. For example, Gritsch et al.[77] performed an impedance analysis on gramicidin-doped SSMs obtained from fusing gramicidin-doped liposomes (1 mol%) on an indium-tin-oxide surface. In the presence of 4 mM NaCl, a relative conductance change of 0.4 mS cm^{-2} was observed. On pore-suspending membranes we obtained a 20-fold change in conductance of about 8 mS cm^{-2} at a similar ionic strength (5 mM NaCl). Krishna et al.[55,80] considered the influence of the bilayer supporting material in detail. Whereas in SSMs the bilayer is in direct contact with the underlying substrate, tBLMs are separated by 10-40 nm from the substrate, thus providing a second buffer-containing reservoir, which facilitates the detection of an ion transport through transmembrane proteins. However, it turned out that the aqueous reservoir in tBLMs is very small so that the ions cannot move freely; at higher concentrations they even form ion pairs, which reduce the effective number of conducting species and, thus, the expected conductivity of the buffer system.[55] With dielectric constants of ε_r = 27-45, the aqueous reservoir is more of a gel-like texture compared to the bulk aqueous phase with ε_r = 80.[80] Under these conditions, the apparent conductance of gramicidin was 7-fold smaller than expected.[55] Similar results were obtained from experiments on α-hemolysin reconstituted in tBLMs.[81] tBLMs were established on gold substrates using tethered lipids of various lengths. The change in conductance was a function of the linker length and, thus, the volume of the aqueous reservoir. In contrast to experiments with tBLMs, the activity of ion channels in pore-spanning membranes or nano-BLMs reflects the expected conductivity.[23,26,69] This led us conclude that the buffer-filled pores of the alumina substrates can be considered as similar to the bulk aqueous phase. However, there are still some limitations, which will be discussed in the following chapter.

(*ii*) *Mass Transport Phenomena*

Besides the conductance changes calculated from $R_{m,o}$, a second parameter is obtained from impedance analysis, namely the concentration resistance σ_W. In previous studies, the Warburg element has been shown to account for the mass transport of ions in

front of the bilayer.[22,82] Not only is the membrane conductance a function of the ion concentration in solution,[22] as demonstrated in the previous Section, but also σ_W:

$$\sigma_W = \frac{RTK}{z^2F^2\sqrt{2D_w}}\frac{1}{c} \quad (7)$$

σ_W is determined by the diffusion coefficient D_w of ions in the aqueous medium and the partition coefficient K of ions between the lipid and aqueous phase. The other parameters in Eq. (7) are denoted as usual. The plots in Fig. 14 B indeed show a linear behaviour of σ_W (c^{-1}). However, the linear regressions do not cross the origin. The slopes s were determined to be s_{Li} = 44.2 kΩ $s^{-0.5}$ mM, s_{Na} = 32.8 kΩ $s^{-0.5}$ mM, and s_K = 29.2 kΩ $s^{-0.5}$ mM. With $D_{Li} < D_{Na} < D_K$, [83] the values for s are expected to follow the trend $s_{Li} > s_{Na} > s_K$, which agrees with the finding. The second parameter K, however, also determines the slope but cannot be readily defined as it depends on the bilayer itself. Assuming that K is similar for Li^+, Na^+ and K^+, the ratio m_I/m_J of the ions I^+ and J^+ reflects the ratio of their diffusion coefficients $D_J^{0.5}/D_I^{0.5}$. Table 1 shows a comparison of the experimentally determined and theoretical ratios of diffusion constants.[83] The main deviation from theory is the observation that the linear regressions do not cross the origin, i.e., $\sigma_{W,0} \neq 0$. $\sigma_{W,0}$ appears to be independent of the cation with an average $\sigma_{W,0}$ = (6800 ± 500) kΩ $s^{-0.5}$. This value implies that even at high ion concentrations, the mass transport cannot be neglected, which might be attributed to the fact that the alkali cations were only added from the *cis* compartment of the cell, resulting in an ion gradient across the bilayer. The ion gradient causes an electrochemical potential driving the ion transport across the bilayer, which is not included in our model.

It is worth noting that the mass transport phenomena cannot be readily investigated in case of SSMs,[22] as the impedance data of gramicidin-doped SSMs at low frequencies are hampered by the capacitance of the underlying gold electrode. This became also obvious in a study of Vallejo and Gervasi[84] on gramicidin-containing SSMs. To account for mass transport, they introduced a Warburg impedance in their electrical model, but did not extract σ_W-values that reflect the expected trend, when varying the mono-

Table 1
Ratio of the Diffusion Coefficients $D_J^{0.5}/D_I^{0.5}$ of Two Alkali Cations. The Experimental Values were Determined from the Slopes of the Linear Regressions to the Data Shown in Fig. 14 B. The Theoretical Values are Based on the Diffusion Coefficients in Aqueous Solution.

I^+ / J^+	Experimental	Theoretical
K^+ / Na^+	0.89	0.83
Na^+ / Li^+	0.74	0.88
K^+ / Li^+	0.66	0.72

valent cations. Others, who investigated ion transport processes on gallium-arsenide-supported membranes included, in addition to a Warburg-element, a *RC*-circuit, which accounts for the properties of the underlying electrode.[85] In most studies that deal with ion channel-doped SSMs, only the properties of the supporting electrode is included, while the mass transport is neglected.[12,77]

(*iii*) *Gramidicin Transfer from Peptide-Doped Liposomes to Pore-Spanning Lipid Bilayers*

The success of the reconstitution protocol is the transfer rate of the peptide from the vesicles into the pore-suspending membranes. To investigate the kinetics of the gramicidin transfer in more detail, gramicidin-doped liposomes were prepared in alkali cation-free buffer and added to a pore-suspending membrane in the presence of KCl. Gramicidin itself serves as an indicator for its insertion, as a conductance change is only observed if it is integrated in the pore-spanning bilayer. As a control, the same experiments were carried out with gramicidin-free vesicles. Impedance spectra were taken in intervals of 30 min and the membrane resistance R_a was extracted using the equivalent circuit from Fig. 7 C (in the absence of KCl) and Fig. 13 D (in the presence of KCl). The change in conductance $\Delta G = G(t) - G(t = 0)$, plotted as a function of time (Fig. 15), demonstrates that only in the presence of gramicidin-doped vesicles an almost exponential increase in conductance is observed, while in the control experiment no increase in conductance was monitored.

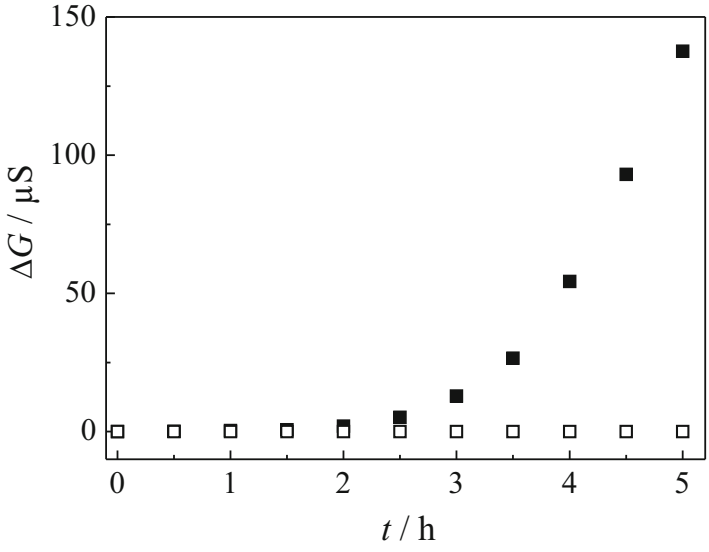

Figure 15. Conductance change ΔG of a pore-spanning membrane during the exposure to gramicidin-doped (2 mol%) DOPC LUVs (●) and gramicidin-free DOPC LUVs (○). Buffer: 10 mM TRIS, 100 mM TMA, 10 mM KCl, pH 8.6.[38]

It can be concluded that a transfer of conducting gramicidin dimers takes place upon incubation of liposomes with a pore-suspending membrane. We suggest that the transfer process is driven by fusion of vesicles with the pore-suspending membrane based on the following facts: It is known that gramicidin, once incorporated into a lipid bilayer, does not readily exchange to another bilayer,[86] i.e., there is no partition of gramicidin between the aqueous and the membrane phase as is known for ion carriers such as valinomycin.[86] Moreover, gramicidin only forms conducting dimers if the peptide is transferred to both leaflets of the bilayer. Since we monitor the conducting transmembrane channels by impedance spectroscopy (monomers in only one leaflet are not conducting), it appears likely that gramicidin is transferred to the pore-suspending bilayers via fusion of the peptide-doped liposomes resulting in gramicidin in both leaflets. The study also reveals that the process of fusion takes several hours. This is a drawback when working with transmembrane proteins, which are prone to fast in-

activation at room temperature. It is apparent that fusion of proteoliposomes to pore-suspending membranes needs to be accelerated to overcome this problem.

V. ACTIVITY OF THE PROTON PUMP BACTERIORHODOPSIN

Bacteriorhodopsin (bR) is an integral membrane protein that uses light to translocate protons across membranes in *Halobacterium salinarium*. The bacteria use the proton gradient in the absence of light to generate ATP. In the lipid bilayers, bR forms trimers packed in highly ordered two-dimensional hexagonal arrays, which make up 75% of the membrane; hence, they are named purple membranes.[87] One monomer is comprised of seven transmembrane helices, connected by short extramembraneous loops, spanning the lipid bilayer.[88] In the inner core of the helix bundle, a retinal moiety is covalently bound to the lysine residue Lys^{216} via a Schiff-base. The retinal is vital for the protein pump mechanism. Upon illumination, it isomerizes from a *trans* to *cis* configuration, which initiates the active transport of a proton. During one photo cycle, a single proton is translocated across the bilayer. Eventually, the retinal moiety is again adapting a *trans* configuration, allowing for a new photo cycle to start.[89,90] In contrast to the above described ion channel gramicidin, bR is an active transporter protein. This class of proteins is characterized by small turnover numbers; in the case of bR, 100 protons are translocated per second.[91] Compared to ion channels, which conduct up to 10^7 species per second, the number of transported molecules is by many orders of magnitude smaller. This fact hampers the investigation of transporters with electrochemical methods due to an unfavourable signal-to-noise ratio. In order to enhance signals from transporters, the density of molecules in the system needs to be sufficiently high. Here, we employed bR to verify that we can establish high protein densities in pore-spanning membranes by fusing proteoliposomes on porous alumina. The characteristic property of bR, the light-induced translocation of protons, is well described, which makes it a suitable model transporter for our research purposes.

1. Theoretical Description of Light-Induced bR-Photocurrents

In this Section, we will first give a theoretical description of the photocurrent observed upon illumination of bR containing lipid membranes. Different membrane setups will be elucidated and the characteristic current traces as a function of time will be simulated. The theoretical approach is based on the work of Herrmann and Rayfield,[92] who described the photocurrent of light activated bR reconstituted in vesicles, partially fused to BLMs. Absorbed light drives a pump current I_p, carried by the transported protons, which generates a voltage V_p across the membrane. According to Herrmann and Rayfield,[92] I_p is a linear function of the voltage V_p:

$$I_p = I_{p,0}\left(1 - \frac{V_p}{V^*}\right) \tag{8}$$

$I_{p,0}$ is the initial pump current at $V_p = 0$, V^* is an intrinsic constant. Only with $V^* >> V_p$, I_p is a linear function of V_p. V_p strongly depends on the electrochemical properties of the environment, which is electrically coupled to the bR-containing membranes. Figure 16 sketches the general setup (A) together with an equivalent circuit (B), in which the upper part represents a bR-containing membrane acting as a current source, while the bottom part needs to be defined by the entire electrochemical system. We will discuss two different scenarios for part X:

Model A: Attachment of purple membranes on nano-BLMs;
Model B: Insertion of bR in pore-spanning membranes.

(*i*) *Purple Membranes Attached to Nano-BLMs*

In the first scenario, a *sandwich*-like structure is assumed, in which purple membranes (PM) are attached to a lipid bilayer (model A). Simulations of the photocurrents induced by bR in these purple membranes are based on the equivalent circuit shown in Fig. 17 A according to the *sandwich* model first described by Bamberg et al.[93] for purple membranes adsorbed to classical BLMs.

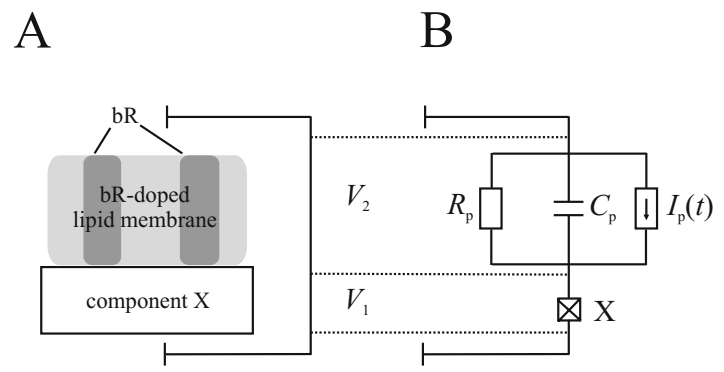

Figure 16. A. Electrochemical model of a bR-containing membrane coupled to a second electrochemically active component X. The light-induced activity of the proton pump bR generates a potential difference $V_p = V_2 = V_1$ under short-circuit conditions. B. Theoretical model of the electrochemical system shown in A. The network comprises a resistance R_p and a capacitance C_p to account for the properties of the bR-doped lipid membrane. In parallel, the proton pump activity is symbolised by the current source $I_p(t)$. X describes a coupled electrochemically active component.

In this case, the electrical conductance G and capacitance C of both, the purple membranes, G_p and C_p as well as the ones of the nano-BLMs, G_m and C_m impact the pump current I_p. In combination with Eq. (8), a differential equation for the voltage V_p can be written (Eq. 9):

$$I_{p,0}\left(1-\frac{V_p}{V^*}\right) = V_p G_m + V_p G_p + \dot{V}_p C_m + \dot{V}_p C_p \tag{9}$$

The solution of the differential equation yields an expression for $V_p(t)$. To obtain the measured photocurrent $I(t)$, Eq. (10) needs to be employed:

$$I(t) = \dot{V}_p C_m + V_p G_m \tag{10}$$

For $t \geq t_{on}$, Eqs. (9) and (10) yield:

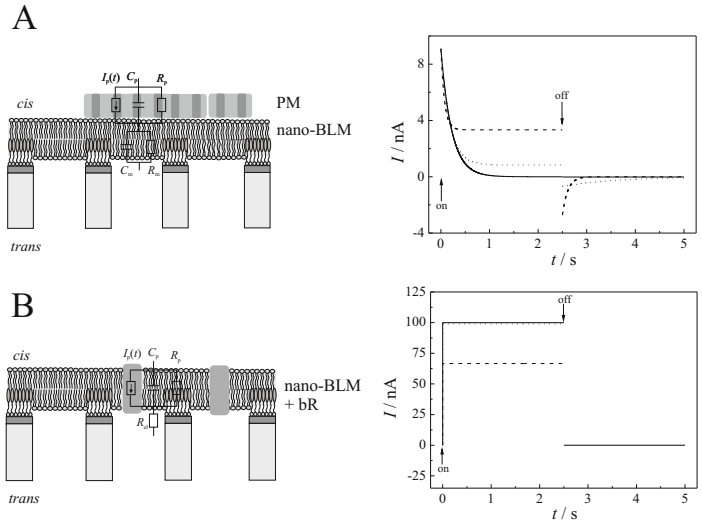

Figure 17. A) Schematic drawing of the membrane setup as proposed for model A together with simulated current traces based on model A using the following parameters: $V^* = 0.2$ V, $I_{p,0} = 10^{-8}$ A, $C_m = 10^{-8}$ F, $C_p = 10^{-9}$ F. (—) $G_p = 10^{-12}$ S, (---) $G_p = 5 \cdot 10^{-9}$ S, (····) $G_p = 5 \cdot 10^{-8}$ S. B) Schematic drawing of the membrane setup as proposed for model B together with simulated current trances based on model B using the following parameters: $V^* = 0.2$ V, $I_{p,0} = 10^{-8}$ A, $C_m = 10^{-8}$ F, $C_p = 10^{-9}$ F. (—) $G_p = 10^{-12}$ S, (---) $G_p = 5 \cdot 10^{-9}$ S, (····) $G_p = 5 \cdot 10^{-8}$ S.

$$I(t) = I_{stat} + \left(I_{on,max} - I_{stat}\right) \exp\left(-\frac{t}{\tau_{on}}\right) \tag{11}$$

with:

$$I_{on,max} = I_{p,0} \frac{C_m}{C_m + C_p} \tag{12}$$

$$I_{\text{stat}} = I_{\text{p,0}} \frac{G_{\text{m}}}{G_{\text{m}} + G_{\text{p}} + \frac{I_{\text{p,0}}}{V^*}} \tag{13}$$

$$\tau_{\text{on}} = \frac{C_{\text{m}} + C_{\text{p}}}{G_{\text{m}} + G_{\text{p}} + \frac{I_{\text{p,0}}}{V^*}} . \tag{14}$$

The time course of the current after switching the light off at time $t \geq t_{\text{off}}$ and with $I_{\text{p,0}} = 0$ can be obtained in the same way resulting in:

$$I(t) = -I_{\text{off,max}} \exp\left(-\frac{t}{\tau_{\text{off}}}\right) \tag{15}$$

with:

$$I_{\text{off,max}} = \frac{I_{\text{p,0}}\left(G_{\text{m}} + G_{\text{p}}\right)}{G_{\text{m}} + G_{\text{p}} + \frac{I_{\text{p,0}}}{V^*}} \left(\frac{G_{\text{m}}}{G_{\text{m}} + G_{\text{p}}} - \frac{C_{\text{m}}}{C_{\text{m}} + C_{\text{p}}}\right) \tag{16}$$

$$\tau_{\text{off}} = \frac{C_{\text{m}} + C_{\text{p}}}{G_{\text{m}} + G_{\text{p}}} . \tag{17}$$

Using these equations, the photocurrent of the proton pump activity of bR in PM-fragments immobilized on nano-BLMs for a designated set of the parameters C_{m}, C_{p}, G_{m}, G_{p}, $I_{\text{p,0}}$ and V^* was simulated. Values for C_{m} and G_{m} were chosen according to results obtained from impedance spectroscopy, whereas C_{p} and G_{p} were set to reasonable values. $I_{\text{p,0}}$ and V^* were adapted in a way that the current simulations resemble the measured photocurrents. For the simulations, G_{p} was varied to account for the conductance changes of the membrane induced by the addition of protonophors (Fig. 17 A). Starting from $G_{\text{p}} = 10^{-12}$ S, the conductance was increased to

$5 \cdot 10^{-9}$ S and $5 \cdot 10^{-8}$ S. All current traces are characterized by two transient currents occurring when switching the light on and off. Dependent on the chosen conductance value for G_p, a certain value for the stationary current I_{stat} is reached. The maximum current of the transient when switching the light on ($I_{max,on}$) is not influenced by G_p, while $I_{max,off}$ decreases with decreasing G_p. A change in the capacitance of the bilayer would evoke significant changes in the time constants τ_{on} and τ_{off} of the transient current. However, as the bilayer capacitance does not vary considerably during the course of a photocurrent experiment, we do not show the corresponding current traces.

(*ii*) *bR Inserted in Pore-Spanning Membranes*

In the second scenario, bR was assumed to be reconstituted into pore-suspending membranes (model B) (Fig. 17 B). While the bR-containing membrane is represented by the elements C_p, R_p and I_p, the underlying electrochemical system composed of the buffer-filled porous alumina substrate is simply represented by an Ohmic resistance R_{el} (Fig. 17 B). By an analysis of the given equivalent circuit, differential Eq. (18) is derived, which contains the electrical properties of the pore-spanning bilayer, C_p and G_p, as well as the conductance G_{el} of the electrolyte including the buffer-filled pores:

$$I_{p,0}\left(1-\frac{V_p}{V^*}\right) = V_p G_m + \dot{V}_p C_p + V_p G_{el} \tag{18}$$

The conductance of the electrolyte G_{el} and the voltage generated by the active bR molecules determine the measured pump current $I(t)$ (Eq. 19):

$$I(t) = U_p G_{el} \tag{19}$$

Together with Eq. (19), the solution of differential Eq. (18) yields the following expression for the light-activated process:

$$I(t) = I_{\text{on,max}} \left(1 - \exp\left(-\frac{t}{\tau_{\text{on}}} \right) \right) \tag{20}$$

with the initial maximum current $I_{\text{on,max}}$ and the time constant τ_{on} defined as:

$$I_{\text{on,max}} = \frac{G_{\text{el}} I_{\text{p,0}}}{G_{\text{el}} + G_{\text{p}} + \frac{I_{\text{p,0}}}{V^*}} \tag{21}$$

$$\tau_{\text{on}} = \frac{C_{\text{p}}}{G_{\text{p}} + G_{\text{el}} + \frac{I_{\text{p,0}}}{V^*}} \tag{22}$$

The measured current after switching the light source off is described by Eq. (23):

$$I(t) = I_{\text{off,max}} \exp\left(-\frac{t}{\tau_{\text{off}}} \right) \tag{23}$$

with the maximum current when switching the light off ($I_{\text{off,max}}$) and its time constant τ_{off}:

$$I_{\text{off,max}} = \frac{G_{\text{el}} I_{\text{p,0}}}{G_{\text{el}} + G_{\text{p}} + \frac{I_{\text{p,0}}}{V^*}} \tag{24}$$

$$\tau_{\text{off}} = \frac{C_{\text{p}}}{G_{\text{p}} + G_{\text{el}}} . \tag{25}$$

Based on these equations, we carried out simulations, which take the electrical properties of the pore-spanning membrane and electrolyte into account, as determined by impedance analysis.

Whilst the conductance of the bilayer was varied between $G_p = 10^{-12}$ S and $5 \cdot 10^{-4}$ S, the electrolyte conductance was kept constant at $G_{el} = 10^{-3}$ S. The resulting theoretical photocurrent curves are displayed in Fig. 17 B. In contrast to the photocurrent that was simulated assuming model A, the initial current after switching the light source on does not decay in a transient fashion but is constant at a certain value. This value is nearly preserved even if the bilayer conductance increased by seven orders of magnitude. Only if G_p is increased to $5 \cdot 10^{-4}$ S, the photocurrent drops significantly and reaches the regime of the electrolyte resistance. Variations in C_p do not change the course of the photocurrent. Therefore, the bR-doped pore-spanning bilayer solely acts as an insulator to enable the detection of an electrical signal between two electrolyte-filled measuring chambers.

2. Attachment of Purple Membranes to Nano-BLMs

(*i*) *Functionality of bR in PM-fragments adsorbed on nano-BLMs*

Purple membranes have been adsorbed on many substrates in order to investigate the light-induced photocurrent generated by bR. Substrates include membranes like BLMs[94-96] and SSMs[97,98] immobilized on inorganic, conducting materials such as gold[99] or tin-oxide. Especially BLMs and SSMs are well-suited for the investigation of electrical properties of ion translocating proteins like bR. However, BLMs suffer from short lifetimes. This problem can be overcome by using SSMs that exhibit a high long-term stability. Unfortunately, they do not allow measuring stationary currents due to the capacitance of the underlying support, which serves as the electrode. For the purpose of detecting proton transport, nano-BLMs were chosen as a suitable alternative as they provide a long-term stable membrane system (Section II) that additionally is expected to allow for monitoring stationary currents generated by immobilized bR. In order to prove this notion, PM-fragments were adsorbed to preformed nano-BLMs. Adsorption was mediated by the addition of octadecylamine, which renders the nano-BLM positively charged so that the negatively charged PM can adsorb electrostatically. Illumination of the membrane-covered porous surface

was achieved through a glass window in the *cis* compartment of the measuring chamber (Fig. 1 A) with the light of a halogen lamp filtered with a 515 nm cut-off filter. Platinised platinum wires immersed into the buffer solution served as electrodes to detect potential differences across the nano-BLMs. Prior to performing photo-induced photocurrent measurements it is essential to check for photoartefacts, which are intrinsic to the applied system. Thus, nano-BLMs were illuminated in the absence of PM-fragments. As illustrated in Fig. 18 A, photoartefacts known from the illumination of solid supported membranes immobilized on gold electrodes[22,97] were not observed using nano-BLMs on porous alumina.

If PM-fragments are attached to the nano-BLM, a characteristic current trace is observed. When switching the light source on, the photocurrent is characterized by a positive net current of protons from the *cis* to the *trans* compartment (Fig. 18 A). After reaching a maximum value, the net current declines to zero. According to the theoretical model A, the photocurrent decreases to zero when the membrane resistance R_m of the underlying bilayer is infinitely large. By EIS measurements prior to the adsorption of PM-fragments, we were able to elucidate the electrical properties of the nano-BLMs. R_m proved to be in the gigaohm range, which suggests that the bilayer acts as a perfect insulator to proton currents. In this case, solely the capacitance of the nano-BLM governs the course of the photocurrent during illumination, as corroborated by the simulations depicted in Fig. 17 A. Upon switching the light source off, a negative transient current is observed. This is a result of the potential difference built up during the proton pumping activity of bR and indicates that the protons diffuse back across the bilayer. The observed net current indicates that there is a favoured orientation of the PM fragments adsorbed on the nano-BLM. Since the adsorption of purple membranes is partially driven by the electrostatic interaction between the negatively charged membrane fragments and the positively charged detergent octadecylamine in the nano-BLM, the favoured orientation might be influenced by the surface charge density of the two leaflets of the PM. The cytoplasmic surface exhibits a surface charge density of -0.22 C m^{-2},

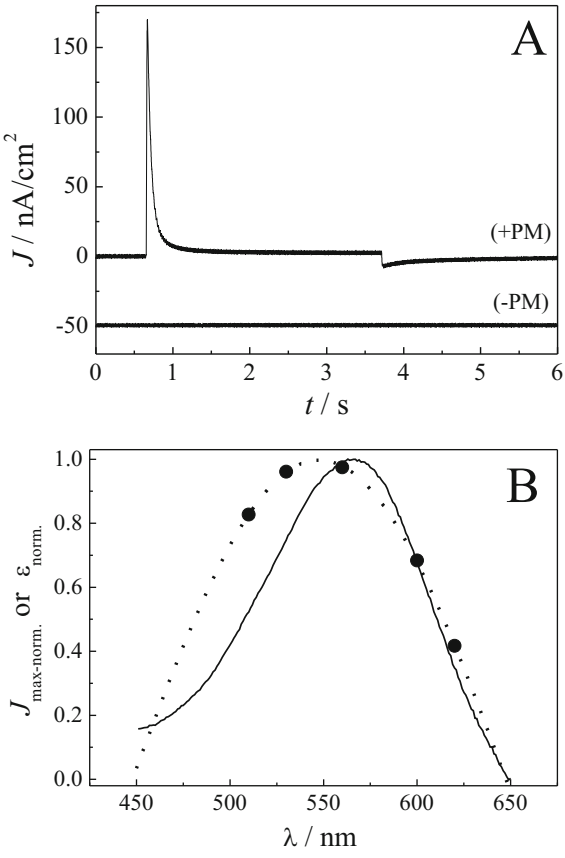

Figure 18. A) Photocurrent before (- PM) and after (+ PM) addition of purple membranes to the *cis* compartment. (+ PM) The first transient corresponds to switching the light on, the second transient to switching the light off. The current was recorded 40 min after addition of purple membranes to a nano-BLM. (- PM) The current trace corresponds to the signal recorded before addition of purple membranes. No significant photoartefact can be detected. For clarity, the current trace is shifted by –50 nA cm^{-2}. B) Action spectrum of bR. The action spectrum is represented as the normalized peak current density. The dashed line is a Gaussian function fit to the spectrum. A peak maximum of λ_{max} = 548 nm is obtained. For comparison, the absorption spectrum of purple membranes in solution was measured (solid line). The characteristic maximum absorbance of bR was found at 568 nm.[107]

while that of the extracellular surface is calculated to be only -0.08 C m^{-2} at neutral pH.[100] This difference in surface charge density would imply a preferential attachment of the cytoplasmic surface to the bilayer, while the extracellular side faces the *cis* compartment, which would in principle result in a proton transport direction from the nano-BLM towards the solution (*cis* compartment). Since the proton transport is observed in the opposite direction, at least part of the purple membrane fragments are oriented in the other direction and the current is dominated by this purple membrane fraction. It is also well conceivable that not the surface charge density but the different morphologies of the extracellular and cytoplasmic side of the PM leads to a preferential adsorption, with the extracellular side facing the nano-BLM.

To further prove that the observed proton currents are a result of bR activity, an action spectrum was measured by monitoring the initial current density using a series of narrow-band filters (Fig. 18 B). Compared to the absorption spectrum of purple membranes in solution, the action spectrum obtained from purple membranes adsorbed on nano-BLMs is shifted from 568 nm by about 20 nm to 548 nm. This observation is in accordance with previously published results, where purple membranes were attached to classical BLMs.[93] The authors monitored an action spectrum that was blue shifted by about 15 nm compared to the absorption spectrum of purple membranes in solution. Furthermore, we were able to identify the light dependence of the maximum current densities after switching the light on and off, respectively (Fig. 19). The pump current $I_{p,0}$ is defined as the current at $V_p = 0$ and, therefore, I_{max} depends on the light intensity L according to Eq. (26):

$$I_{p,0} = I_{p,0}^{s} \frac{L}{L + L_{\frac{1}{2}}} \tag{26}$$

where $I_{p,0}^{s}$ is the saturation current of $I_{p,0}$ for $L \rightarrow \infty$ and $L_{1/2}$ is the half-saturation intensity. We observed that the activity of bR, measured as the maximum current density under illumination as a function of the relative light intensity, follows the theoretically predicted course. Whilst $J_{max,on}$ is strongly dependent on L, $J_{max,off}$ changes only slightly with L.

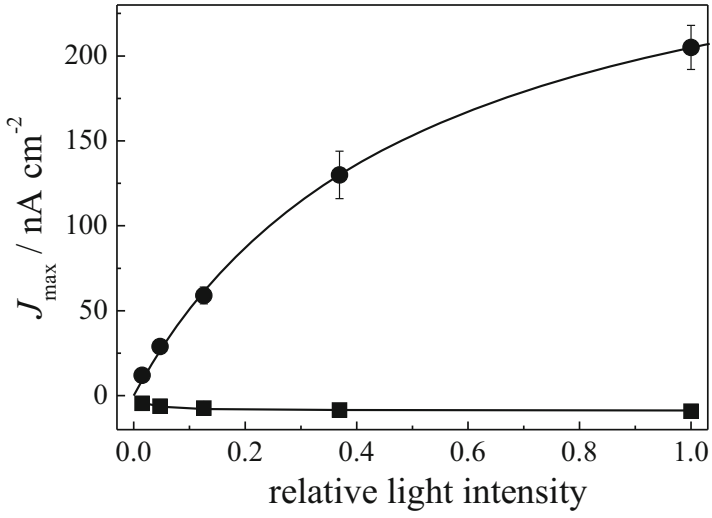

Figure 19. Maximum current density J_{max} as a function of light intensity. (●): $J_{max,on}$, (■): $J_{max,off}$. The solid lines are the results of fitting the parameters of Eqs. (11), (15) and (26) to the data with the following results: C_m = 1 µF cm^{-2} (fixed), C_p = 2 µF cm^{-2} (fixed), G_m = 10 nS cm^{-2} (fixed), G_p = 1 µS cm^{-2} (fixed), $J^s_{p,0}$= (930 ± 30) nA cm^{-2}, $L_{1/2}$ = (0.5 ± 0.1), V^* = (0.010 ± 0.001) V.[107]

(*ii*) *Influence of the Ionophore CCCP*

We stated earlier that one of the advantages of nano-BLMs over SSMs for monitoring light-induced bR-photocurrents lies in the notion that nano-BLMs provide a second aqueous reservoir, which should allow for observing stationary photocurrents. In order to verify this hypothesis, the ionophore carbonyl-cyanide-*m*-chloro-phenylhydrazone (CCCP), a proton gradient decoupler,[101] was used to permeabilise the nano-BLMs when PM-fragments were adsorbed. During the course of illumination in the presence of CCCP, a positive stationary photocurrent of a distinct value, depending on the concentration of the ionophore, is detected (Fig. 20 A).

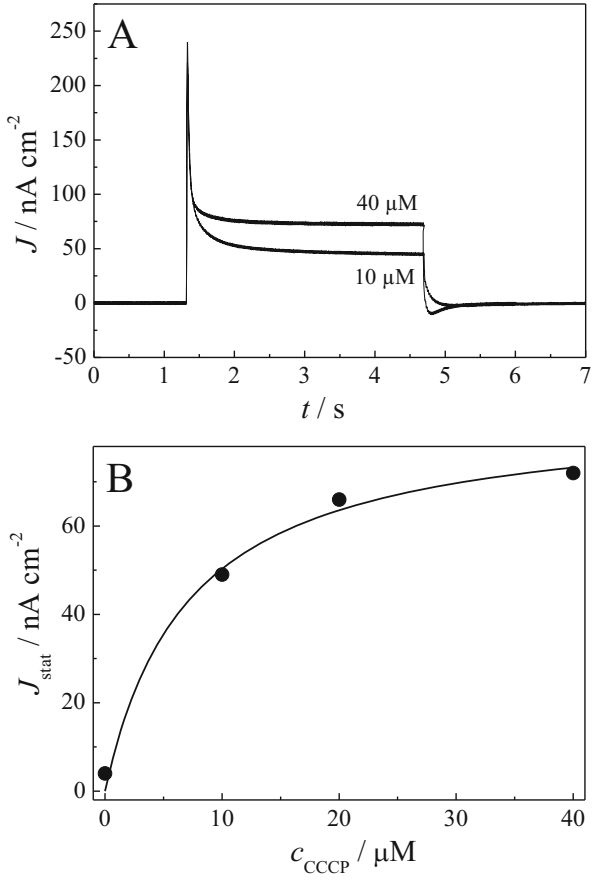

Figure 20. A) Photocurrent 15 min after the addition of 10 and 40 µM CCCP, respectively. B) Stationary current density J_{stat}, obtained 1.5 s after switching the light on as a function of the CCCP-concentration in solution. The solid line demonstrates the saturation behaviour as expected from Eq. (28).[107]

From this result we suggest that the protons flow from the purple membrane across the nano-BLM facilitated by the proton ionophore CCCP into the pores of the underlying porous alumina substrate. Since the stationary current does not decrease within a prolonged time period of continuous illumination (10 min), we conclude that the pores do not form a significant diffusion barrier for protons. It is well conceivable that protons are well directed along the pores down their concentration gradient, as the substrate and, thus, the walls of the pores are composed of a negatively charged oxide.

In Fig. 20 B, the stationary current is shown as a function of the ionophore concentration. Theoretically, if the conductance G_m of the nano-BLMs is linearly dependent on the ionophore concentration,[101] the stationary current changes with the CCCP concentration c_{CCCP} in solution according to Eqs. (27) and (28):

$$G_m = G_0 + s \cdot c_{CCCP} \tag{27}$$

$$J_{stat} = J_{p,0} \frac{G_0 + s \cdot c_{CCCP}}{\left(G_0 + s \cdot c_{CCCP}\right) + G_p + \dfrac{J_{p,0}}{V^*}}. \tag{28}$$

By keeping values for G_0, G_p and V^* constant, Eq. (28) was fit to the data, which results in the solid line shown in Fig. 20 B and which is in good accordance with the data points. For the parameter s, which indicates the change of the stationary current per concentration unit, a value of approximately 1 μS cm^{-2} μM^{-1} is obtained. This value is in the same order of magnitude as that obtained from experiments on BLMs with 6.6 μS cm^{-2} μM^{-1}.[101] However, no stationary photocurrent was detected when PM-fragments adsorbed on SSMs were illuminated.[97] The SSMs in this study were composed of an octadecanethiol monolayer on gold and a second phospholipid monolayer. With no aqueous reservoir between the gold electrode and the bilayer, a stationary current cannot be observed upon addition of ionophore as the underlying substrate limits the ion flux. In this case, the membrane merely acts as a capacitor, so that only the charging of this capacitor is observed. In contrast, nano-BLMs are sensitive to changes in membrane re-

sistance as this system allows the flux of ions from the *cis* to the *trans* compartment and vice versa. Of note, the discussion of stationary currents is based on the hypothesis that only the membrane conductance G_m of the nano-BLMs is modulated by CCCP, whereas the conductive properties of the crystal-like PM-fragments G_p is unaffected. Hendler et al.[102] were able to show that PM-fragments are, however, indeed permeabilised by CCCP. Hence, the analysis of the stationary current following Eq. (28) might be too simplistic and needs to be improved. Another point of discussion is the observation that the stationary current reaches saturation at a CCCP-concentration of about 70 µM (Fig. 20 B). To elucidate this observation, we simulated I_{stat} based on Eq. (13). For $I_{p,0}$, V^* and G_m, values were kept constant, while G_p was varied in a range of 10^{-4} - 10^{-9} S. In the case of $G_p << G_m$, the stationary current I_{stat} reaches a maximum value. For $G_p >> G_m$, however, I_{stat} goes to zero. The most significant change of I_{stat} is observed for G_m in a range of 10^{-5} - 10^{-6} S. This matches the ratio of $I_{p,0}$ and V^*. We reason that the maximum value of the stationary current observed in photocurrent measurements on PM-fragments in the sandwich configuration depends on the intrinsic parameters $I_{p,0}$ and V^*.

3. Insertion of bR in Pore-Spanning Membranes

The ultimate goal is to reconstitute a transporter protein into a pore-spanning membrane by fusing and spreading proteoliposomes to obtain large protein densities. For the experiments described in this chapter, the setup depicted in Fig. 1 B was used with partially open alumina pore arrays. Similar to the protocol used for the reconstitution of gramicidin into pore-suspending membrane, first a bilayer is formed on the functionalized porous alumina substrate followed by the incubation with bR-containing liposomes, which were prepared by the reversed phase method.[103] The vesicles were composed of DPhPC/DOPC/1,2-dipalmitoyl-*sn*-glycero-3-phosphate (DPPA) (6:3:1) doped with 1 mol% bR. It is known that the negatively charged headgroups of DPPA enhance the photocurrents.[104] Prior to the addition of bR-containing vesicles, control experiments were performed to rule out any photoartefacts. The electrical characterisation of the system prior to and after the addition of the proteoliposomes was performed using EIS. The light-induced proton pumping activity was detected by platinised plati-

num electrodes immersed in the buffer-filled compartments of the setup. In the following, we will present two different characteristic photocurrent traces that were obtained during the course of the experiments. The recorded photocurrent upon illumination of the bR-containing membrane, shown in Fig. 21 A (scenario A), is considerably different from that shown in Fig. 21 C (scenario B). The photocurrent depicted in Fig. 21 A rises to a constant value upon switching the light on, and decreases to zero upon switching the light off. However, for the photocurrent shown in Fig. 21 C, first a transient current is observed upon illumination, followed by a small stationary current density of about 0.15 nA cm^{-2}. Upon switching the light off, a second transient current is observed. If 2 µM of the protonophor CCCP is added, the initial maximum current is increased, as well as the steady state current.

To elucidate why, in principle, two different current traces are monitored, impedance spectra were recorded, providing additional information about the electric properties of the bilayers. In both cases, the impedance data revealed that insulating pore-suspending bilayers were formed after the addition of bR-free liposomes. A resistance at low frequencies of more than 10^5 Ω is obtained. However, the impedance spectrum shown in Fig. 21 D exhibits two dispersions, which is an indication of incomplete vesicle fusion (see Fig. 5 B), while that depicted in Fig. 21 B shows only one dispersion. In the same manner, after incubation with bR-containing liposomes, the impedance spectra differ considerably. The absolute value of the impedance depicted in Fig. 21 D still features two dispersions and indicates only a slight drop in the overall resistance, whereas the impedance shown in Fig. 21 B monitored after incubation with bR-containing liposomes has dropped by one order of magnitude.

From these results together with the theoretical considerations (Section V.1), we conclude that pore-suspending membranes doped with bR molecules have been formed in scenario A. The proteins are integrated into the pore-suspending bilayer, thus pumping the protons into the underlying aqueous phase of the pores. In this case, model B (Fig. 17 B) is valid. The simulation based on model B and the experimental data are strikingly similar. The finite increasing and decreasing current in the experiment (Fig. 21 A) is a result of the filter function used to filter the data. The photocurrent shown in Fig. 21 C (scenario B) is interpreted as

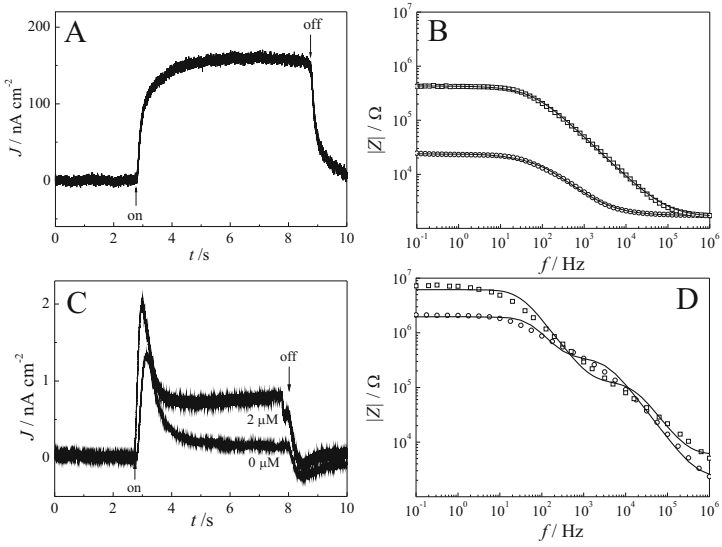

Figure 21. A/C) Photocurrent measurements on pore-spanning membranes incubated with bR-doped liposomes upon illumination using a halogen lamp as a light source and a cut-off-filter of 515 nm. B) (□) Impedance spectrum 7.5 h after the addition of DPhPC/DOPC (6:4) LUVs doped with 0.1 mol% octadecylamine. (○) Impedance spectrum 12 h after the addition of bR-doped vesicles composed of DPhPC/DOPC/DPPA (6:3:1) containing 1 mol% bR. Data analysis was performed using the equivalent circuit depicted in Fig. 5 B with the following results: (□) R_{el} = 1700 Ω, $R_m = 4.3 \cdot 10^5$ Ω, A = $2.4 \cdot 10^{-8}$ F $s^{\alpha-1}$ and $\alpha = 0.77$; (○) R_{el} = 1700 Ω, $R_m = 2.2 \cdot 10^4$ Ω, A = $1.7 \cdot 10^{-7}$ F $s^{\alpha-1}$, and $\alpha = 0.71$. D) (□) Impedance spectrum 24 h after the addition of DPhPC/DOPC (6:4) LUVs doped with 0.1 mol% octadecylamine. (○) Impedance spectrum 14 h after the addition of bR-containing vesicles. Data analysis was based on the equivalent circuit depicted in Fig. 7 C with the following result: (□) R_{el} = 5890 Ω, $R_{m1} = 1.1 \cdot 10^5$ Ω, $C_{m1} = 0.10 \cdot 10^{-9}$ F, $R_{m2} = 6.1 \cdot 10^6$ Ω, and $C_{m2} = 0.9 \cdot 10^{-9}$ F; (○) R_{el} = 2290 Ω, $R_{m1} = 3.1 \cdot 10^5$ Ω, $C_{m1} = 0.15 \cdot 10^{-9}$ F, $R_{m2} = 1.7 \cdot 10^6$ Ω and $C_{m2} = 1.81 \cdot 10^{-9}$ F. Buffer: 10 mM TRIS, 100 mM KCl, pH 7.4.

bR-containing vesicles hemifused to the pore-suspending membrane. In this case, two populations of bR-molecules contribute to the monitored light-induced photocurrent. Proteins that span the bilayer as found in scenario A provide the stationary current, while bR remaining in hemi-fused liposomes build up a transient current similar to what has been found for PM-fragments adsorbed to nano-BMLs. In this case, the equivalent circuit shown in Fig. 17 A

holds, which reproduces the photocurrent quite well. Our results resemble those found by Bamberg et al.,[91] who added bR-doped liposomes to a freestanding lipid bilayer. They also allocated a non-zero stationary photocurrent in the absence of a proton decoupler to the activity of integrated bR.

Independent of the scenario found on the porous surface, the proton pump bR is actively reconstituted. As the proton transport of bR is unidirectional from the C- to the N-terminus, only the net current is monitored as a result of an excess orientation of the proteins in one direction. Thus, we can state that more than 50 % are directed with the C-terminus towards the *cis* side of the membrane. It remains, however, unclear how many proteins have been reconstituted. It is known that, by using the reversed phase method,[103,105] bR is predominantly reconstituted in liposomes with the C-terminus facing the outer membrane leaflet. If one assumes that the direction of integration is preserved, when bR is transferred from the proteoliposomes to the pore-spanning bilayer, a mechanism for liposome spreading can be suggested. Whereas on hydrophilic supports liposomes unroll in a fashion that renders the inner leaflet of the membrane facing upwards, on hydrophobic materials the inner membrane leaflet of liposomes is directed downwards.[39] From the photocurrent results we conclude that liposomes spreading on CPEO3-functionalized porous alumina spread in a way that is described for vesicles on hydrophobic surfaces.

To investigate the net orientation, one could make use of lanthanium cations, which interact with bR at its C-terminus and block the proton pump activity.[106] From the remaining signal, the orientation of the molecules could be estimated. Considering a turnover rate of 100 protons s^{-1}, approximately $6 \cdot 10^7$ molecules contribute to the signal displayed in Fig. 21 A. With a protein area of 11.5 nm^2, 0.06 % of the electrically active area would be covered by protein. This area fraction is significantly smaller than what is expected if all proteins are transferred from the liposomes containing 1 mol% bR to the pore-suspending bilayer.

Another interesting aspect is the susceptibility of pore-spanning membranes to the protonophor CCCP. While, in case of nano-BLMs, up to 40 µM CCCP was added to obtain a significant increase in stationary current, only 2 µM is required to significantly increase the stationary current during the illumination process. This result is in line with the notion that pore-spanning membranes

are, in general, more sensitive to permeabilising agents as they lack remaining organic solvent (see Fig. 12). A similar influence of solvent was observed for SSMs with adsorbed PM-fragments. While the photocurrent signal obtained from SSMs prepared in the presence of organic solvent was not influenced by CCCP up to a concentration of 20 μM, the current signal gained from solvent-free SSMs indicated that an electrically permeable layer is formed.

VI. CONCLUDING REMARKS

We have developed two different methods to prepare pore-suspending membranes, which both exhibit a high long-term stability, while they are accessible from both aqueous sides. While nano-BLMs allow for ion channel recordings on the single channel level, pore-suspending membranes obtained from fusing unilamellar vesicles on a functionalized porous alumina substrate enable us to generate membranes with high protein content. However, these membranes exhibit a considerably lower membrane resistance compared to nano-BLMs. In summary, pore-suspending membranes are available that might pave the way for chip-based technologies, giving access to functional assays for ion channels and transporter proteins.

ACKNOWLEDGMENTS

We like to thank the DFG and BMBF for financial support. E.K. Schmitt thanks the Fonds der Chemischen Industrie for a PhD fellowship.

REFERENCES

[1]B. Hille, *Ion channles of excitable membranes*, ed., Sinauer Associates Inc., 2001.
[2]F. M. Ashcroft, *Ion channels and disease*, ed., Academic Press, 2000.
[3]E. Neher, B. Sakmann, *Nature* **260** (1976) 799.
[4]H. Suzuki, K. V. Tabata, H. Noji, S. Takeuchi, *Biosens. Bioelectron.* **22** (2007) 1111.
[5]M. Zagnoni, M. E. Sandison, P. Marius, A. G. Lee, H. Morgan, *Lab Chip* **7** (2007) 1176.

[6]C. Farre, M. Geroge, A. Brüggemann, N. Fertig, *Drug Discovery Today: Technologies* **5** (2008) e23.
[7]A. Janshoff, C. Steinem, *Anal. Bioanal. Chem.* **385** (2006) 433.
[8]R. Robelek, E. S. Lemker, B. Wiltschi, V. Kirste, R. Naumann, D. Oesterhelt, E. K. Sinner, *Angew. Chem. Int. Ed.* **46** (2007) 605.
[9]A. Michalke, T. Schürholz, H.-J. Galla, C. Steinem, *Langmuir* **17** (2001) 2251.
[10]M. Tanaka, E. Sackmann, *Nature* **437** (2005) 656–663.
[11]W. Knoll, Köper I., R. Naumann, E. K. Sinner, *Electrochimica Acta* **53** (2008) 6680.
[12]V. Atanasov, N. Knorr, R. S. Duran, S. Ingebrandt, A. Offenhäusser, W. Knoll, I. Köper, *Biophys. J.* **89** (2005) 1780.
[13]I. K. Vockenroth, P. P. Atanasova, J. R. Long, A. T. Jenkins, W. Knoll, I. Köper, *Biochim. Biophys. Acta* **1768** (2007) 1114.
[14]S. Terrettaz, M. Mayer, H. Vogel, *Langmuir* **19** (2003) 5567.
[15]R. Naumann, T. Baumgart, P. Gräber, A. Jonczyk, A. Offenhäusser, W. Knoll, *Biosens. Bioelectron.* **17** (2002) 25.
[16]E. Reimhult, K. Kumar, *Trends Biotechnol.* **26** (2007) 82.
[17]M.-C. Chien, G.-J. Wang, W. C. Yu, *Jap. J. Appl. Phys.* **46** (2007) 7436.
[18]C. Danelon, A. Suenaga, M. Winterhalter, I. Yamato, *Biophys. Chem.* **104** (2003) 591.
[19]G. Favero, L. Capanella, S. Cavallo, A. D'Annibale, M. Perrella, E. Mattei, T. Ferri, (2005)
[20]C. Steinem, A. Janshoff, W. P. Ulrich, M. Sieber, H. J. Galla, *Biochim. Biophys. Acta* **1279** (1996) 169.
[21]G. Wiegand, N. Arribas-Layton, H. Hillebrandt, E. Sackmann, P. Wagner, *J. Phys. Chem. B* **106** (2002) 4245.
[22]C. Hennesthal, C. Steinem, *J. Am. Chem. Soc.* **122** (2000) 8085.
[23]W. Römer, Y. H. Lam, D. Fischer, A. Watts, W. B. Fischer, P. Göring, R. B. Wehrspohn, U. Gösele, C. Steinem, *J. Am. Chem. Soc.* **126** (2004) 16267.
[24]W. Römer, C. Steinem, *Biophys. J.* **86** (2004) 955.
[25]C. Steinem, *Advances on planar lipid bilayers and liposomes, Leitmannova Lui, A. (Series Ed.)* **chapter 3** (2008) 59.
[26]E. K. Schmitt, C. Steinem, *Biophys. J* **91** (2006) 2163.
[27]R. Benz, O. Fröhlich, P. Läuger, M. Montal, *Biochim. Biophys. Acta* **394** (1975) 323.
[28]D. Weiskopf, E. K. Schmitt, M. H. Klühr, S. K. Dertinger, C. Steinem, *Langmuir* **23** (2007) 9134.
[29]M. Böcker, S. Muschter, E. K. Schmitt, C. Steinem, T. E. Schäffer, *Langmuir* **5** (2009) 3022.
[30]R. J. White, E.N. Ervin, T. Yang, X. Chen, S. Daniel, P. S. Cremer, H. S. White, *J. Am. Chem. Soc.* **129** (2007) 11766.
[31]M. Sondermann, M. George, N. Fertig, J. C. Behrends, *Biochim. Biophys. Acta* **1758** (2006) 545.
[32]M. Montal, P. Mueller, *Proc. Natl. Acad. Sci. U. S. A.* **69** (1972) 3561.
[33]C. Hennesthal, J. Drexler, C. Steinem, *ChemPhysChem* **3** (2002) 885.
[34]J. Drexler, C. Steinem, *J. Phys. Chem. B* **107** (2003) 11245.
[35]E. K. Schmitt, M. Nurnabi, R. J. Bushby, C. Steinem, *Soft Matter* **4** (2008) 250.
[36]A. T. A. Jenkins, R. J. Bushby, N. Boden, S. D. Evans, P. F. Knowles, Q. Liu, R. E. Miles, S. D. Ogier, *Langmuir* **14** (1998) 4675.

[37]L. J. C. Jeuken, N. N. Daskalakis, X. Han, K. Sheikh, A. Erbe, R. J. Bushby, S. D. Evans, *Sens. Actuators B* **124** (2007) 501.
[38]E. K. Schmitt, C. Weichbrodt, C. Steinem, *Soft Matter* **5** (2009) 2247.
[39]A. T. A. Jenkins, R. J. Bushby, EvansS.D., W. Knoll, A. Offenhäuser, S. D. Ogier, *Langmuir* **18** (2002) 3176.
[40]T. Okazaki, K. Morigaki, T. Taguchi, *Biophys. J.* **91** (2006) 1757.
[41]C. Steinem, A. Janshoff, K. von dem Bruch, K. Reihs, J. Goossens, H.-J. Galla, *Bioelectrochem. Bioenerg.* **45** (1998) 17.
[42]R. Naumann, D. Walz, S. M. Schiller, W. Knoll, *J. Electroanal. Chem.* **550-551** (2003) 241.
[43]G. Favero, L. Campanella, A. D'Annibale, R. Santucci, T. Ferri, *Microchem. J.* **74** (2003) 141.
[44]P. C. Gufler, D. Pum, U. B. Sleytr, B. Schuster, *Biochim. Biophys. Acta* **1661** (2004) 154.
[45]X. J. Han, A. Studer, H. Sehr, I. Geissbühler, M. Di Berardino, F. K. Winkler, L. X. Tiefenauer, *Adv. Mater.* **19** (2007) 4466.
[46]B. Raguse, V. Braach-Maksvytis, B. A. Cornell, L. G. King, P. D. J. Osman, R. J. Pace, L. Wieczorek, *Langmuir* **14** (1998) 648.
[47]C. Kepplinger, I. Höfer, C. Steinem, *Chem. Phys. Lipids* **160** (2009) 109.
[48]S. B. Hladky, D. A. Haydon, *Biochim Biophys Acta* **274** (1972) 294.
[49]R. Sarges, B. Witkop, *J. Am. Chem. Soc.* **87** (1965) 2011.
[50]E. Bamberg, P. Läugner, *J. Membr. Biol.* **35** (1977) 351.
[51]A. Finkelstein, O. S. Andersen, *J. Membr. Biol.* **59** (1981) 155.
[52]B. A. Cornell, V. Braach-Maksvytis, L. G. King, P. D. J. Osman, B. Raguse, L. Wieczorek, R. J. Pace, *Nature* **387** (1997) 580.
[53]O. Purrucker, H. Hillebrandt, K. Adlkofer, M. Tanaka, *Electrochim. Acta* **47** (2001) 791.
[54]B. A. Cornell, V. L. B. Braach-Maksvytis, L. G. King, P. D. J. Osman, L. Wieczorek, B. Raguse, R. J. Pace, *Nature* **387** (1997) 580
[55]G. Krishna, J. Schulte, B. A. Cornell, R. J. Pace, P. D. Osman, *Langmuir* **19** (2003) 2294.
[56]A. D. Milov, R. I. Samiloiva, Y. D. Tsvetkov, F. Formaggio, C. Toniolo, J. Raap, *J. Am. Chem. Soc.* **129** (2007) 9260.
[57]D. S. Cafiso, *Ann. Rev. Biophys. Biomol. Struct.* **23** (1994) 141.
[58]C. Pilz, C. Steinem, *Eur. Biophys. J.* **37** (2008) 1065.
[59]J. D. Lear, Z. R. Wasserman, W. F. DeGrado, *Science* **240** (1988) 1177.
[60]K. S. Akerfeldt, J. D. Lear, Z. R. Wasserman, L. A. Chung, W. F. DeGrado, *Acc Chem. Res.* **26** (1993) 191.
[61]L. A. Chung, J. D. Lear, W. F. DeGrado, *Biochemistry* **31** (1992) 6608.
[62]H. S. Randa, L. Forrest, G. Voth, M. Sansom, *Biophys. J.* **77** (1999) 2400.
[63]R. Hemmler, G. Böse, R. Wagner, R. Peters, *Biophys. J.* **88** (2005) 4000.
[64]L. K. Buehler, S. Kusumoto, H. Zhang, J. P. Rosenbusch, *J. Biol. Chem.* **266** (1991) 24446.
[65]S. W. Cowan, T. Schirmer, G. Rummel, M. Steiert, R. Ghosh, R. A. Pauptit, J. N. Jansonius, J. P. Rosenbusch, *Nature* **358** (1992) 727.
[66]H. Miedema, A. Meter-Arkema, J. Wierenga, J. Tang, B. Eisenberg, W. Nonner, H. Hektor, D. Gillespie, W. Meijberg, *Biophys. J.* **87** (2004) 3137.
[67]E. M. Nestorovich, C. Danelon, M. Winterhalter, S. M. Bezrukov, *Proc. Natl. Acad. Sci. U. S. A.* **99** (2002) 9789.
[68]A. L. Harris, *Q. Rev. Biophys.* **34** (2001) 325.

[69]O. Gaßmann, M. Kreir, C. Ambrosi, J. Pranskevich, A. Oshima, C. Röling, G. Sosinsky, N. Fertig, C. Steinem, *J. Struct. Biol.* **168** (2009) 168.
[70]M. M. Falk, L. K. Buehler, N. M. Kumar, N. B. Gilula, *EMBO J.* **16** (1997) 2703.
[71]D. Gonzalez, J. M. Gomez-Hernandez, L. C. Barrio, *FASEB J.* **20** (2006) 2329.
[72]J. Lasch, *Biochim. Biophys. Acta* **1241** (1995) 269.
[73]F. Ollila, J. P. Slotte, *Biochim. Biophys. Acta* **1564** (2002) 281.
[74]V. B. Myers, D. A. Haydon, *Biochim. Biophys. Acta* **274** (1972) 313.
[75]A. J. Bard, L. R. Faulkner, *John Wiley & Sons: New York* (2001)
[76]R. de Levie, N. G. Seidah, H. Moreira, *J. Membr. Biol.* **16** (1974) 17.
[77]S. Gritsch, P. Nollert, F. Jähnig, E. Sackmann, *Langmuir* **14** (1998) 3118.
[78]E. Neher, J. Sandblom, G. Eisenman, *J. Membr. Biol.* **40** (1978) 97.
[79]L. Becucci, M. V. Carbone, T. Biogiotti, M. D'Amico, M. Olivotto, R. Guidelli, *J. Phys. Chem. B* **112** (2008) 1315.
[80]G. Krishna, J. Schulte, B. A. Cornell, R. J. Pace, L. Wieczorek, P. D. Osman, *Langmuir* **17** (2001) 4858.
[81]I. K. Vockenroth, P. P. Atanasova, A. T. A. Jenkins, I. Köper, *Langmuir* **24** (2008) 496.
[82]D. J. McGillivray, G. Valincius, D. J. Vanderah, W. Febo-Ayala, J. T. Woodward, F. Heinrich, J. J. Kasianowicz, M. Lösche, *Biointerphases* **2** (2007) 21.
[83]Z. Samec, A. Trojanek, E. Samcova, *J. Electroanal. Chem.* **389** (1995) 1.
[84]A. E. Vallejo, C. A. Gervasi, *Bioelectrochemistry* **57** (2002) 1.
[85]D. Gassull, A. Ulman, M. Grunze, M. Tanaka, *J. Phys. Chem. B* **112** (2008) 5736.
[86]N. R. Clement, J. M. Gould, *Biochemistry* **20** (1981) 1544.
[87]D. Oesterhelt, W. Stoeckenius, *Nat. New. Biol.* **233** (1971) 149.
[88]R. Henderson, P. Unwin, *Nature* **257** (1975) 28.
[89]J. K. Lanyi, *J. Biol. Chem.* **272** (1997) 31209.
[90]J. K. Lanyi, *Biochim. Biophys. Acta* **1757** (2007) 1012.
[91]E. Bamberg, N. A. Dencher, A. Fahr, M. P. Heyn, *Proc. Natl. Acad. Sci. U. S. A.* **78** (1981) 7502.
[92]T. R. Herrmann, G. W. Rayfield, *Biophys. J.* **21** (1978) 111.
[93]E. Bamberg, H.-J. Appel, N. A. Dencher, W. Sperling, H. Stieve, P. Läuger, *Biophys. Struct. Mech.* **5** (1979) 277.
[94]L. A. Drachev, A. A. Jasaitis, A. D. Kaulen, A. A. Kondrashin, E. A. Liberman, I. B. Nemecek, S. A. Ostroumov, A. Semenov, V. P. Skulachev, *Nature* **249** (1974) 321.
[95]J. Tittor, U. Schweiger, D. Oesterhelt, E. Bamberg, *Biophys. J.* **67** (1994) 1682.
[96]C. Ganea, J. Tittor, E. Bamberg, D. Oesterhelt, *Biochim. Biophys. Acta* **1368** (1998) 84.
[97]K. Seifert, K. Fendler, E. Bamberg, *Biophys. J.* **64** (1993) 384.
[98]A. Dolfi, F. Tadini-Buoninsegni, M. R. Moncelli, R. Guidelli, *Langmuir* **18** (2002) 6345.
[99]H.-G. Choi, J. Min, W. H. Lee, J.-W. Choi, *Colloids Surf. B* **23** (2002) 327.
[100]R. Renthal, C. H. Cha, *Biophys. J.* **45** (1984) 1001.
[101]O. H. Le Blanc, *J. Mem. Biol.* **4** (1971) 227.
[102]R. W. Hendler, L. A. Drachev, S. Bose, M. K. Joshi, *Eur. J. Biochem.* **267** (2000) 5879.
[103]J.-L. Rigaud, A. Bluzat, S. Buschlen, *Biochem. Biophys. Res. Comm.* **111** (1983) 373.

[104]C. Steinem, A. Janshoff, F. Höhn, M. Sieber, H.-J. Galla, *Chem. Phys. Lipids* **89** (1997) 141.
[105]J.-L. Rigaud, M. T. Paternostre, A. Bluzat, *Biochemistry* **27** (1988) 2677.
[106]C.-H. Chang, J.-G. Chen, R. Govindjee, T. Ebrey, *Proc. Natl. Acad. Sci. U. S. A.* **82** (1985) 396.
[107]C. Horn, C. Steinem, *Biophys. J.* **89** (2005) 1046.

Eva K. Schmitt

Eva K. Schmitt was born in 1980 in Schweinfurt (Germany). She studied Chemistry at the University of Bath (UK) and Regensburg (Germany), where she obtained here diploma in 2005. For her PhD she received a fellowship of the *Fond der Chemischen Industrie* and joined the group of Prof. Dr. Claudia Steinem in Göttingen (Germany) to develop artificial membranes with high protein density on porous supports. A fellowship from Boehringer Ingelheim enabled her to complete a research project on human ions channels in Palmerston North (New Zealand). She finished her PhD in 2009 and is now a postdoctoral research fellow in the group of Dr. Richard Callaghan at the University of Oxford, where she investigates multidrug resistance of proteins reconstituted in artificial membranes.

Claudia Steinem

Claudia Steinem, born in 1967, obtained a B.Sc. in Biology and a M.Sc. in Chemistry from the Westfälische Wilhelms-University Münster. Under the tutelage of Hans-Joachim Galla, she received her PhD in 1997. After a postdoctoral stay at the Scripps Research Institute in La Jolla, CA (USA) in the group of Prof. M. Reza Ghadiri, she returned in 1999 to the Institute of Biochemisty at the University of Münster as a Lise-Meitner fellow. Two years later, in 2001, she got a professorship for Bioanalytical Chemistry at the University of Regensburg and finished her habilitation. In 2005, she received an offer from the University of Göttingen for a professorship of Biomolecular Chemistry. Since April 2006, she is full professor at the Institute of Organic and Biomolecular Chemistry with her main research interests in the development and application of multicomponent lipid membranes.

Index

N. Eliaz (ed.), *Applications of Electrochemistry and Nanotechnology in Biology and Medicine II*, Modern Aspects of Electrochemistry 53,
DOI 10.1007/978-1-4614-2137-5, © Springer Science+Business Media, LLC 2012